DISSERTATION

A STUDY OF THE STABILIZATION, CARBONIZATION, AND GRAPHITIZATION OF MESOPHASE PITCH-BASED CARBON FIBERS

Darren K. Rogers

REPORT DOCUMENTATION PAGE

AFRL-SR-BL-TR-98-

6409

1. AGENCY USE ONLY (Leave Blank)	2. REPORT DATE May 1993	3. REPOF Final

4. TITLE AND SUBTITLE	5. FUNDING NUMBERS
A Study of the Stabilization, Carbonization, and Graphitization of Mesophase Pitch-Based Carbon Fibers	

6. AUTHORS
Darren K. Rogers

7. PERFORMING ORGANIZATION NAME(S) AND ADDRESS(ES) Clemson University	8. PERFORMING ORGANIZATION REPORT NUMBER

9. SPONSORING/MONITORING AGENCY NAME(S) AND ADDRESS(ES) AFOSR/NI 110 Duncan Avenue, Room B-115 Bolling Air Force Base, DC 20332-8080	10. SPONSORING/MONITORING AGENCY REPORT NUMBER

11. SUPPLEMENTARY NOTES

12a. DISTRIBUTION AVAILABILITY STATEMENT Approved for Public Release	12b. DISTRIBUTION CODE

13. ABSTRACT *(Maximum 200 words)*
See attached.

19980505 094

DTIC QUALITY INSPECTED

14. SUBJECT TERMS	15. NUMBER OF PAGES
	16. PRICE CODE

17. SECURITY CLASSIFICATION OF REPORT Unclassified	18. SECURITY CLASSIFICATION OF THIS PAGE Unclassified	19. SECURITY CLASSIFICATION OF ABSTRACT Unclassified	20. LIMITATION OF ABSTRACT UL

April 30, 1993

To the Graduate School:

This dissertation entitled "A Study of the Stabilization, Carbonization, and Graphitization of Mesophase Pitch-Based Carbon Fibers" and written by Darren K. Rogers is presented to the Graduate School of Clemson University. I recommend that it be accepted in partial fulfillment of the requirements for the degree of Doctor of Philosophy with a major in Ceramic Engineering.

_____
Dissertation Advisor

We have reviewed this dissertation
and recommend its acceptance:

_____

_____

_____

Accepted for the Graduate School:

_____

A STUDY OF THE STABILIZATION, CARBONIZATION, AND GRAPHITIZATION OF MESOPHASE PITCH-BASED CARBON FIBERS

A Dissertation

Presented to

the Graduate School of

Clemson University

In Partial Fulfillment

of the Requirements for the Degree

Doctor of Philosophy

Ceramic Engineering

by

Darren K. Rogers

May 1993

ABSTRACT

This study concerns the chemical and structural changes that occur during thermal treatment of mesophase pitch-based carbon fibers. This task was part of a larger project sponsored by the Manufacturing Technology Program of the Department of the Navy aimed at producing high thermal conductivity carbon fibers from a thermally polymerized petroleum residue. The pitch was melt spun into circular- and ribbon cross section fibers, having radial (point) and line-origin textures, respectively. Then, the stabilization and carbonization processes were studied using a combination of dynamic and post-treatment techniques.

As a first step, some fundamental relationships were developed between the fiber crystal structure and lattice-dependent physical properties, such as modulus or thermal conductivity. They were based upon the theory of specific heat capacity and phonon conduction in solids. These relationships provided a useful way of characterizing the quality of graphitic structure developed during thermal treatment and allowed the prediction of lattice-dependent physical properties from a minimum of structural data.

Next, the stabilization and carbonization processes were examined by a series of analytical techniques. Such experiments were designed to clarify the chemical and structural changes that occur, and to use this information to develop thermal treatment processes for the production of high quality carbon fibers. Several significant discoveries were made, but the most important concerned the role of an impurity upon graphite structural development. Large quantities (several mass percent) of sulfur are present in the petroleum-based heat-soaked pitch and cannot be removed from the fiber until temperatures in excess of 1600°C. There, sulfur removal can result in puffing, misorientation of the graphite basal planes with respect to the fiber axis, and cracking. Proper design of the

carbonization schedule, including rapid heating to the maximum temperature, allowed the formation of elongated cracks that aided in sulfur removal, but prevented basal plane misorientation. Improved lattice-dependent physical properties resulted, at the expense of tensile strength. Increasing the time at maximum temperature, however, promoted crack closure and improved tensile strength.

ACKNOWLEDGEMENTS

TABLE OF CONTENTS

Table of Contents (Continued)

LIST OF TABLES

List of Tables (Continued)

List of Tables (Continued)

LIST OF FIGURES

List of Figures (Continued)

List of Figures (Continued)

List of Figures (Continued)

List of Figures (Continued)

List of Figures (Continued)

List of Figures (Continued)

CHAPTER 1

INTRODUCTION

Carbon fibers have been produced commercially from a variety of precursors, including rayon, polyacrylonitrile (PAN), and pitch (both natural and synthetic). Each of these materials has its own advantages and disadvantages in terms of carbon yield, ease of processing, and the physical properties of the resulting fiber. There is, however, one common factor. In each case, the goal is to utilize some combination of the strength, stiffness, conductivity, high temperature stability, chemical resistivity, and low density of the graphite structure (1-3). When combined with a matrix material, these fibers, in turn, impart their physical properties to the composite, providing high-performance, low density alternatives to the design engineer. The applications of carbon fiber-reinforced composites already include aerospace structures, propulsion systems, hypersonic missiles, and electronic packages, where their strength, stiffness, and thermal conductivity have enabled more efficient thermal management and protection. However, continued use of carbon fiber-reinforced composites, as well as their advancement into other high-performance fields, depends upon improvements in fiber quality and reductions in production cost (4, 5).

Such critical applications require reinforcing fibers with excellent axial properties. As the aromatic carbon-carbon bond is one of the strongest bonds found in nature (6), the development of a graphitic structure within the fiber is a good starting point. The graphite structure consists of basal layer planes, each composed of condensed six-membered carbon rings, stacked in an orderly manner. Strong covalent bonding within the planes gives this structure high strength and stiffness when a load is applied parallel to this direction. Weak van der Waals forces provide cohesion in the transverse direction, but are less rigid and allow easy shear between neighboring planes. The same level of anisotropy is observed in

transport properties as well. De-localization of electrons gives graphite metal-like electrical conductivity in the basal plane. These free electrons combine with the excellent lattice wave conduction of the basal plane to give graphite extremely high thermal conductivity. In both cases, the transverse properties are more than an order lower (7). Therefore, the orientation of the graphite basal plane parallel with the fiber axis is important in the determination of fiber axial properties.

It is desirable to begin with a precursor that can be thermally treated in such a way to produce well-oriented graphite. This effectively rules out such precursors as rayon, isotropic pitch, and PAN, which do not graphitize easily (1). Despite their high strength and elongation-to-failure, PAN-based carbon fibers typically display low conductivity (4, 5). A remaining option is the family of anisotropic pitches. Formed either from coal tar or petroleum residue by extraction methods or by synthesis from small aromatic compounds, they provide high carbon yields and graphitize easily. Proper forming and thermal treatment conditions can yield a fiber that imitates the crystal structure and physical properties of graphite. In fact, fibers having a thermal conductivity of up to three times that of copper have been produced. However, high cost has limited their use to only a small fraction of their potential applications. For example, ultra-high modulus fibers, such as Thornel® P-120, may cost as much as $2000/kg (4).

The goal of the present research is to design a thermal treatment process aimed at producing a high quality mesophase pitch-based carbon fiber at a much-reduced cost. As previous work has shown the promise of non-circular fibers in developing a highly-graphitic, parallel microstructure, both circular- and ribbon-shape fibers are considered. In both cases, a greater understanding of the chemical and structural changes that occur during thermal treatment is necessary. Such an understanding may allow the reduction of processing time needed to achieve a specified physical property, or the improvement in physical properties for a specified production rate.

CHAPTER 2

BACKGROUND

As use of carbon fiber-reinforced composites spreads into new high performance applications, increasing demands are made upon the reinforcing fiber. Therefore, understanding the potential of graphite fibers, and the difficulties in the realization of this potential, is essential. The following review concentrates on three broad topics: the nature of carbon and graphite, the development of structure and texture in carbon fibers, and fiber physical properties.

2.1. The Forms and Properties of Carbon

The carbon atom has an atomic mass of 12 amu and an atomic number of six. Of the six electrons, four from the outer shell are capable of forming chemical bonds with other atoms. The ground state of the electrons in an isolated carbon atom is $1s^2 2s^2 2p^2$, but in the solid state, one 2s electron is excited to the π-suborbital, where it can participate in covalent bonding. In diamond, sp^3-hybridized bonds are arranged tetrahedrally, with an average bond length of 1.54 Å. Graphite, however, employs sp^2-hybridized bonding to arrange the carbon atoms in two-dimensional hexagonal network with an average in-plane atomic separation of 1.415 Å. Unlike close-packed structures in which the interatomic separation is similar to that achieved by the packing of rigid spheres, graphite planes are separated by a equilibrium distance of 3.354 Å at room temperature (8). Another characteristic of the graphite structure is the presence of an extra π-electron. It is used in the development of out-of plane forces and in-plane resonance bonding, as well as in electrical conduction. (7, 9).

The unit cell structures of diamond and graphite are shown in Figures 2.1 and 2.2 (10). Diamond forms a highly-crystalline, face-centered cubic structure with well-defined
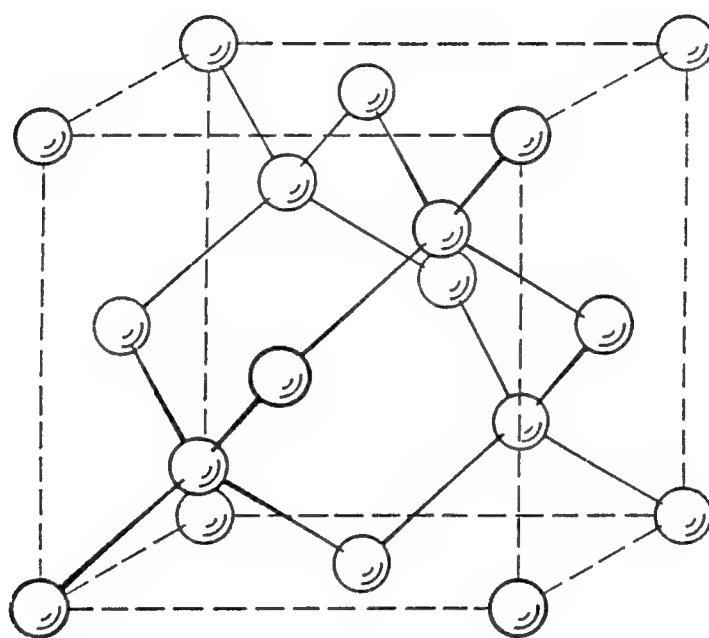
Figure 2.1. The diamond crystal structure (10).
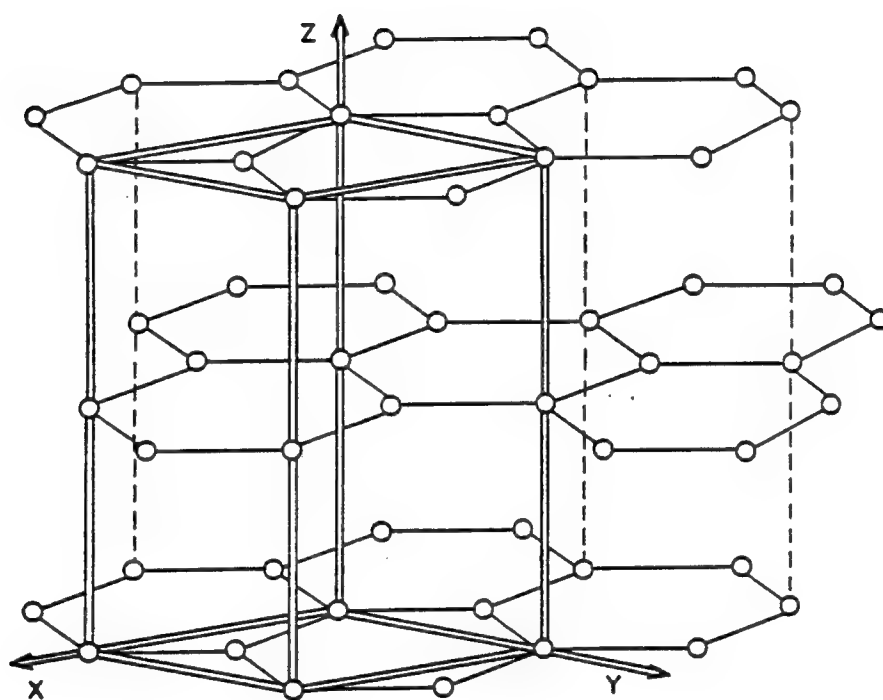
Figure 2.2. The hexagonal graphite crystal structure (10).

lattice constants. Graphite, on the other hand, is related to several other forms of carbon, such as glassy carbon, soot, and carbon black, each having very different crystal perfection and physical properties (7). The difference between these classifications lies in the degree of order with which the graphite-like planes are stacked.

The ideal graphite lattice can be described by the hexagonal stacking sequence ABAB, in which alternating planes are in the same registry. The carbon atoms in any one plane lie over the centroids of the six-membered rings in the plane directly below, as shown in Figure 2.3 (11). With four atoms per unit cell and the interatomic separations presented earlier, the theoretical density of graphite is 2.265 g/cm^3 (9). Carbon atoms are bound to in-plane neighbors by an energy of around 10.5 eV (11), and the planes themselves are stabilized by the resonance and mobility of the delocalized π–electrons (12). In the out-of-plane direction, however, van der Waals forces, approximately 1/25th the strength of the in-plane bonds, bind the planes together (7, 11). Therefore, stacking defects are quite easily formed by the displacement of adjacent planes. So, while virtually all carbons exhibit the hexagonal planar structure (7), deviations from the stable atomic positions cause a relatively little increase in repulsive interaction between neighboring planes and allow a decrease in stacking order.

An extreme example is the formation of the unstable rhombohedral structure, shown in Figure 2.4 (11). It is created by arranging the planes in an ABCABC stacking sequence, so that the third layer bears the same relationship to the second layer as the second does to the first (12). Natural graphite may consist of up to 30% rhombohedral phase (14), while grinding of highly crystalline graphite may increase the proportion from 5 to 15% (15). The rhombohedral phase is unstable and cannot be isolated. In fact, it cannot be created in synthetic graphite and disappears upon the heating of natural graphite to temperatures between 2000 and 3000°C (9).

Stacking defects of a more random nature give rise to what Warren termed a turbostratic structure. It consists of "true graphite layers arranged roughly parallel and
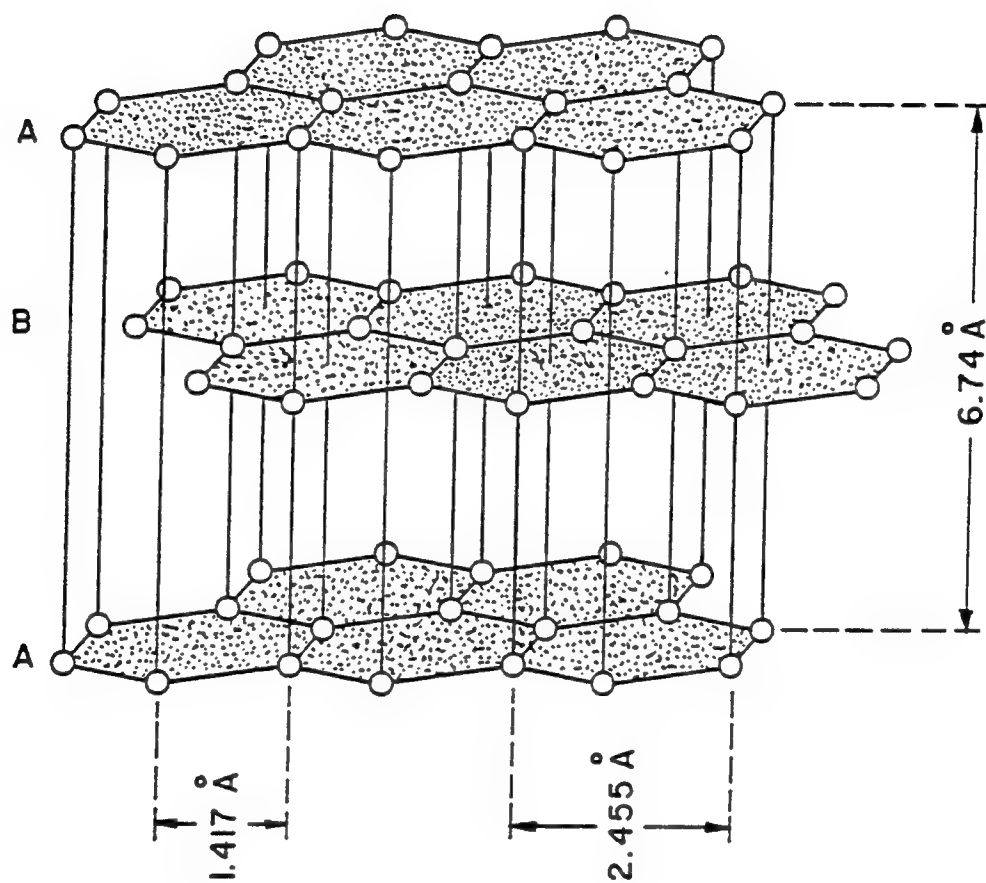
Figure 2.3. The ABAB stacking of hexagonal graphite (11).
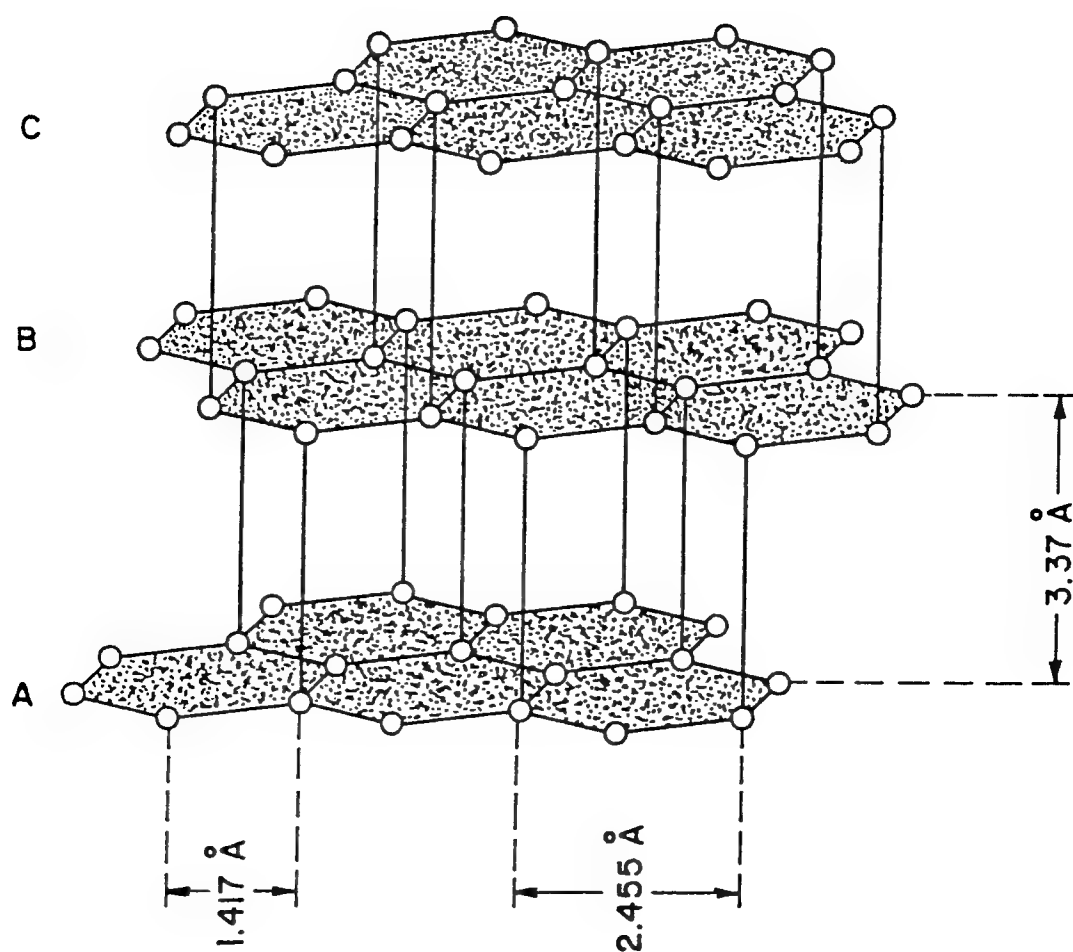
Figure 2.4. The rhombohedral graphite structure (11).

equidistant, but otherwise completely random" (16, 17). Traditionally, this term was used to describe carbons that had not been heat treated to sufficiently high temperatures to develop the graphite stacking order. More recently, however, the term has been used to describe a geometry rather than thermal history. The most obvious result of this disorder is an increase in spacing between graphite basal planes to a value near 3.44 Å for graphitizing carbons (8, 18, 19). A schematic of the disordered stacking that occurs is shown in Figure 2.5 (20). As will be seen in the discussion of physical properties, both interplanar spacing and the crystallite size are related to the degree to which the physical properties of a carbon approach those of graphite (9).

There is also the potential for forming in-plane defects. A common example is edge defects in layer planes of finite dimension. Because a C-C bond cannot be formed at the molecule edge, some way of satisfying the carbon valence must be found. One possibility is the localization of an electron, resulting in a loss of resonance energy and electrical conduction in carbons of small crystal size. Otherwise, the valence may be satisfied by bonding foreign atoms or groups, such as -H, $-CH_3$, or -OH, to the periphery. These impurities must be eliminated before complete ordering can occur (9).

Another example is the presence of vacancies, or holes, in the aromatic planes, as shown in Figure 2.6 (9). If the valences of carbon atoms surrounding the holes are satisfied by functional groups, repulsion between adjacent planes increases and the hexagonal network buckles (21). Or, the electrons may remain unpaired in the vicinity of the hole, inhibiting π-electron mobility and, again, electrical conduction (9). There is also evidence of other in-plane defects, such as "claw defects", c-axis screw dislocations (9, 11, 12), and twinning, as studied by electron microscopy (22).

On a more macroscopic scale, carbons often contain large voids, that can arise from the removal of volatiles or from thermal stresses. Mrozowski (23) predicted that misorientation of anisotropic graphite grains would result in thermal stresses upon cooling from graphitization temperatures. These stresses might be relieved by the formation of
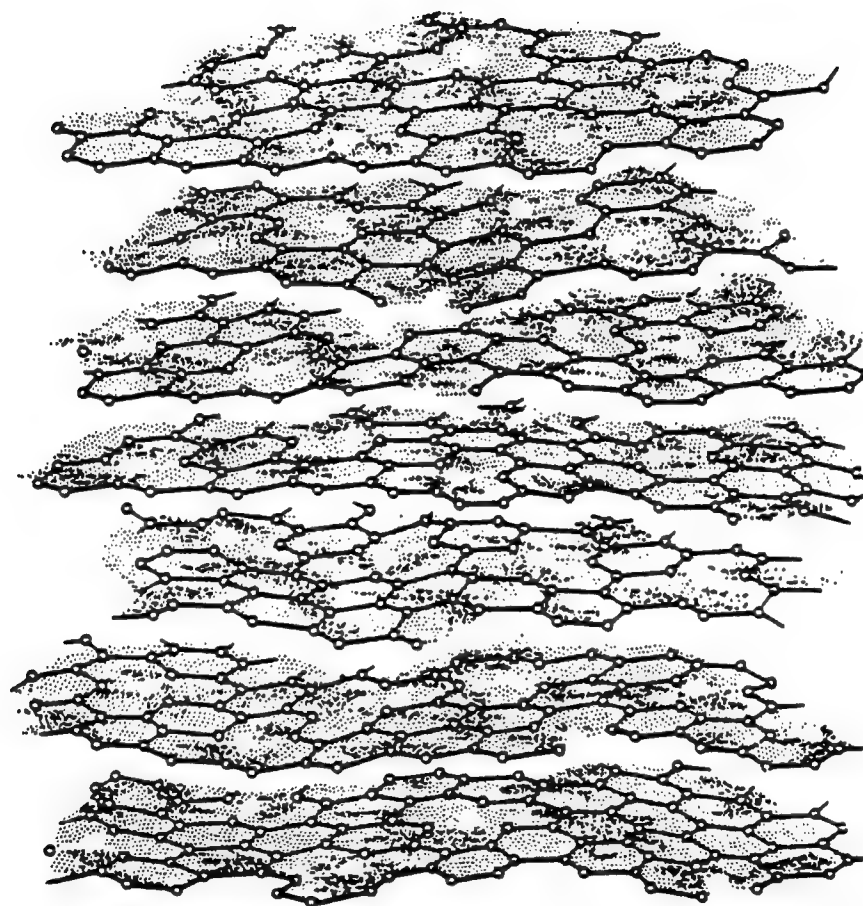
Figure 2.5. The turbostratic defect structure (20).
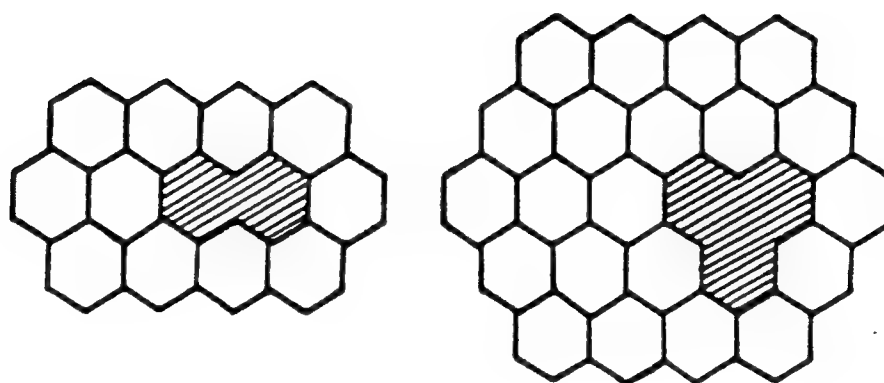
Figure 2.6. Sketch of a graphite-like plane having vacancies (9).

microcracks parallel to the basal plane. In both cases, pores or microcracks reduce the strength, density, and thermal expansion of the carbon body (24).

From this brief description of the graphite crystal structure, it is apparent that graphitic carbons have the potential to develop excellent mechanical, thermal, and electrical properties along their basal plane. The extreme anisotropy of graphite, however, dictates that the same properties will be lower in the transverse direction. For that reason, polycrystalline graphite is often utilized in the form of fibers and films, in which the basal planes of the individual crystals are arranged nearly parallel to the fiber axis or to the film surface. The physical properties of such a product are limited only by basal plane misorientation, finite crystal size, stacking defects, point defects, and porosity. In the next section, the development of a graphite-like structure in mesophase pitch-based carbon fibers is examined.

2.2 Development of Structure in Carbon Fibers

Carbon fibers are produced commercially from several precursors, such as rayon, polyacrylonitrile (PAN), isotropic pitch, and mesophase pitch. Each requires different forming and thermal treatment conditions, but all approach, to some degree, a structure similar to that of graphite. The spinning conditions determine the structure of the raw fibers, and this structure, together with the nature of the precursor, determines the fibers' potential for developing an ordered graphite structure. Fibers then must be prevented from melting during subsequent thermal treatment. This is done by reacting the fibers with oxygen at a temperature just below their softening point. Following this treatment, known as stabilization, the fibers are heated to temperatures up to 3000°C under an inert atmosphere to obtain the desired structure and properties. Neither rayon-based nor PAN-based fibers achieve a highly-graphitic structure, even upon heat treatment to such high temperatures. However, fibers produced from mesophase pitches graphitize readily (1-5).

The changes in crystal structure and physical properties that occur during pitch formation, melt-spinning, and thermal treatment will be discussed in the following sections.

2.2.1. Carbonaceous Mesophase

Carbonaceous mesophase is a nematic liquid crystal, composed of disk-like molecules that orient parallel to one another when heated or subjected to a stress field (25). It can be produced from isotropic pitches by one of two techniques. The first is thermal polymerization, patented by Singer (26) in 1977. In this technique, an isotropic pitch was heated to a temperature between 400 and 450°C under an inert atmosphere for around 40 hours. Approximately 50% of the isotropic phase was converted to an anisotropic mesophase. Because its density was greater than that of the isotropic phase, it was collected at the bottom of the heating vessel. The mesophase produced in this manner, however, had a broad molecular weight distribution and a high softening point. Therefore, it was difficult to melt spin into fibers. Improvements were made on this process by Lewis (27) and Lewis and Chwastiak (28), who included agitation and an inert gas sparge, respectively. A schematic of their process modifications are shown in Figure 2.7. While processing remained lengthy, the final product was 100% mesophase and was easier to melt spin. However, the mesophase still exhibited a broad molecular weight distribution and had a high softening point.

An alternate technique was developed by Riggs and Diefendorf (29). Their process employed solvents such as toluene, heptane, and benzene to extract the high molecular weight fractions for the isotropic pitch. The extract then could be converted to mesophase by heating to between 230 and 400°C for only 10 minutes.

The isotropic pitch feedstock used in these processes comes from the petroleum or coal tar industry. While it is an inexpensive material, it may contain insoluble carbon solids that decrease the mechanical properties of carbon fibers. In addition, the composition of these pitches varies with time, depending upon the composition of the crude oil or coal.

A-240 heated to 400°C for 40 hours (50% converted to high molecular weight mesophase)

Singer (1977)

Added stirring: lower molecular weight mesophase - still two phase product

Lewis (1978)

Inert gas sparge used to agitate. Single phase product - 90% of the mesophase < 1500 molecular weight

Chwastiak (1978)
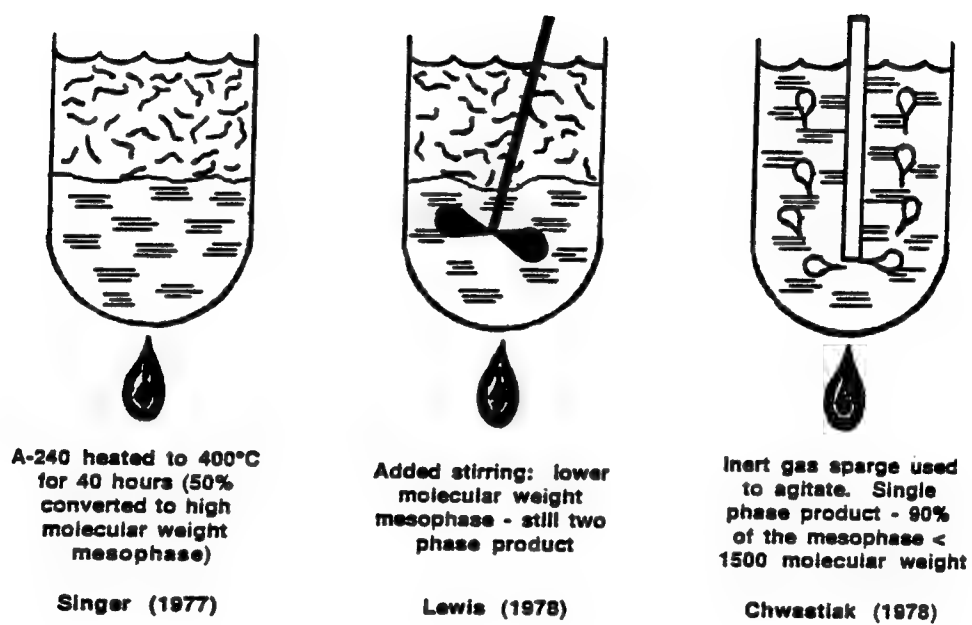
Figure 2.7. Production of mesophase pitch by thermal polymerization.

Therefore, production of consistent, high-quality carbon fibers from these materials is difficult (4).

Recently, mesophases of narrower molecular weight distribution and low impurity content have been produced from pure aromatic hydrocarbons, such as naphthalene (30-32). A process for producing mesophase commercially from naphthalene is being developed by Mitsubishi Gas Chemical, Inc. In this process, naphthalene is polymerized using HF/BF_3 as a catalyst. Polymerization is conducted in an autoclave, held at a temperature between 260 and 300°C and a pressure between 2 and 3 MPa for around four hours. Afterwards, the material is distilled to remove the catalyst, any unreacted monomer, and impurities, leaving a 100% mesophase. Figure 2.8 shows a schematic of the Mitsubishi process for producing their so-called AR mesophase (31). The advantages of this material are its consistency of composition, improved melt-spinning, and its enhanced stabilization reactivity as a result of increased hydrogen content.

2.2.2. Melt-spinning

Melt-spinning involves three steps: melting the precursor, extrusion through a spinnerette capillary, and drawing the fibers as they cool. Many investigators have concluded that this process is the primary source of structure in mesophase pitch-based carbon fibers, and that thermal treatment only enhances this structure (4, 33). The effects of melt-spinning conditions on the structure and properties of carbon fibers will be discussed in this section.

Several process variables are important in determining the fibers' potential for developing an ordered graphitic structure. The first is melt temperature. Each mesophase has a range of temperature over which melt-spinning is possible. Spinning at temperatures beneath this range results in high viscosities and brittle fracture during drawdown, while at temperatures above this range, thermal degradation of the pitch (34) and dripping due to low viscosity occur (4). The viscosities of all mesophases are highly dependent upon
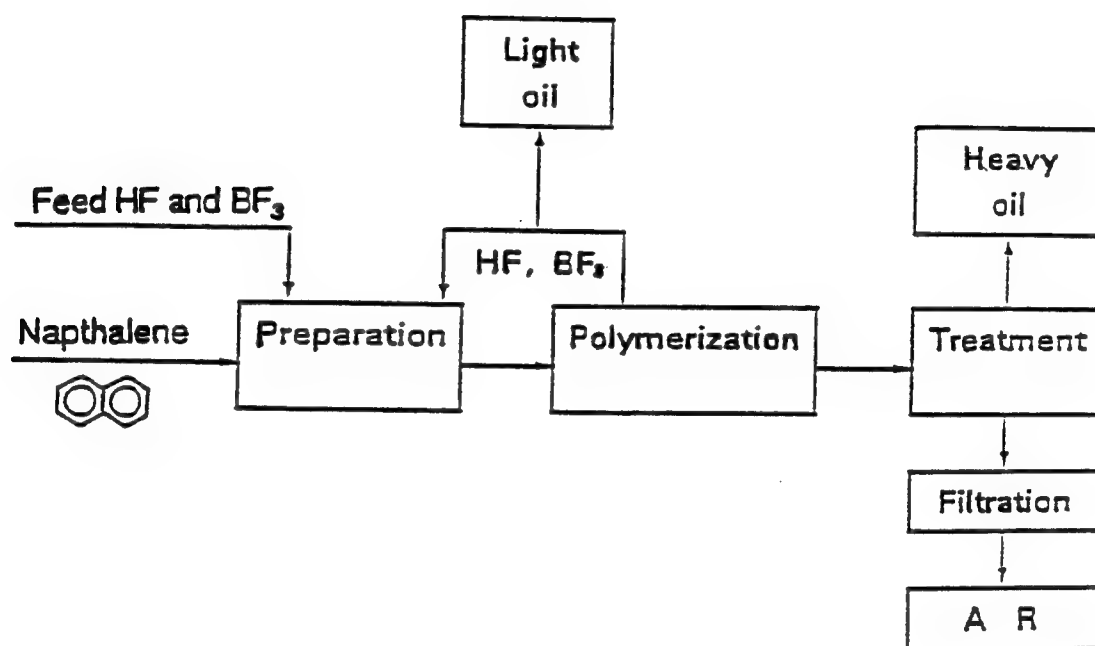
Figure 2.8. The process for producing AR mesophase (31).

temperature, as shown in Figure 2.9 (35, 36); therefore, the temperature range for successful melt-spinning is quite narrow. Using the AR mesophase, Mochida (37) found that decreasing the melt-spinning temperature by even 15 degrees resulted in a four-fold increase in viscosity and, in turn, significant decreases in tensile strength and Young's modulus. It was concluded that a low melt viscosity was necessary for production of a high quality carbon fibers.

The pitch flow profile in the capillaries is also important in terms of transverse basal plane arrangement. A schematic of the transverse textures typically observed for carbon fibers is shown in Figure 2.10 (4). They include the radial-folded texture, observed in Du Pont's Fiber E and Kashima fibers (33), and the "flat-layer," or "Pan-Am," texture observed in fibers produced by Amoco. Hamada et al. (38) showed that these textures of fibers were developed during extrusion. By stirring the pitch just before it reached the capillaries, they produced fibers having an onion-skin texture. Changing the shape of the stirrer and moving it closer to the capillary resulted in a random texture. Stirring, however, did not affect the orientation of basal planes about the fiber axis.

Similar results can be achieved through capillary design. For example, Matsumoto (39) found that increasing the capillary length-to-diameter ratio produced a more radial texture in circular fibers. He concluded that both shear rate and the residence time of the pitch in the capillary were important parameters in texture determination. Die taper has also been investigated; Riggs and Redick (40) patented a process by which the textures of the fibers are changed from radial to onion-skin by increasing the capillary entry angle. And, finally, Edie et al. (41) showed that extruding mesophase pitch through non-circular capillaries generated a line-origin texture, in which aromatic molecules appear to emanate from a central line.

These examples imply that texture and basal plane orientation are developed in the spinnerette capillary, but that orientation is enhanced by conditions after exit from the capillaries. These findings were confirmed by Edie at al. (41). After exiting the
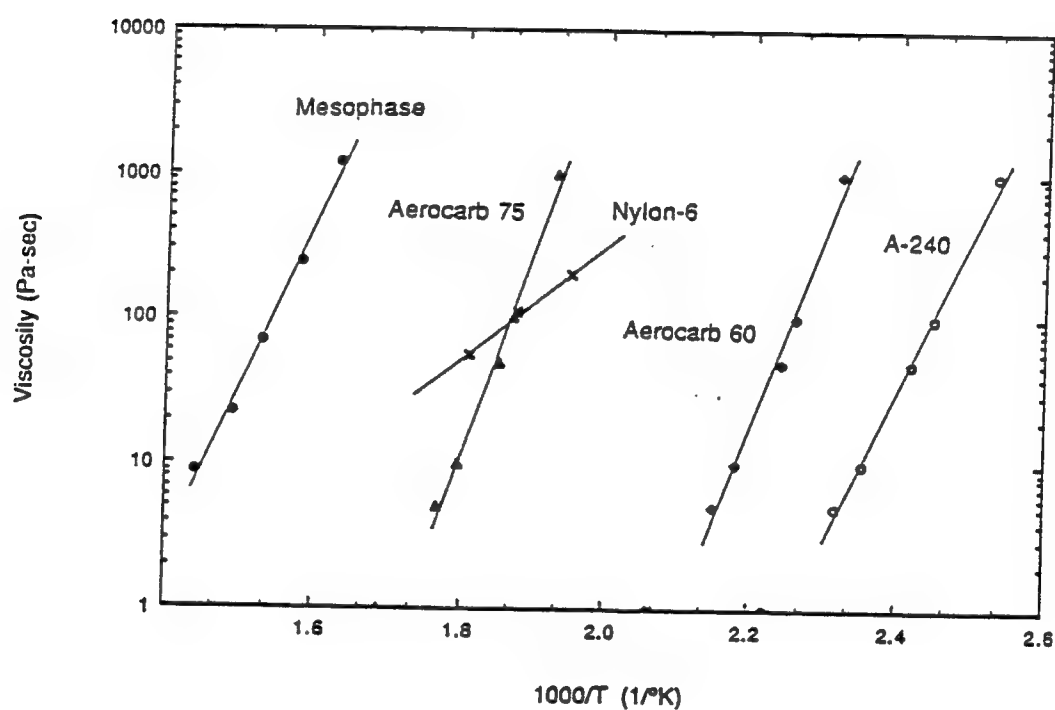
Figure 2.9. The dependence of viscosity on temperature for three isotropic pitches, a mesophase pitch, and a common polymer (35, 36).
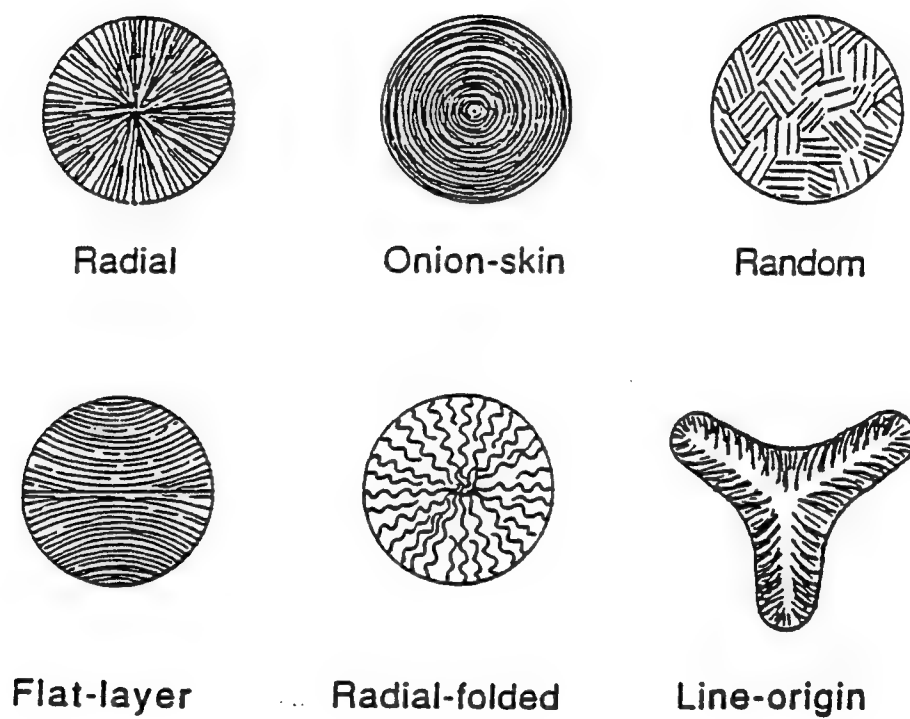
Figure 2.10. Typical textures observed in carbon fibers (4, 33).

spinnerette, fibers are drawn during cooling and wound. During this step, the fiber area decreases and the aromatic molecules are further oriented with the fiber axis, as shown in Figure 2.11. Such orientation is necessary if the fibers are to achieve an ordered graphitic structure during thermal treatment.

Other important variables include the mass flow rate, quench (or ambient) temperature, and the cross-flow air velocity (4). Models to describe their effects on drawdown and thread-line tension have been developed by Kase and Matsuo (42), and Kase (43), and applied to mesophase pitch by and Edie and Dunham (34). Currently, McHugh is using a model of the flow of discotic mesophases through converging channels in the design of non-circular spinnerettes (44).

2.2.3. Stabilization

Carbons having low concentrations of oxygen, such as mesophase pitches, melt upon heating to temperatures in excess of around 300°C. Therefore, fibers made from these pitches must be stabilized, or thermoset, prior to the high temperature treatment (45). Several methods exist for stabilization by oxidizing acids and ozone (46, 47), but the most common method is thermal oxidation in air. Oxygen reacts rapidly with the α-carbon sites on aromatic molecules that include alkyl side groups. Thus, materials with higher concentrations of these side groups react more rapidly with oxygen, resulting in greater oxygen concentrations after stabilization. Once the initial reaction of the alpha carbon sites has taken place, dehydrogenation and polymerization can occur (48).

Several studies of stabilization have been conducted using infrared spectroscopy. The most extensive was by Otani for ozone stabilization of a pitch derived from PVC (47). The IR spectra from that study as a function of heat treatment temperature are shown in Figure 2.12. Otani showed that carbonyl and some C-O groups are formed by the oxidation of alkyl side groups. Then, the formation of acid anhydride groups at elevated temperatures crosslinked the structure. The use of ozone contributed to the formation of a highly
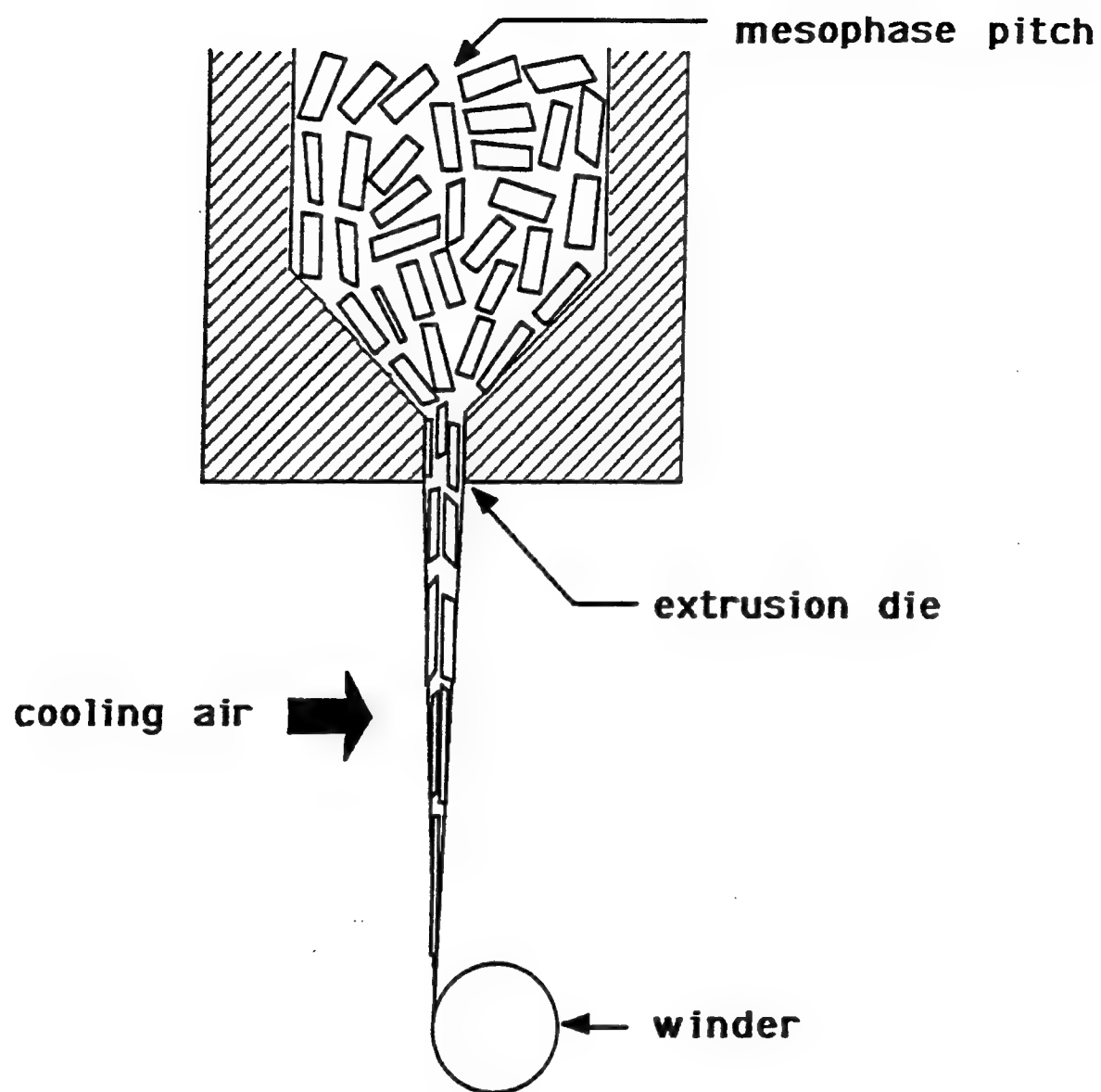
Figure 2.11. Orientation of a mesophase during extrusion and drawdown.
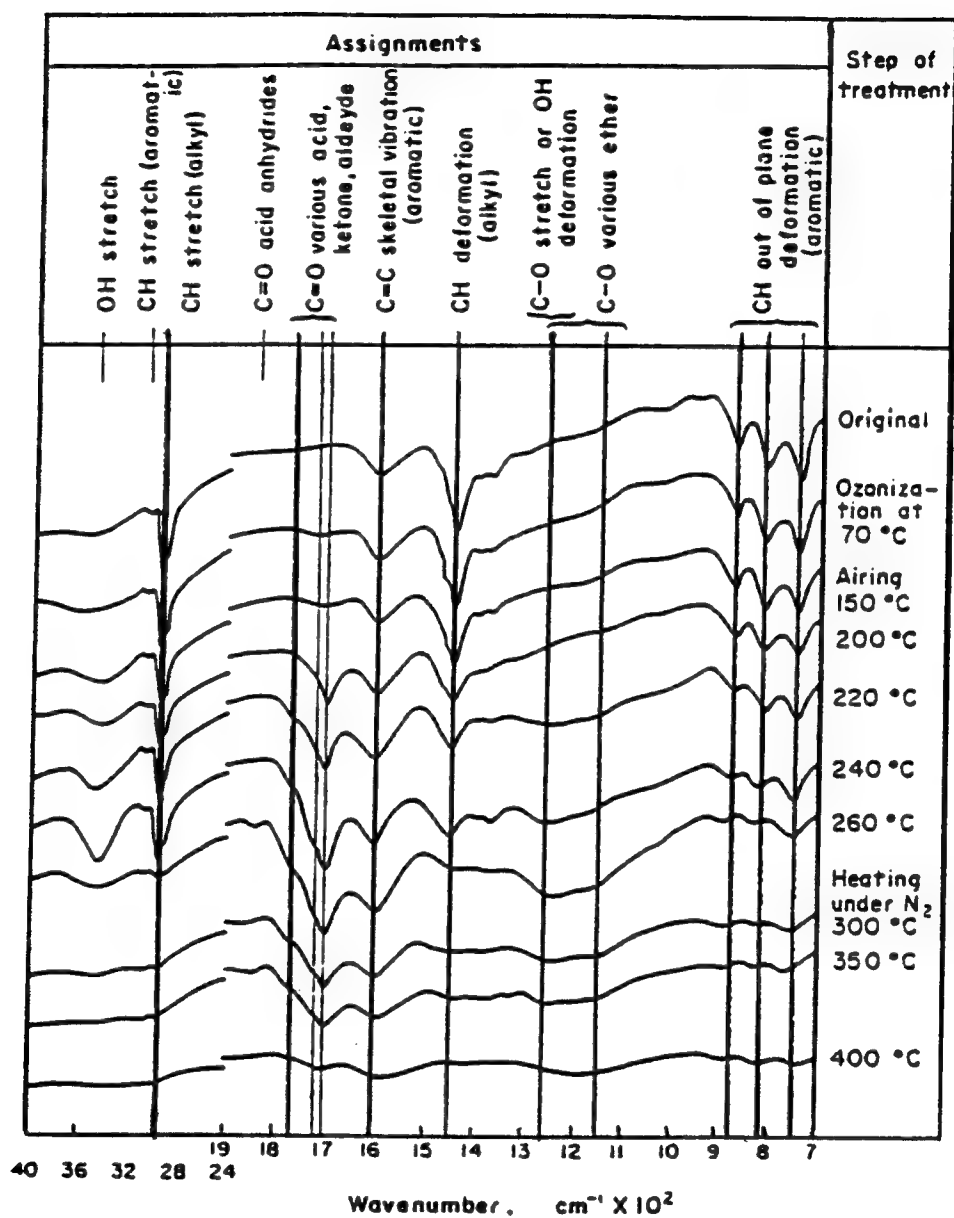
Figure 2.12. IR spectra of partially stabilized and thermolyzed PVC pitch-based fibers (47).

crosslinked surface layer, but a less-stabilized interior. A similar result is observed, in general, for stabilization under high oxygen concentrations (49), as stabilization has been shown to be a diffusion-limited process (50-53). Thus, non-linear oxygen concentration profiles are observed after stabilization, as shown in Figure 2.13 by Kasuh and Marsh for pitch-based fibers (54).

The stabilization process also has been examined by thermogravimetric analysis (50, 55). Typically, mass gain begins around 180°C, but the actual temperature and rate of mass gain depends upon the pitch. Stevens and Diefendorf (51) found that a specific mesophase pitch could be adequately stabilized at about 6% increase in mass. The exact amount, however, is dependent upon the chemical composition of the mesophase, its molecular architecture, and conditions in the stabilization oven (4). These crosslinking reactions are highly exothermic, and they have been investigated by Hein and Weber (56) for a coal tar pitch and Lavin (57) for model compound pitches using differential scanning calorimetry. Typical dynamic DSC heat flow curves versus temperature are shown in Figure 2.14 for four model compound pitches, such as anthracene, anthraquinone, dihydroanthracene, and dimethylanthracene (57).

Structurally, stabilization serves to freeze the orientation of the aromatic layers in the fibers. However, stabilization at temperatures near or above its softening point may result in relaxation. As shown by Riggs et al. (2) in Figure 2.15, this leads to a decrease in Young's modulus with increasing stabilization temperature. Stabilization also has the effect of increasing the separation of the basal planes. As stabilization time and, therefore, oxygen content, are increased, the basal plane separation becomes greater.

Clearly, stabilization has a dramatic effect upon structural development during the subsequent processes (58). The formation of an infusible surface layer on the fiber is essential to the prevention of fiber sticking (47), but the orientation of the basal planes must be preserved throughout the fiber. In addition, an optimum oxygen content is desirable to reduce mass loss during the following processes.
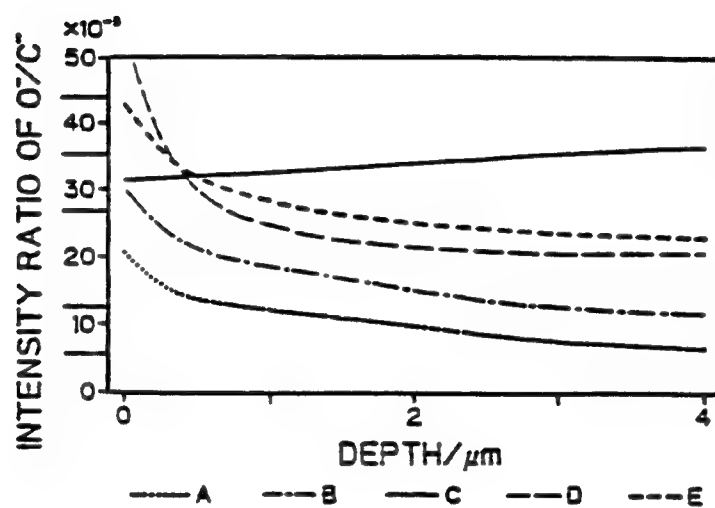
Legend: A   heated at 3°C per minute to 250°C

                     B   treated at 300°C

                     C   treated at 400°C

                     D   held at 250°C for 12 hours

                     E   treated at 300°C for 1 hour

Figure 2.13. Oxygen concentration profiles in mesophase pitch-based fibers (54).
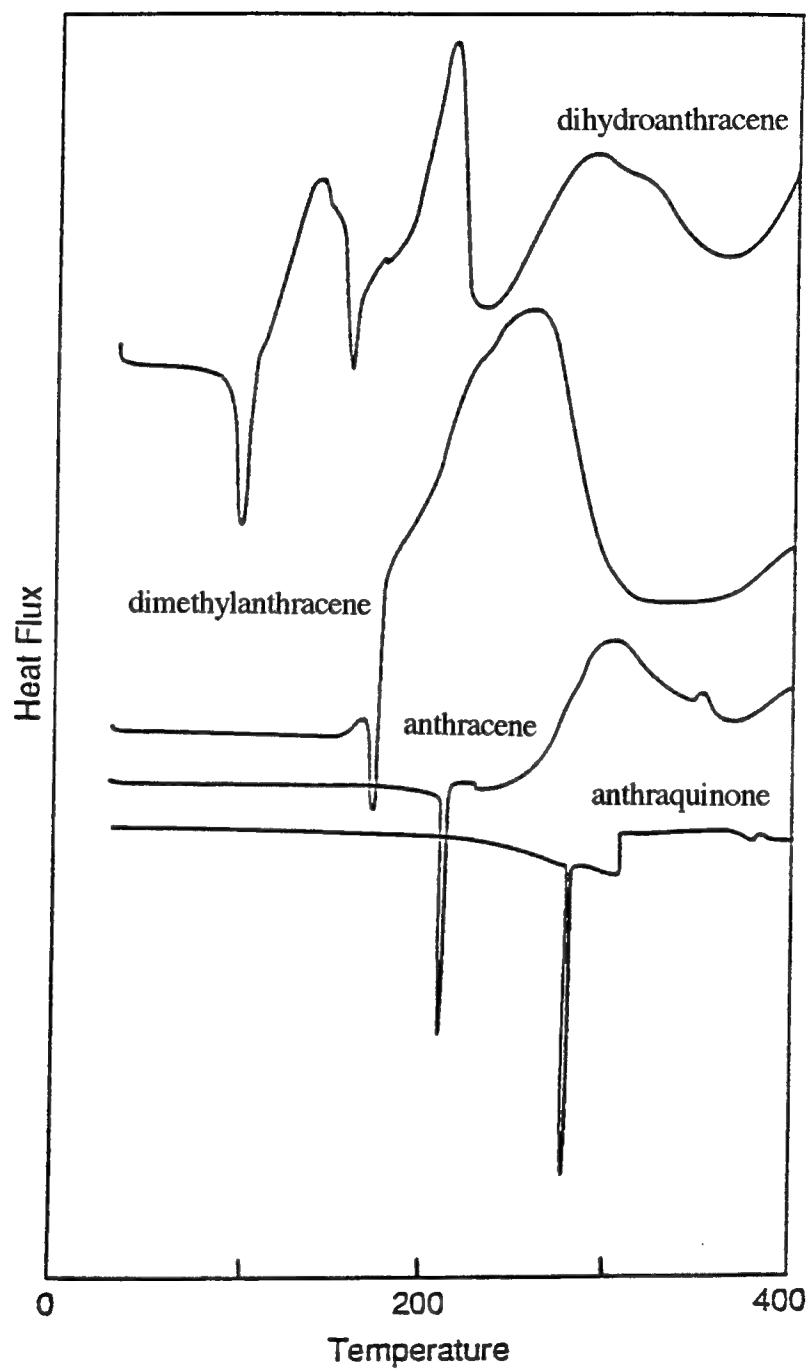
Figure 2.14. Typical dynamic DSC curves for model compound pitches in air (56).
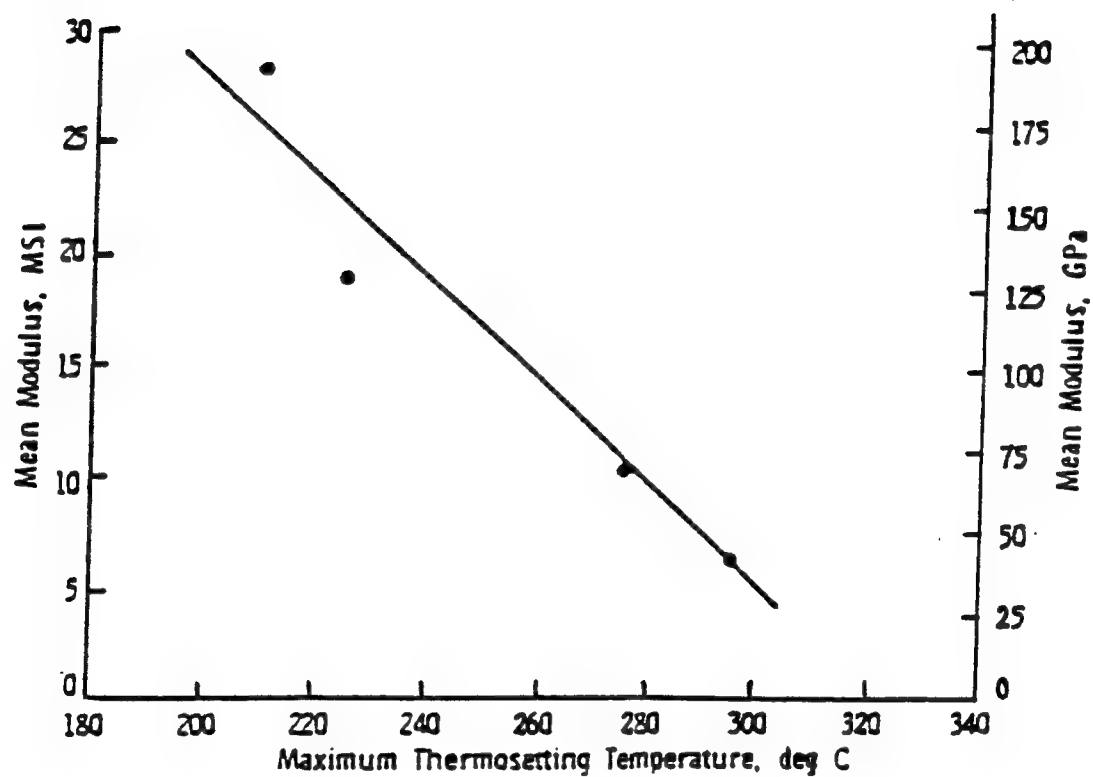
Figure 2.15. Dependence of post-graphitization Young's modulus upon stabilization temperature (2).

2.2.4. Thermolysis

After stabilization, fibers are able to withstand subsequent thermal treatment. However, they still contain large quantities of hydrogen and oxygen, which form volatile species upon heating (59). Such a treatment is termed carbonization, or thermolysis (45). As used here, both terms will imply thermal decomposition of the carbonaceous material, resulting in a composition consisting of at least 95% carbon. Thus, thermolysis primarily involves the removal of non-carbon elements in the form of low molecular weight gases, such as methane, carbon dioxide, and hydrogen. Much of the mass loss occurs at temperatures below 1000°C (4, 59). Heating the fibers too rapidly during this period may cause bloating (60, 61) or cracking (48). To minimize these flaws, a low heating rate is often employed between 700 and 900°C, with a brief soak at maximum temperature to insure complete devolatilization (4, 59).

Several researchers have investigated the chemical changes that occur during thermolysis of carbons (62-67). Kasuh and Marsh (62) studied the carbonization of oxidized mesophase pitch fibers and identified the evolved gases as, in order with increasing temperature, CO_2, CO, CH_4, and H_2. A plot of the concentrations of these gases with temperature is shown in Figure 2.16. No change in composition was observed below 300°C, but further heating was accompanied by rapid loss of oxygen and an increase in the quinoline insoluble (QI) content. Quinoline, and sometimes benzene, insoluble contents are used as measures of aromatic carbon content and infusibility of carbonaceous materials. A high QI means that a material will give a high carbon yield upon further thermal treatment (4). Assuming that the QI value was related to the degree of ring condensation, they concluded that deoxygenation caused condensation at low temperatures. Infrared spectra showed that the carboxyl absorption band near 1750 cm^{-1} disappeared, while the carbonyl band near 1700 cm^{-1} remained strong. Thus, the removal of oxygen that lead to condensation between 300 and 400°C was by decarboxylation. Infrared and elemental analysis confirmed that evolution of carbon dioxide occurred between 300 and
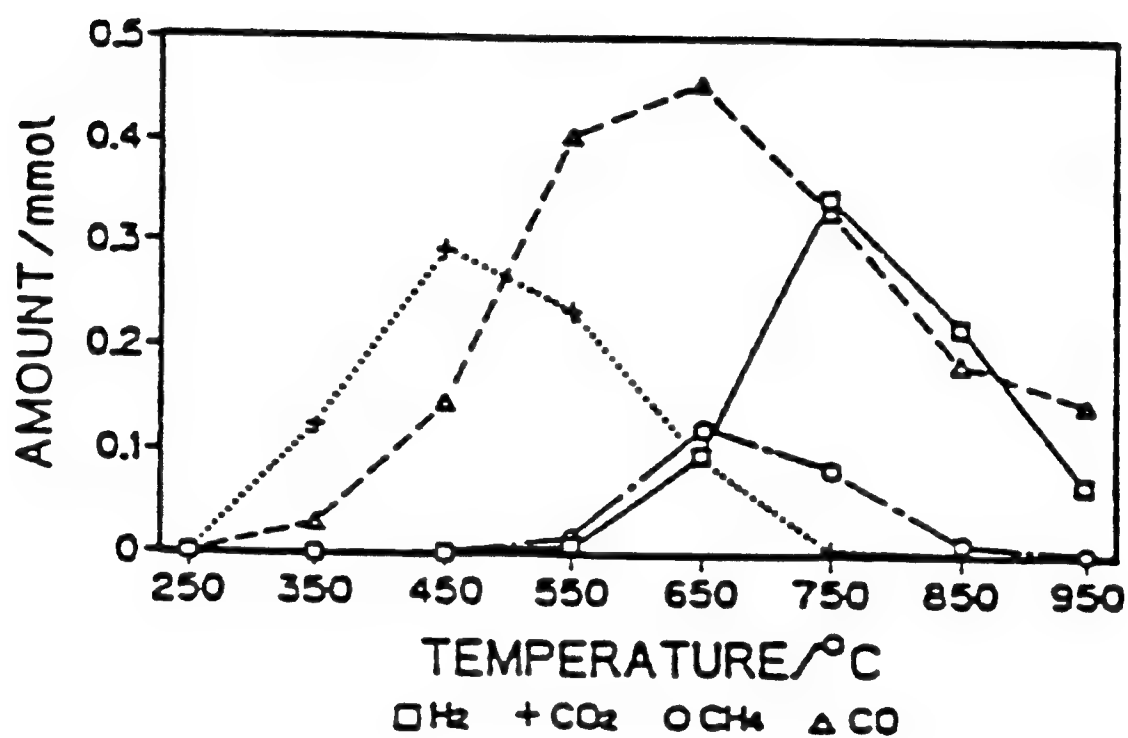
Figure 2.16. Evolution of gases with thermolysis temperature (62).

600°C, and carbon monoxide between 350 and 900°C. A similar phenomenon was observed by Otani (47) in the thermolysis of PVC pitch under nitrogen.

At temperatures nearer 1000°C, hydrogen evolution becomes more pronounced. Carbonization kinetics have been studied by hydrogen evolution measurements from cokes containing little or no oxygen (68-70). According to Singer and Lewis (71, 72), coke formation is accomplished through the removal of hydrogen, and the cumulative hydrogen evolution is an indicator of the mean size of aromatic molecules. Carbonization, then, is viewed as free-radical process, in which the rate-limiting step is the cleavage of carbon-hydrogen bonds to form free-radicals.

Subsequently, Kawamura and Bragg (69) studied the carbonization kinetics of several pitch cokes using thermogravimetric analysis. They found an activation energy for carbonization of around 100 kcal/mole, and related this to the C-H bond energy. Thus, they concluded that the rupture of C-H bonds was the rate-limiting step in carbonization. This study of a graphitizing carbon confirmed a previous study by Lapina et al. (68), who concluded that the activation energy of carbonization for a given coke was an indicator of its graphitizability. They found that activation energies ranged between 17 and 112 kcal/mole for a variety of pitches, coals, resins, and polymers. Bond rupture, creating free-radicals, gave rise to highly endothermic reactions, requiring large activation energies. On the other hand, immediate condensation resulted in heat evolution, and an activation energy near zero. Such materials as furan resins, for example, which develop a rigid, disordered structure and do not graphitize, exhibited low activation energies. Using activation energy data and the basal plane separations of these materials after heat treatment to 2700°C, they showed a correlation between carbonization and graphitizability: non-graphitizing carbons have activation energies below 30 kcal/mole, while graphitizable carbons have values above 60 kcal/mole.

Newman (70) also concluded that the development of high molecular weight compounds at low temperatures resulted in a poorly-graphitizing carbon. He employed

measurement of hydrogen evolution to study the carbonization kinetics of several materials. He found a value of 97.5 kcal/mole, similar to that found by Kawamura and Bragg (69), for a vacuum residue used to make "normal" coke, but values of 43.5 and 57.8 kcal/mole for "premium" and "intermediate" petroleum tars used for needle-coke production, respectively. The latter values agreed with the values previously reported by Singer and Lewis (71) for petroleum pitches. Newman concluded that the rate of carbonization was not as important to the quality of coke produced as was the molecular weight of the polymer early in the carbonization process. It was essential, he believed, to limit condensation at low temperatures in order to prevent the development of a non-graphitizing carbon. This finding is dependent upon the molecular structure and viscosity of the coke.

The effect of carbonization conditions upon the structure and properties of PAN-based carbon fibers has been studied by Fitzer et al. (73, 74). Their work showed that high heating rate during carbonization had a deleterious effect upon tensile strength and modulus. In addition, employing a two-step process of heating the fiber to the devolatilization range and cooling prior to high temperature treatment produced improved physical properties. Using mesophase pitch, Schikner (75) found that precarbonization rate had little effect upon the tensile properties of graphitized fibers. He did, however, find that a two-step process, consisting of pre-carbonization to 1000°C and cooling, gave improved tensile properties. As the two-step process was devised to allow gas evolution and then to re-densify the fiber through thermal contraction during cooling (76), crack population was deemed an important factor. It follows that reduced mass loss during this treatment would reduce cracking, and result in improved tensile properties.

2.2.5. Graphitization

The final stage of heat treatment is called graphitization and it involves the transformation of disordered carbon lamellae into a three dimensional graphite structure. Prior to graphitization, graphitizable carbons usually consist of small domains of two-

dimensional aromatic layer planes, each misoriented with respect to its neighbor by a twist or translation. Pure graphite has a regular hexagonal stacking sequence, ABAB, whereas carbonized materials display a random layer order and a greater repulsive force between planes (77). Together with the influence of sp^3 hybridized linkages at plane peripheries, this produces a d(0002) spacing, or basal plane separation, greater than that of graphite (78). During graphitization, these interplanar defects are removed thermally and the planes form ordered stacks with graphite-like spacings in the lattice c-direction. Stacking changes are accompanied by a growth of the graphite domains in the a-direction and orientation of the planes along the fiber axis. These are the result of both large-scale motion and the removal of chemical species attached to the plane edges. Graphitization, then, is accomplished primarily by atomic diffusion and crystallite growth, both thermally activated processes with well-defined and physically-significant activation energies (79). Several authors have attempted to quantify the graphitization reactions and relate their rate properties to atomic-level processes. An explanation of the process and its kinetics are presented here.

Entering the graphitization process, carbon fibers might consist of greater than 95% carbon by mass, with trace impurities such as hydrogen. According to Mrozowski (80), almost all of the gaseous products have been removed and the structure is purely carbon with only a few hydrogen atoms attached at plane edges. There is an orderly arrangement of atoms in each plane but a random layer stacking. To describe this, Warren proposed a "turbostratic" model in which perfect platelets are stacked in a completely disordered manner (16, 17). He suggested that graphitizable layer planes had firmly attached interstitials on both sides and that these interstitials contributed to the lattice distortion. Graphitization was described as the process of removing these point defects and ordering the graphite stacks. A subsequent model by Maire and Mering (78) considered imperfect layer planes with attached interstitials and obtained a range of d(0002) spacings between 3.354 and 3.440 Å, better explaining experimental observations, such as electronic and magnetic measurements. Other models exist, e.g., Ruland (81) and Ergun (82), that rely

primarily on the annealing of in-plane defects and preclude non-graphitic d(0002) spacings. For example, Ruland proposed that graphitization involves translation of layers in the a and b crystallographic directions. The initial displacement of these layers is the result of basal plane unevenness, which in turn is the result of interstitials.

For the structure to homogenize on a large three-dimensional scale, it is necessary for defects between layer planes to be annealed away and for planes to move into ordered arrays. Most of the hydrogen is released from the fiber by around 1200°C, allowing the interplanar spacing to decrease slightly (83, 84). More significantly, the destruction of attached hydrocarbon species results in the formation of active sites for condensation (85). This period is characterized by rapid growth of crystallites in the c-direction and a slight decrease in d(0002), while little change occurs in the a-direction (79). The difference in growth rate may be related to the comparative ease with which π-bonds are formed between basal planes as compared to σ-bonds within the planes. In addition, it is believed that the development of three-dimensional order (decrease in basal plane separation) is necessary prior to a-directional crystal growth (86). Figure 2.17 illustrates the behavior of the L_a/L_c ratio with heat treatment temperature according to Richards (87).

The subsequent stage involves growth of the crystallites in both the a- and c-directions by drawing on material from the surrounding disordered phase. This occurs until the phase is depleted, which Mrozowski observed at 1300°C. From that point, the crystallites must grow at the expense of their neighbors. Unlike ceramic grain growth processes, however, in which abnormal grain growth can occur, the crystallites grow to an average size determined by the time-temperature conditions of heat treatment and practically stop there (80, 86).

According to Mrozowski (80) and Heintz (86), once the crystallites reach a certain size in the a-direction, the turbostratic to graphite conversion becomes energetically favorable. A d(0002) spacing decrease caused by the rotation or translation of neighboring planes with respect to one another is accompanied by a release of energy proportional to the crystallite
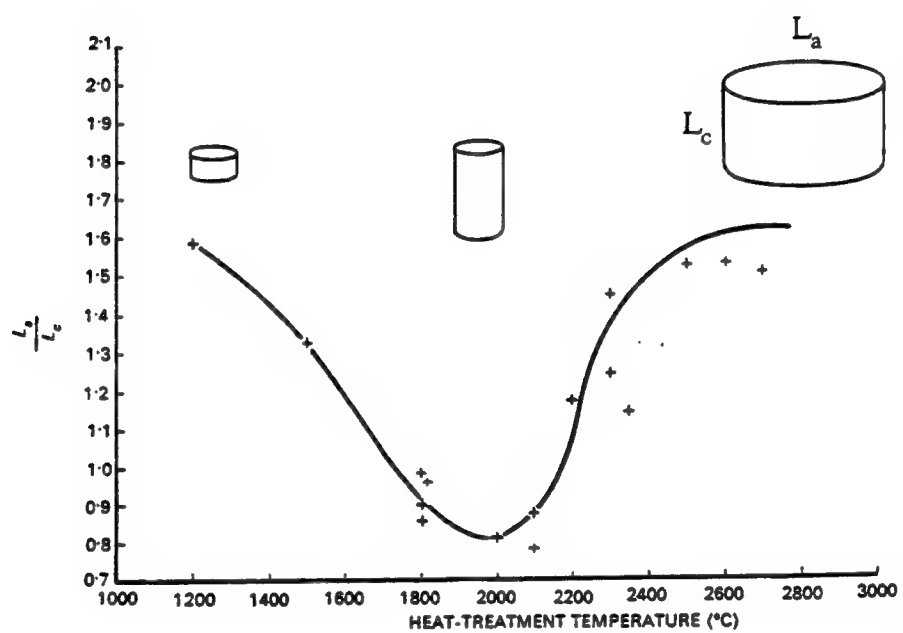
Figure 2.17. Ratio of coherence length to stack height with graphitization temperature (86).

area, or L_a^2. However, an amount of energy proportional to the crystallite circumference is needed to break some, or all, peripheral bonds and to orient the planes. At a crystallite size (L_a) of around 100 Å, the released energy exceeds the required energy and the transformation becomes energetically possible. This condition to break all bonds occurs somewhere in excess of 1700°C, depending upon size distribution and peripheral bond density (80). Conditions are then favorable for macroscopic orientation and rapid a-directional crystallite growth. This explains the somewhat arbitrary demarcation between the terms carbonization and graphitization at 1700°C (4). The presence of dislocations and vacancies might allow this this process to occur without breaking all peripheral bonds and, therefore, at lower energy.

For rapid growth to occur, the platelets should be straight and arranged in graphite-like stacks. A. Oberlin (88) observed that all graphitizing carbons behave in a similar way: below 2000°C, they consist of small mosaic elements, each almost parallel with its neighbor in a wrinkled layer structure. Above 2000°C, de-wrinkling occurs as a-axis misorientation is eliminated and L_a increases rapidly. Oberlin divides the graphitization process into three stages: an increase in the number of layers per stack, development of large, wrinkled sheets, and sheet perfection by unwrinkling. Figure 2.18 illustrates the relative temperature relationship of stack height, L_c, and coherence length, L_a. Specific to pitch-based fibers, Johnson concluded that increase in crystallite size is enhanced when the majority of the layer planes are in the fiber axis direction (89). His model of orientation change, minus the possibility of polygonization for such drastic bending, is presented in Figure 2.19.

The nature of crystallite growth, especially in the a-direction, can be described on the basis of vacancy diffusion within the layer planes. Vacant positions have additional energy as a result of four factors:
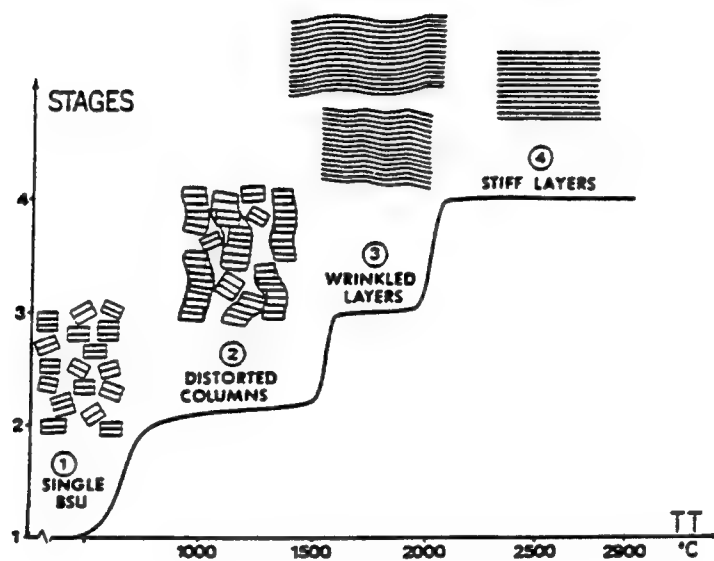
Figure 2.18. Illustration of structural changes with temperature (88).
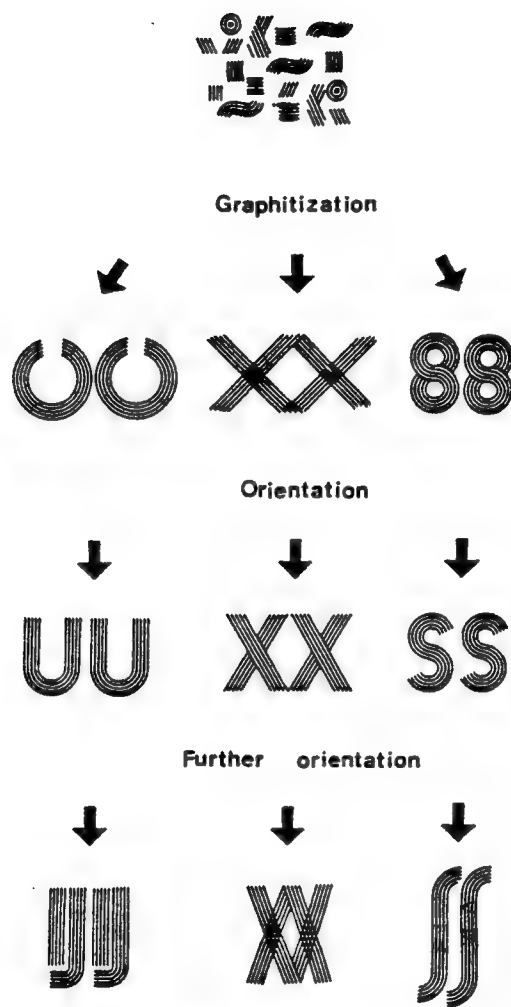
Figure 2.19. Model of the change in basal plane orientation during graphitization (89).

(1) rupture of 3 σ-bonds that bind the atom to its neighbors,

(2) loss of π-electron delocalization (resonance energy),

(3) interaction of the 3 sp^2 hybrids left dangling, and

(4) energy of attraction and repulsion between the layers.

Such vacant sites, naturally present in a disordered graphene plane, migrate to the edges of growing planes and account for the large increase in L_a at high temperatures (90).

In summary, the graphitization process consists of several discrete stages which, due to the non-uniform nature of the starting material, overlap to form a "smooth" transition. The stepwise nature of the process has been observed by several authors (79, 91-93) from the discrete values of d(0002) which occur at 3.44, 3.40, 3.37, and 3.36 Å, as well as from discontinuities in magnetic susceptibility, with increasing treatment time at a given temperature. In particular, Pacault (91) observed this phenomena using "electron micro-diffraction". He found that carbons having magnetic susceptibility data points falling on the same plateau gave similar electron diffraction patterns, while those having data near a step or discontinuity gave very different patterns. A possible explanation for the discrete values of d(0002) is that a given time interval is necessary for the elimination of a given structural fault. He reasoned that, when the number of defects fell below some critical level, evolution of structure occurs and the corresponding properties (e.g., d(0002) and magnetic susceptibility) attain another plateau. It is also possible that a carbon passes through a rhombohedral form during graphitization, resulting in d(0002) that reflect the proportion of rhombohedral (larger plane separation) and graphitic (smaller plane separation) phases.

Clarification of the mechanism by which graphitization occurs lead to studies of its kinetics. Using the d(0002) spacing as the criterion, the rate of disappearance of disordered carbon can be expressed as

$$\frac{dc}{dt} = -kc^n, \tag{2.1}$$

where k is the reaction rate constant and n is the reaction order (79, 91). The concentration

of disordered carbon, c, given by

$$c = \frac{d(0002) - 3.354 \text{ Å}}{3.440 \text{ Å} - 3.354 \text{ Å}},$$ (2.2)

is the inverse of Mering's degree of graphitization (78). Several authors (77, 79, 84) have shown graphitization to obey first order kinetics (n = 1). Then, equation 2.1 can be integrated to obtain

$$c(T,t) = c_o \exp(-kt);$$ (2.3)

c_o is the initial value of c and equals 1 when d(0002) = 3.440 Å. The rate constant, k, obeys an Arrhenius-type temperature relationship,

$$k = k_o e(-\Delta E/RT),$$ (2.4)

where the pre-exponential term, k_o, is related to the entropy change, ΔE is the process activation energy, R is the gas constant, and T is the absolute temperature. The major argument with the expression of a graphitization rate equation is the use of a constant activation energy to define the entire process.

The activation energy has been determined by a variety of experiments, including isothermal hydrogen evolution (68, 84), crystallite growth, and dynamic/isothermal X-ray diffraction (69, 79, 94). In 1951, Franklin (95), proposed a graphitization mechanism by which small layer plane segments are joined together to form larger planes. Then, the larger planes are rotated and translated into position as a whole. From these assumptions, she concluded that the activation energy increased with increasing crystallite size. However, Fischbach (79) showed that pitch-based carbons have a constant activation energy of between 240 and 280 kcal/mole above 2000°C, but a distribution of rate constants for a collection of first order reactions. His isothermal studies illustrated that graphitization behavior is independent of heat treatment temperature and that the activation energies for d(0002) spacing decrease, crystallite growth, and orientation increase are the same. This activation energy has a physical meaning if atomic transport within the layer planes is considered. The energy required to form a carbon vacancy is approximately 170 kcal/mole and the energy necessary for its migration through the graphite lattice is 70

kcal/mole. Thus, vacancy diffusion, which is the summation of these two processes, has an effective activation energy of 240 kcal/mole. An interstitial transport mechanism may also occur, with an activation energy of around 220 kcal/mole in the c-direction or 166 kcal/mole in the a-direction (69, 79, 94, 96, 97). Because of their proximity in value and the lack of precision of high temperature measurement, these mechanisms cannot be distinguished. Therefore, both are considered together as point defect mechanisms. Much lower activation energies (10 kcal/mole during heating and 65 kcal/mole prior to stabilization at the isotherm) have been observed during heating or within the first minute of isothermal treatment, emphasizing the dependence of these data on equilibrium thermal conditions (94). These low activation energies were attributed to elimination of mobile single interstitial atoms or loops ($\Delta E = 10$ kcal/mole) and interstitial migration ($\Delta E = 65$ kcal/mole) (69, 94). They admit, however, that it is unlikely a single activation energy can be used to describe this region. It is also possible that graphitization during rapid heating is stress-induced.

The graphitizability of carbon is heavily dependent upon the chemical structure of the material entering the graphitization process (98). Carbonaceous materials with a high degree of crosslinking develop a rigid turbostratic structure at low temperatures and are difficult to graphitize. Their aromatic clusters are linked together in a random way by thermally stable crosslinks, restricting axial orientation and growth. Such "hard carbons" do no graphitize easily until temperatures in excess of 3000°C (95) are used. However, removing oxygen or adding hydrogen to the starting material increases its graphitizability (84, 98-100). "Soft" carbons such as petroleum- or tar-derived pitches are less rigid and more oriented, and graphitize more readily (95).

Beyond the chemical nature of the carbonaceous precursor, graphitization can be strongly influenced by the rate and conditions of thermal treatment. Patrick et al. (101) showed that increased heating rate results in an increased rate of graphite transformation and that prolonged dwell at high temperatures enhances anisotropy. In addition, the

application of tensile stress during treatment serves to de-wrinkle layer planes once a temperature favorable for lattice creep is attained. De-wrinkling the planes at an earlier stage allows more rapid orientation toward the fiber axis and, consequently, more rapid crystallite growth (102).

The effects of graphitization temperature and time-at-temperature on both the crystal structure and physical properties of carbon fibers are well known. For example, Riggs (2) showed that increasing the maximum graphitization temperature, as shown in Figure 2.20. And, because the degree of graphitization, crystallite size, degree of basal plane orientation are known to increase with graphitization temperature (88), other lattice-dependent physical properties such as electrical and thermal conductivity would also be expected to increase as well (5, 7, 9, 11, 12).

2.2.6. Influence of Sulfur upon Graphitization

Impurities may have a pronounced effect upon the graphitization process. Sulfur, in particular, is a common impurity in petroleum feedstocks and has been found to affect their behavior during thermal treatment. Interestingly, it is both blamed for the irreversible volumetric expansion that accompanies its removal, and labelled a graphitization catalyst for its ability to remove disordered carbon atoms. It is well known that carbon can be used to bind sulfur, but the nature of this binding is not understood (103, 104). Liquid chromatography allows the identification of thiophene functional groups only (105), but other analytical methods have located various aliphatic arrangements (103).

As sulfur may take a variety of forms in carbons, there is considerable disagreement with regard to its role during thermal treatment. Understanding the nature of sulfur's influence is becoming increasingly important as the sulfur content observed in cokes continues to rise (86, 106).

The irreversible volumetric expansion of soft carbons at high temperatures, known as puffing, has been reported by many researchers. Present in the form of organic complex compounds (107), sulfur has been associated with puffing because expansion occurs over
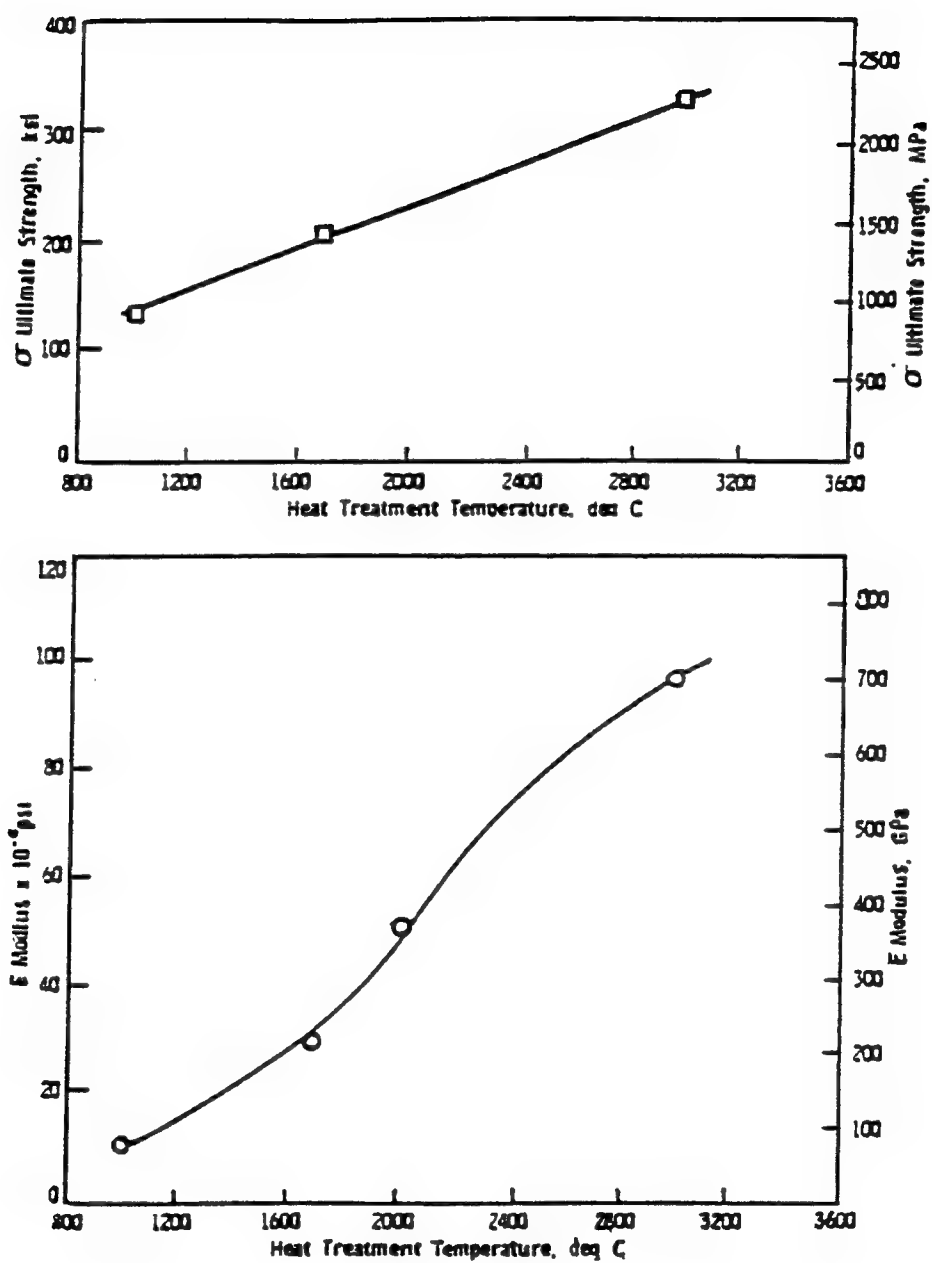
Figure 2.20. The increase of tensile strength and Young's modulus with graphitization temperature (2).

the same temperature range as its removal. Other impurities that could be related to puffing, such as oxygen and nitrogen, are lost at lower temperatures (108). Figure 2.21 shows the relative volume expansion and sulfur content of a typical puffing coke during high temperature treatment. Therefore, puffing is thought to result from the intercrystalline pressures generated by resistance to sulfur migration out of the carbon (108, 109).

Generally speaking, puffing occurs in the treatment of soft carbons to temperatures in excess of 1400°C. (107, 110-112). The exact temperature range, however, depends upon the sulfur content of the starting material, and the structure of the host carbon (86, 105, 111) For example, Brandtzœg (111, 113) reported a decrease in density and an increase in pore volume upon the treatment of cokes between 1400 and 1800°C. He also concluded that cokes of high sulfur content have a lower onset temperature for irreversible expansion than those of low sulfur content. While this temperature range agrees with that of most reports (86, 107, 108, 110-112), puffing at more elevated temperatures has been observed. Fujimoto et al. reported puffing between 1700 and 2200°C for a coal tar-based needle coke (114). In fact, although the rate of sulfur release is at a maximum in the range of 1400 to 1600°C, substantial quantities are removed from 1200 to 2500°C (110, 114). There is even the possibility that sulfur removal above 2500°C, coupled with the inherent reduction in strength of graphite bodies due to slip at those temperatures, can result in delayed puffing (108).

Just as there is difficulty in assigning a temperature range to puffing, there is difficulty in a priori prediction of whether a coke will experience puffing based solely upon its sulfur content (105, 111). For example, hard carbons having a high degree of crosslinking are more resistant to puffing that are soft, graphitizing carbons (108). There are also cases such as Gilsonite, which is an isotropic coke that releases a large quantity of sulfur over a broad temperature range and resists puffing (86). Even within a specific type of carbon, no simple rule can be made. It seems, then, that the form of the sulfur within the carbon structure is the dominating factor.
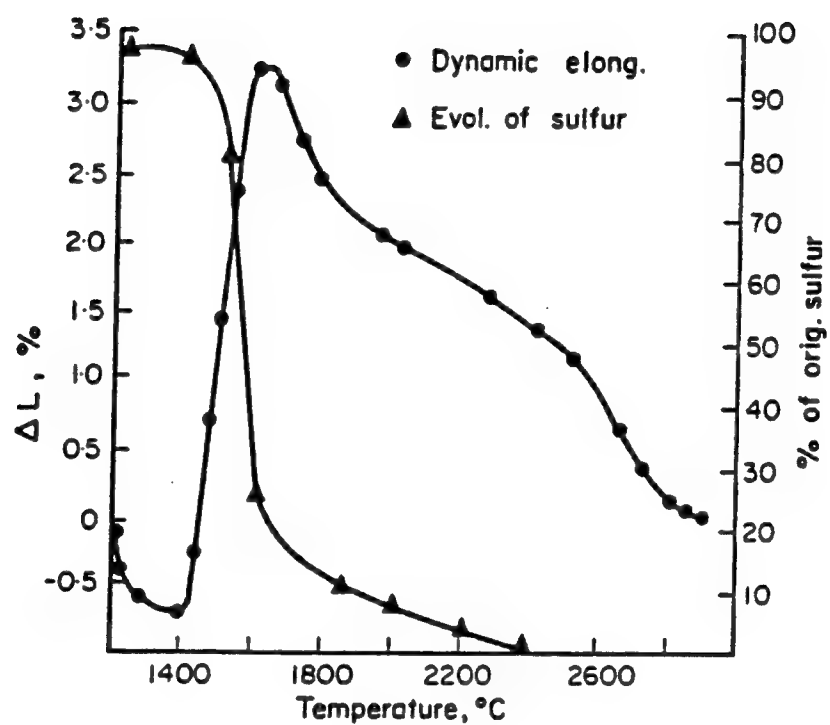
Figure 2.21. Volumetric expansion and sulfur content of a coke with temperature (108).

Bourrat et al. proposed that there are three types of sulfur present in carbon bodies (105). The first, primarily in the form of -SH groups, is associated with the labile aromatic fractions of tars, including small aromatic compounds. It is released at low temperatures, prior to the formation of local molecular orientation (LMO), as H_2S. It influences the condensation of polyaromatics and acts as a dehydrogenating agent, but is removed long before the puffing temperature range. The second type is most often related to puffing. It is released between 1300 and 1700°C and because its removal coincides with a decrease in d(0002) spacing, it is called a graphitization catalyst. Bourrat points out that it does not act repeatedly, as does a catalyst, but rather acts only once, upon sulfur removal. Therefore, it is more accurately called a modifier. Type III sulfur remains firmly bound, even at temperatures above 1700°C, and is removed only gradually. It acts as a very stable crosslinker and restricts graphite development. Figure 2.22 shows the temperature dependence of type I, II, and III sulfur content for carbons of differing heavy asphaltene fractions.

The influence of type II sulfur upon the (0002) separation in carbons is responsible for sulfur's label as a graphitization catalyst. Several investigators have observed a high angle shoulder on the (0002) diffraction peak during desulfurization, suggesting the creation of a phase having greater graphitic ordering (86, 110, 111, 113, 115). The best presentation of this phenomenon, by Brandtzœg and Øye (113), is shown in Figure 2.23. In each investigation, the low angle component was found to correspond to a d(0002) spacing of around 3.44 Å, or a degree of graphitization (18) of approximately zero. Fitzer and Weisenburger (115) also reported that the low-angle peak shifted toward higher angles during heat treatment, and that this effect was more pronounced in carbons with higher sulfur contents. They calculated an activation energy of 65 to 90 kcal/mole for graphitization based upon d(0002) changes and, as this value was significantly lower than the 220-260 kcal/mole reported for homogeneous graphitization, they viewed sulfur as a graphitization catalyst. In addition, they were able to rule out other possible causes for
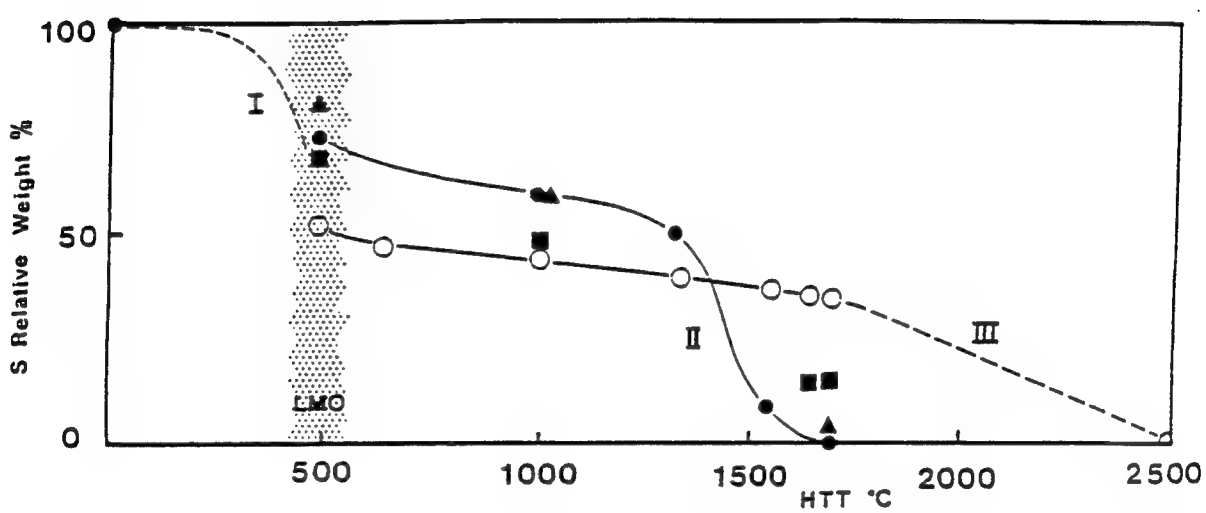
Legend:

LMO	zone of appearance of local molecular order
●	asphalt extracted from Arabian light crude oil
▲	asphalt extracted from Safaniya, or Arabian heavy
■	asphalt extracted from Athabasca crude oil
○	asphalt extracted from Boscan crude oil

Figure 2.22. Type I, II, and III sulfur content with temperature (105).
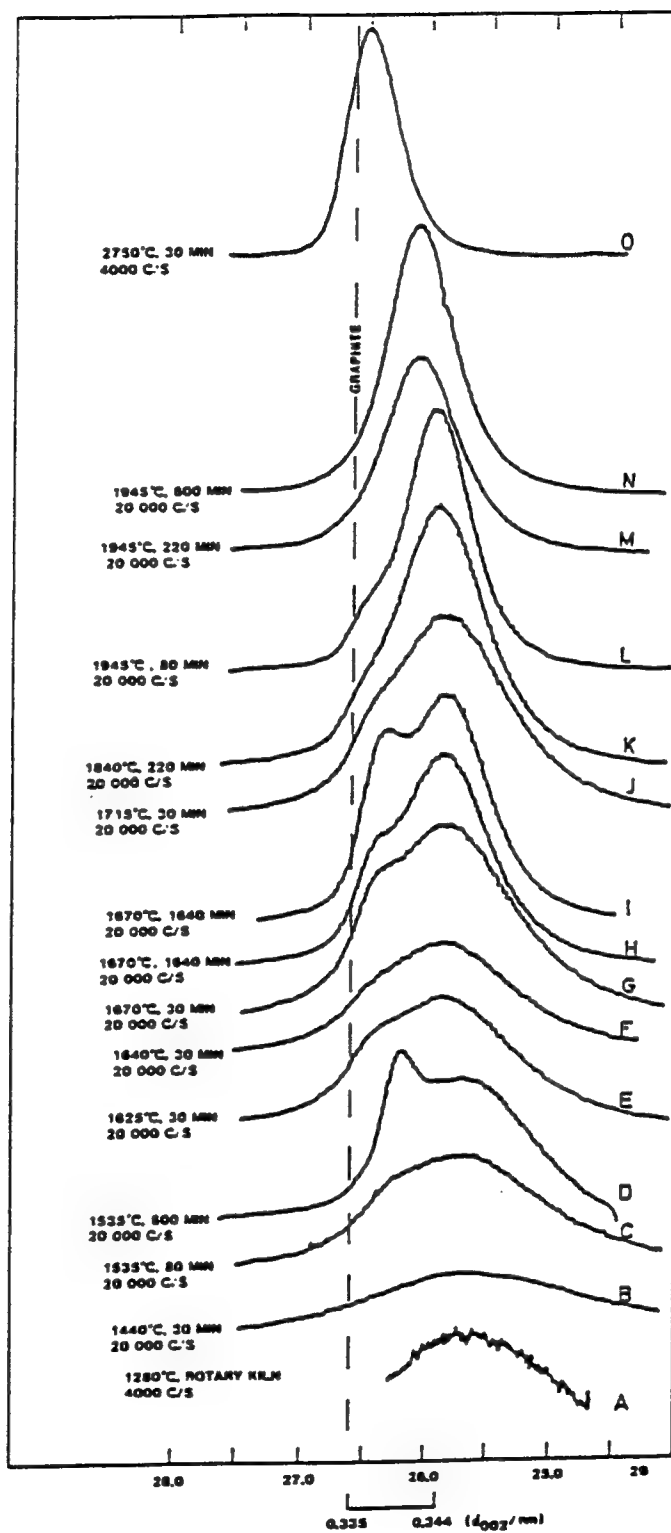
Figure 2.23. The (0002) diffraction peak for a petroleum coke heated at 10°C per minute (113).

(0002) peak splitting, such as metal inclusions, which tend to catalyze graphitization (116), and stress graphitization.

Heintz (86) explained these results using the following reasoning: the observed broadening of the (0002) diffraction peak (111, 113) is caused by a combination of small mean stack height, non-uniform strain, and a distribution of d(0002) spacings. If it is assumed that crystallites having the largest d(0002) contain the greatest concentration of impurities, then crystallites having d(0002) greater than some arbitrary value (Heintz chose 3.36 Å) would be mechanically strained by the removal of impurities, while those having d(0002) less than 3.36 Å would be unaffected. The high-angle peak is developed with increasing temperature as its d(0002) is less than 3.36 Å. The broad, low-angle portion, however, represents the bulk of the material where the impurities are concentrated, and its intensity decreases as the impurities are removed. Thus, sulfur removal results in the general shift of the (0002) diffraction peak to higher angles (lower d(0002)). As it is the disordered regions that are affected by desulfurization, sulfur is considered a graphitization catalyst.

The method by which the sulfur promotes ordering of disordered regions was further clarified by Brandtzœg and Øye (113, 116, 117). They proposed that graphitization first required the build-up of sufficient vapor pressure to initiate puffing. Then, the evolved sulfur reacts with imperfect carbon atoms to from CS or CS_2, while hydrogen is also removed as H_2 or H_2S, leaving behind perfectly oriented carbon. Two other possible mechanisms were proposed by Fitzer and Weisenburger (115). The first is that sulfur atoms may be predominantly located along dislocations and, upon their removal, the dislocations move toward grain boundaries. The second is that structural ordering is facilitated by the formation of vacancies during sulfur removal. In either case, it appears to be the ability of sulfur to remove carbon that creates mobile defects and leads to graphitic ordering.

Despite being considered a graphitization catalyst, or at least a modifier, "degraphitization" has been observed during sulfur removal. Fitzer and Weisenburger (115) concluded that "graphitization stops temporarily between 1700 and 2100°C" in sulfur-containing cokes. By this, they meant that d(0002) showed no decrease toward the graphite equilibrium value during this temperature range. Heintz (86) also observed that d(0002) increased with time at constant temperature. As the previous conclusions on sulfur catalysis were based solely on the (0002) diffraction peak and did not consider non-uniform strain, the decrease in d(0002) during desulfurization could have been the result of localized strain (118). With time, this pressure may be relieved and the apparent decrease in d(0002) may be reversed.

The gaseous form in which sulfur is removed is also open to debate. Most investigators have reported that hydrogen sulfide is its most likely form at all temperatures (110, 115). However, Pearce and Heintz (116) showed that the formation of carbon-sulfur compounds, such as CS and CS_2, would be the most effective in promoting order in a disordered carbon. In addition, Brandtzœg and Øye (113) proved that formation of hydrogen sulfide is thermodynamically more favorable than the formation of carbon-sulfur compounds only at temperatures below around 1400°C. Above this temperature, formation of carbon disulfide, and later, carbon sulfide, are thermodynamically favorable. Figure 2.24 shows a plot of the equilibrium constants of formation, K_f, of some C-H, H-S, and C-S compounds with temperature (113). Therefore, it is likely that sulfur is given off in the form of carbon disulfide from carbons which experience puffing at relatively high temperatures, or which are composed of predominantly type III sulfur (105).

This finding limits the applicability of a proposed method of desulfurization at low temperatures, proposed by Sugimoto et al. (110), Gillot et al. (117), and Mochida et al. (119). They proposed heating a sulfur-bearing carbon to a temperature below 1500°C under hydrogen and remaining at that temperature until sulfur is depleted. For this to
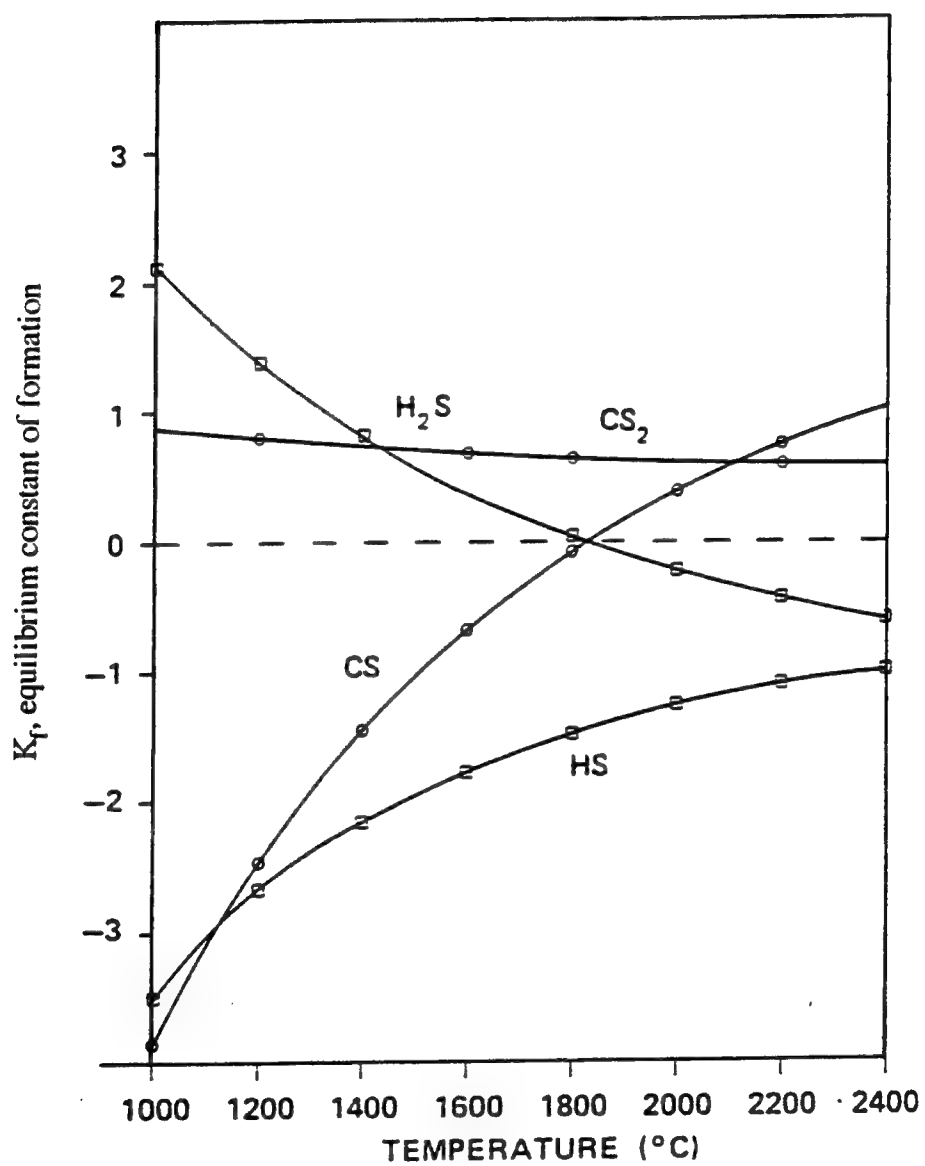
Figure 2.24. Equilibrium constants of formation of some C-H, H-S, and C-S compounds with temperature (113).

occur, the sulfur would have to be loosely bound, either as interstitials between graphite basal planes or at plane edges. Thiophenic, or other aromatic groups, would be unaffected.

Finally, desulfurization was found to have a deleterious effect upon lattice-dependent transport properties, such as electrical resistivity (111, 113). Brandtzœg and Øye show that the electrical resistivities of petroleum cokes decrease with heat treatment temperature to a local minimum value near 1600°C. Further heating resulted in an increase in resistivity that is not recovered until heat treatment temperatures well in excess of 2000°C, as shown in Figure 2.25 (113).

2.2.7. Solvent Etching of Graphitic Carbons

Several investigators have proposed solvent treatments for carbons and carbon fibers. Such a treatment might be applied to as-spun fibers to enhance stabilization (120-122) or, in an extreme case, to form graphite oxide from graphite powder or fibers (123-125). In the case of stabilization, the aim was to incorporate oxygen-containing functional groups into the pitch. Thus, these solvents included nitric acid, mixed acids (120), such as nitric-sulfuric, and organics, such as THF (121) and acetone (122). The formation of graphite oxide, however, is a destructive process that has been used to study the textural and structural differences between graphites. Typically, graphites are exposed to mixtures of concentrating acids and/or strongly oxidizing compounds. One example is Staudenmaier's reagent, consisting of potassium chlorate in a mixture of concentrated sulfuric and nitric acids. Explosion upon the addition of graphite was a constant hazard (123). Hummers recommended a less violent oxidizer, consisting of concentrated sulfuric acid, sodium nitrate, and potassium permanganate. Again, however, tight temperature control must be maintained when graphite is added to prevent explosion.

Maire and Mering (18) proposed a method of grading graphites based upon their reaction with a more tame oxidizer, potassium dichromate in sulfuric acid. They believed that all carbon within a graphite would eventually react with the solvent, but that more
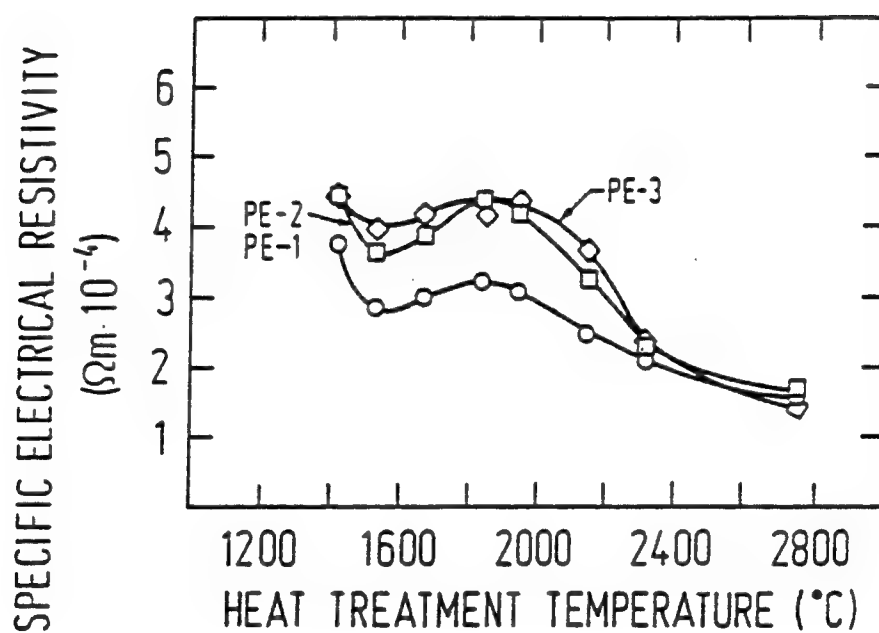
Figure 2.25. Electrical resistivities of heat treated petroleum cokes with treatment temperature (113).

ordered regions would react more slowly than disordered regions. Their results suggested a way of determining the graphite crystalline fraction within a carbon, and agreed well with physical property measurements. However, disagreement over whether highly-ordered regions react more or less slowly than disordered regions continues, as Oya et al. (126) showed, using a similar oxidizer on cokes of differing quality.

2.2.8. Models of the Graphite Structure in Fibers

Several models have been developed to describe the network of graphite crystallites that comprise a pitch-based carbon fiber. The first was the ribbon model (1), which represented the structure as a collection of continuous graphite crystallites that wind and twist, but are basically aligned with the fiber axis. Crystallite dimensions L_c and L_a correspond to the thickness of the crystallite and the length of a linear portion, respectively. A second model, very similar to the ribbon model, was developed by Johnson (59), but allowed basal plane segments to branch and join new crystallites. These two models are shown schematically in Figures 2.26 and 2.27.

Both of these models would give rise to flat, elongated voids having smooth surfaces between crystallites. While pores are typically elongated and roughly parallel to the fiber axis, they are not smooth, especially in the case of very ordered fibers (45, 127, 128). Bourrat et al. (105) and others have shown that such voids have a fractal nature, being rough and irregular. A model of high-modulus carbon fiber structure, shown in Figure 2.28, that includes irregular void boundaries, crystallite curvature, and wrinkling has been proposed by Johnson (129).

2.3 Mechanical Properties of Carbon Fibers

The elastic constants of a material are strongly related to the lattice dynamics of its crystalline building blocks. Thus, the subject of lattice dynamics leads to the definition of elastic constants that describe moduli, in addition to the phonon dispersion principles that
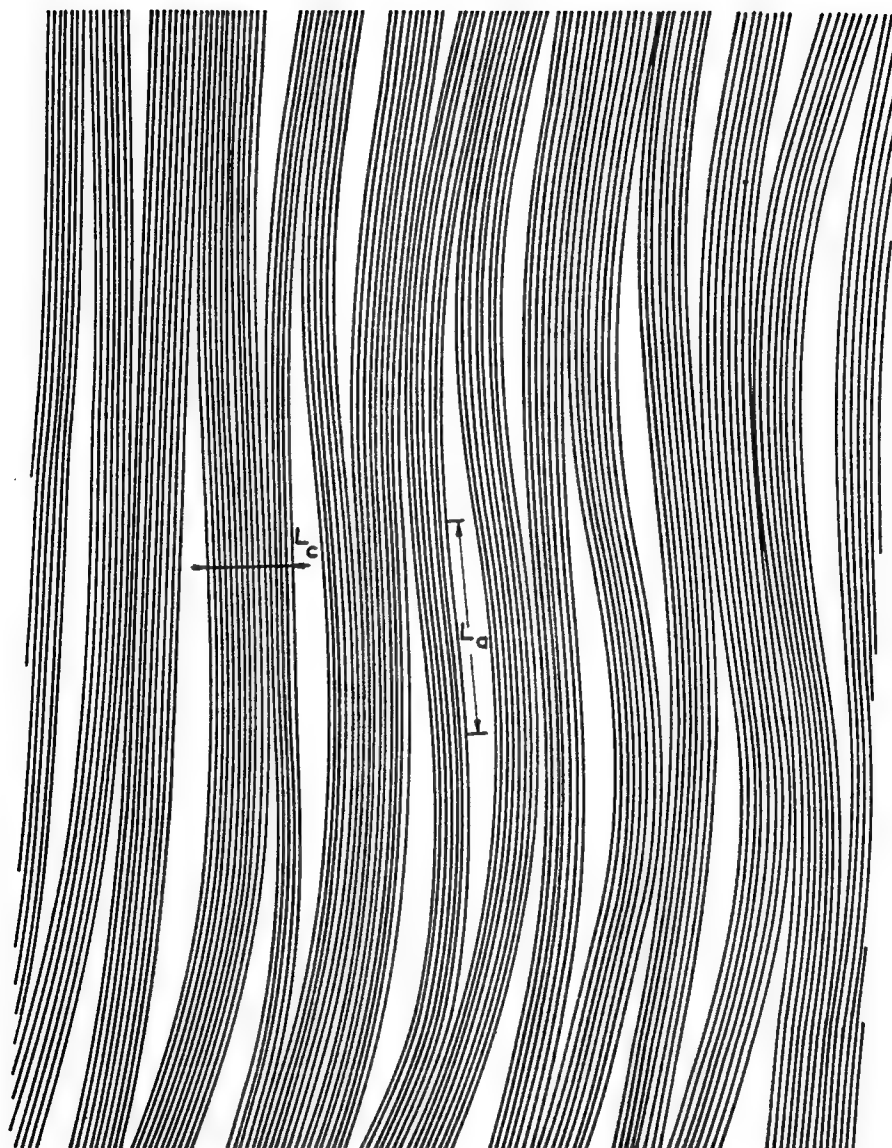
Figure 2.26. The ribbon model (1).
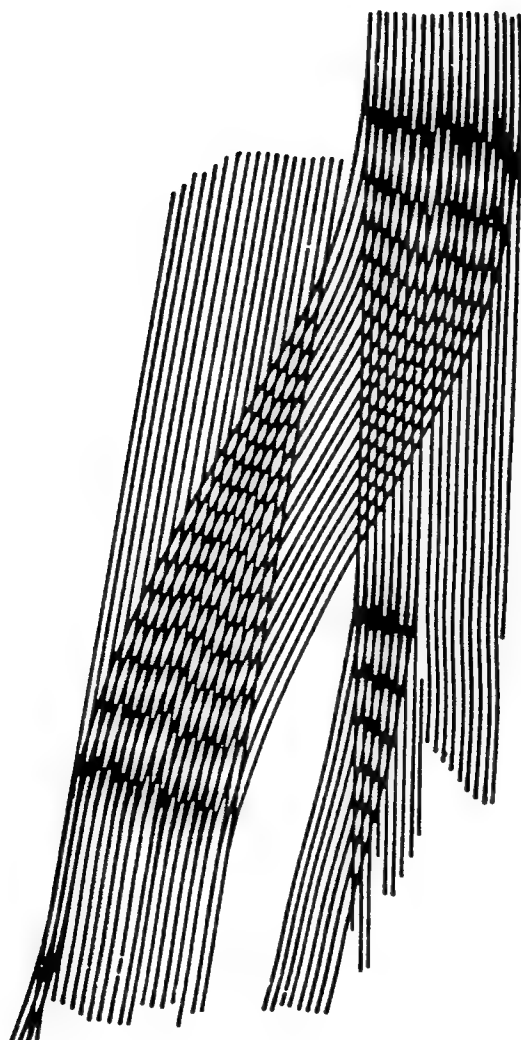
Figure 2.27. Johnson's tangled network model (59).
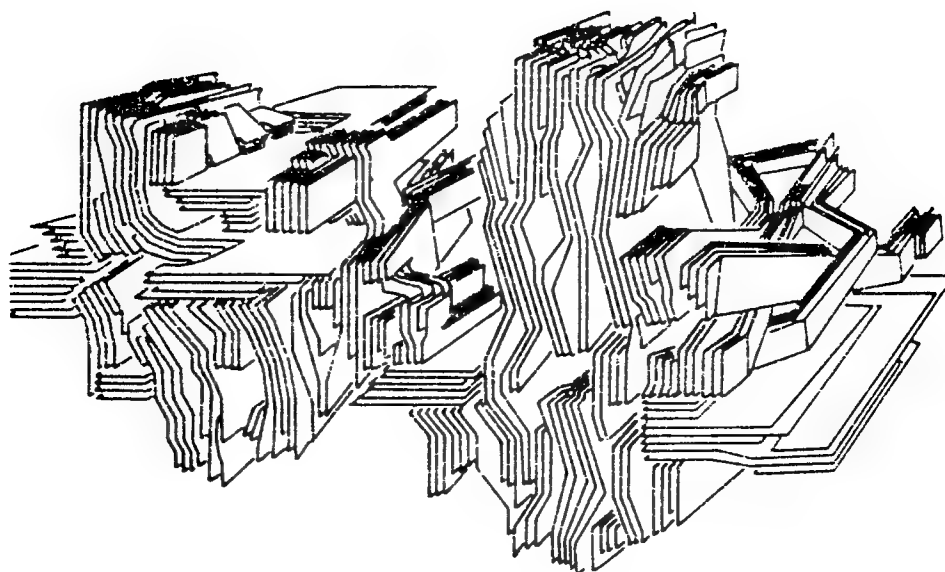
Figure 2.28. Johnson's model of high-modulus carbon fiber structure (129).

affect specific heat capacity and thermal conductivity. Here, the elastic nature of graphite will be discussed, followed by the mechanical properties of polycrystalline carbon fibers.

2.3.1. Elasticity of Graphite

The initial work in the field of lattice dynamics was aimed at explaining the heat capacity of graphite at low temperatures using a long wavelength model (129, 130). The elastic constants were calculated from experimental values of the Debye, or characteristic, temperatures of lattice vibration. However, this semi-continuum approach was found unsatisfactory at high frequencies and has been replaced by force constant models. Girifalco and Lad (131), and Kelly and Duff (132), showed that the elastic constants of a graphite crystal could be calculated from Lennard-Jones potentials, and their results agreed with the experimentally-determined compressibility and surface energy of graphite. The latest adaptation of this model was by Al-Jishi and Deresselhaus (133), and the elastic constants of graphite have been most recently determined by Jansen and Freeman (134). Their model fits both the phonon frequencies and the elastic constants observed for graphite. The currently accepted values, given in a review of the subject by Kelly (135) are presented in Table 2.1.

Table 2.1. Elastic constants of graphite (135).

C_{11}	1060±20 (GPa)	S_{11}	0.98±0.03 (10^{-12} Pa^{-1})
C_{12}	180±20	S_{12}	-0.16±0.06
C_{13}	15±5	S_{13}	-0.33±0.08
C_{33}	36.5±1	S_{33}	27.5±1
C_{44}	4.5±0.5	S_{44}	240±30

The C_{ij} are the elastic moduli (or stiffnesses) and the S_{ij} are the compliances in the different crystallographic directions. Thus, there are five independent elastic constants that

describe the graphite crystal, and their values show the striking anisotropy of this structure. The high values of C_{11} and C_{12}, representing the in-plane tensile and in-plane transverse moduli, respectively, are a result of the strong sp^2 hybridized bonding in the basal planes. On the other hand, the low value of C_{33} reflects the weak forces that bind the planes in the transverse direction. Similarly, the low value of C_{44} indicates poor resistance to shear parallel to the basal plane (5, 7).

Applying constants developed for single crystal graphite to disordered polycrystalline carbons is difficult. First, the dependences of the C_{ij} upon defect concentration and crystallite size must be considered. Then, a description of the orientation of individual crystallites is needed if bulk elastic properties of a carbon body are to be estimated.

In-plane elastic constants C_{11} and C_{12} decrease slightly with the introduction of point defects, but are relatively insensitive to stacking faults (135). The out-of-plane constants vary much more, however. C_{13} is expected to vary with defect concentration, but the nature of this variation is unknown. Fortunately, neither the tensile nor the torsional modulus of carbon fibers depend strongly upon C_{13} (5). Both C_{33} and C_{44} decrease with the decrease in interplanar bonding that accompanies turbostratic disorder. Therefore, both constants are correlated with the lattice constant, c. Using inelastic neutron scattering, Collins and Haywood (136) observed that C_{33} was reduced by 15% as the (0002) separation increased from 3.354 to 3.40 Å. The value of C_{33} should increase rapidly toward the single crystal value, 36.5 GPa, with graphitic ordering. There is a lesser dependence of C_{44} upon interplanar spacing as it describes the resistance to interplanar shear rather than interplanar tensile deformation (135). Typically, C_{44} was determined for single crystals from low temperature heat capacity measurements (130, 137). By the same method, van der Hoeven and Keesom (138) showed that carbons, which they assumed to contain a large quantity of stacking faults, such as graphitized lampblack and pyrographite, had values of C_{44} as low as 0.7 GPa, compared to 4.5 GPa for a single crystal. This result may be a good approximation to the value for carbon fibers prior to graphitization (5).

2.3.2. Polycrystalline Carbons and Fibers

The orientation of graphite basal planes within a body are determined by the forming process. As carbon fibers are produced by thermal treatment of a melt- or solution-spun polymer or macromolecule, the molecular chains or basal planes are arranged essentially parallel to the fiber axis by the spinning process (4). Hence, the in-plane elastic behavior of the graphite crystal should dominate the axial elasticity of the fiber, and that misorientation of the crystals with respect to the fiber axis will result in a significant loss of stiffness. Figure 2.29 illustrates a graphite crystallite, misoriented with respect to the fiber axis by an angle ϕ, the angle made by the crystallite c-axis and a line perpendicular to the fiber axis. Measurement of this angle using X-ray diffraction or electron microscopy will be discussed in a later section. Either method can be used to formulate a function, $I(\phi)$, that describes the distribution of crystallite orientations.

Several forms of $I(\phi)$ have been proposed (139, 140). The most widely accepted of these is the Bacon anisotropy function

$$I(\phi) = I_o \cos^n \phi \ (139).\tag{2.5}$$

Then, assuming that the body is composed of a large number of crystallites with orientations described by $I(\phi)$, the polycrystalline elastic constants can be estimated.

One method of estimating the tensile modulus of carbon fibers, discussed because of its simplicity, has been proposed by Ruland (141). Labelled the "elastic unwrinkling" model, it describes a fiber as a collection of wrinkled graphite layers arranged nearly parallel to the fiber axis. Application of an external stress causes these layers to unwrinkle. Young's modulus, E, is given by

$$\frac{1}{E} = l_z S_{11} + m_z k_e,\tag{2.6}$$

where
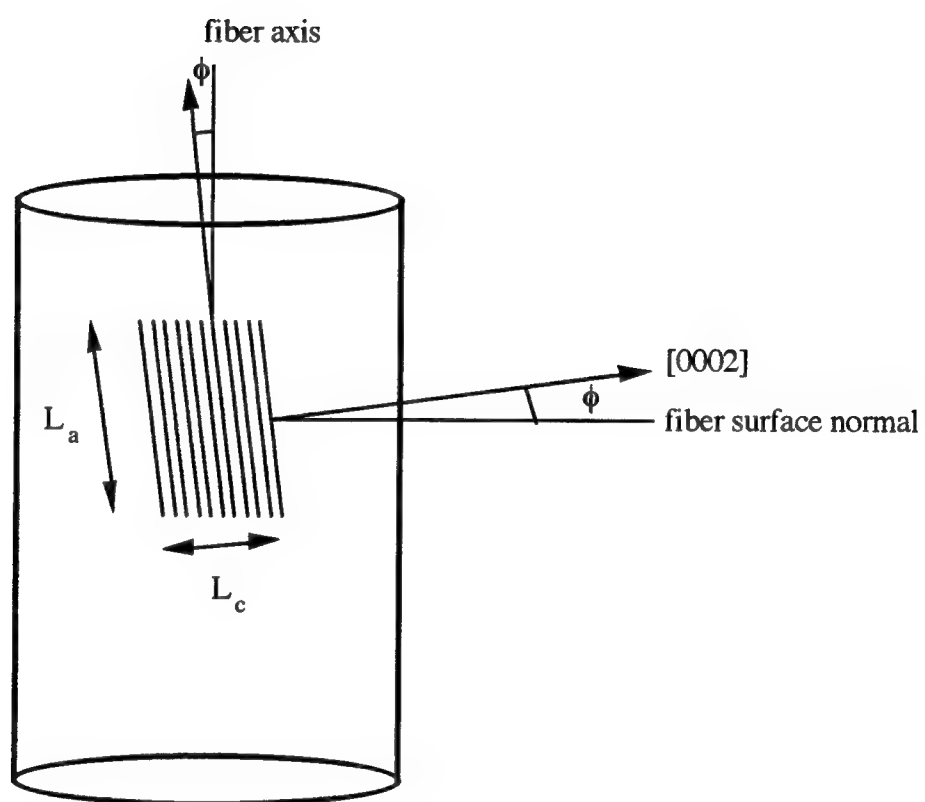
Figure 2.29. The crystallite misorientation angle ϕ (5).

$$l_Z = \frac{\int_0^\pi I(\theta) \sin^2 \theta \, d\theta}{\int_0^\pi I(\theta) \sin \theta \, d\theta}, \qquad (2.7)$$

and

$$m_Z = \frac{\int_0^\pi I(\theta) \cos^2 \theta \, d\theta}{\int_0^\pi I(\theta) \sin \theta \, d\theta}. \qquad (2.8)$$

k_e is a compliance, set equal to 0.03 GPa^{-1}. The angle that appears in the integrand, θ, is the compliment of ϕ, or

$$\theta = \frac{\pi}{2} - \phi. \qquad (2.9)$$

The arbitrary definition of k_e without physical basis has limited its acceptance (5).

2.3.3. Tensile Properties of Carbon Fibers

Carbon fibers are produced from mesophase pitches by a number of manufacturers. Table 2.2 compares the manufacturer-supplied mechanical property data for some of these, as well as basic crystal structural parameters. Data for fibers produced by Amoco Performance Products (Thornel fibers), E. I. Du Pont de Nemours and Company (Fiber G), and Mitsubishi Gas Chemical Company (AR synthetic pitch-based fibers) are shown, with the properties of single crystal graphite presented for comparison.

Strong correlations exist between many structural parameters and the Young's moduli of these fibers. The two most important are the degree of crystallinity, determined from the (0002) separation, and the orientation of basal planes about the fiber axis. Several investigators have proposed empirical relationships between these data. Barr et al. (142) and Bright and Singer (143) found that the measured value of Z, a commonly-used preferred orientation parameter, decreased as the modulus of the fiber increased. This

finding was explained by Johnson (59), who pointed out that the modulus would be expected to increase as the rigid basal planes become more oriented about the fiber axis.

Table 2.2. Mechanical and structural properties of various mesophase pitch-based fibers.

Fiber	T. strength (GPa)	Y. modulus (GPa)	d(0002) (Å)	L_c (Å)	Z (°)
Thornel P-25[1,2]	1.4	160	3.431	26	31.9
P-55[1,2]	1.9	380	3.423	114	14.1
P-75[1,2]	2.1	520	3.410	157	11.0
P-100[1,2]	2.2	720	3.381	208	5.6
P-120[1,2]	2.2	830	3.376	228	5.6
Du Pont E-35[3,2]	2.8	241	3.439	37	21.6
E-75[3,2]	3.1	516	3.423	105	10.9
E-105[3,2]	3.3	724	3.420	121	7.2
E-120[3,4]	3.4	827	3.410	190	-
E-130[3,4]	3.9	894	3.380	240	-
AR pitch[5]	4.0	880	3.390	210	-
graphite[6]	≈106	1060	3.354	≈∞	0.0

[1] Thornel Product Information, Amoco Performance Products, Inc. (144)
[2] courtesy of D. P. Anderson (145)
[3] Du Pont de Nemours and Co. (product data sheet) (146)
[4] Nysten et al. (147)
[5] Mitsubishi Gas and Chemical Co. (product data sheet) (148)
[6] Dresselhaus et al. (5)

Higher degrees of crystallinity, too, result in greater values for Young's modulus. Schulz (149) showed that a decrease in (0002) separation toward the equilibrium value for graphite, 3.354 Å, resulted in an increase in Young's modulus. A subsequent study by Guigon and Oberlin (150) showed the correlation between several structural parameters, such as coherence length (L_a), pore dimension, and crystallite radius of curvature, including the (0002) separation, with Young's modulus for Amoco mesophase pitch-based carbon fibers. Specific studies of the relationships between Young's modulus and

coherence length, and Young's modulus and pore dimension, have been conducted by Rosen and Sullivan (151) and Johnson (59), respectively. The former showed that Young's modulus increases with increasing coherence length. Johnson's study suggested that fibers having a high modulus will possess a more developed void network, consisting of fine, irregularly-shaped voids.

Tensile strength is a different matter. As seen in Table 2.2, a correlation exists between the crystallographic parameters and the mechanical properties within each fiber manufacturer's group. However, both the Du Pont and the AR pitch-based fibers have significantly higher tensile strengths than those produced by Amoco, even for nearly equivalent structural parameters. Therefore, the tensile strengths of pitch-based carbon fibers are related to other parameters in addition to crystal structure data. According to Johnson (59, 152), the tensile strength of a fiber is determined by the concentration of flaws within the fiber. These flaws result from processing conditions or impurities present in the feedstock. Also, simply altering the transverse arrangement of the graphite basal planes may influence mechanical properties. Endo proposed that the texture of a fiber may affect tensile strength (33), and concluded that some, such as the radial-folded texture shown in Figure 2.10, may prevent the propagation of microcracks in the radial direction, thereby increasing the tensile strength. It is believed that fibers having a radial-folded texture are more resistant to crack propagation than are fibers with a purely radial texture (4, 33). Also, fibers having a line-origin texture seem to fracture by successive failures, accompanied by longitudinal splitting in the fiber. This acts as a toughening mechanism (41, 153, 154). A plot comparing the tensile strengths of a radial-texture circular fiber and a trilobal fiber possessing a line-origin texture at different treatment temperatures is shown in Figure 2.30 (153). As a result, there has been considerable effort aimed at improving tensile strength through texture modification (38, 155, 156).
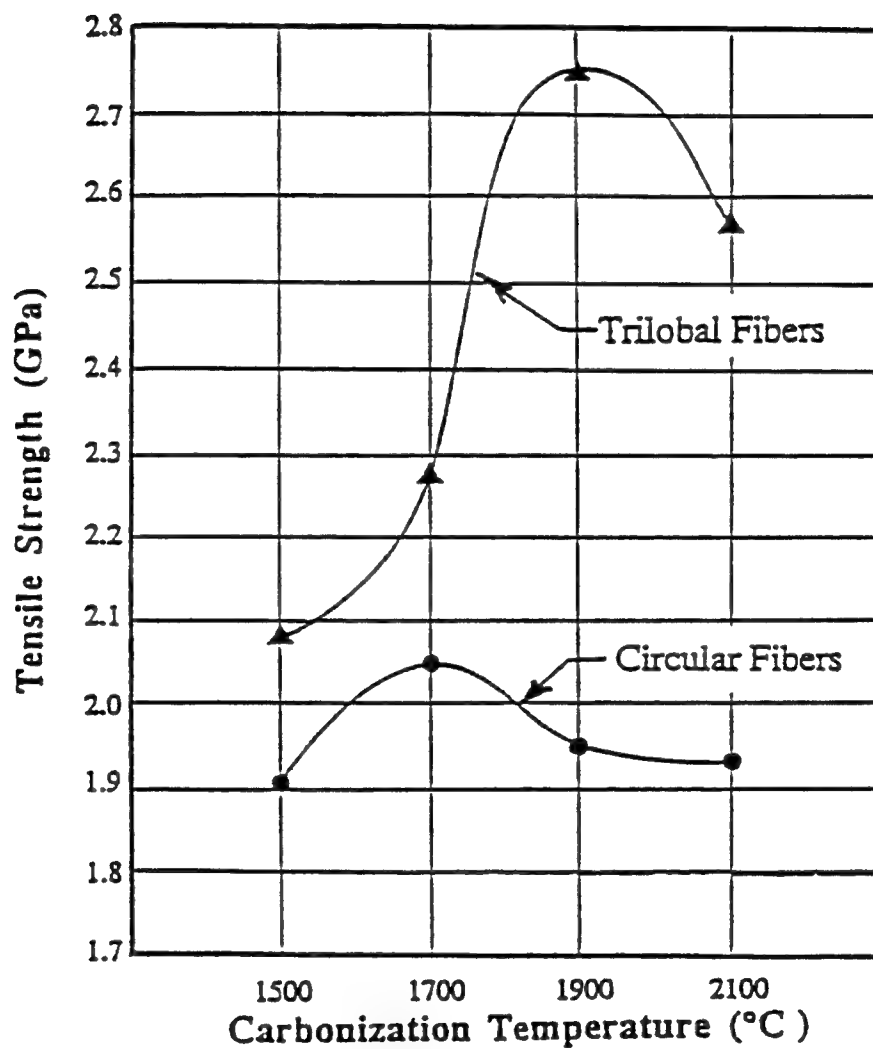
Figure 2.30. Tensile strengths of circular and trilobal pitch-based fibers with graphitization temperature (153).

2.4. Thermal Properties of Carbon Fibers

Thermal properties can be divided into two areas: equilibrium and transport. Included in the former is specific heat capacity, which is an indicator of the population and energy of phonon modes within a material, while transport is characterized by thermal conductivity. The two areas are related by the fact heat is transferred by the motion of phonons, and the phonon concentration determines the rate of energy transfer.

2.4.1. Specific Heat Capacity

Very little work has been published regarding the specific heat capacity of carbon fibers (157, 158). However, several researchers have studied the heat capacity of graphite and polycrystalline carbons as a function of thermal history (159-161). Heat capacity is defined as the quantity of energy per unit mass required to produce a specified temperature change in a substance. This quantity depends strongly on temperature as shown in Figure 2.31 (136), and for graphite, at least three distinct regions of temperature dependence have been observed. At temperatures below about 10K, a cubic temperature dependence was found by Krumhansl and Brooks (162) and van der Hoeven and Keesom (138), but an additional linear term was needed to fit the data. Thus, the heat capacity, $C_p(T)$, over this temperature range can be written

$$C_p(T) = gT + aT^3, \qquad (2.10)$$

where g was assumed to be due to an electronic contribution. Van der Hoeven and Keesom found values for g of 5.57 and 3.3 μcal/mole/K for reactor graphite and single crystal graphite, respectively. The difference in g may be a result of the difference in defect concentration between the two materials. In fact, for non-graphitic carbons, the effect of defects may outweigh the electronic contribution (5). At temperatures above 10K, the heat capacity assumes a quadratic or nearly-quadratic temperature dependence (137, 159, 163). Finally, at temperatures above about 3200°C, the heat capacity remains approximately constant near the Dulong and Petit value of 6 cal/mole/K (164) until the fusion temperature
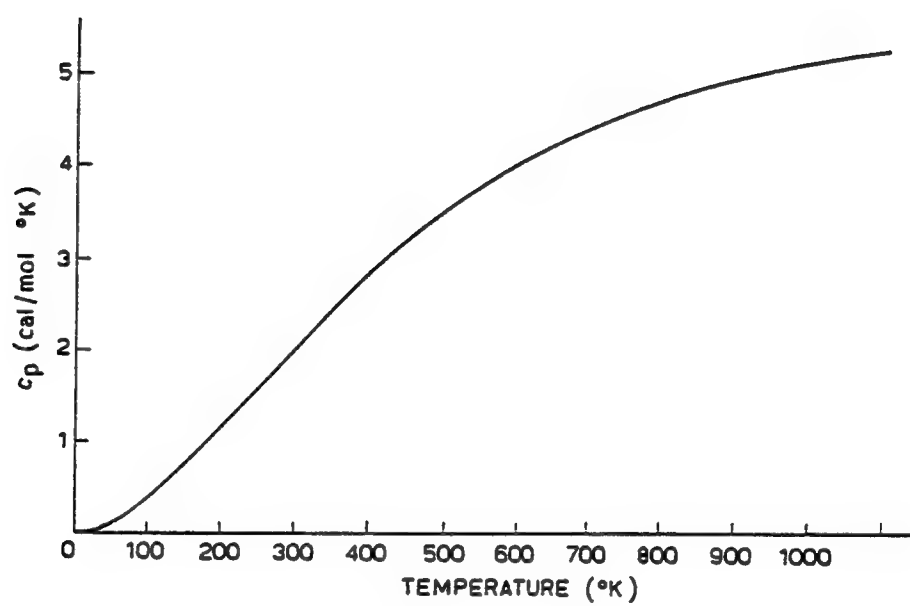
Figure 2.31. The heat capacity of graphite with temperature (135).

is reached above 3800°C. At that point, there is a sharp rise in heat capacity and the concentration of thermally induced defects increases (7, 9).

These findings may be reconciled based on the theory of graphite lattice dynamics. The equations for atomic motion have been developed by Komatsu and Nagamiya (129, 130) and Kelly (135, 165). For each carbon atom, there are three acoustic modes of vibration: longitudinal in-plane, transverse in-plane, and transverse out-of-plane. The nine optical modes are neglected as their excitation requires much more energy. An examination of the elastic constants in these directions led Komatsu (130), and later Bowman and Krumhansl (137) to conclude that these could be effectively reduced to two, an in-plane and an out-of-plane, acoustic modes at low temperatures. Each is characterized by a Debye temperature, θ_D, which is related to their maximum frequency by the following formula:

$$\theta_D = \frac{h\nu_{max}}{k}, \tag{2.11}$$

where h is Planck's constant and k is Boltzmann's constant. At this temperature, the contribution to the heat capacity by the phonon mode considered reaches a constant value. These values were determined from phonon velocities to be 2350 and 180.5K for the in-plane and out-of-plane phonons, respectively. Because the in-plane term still consists of the contributions of two phonon motion (longitudinal and transverse), a T^3 dependence would be observed for the heat capacity at all temperatures. However, the constant wavelength surfaces are truncated by the c-directional boundary of the first Brillouin zone. This occurs at a temperature given by

$$T' = \frac{h}{k\pi c}\sqrt{\frac{C_{44}}{\rho}} = 26.7K, \tag{2.12}$$

where ρ is the mass density and c is the velocity of sound. Thus, a T^3 dependence should be observed below this temperature and a T^2 dependence above (130). As will be discussed in the following sections, the same temperature dependence is also observed in thermal conductivity measurements (165). In fact, specific heat capacity measurement, and the study of phonons in general, is quite useful in the characterization of carbons (166, 167).

2.4.2. Thermal Conductivity of Graphite

Heat transfer occurs by the flow of energy from a region of high energy (high temperature) to a region of low energy (low temperature). In a solid, possible energy carriers include conduction band electrons and lattice waves, or phonons. Each is active over the entire range of temperatures and makes a finite contribution to the thermal conductivity. However, dominance of one carrier in a given temperature range can result from differing temperature dependences of their scattering.

The basics of phonon conduction and how thermal conductivity is related to the specific heat capacity are presented in Appendix A.2. Therefore, in this section, only some interesting features of phonon and electronic conduction will be considered.

If phonon motion were completely harmonic, their mean-free-path, Λ, or average distance between collisions, would be limited only by crystal boundaries or other lattice imperfections. However, anharmonic interactions do occur, resulting in phonon coupling and a reduction in mean-free-path. Therefore, Λ is principally determined by two processes, phonon-phonon interactions and geometric scattering. The theory of anharmonic coupling (168) predicts an inverse relationship of Λ and T, which can be understood on the basis of phonon concentration. As temperature is increased, the phonon concentration increases monotonically. The phonon collision frequency is proportional to the concentration, so the mean time between collisions, $\tau = $ frequency^{-1}, is inversely proportional to T. As $\Lambda = \vartheta\tau$, the mean-free-path is inversely proportional to temperature.

Phonon collisions can only result in a temperature gradient if they are inelastic, resulting in an energy loss. In a Normal (N) process, such as shown in Figure 2.32 (169) for a simple two phonon interaction, two phonons of wavevectors K_1 and K_2 interact to produce a third of wavevector K_3 still within the first Brillouin zone, so that

$$K_1 + K_2 = K_3. \qquad (2.13)$$

Thus, the wavevector of phonon three is equal to the vector sum of the wavevectors of
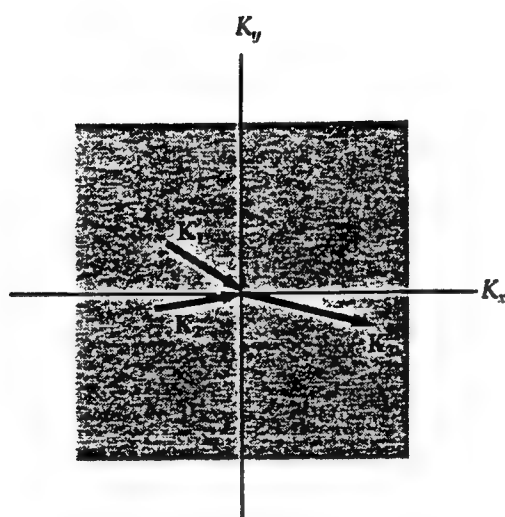
Figure 2.32. A normal (N) phonon-phonon interaction (169).

phonons one and two. There is no energy loss and, if only this type of phonon interaction were possible, there would be no thermal gradient and no resistance to thermal conduction.

Incident phonons of higher energy, however, may interact to form a phonon with a wavevector extending out of the first Brillouin zone of the host crystal, as shown in Figure 2.33. It must be brought back into the zone by the addition of a reciprocal lattice vector, $\mathbf{G}$, of magnitude $2\pi a$, where a is the lattice constant of the crystal.

$$\mathbf{K}_1 + \mathbf{K}_2 = \mathbf{K}_3 + \mathbf{G}. \tag{2.14}$$

This type of interaction is known as an Umklapp (U) process. The energy of phonons one and two must be on the order of $\frac{1}{2}k\theta_D$, because both must have wavevectors of magnitudes near $\frac{1}{2}G$ for Umklapp scattering to occur. The number of phonons meeting this criterion varies approximately as $\exp(-\theta_D/bT)$, where b is usually taken to be around 2.2 (170).

Geometrical scattering may also limit the phonon mean-free-path. Scattering of this sort arises from phonon collisions with crystal boundaries, impurities, lattice imperfections, pores, and non-crystalline regions. As the temperature is reduced, the phonon-phonon interaction mean-free-path becomes comparable to the crystal dimension. This effect, discovered by de Haas and Biermasz (171), is responsible for the sharp decrease in thermal conductivity at low temperatures. There, the thermal conductivity becomes

$$K = \frac{1}{3}C_v \vartheta D \tag{2.15}$$

for the isotropic case, where D is the crystallite dimension (172). Because both ϑ and D are constant, K takes on the temperature dependence of C_v, the heat capacity, at low temperatures. Actually, the mean-free-path is not constant with temperature, but is related to the Umklapp (U) and boundary (b) scattering values by

$$\frac{1}{\Lambda_{eff}} = \frac{1}{\Lambda_U} + \frac{1}{\Lambda_b} = \frac{1}{A \cdot \exp\left(\frac{\theta_D}{2T}\right)} + \frac{1}{D}, \tag{2.16}$$

but Λ_{eff}, the effective mean-free-path, approaches D at sufficiently low temperatures (169). As several researchers have reported, the position of this thermal conductivity maximum
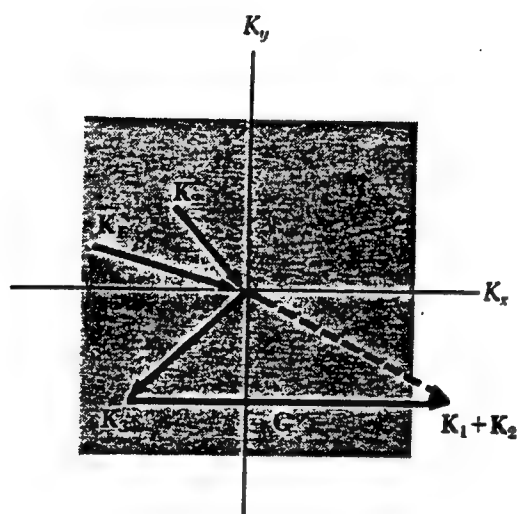
Figure 2.33. An Umklapp (U) phonon-phonon interaction (169).

varies with perfection of the graphite lattice, occurring at lower temperatures for more ordered carbons (5, 166, 167, 173, 174). Typical thermal conductivity curves versus temperature for graphite are shown in Figure 2.34 (170).

The same principle can be used to describe the electronic contribution to thermal conductivity in terms of C_v, ϑ, and Λ. In this case, however, C_v is the heat capacity of a Fermi electron gas, ϑ is the electron velocity, and Λ is the electron mean-free-path. The heat capacity of an electron gas can be shown to be

$$C_{v,\text{electronic}} = \frac{1}{3}\pi^2 Nk\frac{T}{T_F}, \qquad (2.17)$$

where $D(\varepsilon_F) = \frac{3N}{2\varepsilon_F}$ is the electronic density of states at the Fermi temperature (T_F), k is Boltzmann's constant, and m is the electron mass. Using the definition of the Fermi energy, $\varepsilon_F = \frac{1}{2}m\vartheta^2$, where m is the electron mass and ϑ_F is the Fermi electron velocity, and setting $\Lambda = \vartheta\tau$, the electronic component of thermal conductivity becomes

$$K_{\text{electronic}} = \frac{\pi^2 nk^2 T\Lambda}{3m\vartheta_F} \text{ (169)}. \qquad (2.18)$$

In pure metals, electrons are responsible for the greater part of the thermal conductivity at all temperatures. The addition of impurities reduces the electron mean-free-path and, under certain circumstances, the phonon contribution may be comparable to the electronic contribution. In the case of graphite, however, electronic conduction is negligible except at very low (165), and possibly very high (175), temperatures.

A way of describing the electronic contribution to thermal conductivity lies in the Wiedemann-Franz law. It states that the ratio of thermal conductivity to electrical conductivity is directly proportional to temperature. The constant of proportionality, the Lorenz number (L), is independent of the material being considered.

$$L \equiv \frac{K}{\sigma}T. \qquad (2.19)$$

L should have the value of $\frac{\pi^2}{3}\left(\frac{k}{e}\right)^2 = 2.45\times10^{-8}$ V^2/K^2 for all materials (169). Early work by Bowman et al. (176) showed that the Lorentz number for various carbons was much greater than that for conductivity dominated by free electrons. Their plot of L versus T,
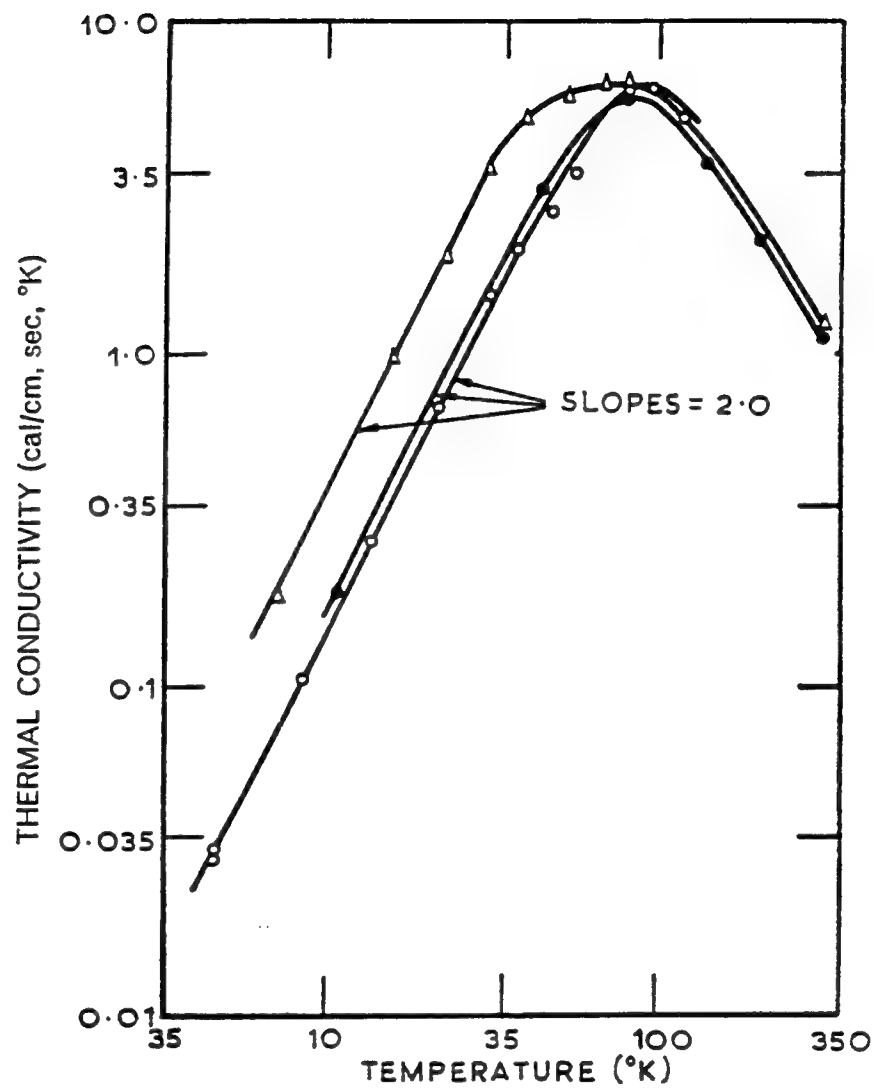
Legend:

Δ   Canadian natural graphite, crystallite size = 14 μm

●   AWG-I artificial graphite, crystallite size = 3400 Å

○   AWG-II artificial graphite, crystallite size = 3200 Å

Figure 2.34. Graphite thermal conductivity versus temperature (9).

shown in Figure 2.35, also shows that this ratio is not constant with temperature or with varying crystal quality. Thus, it was concluded that the thermal conductivity of carbon is dominated by phonon transport (177). As a result, the accepted description of graphite thermal conductivity is based almost entirely on lattice conduction. Only below around 10K do electrons make a noticeable contribution in graphite (178). While this temperature increases with increasing disorder, as does the position of the thermal conductivity maximum, phonon transport is still the dominant mechanism for thermal conduction at most temperatures (174).

2.4.3. Thermal Conductivity of Carbon Fibers

The increasing interest in carbon fiber-based composites for thermal management systems has resulted in several investigations into thermal conductivity (179-185). The relationship between thermal conductivity and fiber crystal structure is so strong that thermal conductivity measurements have been employed by several researchers to characterize fiber quality (145, 166, 173). As is the case for graphite, the low temperature thermal conductivity of carbon fibers is linearly-dependent upon the phonon mean-free-path. Therefore, fibers, having larger and more perfect crystallites and containing fewer sites for phonon scattering, will have higher thermal conductivities (33, 149). Figure 2.36 shows the low temperature thermal conductivities of several types of carbon fibers, including a vapor-grown fiber (CVD HT) and two mesophase pitch-based fibers (Thornel P-55 and P-100) (166). A similar plot is shown in Figure 2.37 for six grades of pitch-based fibers formerly produced by Du Pont as Fiber G (145).

The slopes of these curves indicate the power law temperature dependence of thermal conductivity and are approximately equal to the temperature dependence specific heat capacity for graphite, or around 2.3. Thus, the only difference between the thermal conductivities of these fibers can be attributed to the difference in their specific heat capacities and in their phonon mean-free-paths. As the structure of a carbon fiber becomes
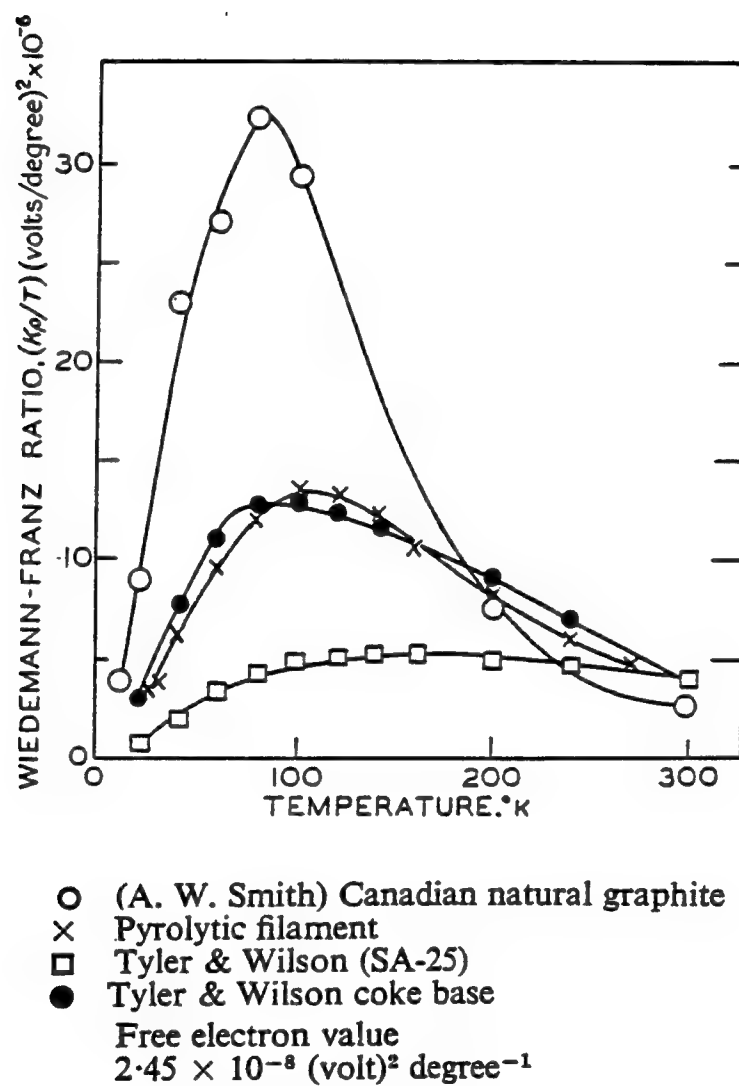
Figure 2.35. Variation in Lorenz number with temperature and crystal quality (176).
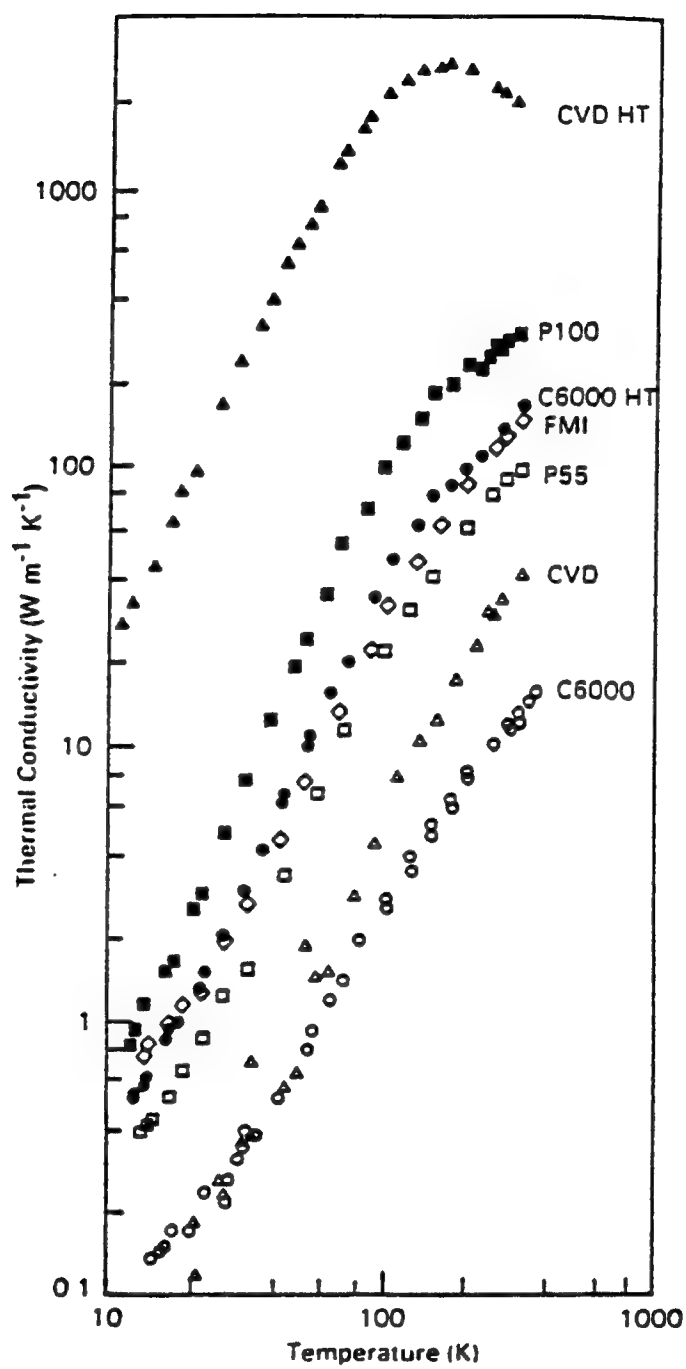
Figure 2.36. The low temperature thermal conductivities of several carbon fibers (166).
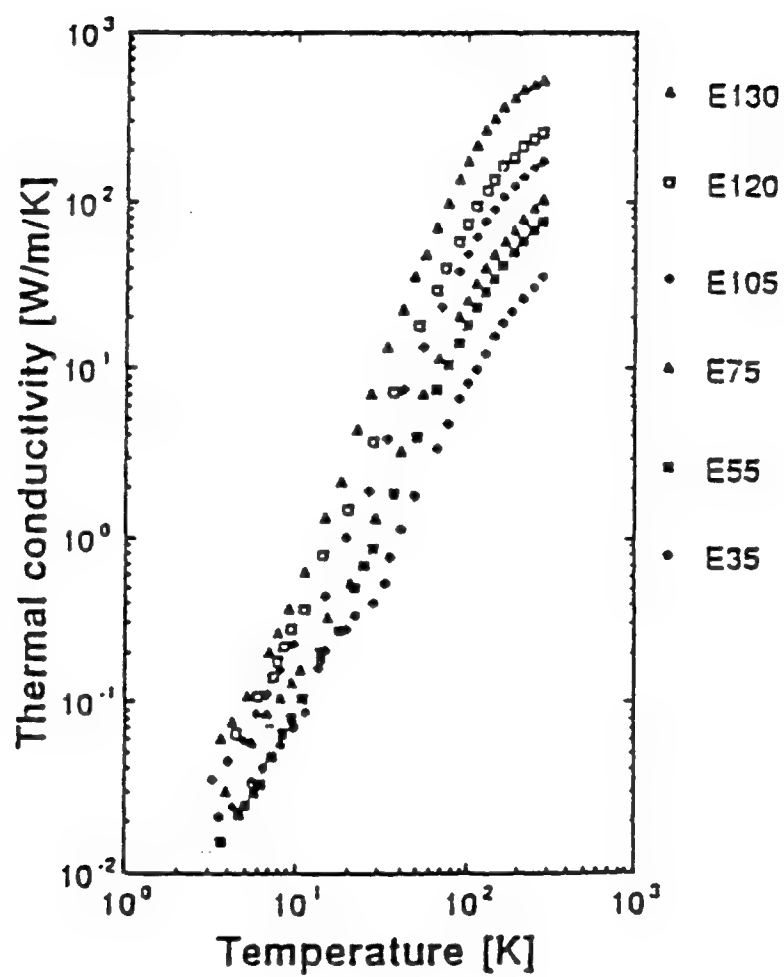
Figure 2.37. The low temperature thermal conductivities of several mesophase pitch-based fibers produced by Du Pont (145).

more perfect, the magnitude of thermal conductivity at any temperature increases and the position of the thermal conductivity maximum moves toward lower temperatures. Table 2.3 presents the measured room temperature thermal conductivities of several of the same fiber types with structural data from X-ray diffraction studies. Also presented are the calculated phonon mean-free paths, Λ, which should correspond to the coherence length, L_a. The discrepancy between mean-free-path and coherence length is a result of the difference in susceptibility to scattering between X-rays and phonons. Typically, the coherence length as determined by X-ray diffraction is around 30 percent of the phonon-mean-free-path.

Table 2.3. Correlation between room temperature thermal conductivities and structural parameters of some carbon fibers.

Fiber	K (W/m/K)	d(0002) (Å)	Λ (Å)	L_a (Å)
E-35[1,2,3]	30	3.445	79	50
E-55[1,2,3]	90	3.427	134	99
E-75[1,2,3]	125	3.426	212	113
E-105[1,2,3]	190	3.421	410	135
E-120[1,2,3]	300	3.410	656	206
E-130[1,2,3]	450	3.382	1531	220
P-55[4,2,5]	100	3.423	39	111
P-100[4,2,5]	500	3.381	114	306
CVD HT[6]	1950	3.35	549	N/A

[1] Du Pont Fiber-G product data sheets (146)
[2] Nysten et al. (147)
[3] Rogers and Hayes (186)
[4] Thornel Product Information (144)
[5] courtesy of D. P. Anderson (146)
[6] Heremans et al. (166)

3.4.4. Electrical Resistivity Analog to Thermal Conductivity

In the previous section, a discrepancy was mentioned between the coherence length as determined by X-ray diffraction and the phonon mean-free-path found by thermal conductivity measurement. A better way of estimating the phonon mean-free-path is by electrical resistivity measurement. Kelly (187) showed that the mean-free-path calculated from the measurement of electrical properties was equivalent to the phonon-mean-free path, as illustrated in Figure 2.38.

This suggests that phonons and electrons are scattered similarly by crystal defects, and a correlation should exist between electrical resistivity and thermal conductivity. Kowalsky (188) found that a strong relationship does exist, although not as simple as is the case for metals. His correlation for several commercially-available carbon fibers and a pyrolytic graphite is shown in Figure 2.39. It follows, then, that electrical resistivity should be affected by the same structural features as thermal conductivity. Work conducted by Bright and Singer (148) and Heremans et al. (166) illustrated the influence of texture and crystallite dimension and perfection on the electrical resistivity of carbon fibers. Lower electrical resistivities were found for fibers having a more ordered transverse texture, such as radial, than in fibers of random texture (148). In addition, electrical resistivity was found to decrease as the crystallite dimensions and the degree of graphitization increased (166). From these results, it is clear that electrical resistivity is an excellent analog measurement to thermal conductivity. Also, the ease and quickness of electrical measurement makes it attractive for quality control or predictive applications.

2.5. Previous Work on This Project

Because of their unique line-origin texture, non-circular fibers are considered to have excellent potential as high thermal conductivity fibers. In this section, background research into non-circular fibers at Clemson University, as well as early efforts in the High Thermal Conductivity Fiber project are discussed.
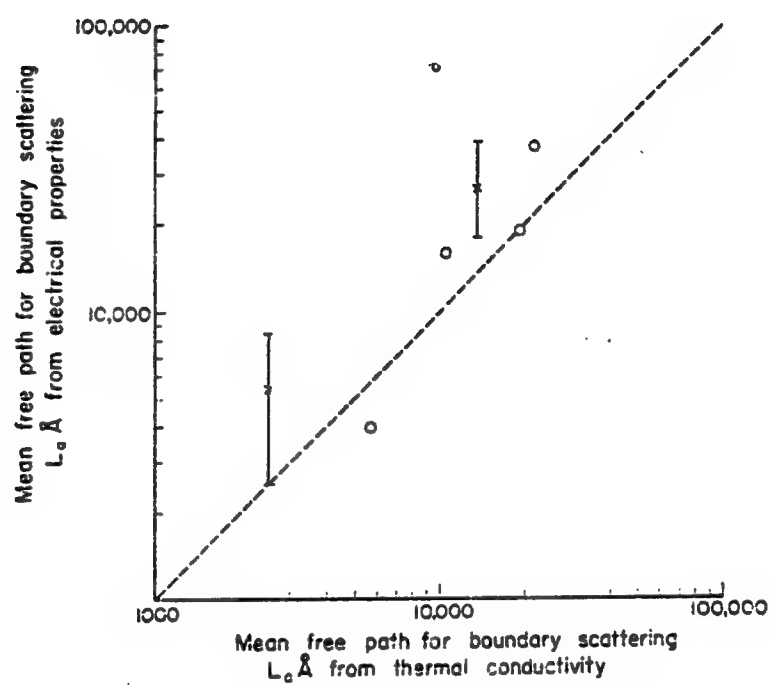
Figure 2.38. Phonon mean-free-path estimation using electrical measurements (187).
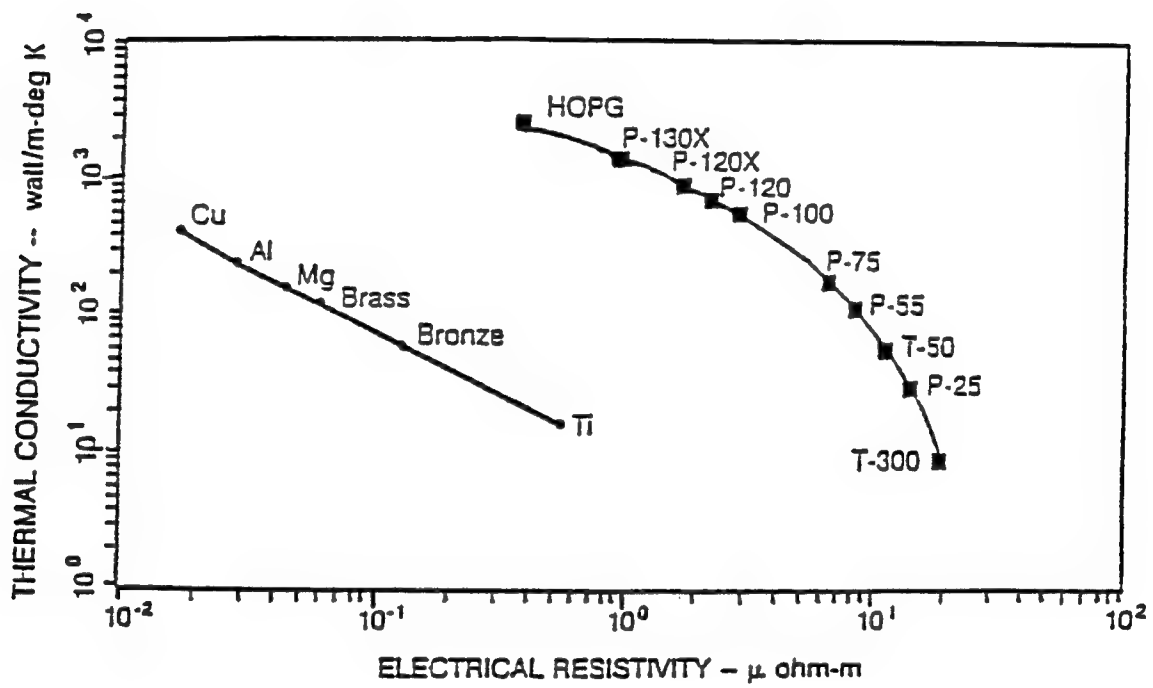
Figure 2.39. Thermal conductivity versus electrical resistivity for carbons and metals (188).

Fox (189) first melt-spun trilobal and octalobal fibers at Clemson University, and concluded that non-circular fibers exhibited potential for attaining higher strength and modulus than circular fibers. Since that study, several researchers have considered various shapes and aspect ratios of fibers. Harrison (190) produced C-shape fibers having 4 to 6 times the cross-sectional area of circular fibers, but 60% greater strength and up to 450% greater modulus. Subsequent research was directed at clarifying the effect of melt-spinning (60, 191), stabilization (55), and carbonization (75) conditions upon mechanical properties.

Much of the early work on the High Thermal Conductivity project was directed toward understanding the effects of melt-spinning conditions on fiber structure and properties. Harper applied a variety of melt-spinning conditions to the production of circular and ribbon-shape fibers from heat-soaked pitch (192). The textures of these fibers were studied by Robinson, who also developed the quantitative analysis techniques used in transmission electron microscopy (193). With the availability of the synthetic AR pitch, Fleurot duplicated Harper's spinning conditions and showed that the AR pitch had a much greater potential for producing high thermal conductivity, high modulus fibers (194). Some highlights of these studies will be presented.

Using heat-soaked pitch, Harper produced ribbon-shape fibers having different aspect ratios (the ratio of width to thickness in the fiber cross-section) and drawdown (the ratio of fiber area as it leaves the spinnerette to the area of the wound fiber), as well as circular and trilobal-shaped fibers for comparison. The line-origin texture of the trilobal and ribbon-shape fibers was thought to alleviate the stresses encountered during the thermal treatment of circular fibers. In addition, the ordered arrangement of layer planes, emanating from a central line-origin, was thought to allow greater graphitization.

Harper showed that ribbon-shape fibers had the potential for attaining higher modulus and lower electrical resistivity than circular fibers. The highest average modulus (613 GPa) and lowest mean electrical resistivity (6.5 $\mu\Omega$m) were observed for the same fiber set, a ribbon-shape fiber melt-spun from a 9:1 aspect ratio spinnerette and graphitized at 2550°C.

The strengths of fibers produced during that study ranged from 1.35 to 2.14 GPa, the lowest value representing a trilobal-shape fiber and the highest a 5:1 ribbon-shape fiber. In general, the electrical resistivity decreased with increasing aspect ratio, as shown in Figure 2.40. It appeared that the extent of line-origin texture in the fiber was at least partially responsible. The tensile strength, however, decreased with increasing aspect ratio. This is reasonable, as larger aspect ratios mean larger fiber areas, and tensile strength is usually found to decrease with increasing fiber area.

It was also concluded that drawdown influences modulus and electrical resistivity. As Figures 2.41 and 2.42 show, however, the statistical significance of these trends is limited by the large scatter in both modulus and electrical resistivity data . Thus, these conclusions were based upon the *a priori* belief that high winder speed would produce an increase in liquid crystal orientation with the fiber axis.

Next, the resistivities of these fibers were compared to those of commercially available circular fibers. At equal modulus, the ribbon-shape fibers produced at Clemson had a lower electrical resistivity. This is shown in Figures 2.43 and 2.44 for Du Pont and Amoco mesophase pitch-based fibers, respectively. The latter comparison is more valid because both the pitch used in Harper's work and the pitch used Amoco's process were produced by the heat soak method, whereas the pitch used by Du Pont was made by solvent extraction. In both cases, however, ribbon-shape fibers of three to five times larger area had lower electrical resistivities compared to commercial carbon fibers.

Fleurot employed similar melt-spinning conditions in the production of fibers from AR mesophase pitch. However, differences in molecular weight and architecture forced him to use lower spinning temperatures to achieve the desired viscosity of around 24 Pa·s. Also, the AR pitch fibers were much more uniform in cross-sectional area than those produced from the heat-soaked pitch. As Figures 2.45 and 2.46 show, little difference in modulus or electrical resistivity was observed with increasing aspect ratio for the AR pitch (194).
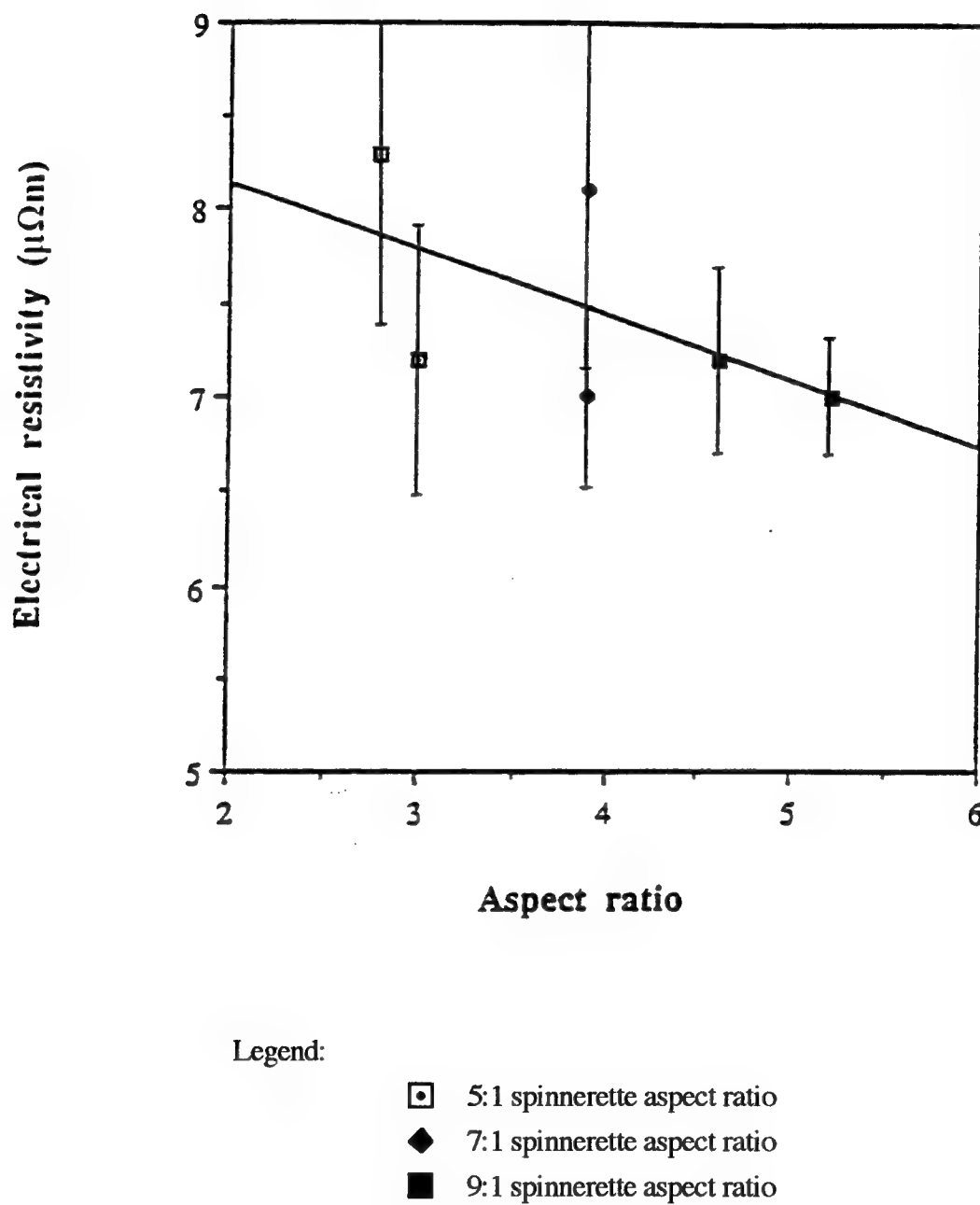
Figure 2.40. Electrical resistivity versus aspect ratio for ribbon-shape fibers (192).
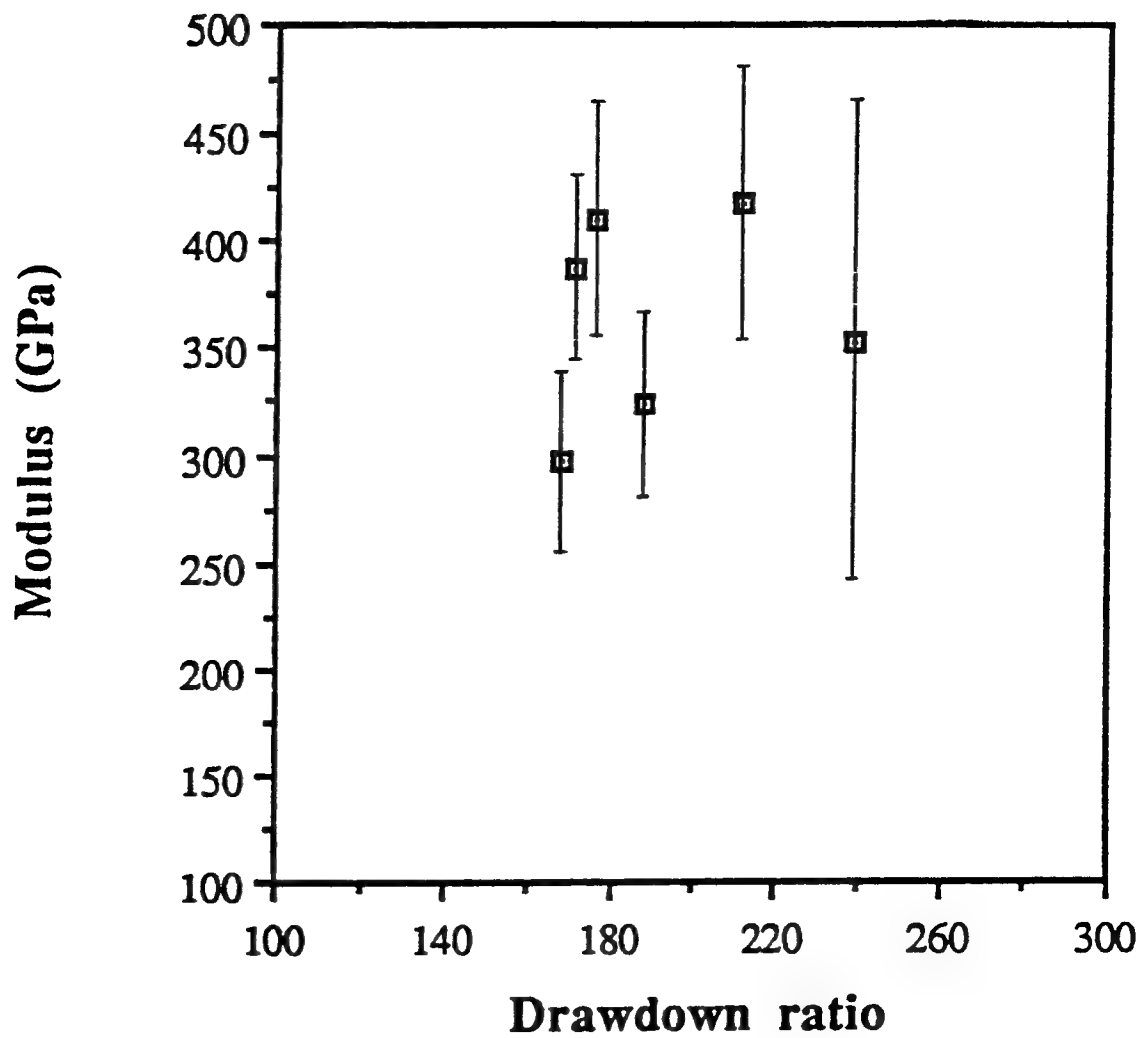
Figure 2.41. Young's modulus versus drawdown ratio for ribbon-shape fibers (192).
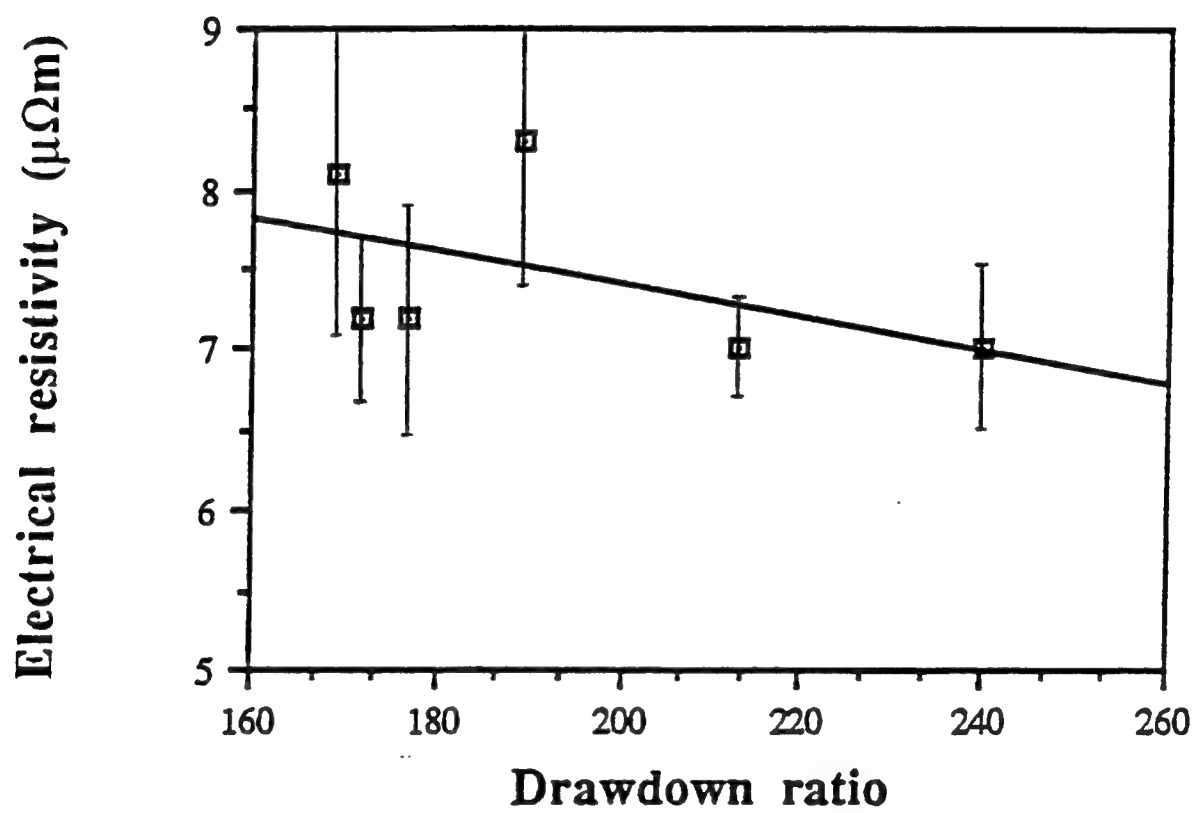
Figure 2.42. Electrical resistivity versus drawdown ratio for ribbon-shape fibers (192).
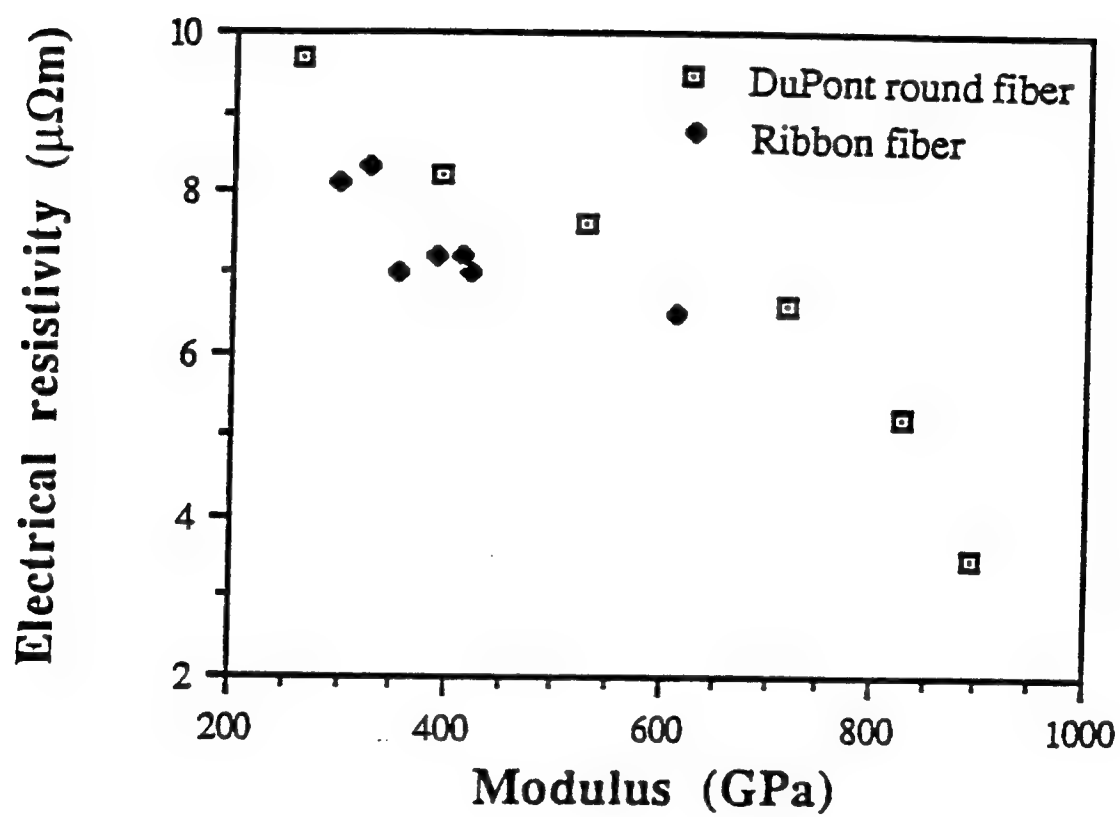
Figure 2.43. Electrical resistivities of ribbon-shape fibers compared with those of Du Pont's E-series circular fiber (192).
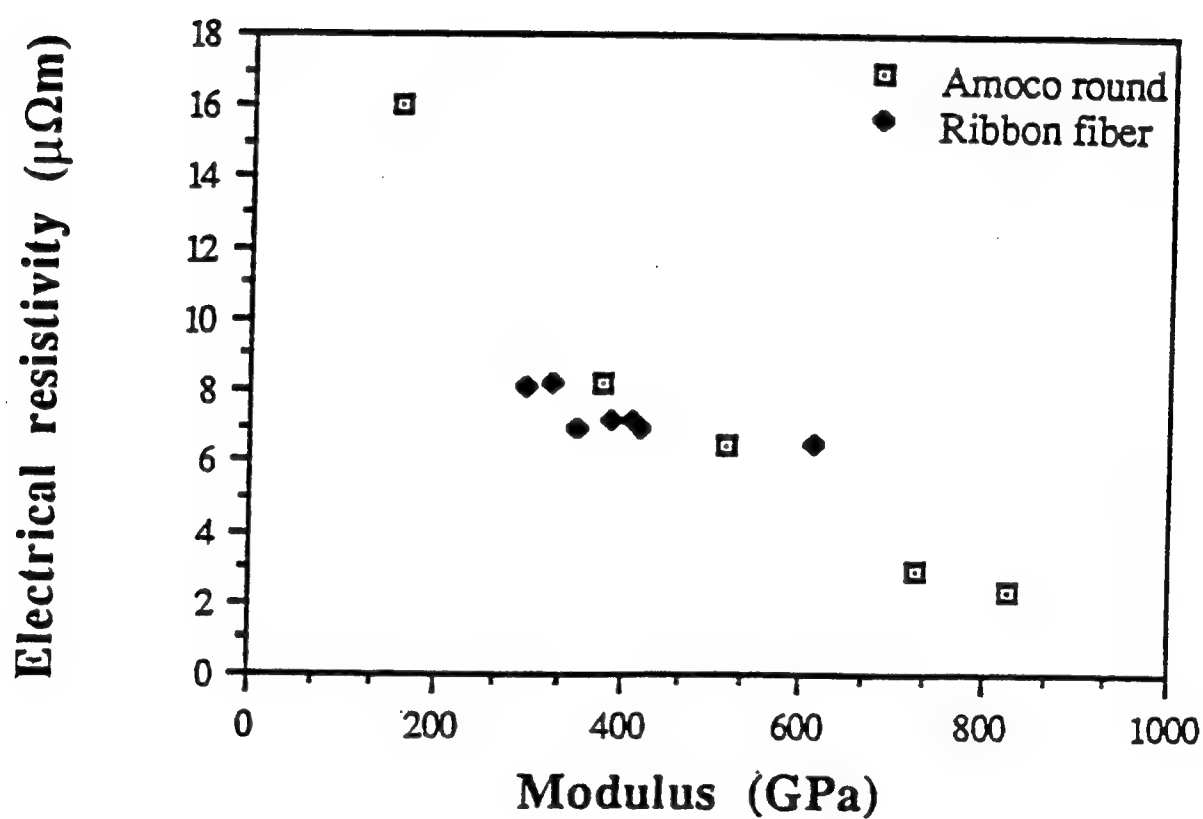
Figure 2.44. Electrical resistivities of ribbon-shape fibers compared with those of Amoco's Thornel® circular fiber (192).
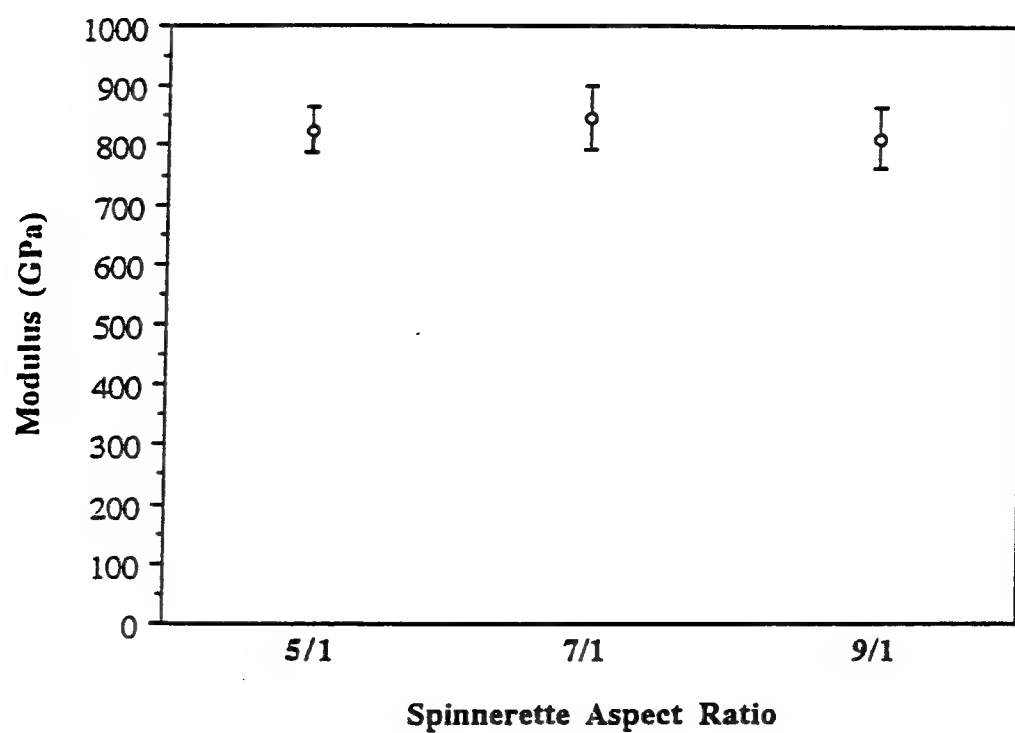
Figure 2.45. Young's modulus versus aspect ratio for AR ribbon-shape fibers (194).
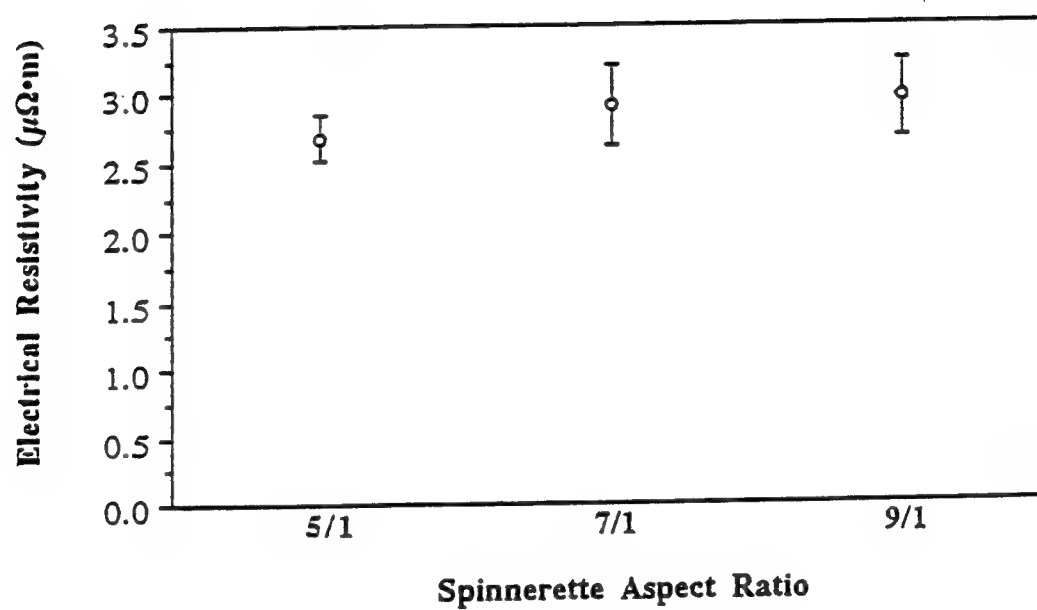
Figure 2.46. Electrical resistivity versus aspect ratio for AR ribbon-shape fibers (194).

Using the same graphitization temperature of 2250°C as in Harper's study, Fleurot found that AR ribbon-shape fibers developed a highly-graphitic structure and excellent lattice-dependent physical properties. Table 2.4 shows the measured values for d(0002), coherence length (L_a), and stack height (L_c) for ribbon-shape fibers of different aspect ratio, circular fibers, and two commercially available fibers produced by Amoco. While the differences may not be statistically significant, increased aspect ratio appeared to result in reduced (0002) separation and increased crystallite size. Table 2.5 presents the mechanical properties measured for the AR pitch-based fibers produced in that study.

Table 2.4. Structural properties of AR pitch-based fibers and Amoco circular fibers (194).

Fiber	d(0002) (Å)	L_a (Å)	L_c (Å)
9:1 ribbon, 3000°C	3.365±0.004	640±6	164±6
9:1 ribbon, 2250°C	3.364±0.004	N/A	≈160
7:1 ribbon	3.364±0.004	289±6	155±6
5:1 ribbon	3.370±0.004	354±6	149±6
circular	3.388±0.004	431±6	140±6
P55[1]	3.41	150	80
P100[1]	3.37	1300	180

[1] courtesy of D. P. Anderson (145).

Table 2.5. Mechanical properties of graphitized AR pitch-based fibers (194).

Fiber	Cross-sectional area (μm^2)	Tensile strength (GPa)	Tensile Modulus (GPa)
9:1 ribbon, 3000°C	151.3±16.0	2.92±0.26	922±34
9:1 ribbon, 2250°C	162.8±12.2	2.68±0.26	812±52
7:1 ribbon	144.8±18.5	2.46±0.26	847±52
5:1 ribbon	158.7±8.3	2.29±0.21	826±37
circular	59.7±2.7	1.94±0.22	435±31

CHAPTER 3

EXPERIMENTAL PROCEDURE

In the present study, a heat-soaked and a synthetic mesophase pitch were melt spun into circular and ribbon-shape fibers using a pilot-scale extruder. Then, these fibers were made infusible by oxygen stabilization, and carbonized. Stabilization and carbonization conditions were varied in a systematic manner so that their effects on the structure and properties of the resulting fiber might be evaluated. Several analytical techniques were employed to characterize the fiber both during and after thermal treatment. Therefore, this chapter will be divided into two sections, the first dealing with fiber processing, and the latter with analytical methods.

3.1. Fiber Processing

The fibers used in this study were produced at Clemson University from both a heat-soaked and a synthetic (AR) mesophase pitch. Both materials were melt-spun into fibers of various cross-sectional shapes and sizes, and heat treated. In this section, the procedures employed in melt-spinning and heat treatment are discussed.

3.1.1. Melt-spinning

A mesophase pitch derived from isotropic pitch by the heat-soaked, or Singer, process (26) was melt-spun into circular- and ribbon-shape fibers by a pilot-scale melt spinning unit, shown schematically in Figure 3.1. Zone one of the extruder conveyed the solid pitch into the melting zone (zone two), and zone three transferred the pitch from the extruder to the die. Within the die, the melt was forced through a 5 μm mean pore diameter sintered metal filter. This was followed by a spinnerette, containing either 24 circular or 12 rectangular cross-section capillaries, 100 μm in diameter or limb-width, respectively. Upon exiting the capillaries, fibers were drawn and collected under ambient conditions on a
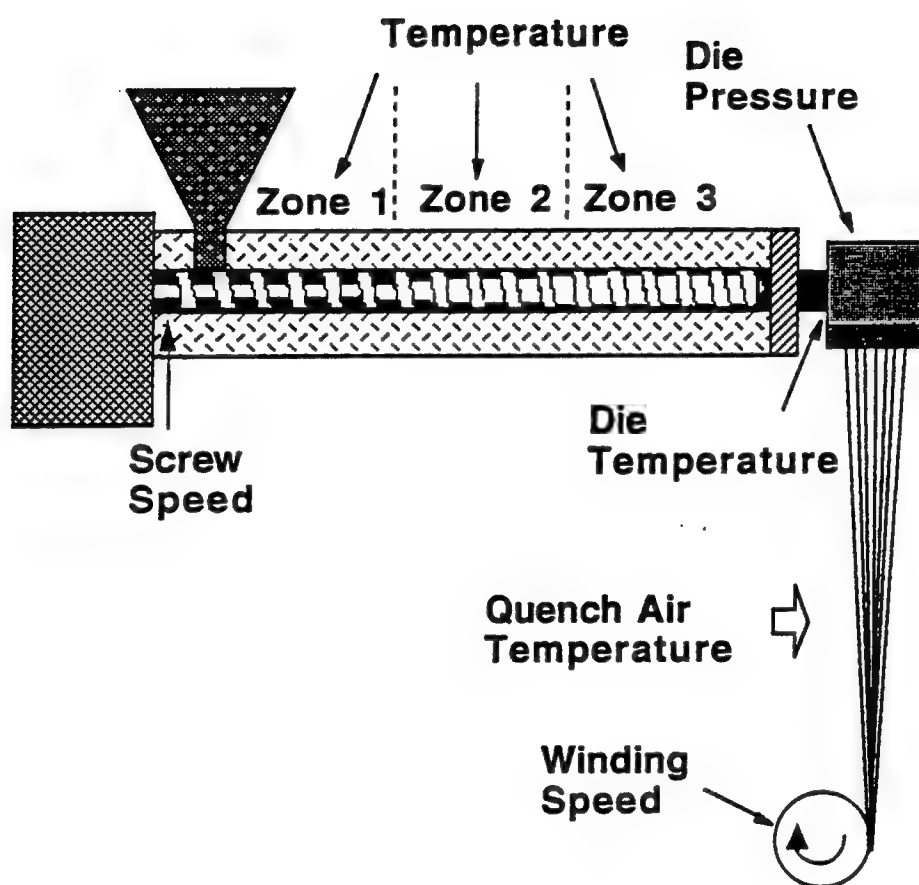
Figure 3.1. Pilot-scale melt-spinning apparatus.

Fincor variable speed winder. A nitrogen atmosphere was maintained during operation to prevent oxidation of the pitch. The spinning conditions employed are shown in Table 3.1.

Table 3.1. Melt-spinning conditions employed in the production of heat-soaked pitch fibers.

Spin condition	Ribbon-shape	Circular
Melt temperature, °C	339	343
Pressure, GPa	0.99	7.86
Winder speed, m/sec	5.67	3.26
Mass flow rate, Kg/sec	5.83×10^{-5}	4.83×10^{-5}

An abbreviated thermal treatment study was also conducted using the AR mesophase pitch. This material was derived from methylnaphthalene using a HF/BF_3 catalyst, in a process described by Mochida et al. (30, 31). Basically, the melt-spinning technique was the same as that described earlier. However, the molecular weight distribution and molecular structure of this pitch necessitated very different operating conditions. These are presented in Table 3.2.

Table 3.2. Melt-spinning conditions employed in the production of ribbon-shape fibers from AR pitch.

Spin condition	Ribbon-shape fibers
Melt temperature, °C	299
Pressure, kPa	6.55
Winder speed, m/sec	3.12
Mass flow rate, Kg/sec	2.25×10^{-5}

3.1.2. Stabilization

Two types of stabilization treatments were employed during this study. The first was aimed at producing a large quantity of equivalently stabilized fibers for subsequent thermal treatment experiments. The second involved variation of the stabilization temperature and time for the purpose of studying stabilization chemistry.

In the former, fibers from each set were cut into 12.5 cm lengths and stabilized by placing them on stainless steel gauze inside a forced convection oven. The temperature of the oven was controlled and monitored using a Leeds and Northrup Electromax® V programmable controller and a Type K (Chromel-Alumel) thermocouple probe. For the heat-soaked pitch fiber sets, the oven was heated at 1°C per minute to 280°C and held at this temperature for two or more hours. Weighing the fibers before and after stabilization allowed the mass gain to be estimated. The soak time at 280°C was varied so that each fiber set would achieve around 8.5 mass % gain during stabilization.

Just as with melt spinning, the AR pitch fibers required different stabilization conditions. As suggested by the Mitsubishi Gas Chemical Company (146), these fibers could be stabilized by heating at 5°C per minute to 270°C, followed by a 15 to 20 minute soak at this temperature. This resulted in a mass gain roughly equal to that observed for the heat-soaked pitch fibers. In the case of both pitches, fibers stabilized by this method were able to be carbonized without melting or bloating.

Study of stabilization chemistry involved a combination of elemental analysis and FT-IR data from fiber samples treated to various points in the process with dynamic DSC and TGA data. The same forced-convection furnace and control system was used to treat these fibers. However, samples were removed from the furnace either during a linear heating period or at a series of soak times at a prescribed temperature. The temperatures and soak times considered ranged from 160 to 310°C and 0 to 100 hours, respectively. Obviously, some of these conditions could not produce an infusible sample, but could give meaningful data on chemical composition and bonding. All samples were ground to a fine powder

using a glass mortar and pestal. Then, portions were used for elemental analysis, FT-IR, and thermolysis TGA experiments.

3.1.3. Thermolysis and Graphitization

Stabilized fiber sets were divided into approximately 0.5 gram samples for the various thermal treatment schedules to be studied. Most samples were carbonized and/or graphitized in a carbon resistance furnace, configured for batch operation as shown in Figure 3.2. However, a subsequent time-at-temperature study required that the furnace be operated in open, or continuous, mode so that fiber samples could be rapidly removed from the heating zone. This arrangement is shown in Figure 3.3. In both cases, a Raytec pyrometer was used to monitor the furnace temperature, and its output was fed to a Leeds and Northrup Electromax® V programmable controller.

In batch operation, a fiber sample was placed in a graphite boat attached to the hearth of the furnace. The furnace was sealed and evacuated, then filled with helium to a positive pressure of 20-30 kPa. With the pressure maintained at this level, the furnace was heated at the desired rate to a maximum temperature, held there for a prescribed time, and cooled.

A time-temperature experiment was conducted in which fiber sets were heat treated to temperatures between 1800°C and 3000°C at 200°C increments and held at maximum temperature for 5, 10, 15, and 20 minutes. Two additional experiments involved varying the heating and cooling rates to and from a common temperature of 2400°C and dwell time of 15 minutes. Finally, "mixed" heat treatment schedules, including a change in heating rate between 1600 and 2000°C, were conducted to locate secondary crystallization processes.

After the observation of an discontinuity in structural development between 1800 and 2000°C, a series of isothermal treatments were conducted over this temperature range to identify its cause. For this experiment, it was necessary to rapidly introduce and remove fiber samples from the heating zone of the furnace. Water-cooled, open doors were added
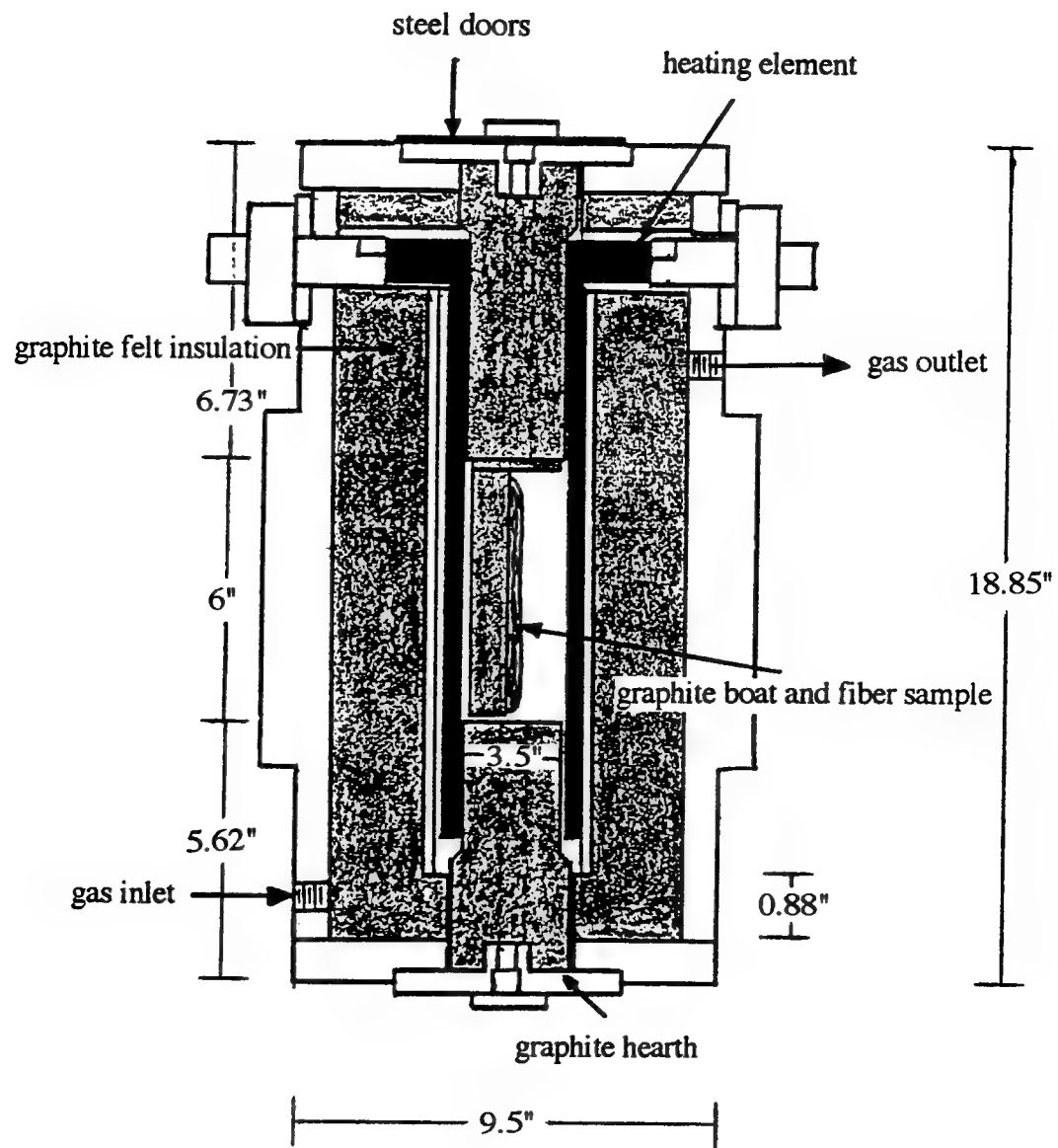
Figure 3.2. Carbon resistance furnace: batch operation.
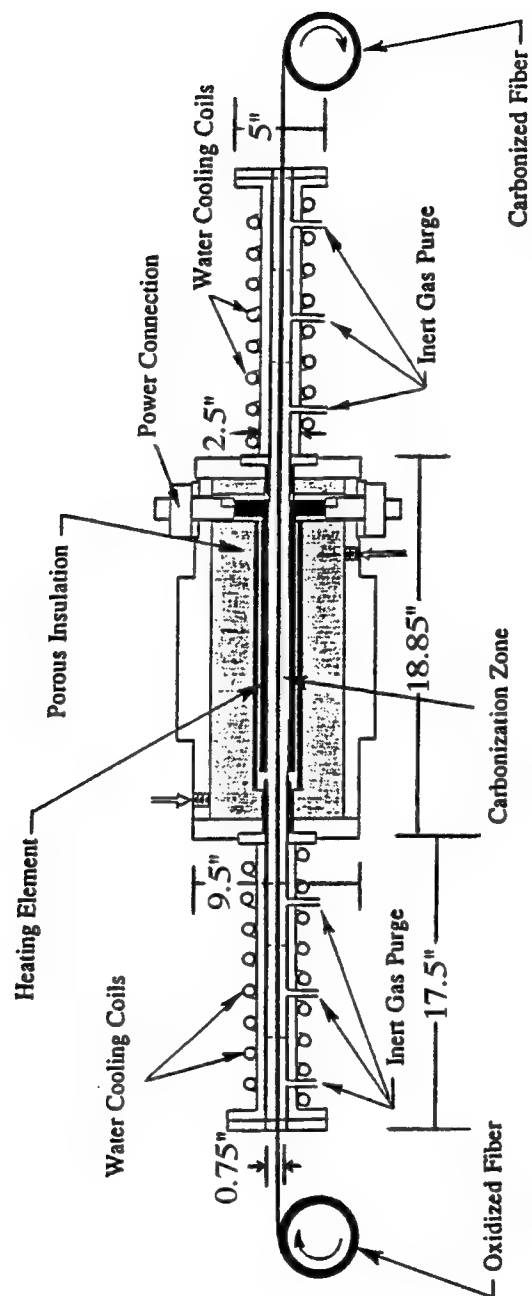
Figure 3.3. Carbon resistance furnace: continuous operation.

and argon was allowed to flow out of the their ends to prevent oxidation of the carbon furnace parts. Then, a tow of commercial carbon fiber was fed through the furnace andattached to a filament winder unit. Fiber samples were tied onto the commercial fiber tow and pulled rapidly into the heating zone, held there for a prescribed time, and removed. The winder speed was adjusted so that the heating and cooling periods were very small compared to the isothermal time. By this method, treatment times of 1, 2, 4, 8, 16, and 32 minutes were examined at temperatures of 1800, 1900, and 2000°C. As a control, a duplicate set of treatments were conducted at 3000°C, far removed from the discontinuity.

A final experiment, labelled hydrodesulfurization (107), performed in this furnace involved the introduction of hydrogen to the furnace atmosphere at either 750 or 1500°C to possibly aid in volatile removal. This was done by connecting both a hydrogen and a helium cylinder to the furnace gas manifold. At the proper temperature, the helium flow was restricted and the furnace evacuated. Then, the furnace was filled with hydrogen to the normal operation pressure and held there for the prescribed time. The same procedure was used to return to a helium atmosphere after completing the isothermal soak period. In this experiment, the heating rates above and below the gas change took two possible values, 20 and 100°C per minute.

Carbonization chemistry was studied by a method similar to that presented for stabilization: ground fiber samples representing various thermal treatment conditions were subjected to elemental analysis and FT-IR spectroscopy. However, the carbon resistance furnace described earlier could not be used to give controlled temperature or heating rates below 1000°C because the Raytec pyrometer is reliable only above about 450°C. Therefore, low temperature samples were treated in a Lindberg Hevi-Duty® tube furnace, heated by silicon carbide heating elements. The horizontal mullite tube was sealed at both ends, except for a gas inlet and, on the opposite end, a small opening for the thermocouple. Using Thornel® T-300 PAN carbon fiber, fiber samples were tied to the end of 60 cm long wires made of a nickel-chrome alloy. The samples were placed into the center zone of the

furnace and the ends of the metal wire were allowed to pass through the thermocouple opening. With argon flow set at 4 s.c.f.h., the furnace was heated at the selected rate to 1000°C. At 200° increments, fiber samples were removed by pulling wires out of the furnace. These samples were ground as described earlier and prepared for analysis.

3.1.4. Solvent Etching

A method of enhancing graphitization of a pitch fiber by first selectively extracting disordered regions by wet oxidative etching was devised during this study. The potential of this technique was evaluated using one AR pitch (ribbon-shape) and two heat-soaked (a circular and a ribbon-shape) fiber sets. The oxidant was a 0.15 M solution of potassium dichromate ($K_2Cr_2O_7$) in concentrated sulfuric acid. As the liquid aged, its color changed from orange to green with the change in valence of the chromium ion. Then, fiber samples were bound with strands of Thornel® T-300 PAN fiber and dipped into the liquid for a period of 1, 3, 10, or 30 minutes. After removal, the fiber samples were washed thoroughly with distilled water, and dried. Ground portions of each sample were studied using FT-IR and wide angle X-ray diffraction. The remainder, still in fiber form, were carbonized to 2400°C at 20°C per minute and held at that temperature for 15 minutes.

3.2. Analysis Methods

Several techniques were used to study the changes that occur during thermal treatment, as well as to characterize fibers produced by the above processes. Dynamic differential scanning calorimetry (DSC) and thermogravimetric analysis (TGA) were used to study both chemical and structural changes as they occurred. When combined with post-treatment techniques such as wide angle X-ray diffraction and physical property measurements, an understanding of the thermal treatment process could be developed. The procedures employed for each of these analysis techniques are described in the following sections.

3.2.1. Differential Scanning Calorimetry (DSC)

Differential scanning calorimetry (DSC) was used to study the chemical reactions that occur during stabilization and the early stages of carbonization. As-received, melt spun, and partially stabilized fibers were studied in this manner. First, the material was ground to a fine powder using a glass mortar and pestal. Then, about 0.025 g were placed in an aluminum sample pan, which was weighed to ±0.0001 g before and after loading by a Mettler analog balance. The filled pan was placed on the front, or sample, thermocouple junction of a Du Pont 910 DSC unit, shown in Figure 3.4. An empty pan of approximately equal mass was placed on the rear junction. Then, the cell was sealed and the accompanying 990 thermal analyzer module was programmed to give the desired heating rate and maximum temperature for the trial. In the rear of the 990 module, the "Y+" and "Y ground" pins, giving a millivolt output proportional to the cell heat flow, were connected to a 0-100 mV input module of an Omega OM-160 four channel data logger. A second 0-100 mV module was connected to the "T+" and "T ground" pins, which gave a linear voltage output with temperature. Finally, the desired furnace atmosphere was achieved by connecting a gas cylinder to the gas/purge inlet, or allowing the unit to operate under ambient conditions.

For stabilization experiments, a typical trial employed an ambient atmosphere and a heating rate of 1°C per minute from room temperature to 450°C. Higher and lower heating rates were also employed, with little change in the heat flow data. The 1°C per minute heating rate was chosen for two reasons: (1) it gave reproducible data for a reasonable trial length, and (2) it simulated the heating rate used in the production of petroleum pitch fibers used in this study. The trials were extended to 450°C to include all stabilization reactions, even degradation of the pitch at high temperatures. Low temperature thermolysis trials were conducted using heating rates ranging from 1 to 20°C per minute between room temperature and 580°C, the limit of the DSC cell, in flowing argon.
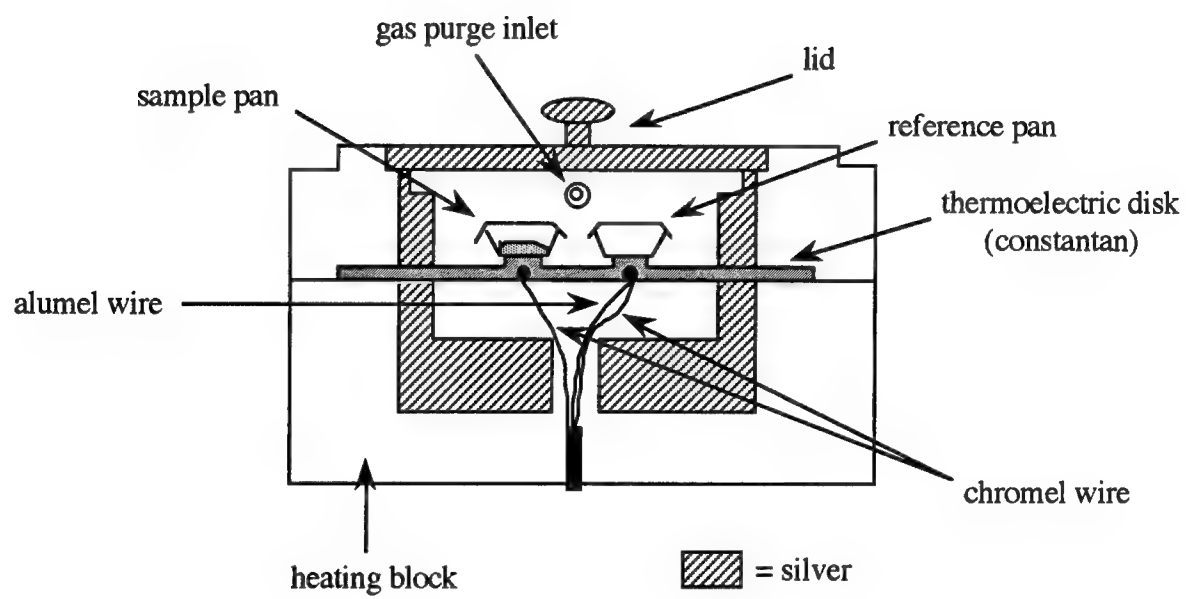
Figure 3.4. DSC cell schematic.

In both cases, a second trial was conducted with the sample pan empty to act as a baseline. Then the cell heat flow at any temperature was proportional to the difference in heat capacity between the two pans. Because they were made of the same material and, therefore, had approximately the same specific heat capacity, the difference was proportional to their mass difference. As an attempt was made to select pans of equal mass, this effect was often negligible.

At the completion of a trial, the data logger was removed and interfaced with an IBM PC using a RS-232C serial port. Then, data from the trial were transferred to the PC hard disk by means of Omega's "Pronto" data acquisition software. This package also converted the files to a ASCII format so that they could be manipulated by other software. A program, presented in Appendix D, was written to convert the millivolt readings to heat flow values, subtract the background from the heat flow versus temperature profile, and separate convoluted reaction contributions.

First, the millivolt readings were converted to heat flow values by multiplication of a cell conversion factor, 200 μW/mV (195). Next, the heat flow values from the empty pan trial were subtracted from those from the sample trial. Then, the heat flow due to the change in sample heat capacity with temperature was subtracted. This could be estimated from a trial of material from the same sample under an inert atmosphere. The sample heat capacity was assumed to take the form

$$C_p(T) = a + bT + cT^{-2}, \tag{3.1}$$

where C_p is the constant pressure heat capacity and a, b, and c are fittable constants, determined by multiple regression of $C_p(T)$ on T. Subtraction of the background and sample heat capacity contributions left the heat flow profile as just the summation of multiple convoluted reaction peaks.

Peaks were deconvoluted using a simplex minimization routine, known as Amoeba (196). The entire DSC pattern was assumed to be the summation of n Gaussian peaks, or

$$\text{heat flux } (T) = \sum_{i=1}^{n} A_i \exp\left[-\left(\frac{T - B_i}{C_i}\right)^2\right], \tag{3.2}$$

which required three fittable parameters, A_i, B_i, and C_i, per peak. The number of peaks, n, was input by the user, as were initial guesses for the temperatures, B_i, of their heat flow maxima. Initial guesses for their heights, A_i, and breadths, C_i, were held constant. Thus, the sum-of-squares of the differences between measured and estimated heat flows was minimized using 3n fittable parameters. These parameters, describing the magnitude and temperature dependence of each reaction, were used to analyze the reactions.

Reaction analysis included determination of the heats of reaction, ΔH_i, and activation energies, ΔE_i. The former required the use of a reference material that exhibited a clearly defined thermal event to determine the cell calibration constant. Silver nitrate, which has a melting point of 212°C and a heat of fusion of 16.2 cal/g was chosen as the reference. The calibration constant, E, was determined from the equation

$$E = \frac{m\,\Delta H\,hr}{60\,area},$$

(3.3)

where m is the $AgNO_3$ mass in grams, ΔH is its heat of fusion, hr is the heating rate in degrees per minute, and the endothermic fusion peak area is expressed in W·K (195).

The area of a single peak was determined by integrating its Gaussian profile over the temperature range of the peak. Because C_i is related to the standard deviation of a probability distribution, over 99% of the peak area will be contained in $B_i \pm C_i$ (197). Using these limits of integration, the area of peak i was calculated from

$$area = \int_{B_i - C_i}^{B_i + C_i} A_i \exp\left[-\left(\frac{T - B_i}{C_i}\right)^2\right] dT.$$

(3.4)

The heat of reaction, ΔH, then can be estimated by the following formula:

$$\Delta H = \frac{60\,E\,area}{m\,hr}$$

(3.5)

in which E is the cell calibration constant determined earlier from the $AgNO_3$ trial, S is the DSC scale factor 200 μW/mV, m is the pitch sample mass in grams, and hr is the heating rate in degrees per minute.

The activation energy of a reaction could be estimated from its temperature dependence, using a simple kinetic expression. Assuming a first-order reaction, the rate of

reaction at a given temperature, dα/dt, can be written

$$\frac{d\alpha}{dt} = k(1 - \alpha), \tag{3.6}$$

where α is the fractional extent of reaction. In terms of the reaction peak from the DSC pattern, $\alpha(T)$ is simply the ratio of the area under the peak to the left of T to the area of the entire peak, found by a Simpson's rule integration of the raw data. The reaction rate constant, k, is assumed to be related to temperature by the Arrhenius equation,

$$k = k_o \exp\left(-\frac{\Delta E}{RT}\right), \tag{3.7}$$

in which ΔE is the activation energy and R is the gas constant. Substituting this expression, and the relationship $t = T/hr$, into the kinetic expression above, allowed the reaction rate to be written

$$\frac{d\alpha}{dT} = \frac{k_o}{hr}(1 - \alpha) \exp\left(\frac{-\Delta E}{RT}\right). \tag{3.8}$$

Thus, a plot of $\ln[(d\alpha/dT)(1 - \alpha)^{-1}]$ versus $1/T$ yielded a straight line having a slope equal to $-\Delta E/R$ and an intercept equal to $\ln(k_o/hr)$. The derivative $d\alpha/dT$ was estimated at each temperature from the slope of the two surrounding data points.

3.2.2. Thermogravimetric Analysis (TGA)

As-spun, partially stabilized, or stabilized fibers from the various stabilization treatments were cut into small lengths. Around 0.0500 to 0.1000 g of fiber were placed in an alumina crucible, hung from the sample arm of a Cahn model RH electrobalance and into a vertical tube furnace heated by silicon carbide heating elements, as shown schematically in Figure 3.5 (198). The area surrounding the balance and sample arm was enclosed by two glass chambers, which were sealed together at a ground glass junction. The lower chamber extended to the top of the tube furnace, where it joined with the mullite furnace tube. Industrial grade argon, flowing at 2 s.c.f.h., was passed through calcium sulfate drying material to remove moisture before entering the furnace. The gas exhaust was fed into an hydraulic oil bath beneath the furnace. This prevented air from entering the furnace in the event of gas flow loss. A linear heating rate of 7°C per minute from room

CONTROLS CIRCUITS INDICATORS

photo-cell

balance beam

LED

flag

'A' loop

'B' loop

torque motor

taut band suspension and torque motor coil connection

flag

tare loop

tare

rotational axis of beam and coil assembly

ceramic wool insulation

silicon carbide heating elements

sample crucible

gas baffle

gas inlet
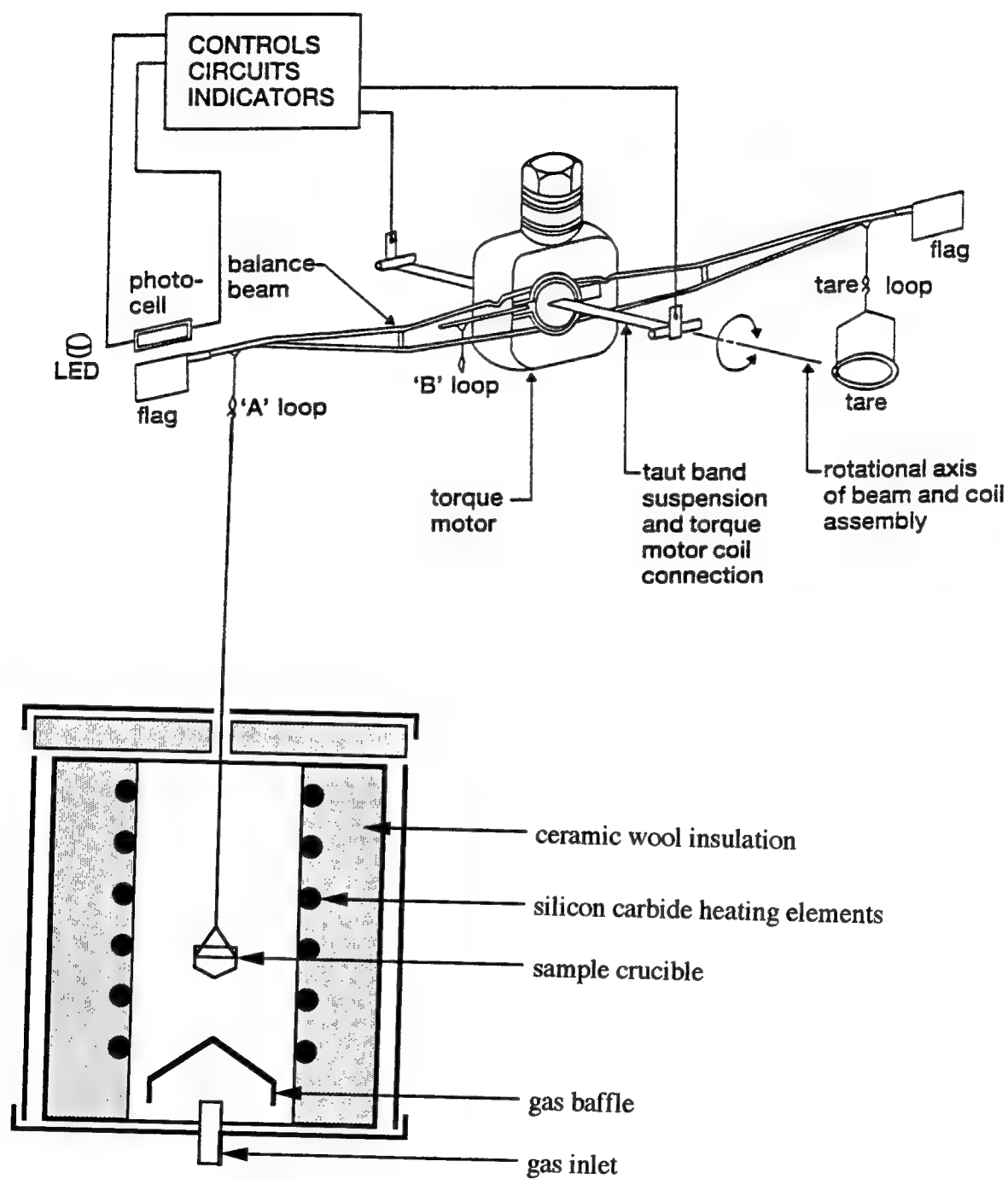
Figure 3.5. Electrobalance and TGA furnace configuration (198).

temperature to over 1000°C was provided by a cam set point programmer and on-off controller.

Temperature and mass data from a trial were recorded on two separate chart recorders. The first recorded the temperature over a 0 to 1000°C range with five minute time gradations. The second recorder was set at a speed of 20 cm/hr so that its 0.5 cm divisions corresponded to 1.5 minute increments. It recorded the mass on a 40 mg range below the tare weight.

Thermogravimetric data were analyzed by the following procedure. The temperatures and sample masses were read from the recorder paper and input into a computer spreadsheet. Plotting both the mass loss and the derivative mass loss curves allowed the number of processes, and their effective temperature ranges, to be determined. For each reaction, an onset and completion temperature were defined, and the sample mass at these two points was recorded. Then, a fractional conversion parameter, $\delta(T)$, was defined as

$$\delta(T) = \frac{M(T) - b}{a - b}, \tag{3.9}$$

where $M(T)$ was the sample mass at any temperature within the reaction temperature range, a was the sample mass at the onset of that reaction, and b was the sample mass at the completion of that reaction. Thus, δ decreased from 1 to 0 as the reaction proceeded. Figure 3.6 shows a hypothetical multi-reaction TGA pattern with the definitions of a, b, and $M(T)$ illustrated.

Using the expression

$$\frac{d\delta}{dt} = -k\delta, \tag{3.10}$$

and substituting in the Arrhenius temperature dependence of k and the furnace heating rate gives

$$\frac{-\ln\delta(T)\ hr}{(T - T_o)} = k_o \exp\left(\frac{-\Delta E}{RT}\right). \tag{3.11}$$

Plotting the natural logarithm of the left-hand side against $1/T$ gave an approximately

Sample Mass

(% of original)

$$\delta(T) = \frac{M(T) - b_2}{a_2 - b_2}$$
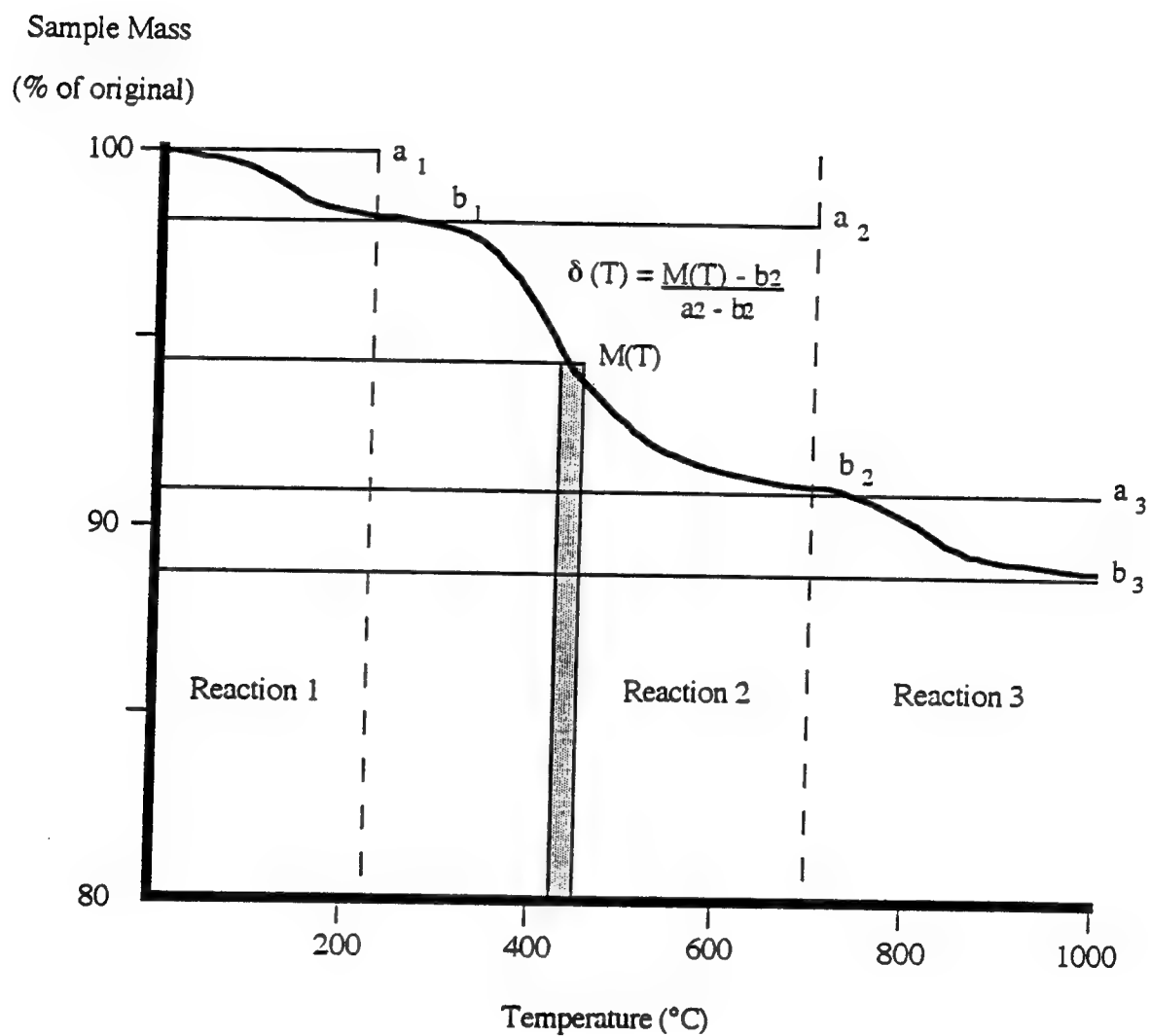
Figure 3.6. Hypothetical TGA pattern showing reaction analysis nomenclature.

straight line with an intercept equal to $\ln(k_0)$ and a slope equal to $-\Delta E/R$. This analysis assumed that a single first-order process was occurring at any one time.

The use of a first-order kinetic expression was based upon the results of previous workers in the carbonization of petroleum pitch coke (69) and upon testing of several likely kinetic expressions from those presented in Appendix A.5. Low values for the activation energies led to the conclusion that thermolysis was diffusion-limited. As a result, a combined reaction/transport model, developed in Appendix A.4, was developed to describe the process and to allow kinetic analysis of the reactions. Each thermolysis reaction is assumed to have the form

$$AB \rightarrow A + B, \tag{3.12}$$

in which the initial stabilized hydrocarbon AB is decomposed to form volatile product A and carbonaceous solid B. The basic differential equation was

$$\frac{\partial c_A}{\partial t} = D\nabla^2 c_A + k_1''' c_A, \tag{3.13}$$

where D is an effective diffusion coefficient that describes transport of species A out of a bundle of fibers. The symbol ∇ is the Laplacean operator, c_A is the mean concentration of product A in the bundle as a function of time, and k_1''' is the first-order reaction rate constant (199). Then, the Arrhenius temperature dependence of both the diffusion coefficient and the reaction rate constant upon temperature, as well as the relationship between time and temperature, $T = t \cdot hr$, were added. Finally, the decrease in mean concentration with temperature was related to a mass flux out of the fiber bundle (200). Thus, TGA data could be used to determine the Arrhenius pre-exponential term and the activation energy for both the diffusion and the reaction rate of each thermolysis reaction. Numerical solution of the differential equation was performed by Brandes (201).

3.2.3. Elemental Analysis

The composition of fiber samples from various points in the thermal treatment process was determined by elemental analysis. This work was performed by Galbraith Laboratories of Knoxville, TN, using the following methods (202).

Carbon, hydrogen, and nitrogen contents were measured using a Leco CHN 800 Determinator. A 2 to 25 mg sample was weighed into a tin capsule to the nearest 0.001 mg. The capsule was sealed and then heated to 950-1000°C under a constant flow of oxygen. Quantitative analysis of infrared absorption gave the quantities of CO_2 and H_2O, from which the amounts of carbon and hydrogen were calculated. The nitrogen content was determined by hot-wire thermal conductivity measurement of the combustion gas. Acetanilide (71.09 %C, 6.72 %H, and 10.36 %N) was used as the calibration standard.

Oxygen content was determined by a Leco RO-478 Oxygen Determinator. A two milligram sample was weighed and placed in a tin capsule. Then the sample was thermolyzed in a stream of nitrogen at 1200°C. Separate infrared detectors reported the CO and CO_2 content of the thermolysis gas, used to calculate the oxygen content of the fiber sample. Again, acetanilide was used as the calibration standard.

Sulfur content was determined using a Leco SC 432DR Sulfur Analyzer. Samples were weighed to the nearest 0.01 mg and placed in a tin sample boat. The sample was covered by combustion accelerator V205 and burned under flowing oxygen at 1230°C. Infrared absorption was used to quantitatively determine the SO_2 content in the combustion gas, from which the sulfur content in the fiber samples was calculated. NBS Sulfur reference material 143c, cystine, with 26.69 %S was used as the calibration standard.

3.2.4. Evolved Gas Analysis

Gas samples could be taken from the carbon resistance furnace by means of a Teflon® septum located in the gas exhaust line. Approximately 10 g of ground mesophase pitch were placed in a cylindrical graphite crucible and covered with a graphite lid. The crucible

was placed on the lower hearth of the carbon resistance furnace, turned vertical for this experiment. The furnace was filled with argon to atmospheric pressure and heated at 20°C per minute from room temperature to 2400°C. Furnace chamber pressure was monitored during heating and, at points where the pressure seemed to increase, a gas sample was taken. This was done by inserting a syringe into the septum, drawing a sample of >250 μL, and injecting the sample into a glass sample vial with a Teflon® lid and crimped seal. Samples were taken at 900, 1900, and 2200°C, and identification of gas species was accomplished by comparing the reported retention time and ion mass of the unknown sample with those of pure standards of suspected species using a Hewlett-Packard gas chromatograph/mass spectrometer, located in the School of Textiles.

3.2.5. Wide Angle X-ray Diffraction

The crystal structure of fibers from various points in the thermal treatment process was characterized by wide angle X-ray diffraction. Lattice constants and uniform lattice strain in both the a- and c-crystallographic directions were determined from at least two orders of the same reflection. Likewise, the crystallite size and non-uniform strain were determined from the shape and breadth of multiple orders. Because of the high degree of orientation of basal planes parallel to the fiber axis, the (hki0) diffraction peaks, from which a-directional crystal information is obtained, were very weak, or nonexistent, for the fiber samples. Therefore, to obtain a measure of a-directional order, ground fiber samples were used. The extent of this basal plane orientation was quantified by an azimuthal scan of (0002) peak intensity.

All data was collected using a Scintag XDS 2000 diffractometer, equipped with a copper X-ray source and a lithium-drifted silicon solid state detector. Figure 3.7 shows the configuration of the Scintag XDS 2000 diffractometer.

Samples for both experiments consisted of a uniaxial fiber-resin or fiber-paraffin composite affixed to an aluminum ring as shown in Figure 3.8. Their preparation was as follows: first, an approximately 7.5 cm length of fiber was cut from each fiber set. It then
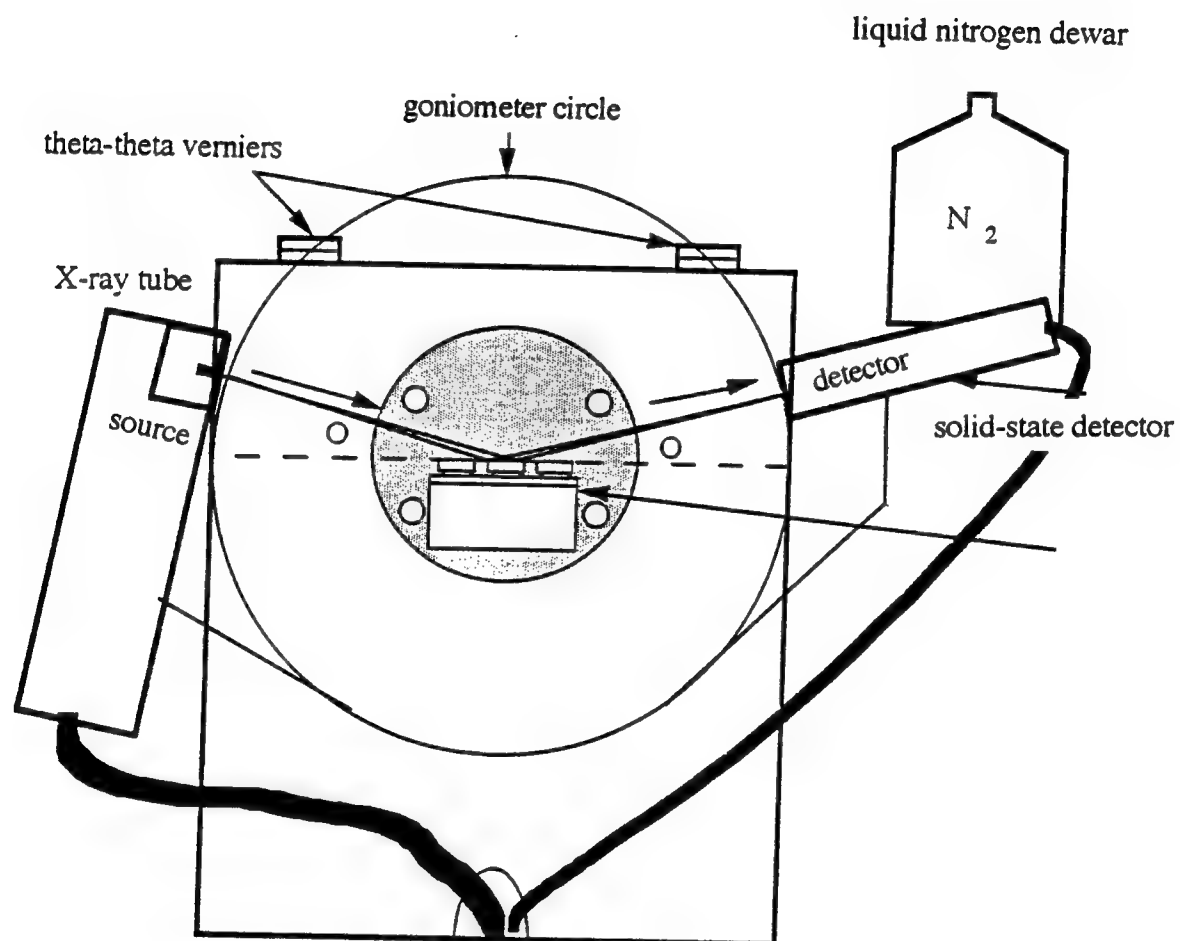
Figure 3.7. Diffractometer configured for two-theta scan.
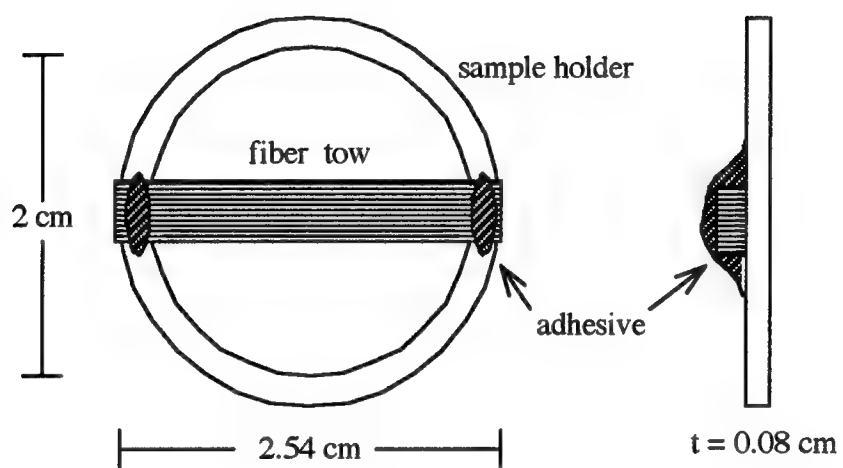
Figure 3.8. Fiber diffraction sample.

was dipped in either thermosetting polyester resin or melted paraffin wax. Neither matrix gave strong diffraction peaks and their contribution could be easily subtracted from the diffraction profile. However, the thermosetting resin, used to mount fibers for cross-sectional area measurements, proved poor for this application. It was often slow in curing and resulted in fiber slumping. For that reason, all subsequent samples were made using paraffin wax. The wax was placed in a stainless steel bowl and held at 100-150°C until completely melted. After dipping the fiber strand, excess wax could be removed and the fibers oriented uniaxially by hand. Once the wax cooled to room temperature, the composite was rigid and could be affixed to the aluminum ring by any household cement. This fiber holder, measuring 2.54 cm outside diameter and 0.8 cm thick, fit both the powder diffraction holder and the transmission attachment of the diffractometer, allowing efficient use of sample.

Bragg, or two-theta, fiber diffraction scans were conducted using the six-position powder holder. A fiber sample was placed on top of a 0.5 mm thick, 2.54 cm diameter sapphire disk, cut so that its (0001) plane was parallel to the disk surface. The disk served two purposes: (1) it raised the fiber sample at the correct height (even with the lip of the powder holder), and (2) it prevented fluorescence of the stainless steel powder holder under the Cu K_α radiation. Preliminary diffraction trials showed that iron fluorescence resulted in an increasing background with diffraction angle, and an anomalous peak located near the (10$\underline{1}$0) peak for graphite.

A typical Bragg scan involved scanning the angular range of 22 to 85° two-theta at a scan rate of 0.25° per minute. This meant that both arms of the goniometer moved at a rate of 0.125° per minute. When greater precision was required for a-directional crystallite size measurements, the scan range was reduced to 6° symmetrically surrounding the diffraction peak of interest and the diffractometer was operated in step-scan mode. The step increment was chosen to be 0.025° and the count time at each increment was 10 seconds. In both

cases, the X-ray source was operated at a voltage of 40 kV and a tube current of 30 mA, while the solid state detector was operated at a negative bias of 1000 mV.

While the composite method was adequate for the study of basal plane spacing and stack height, L_c, there were too few (hki0) planes capable of producing diffraction to estimate a-directional properties. To increase the contribution of these planes, fiber sets from the isothermal study were ground using a glass mortar and pestal and placed in the powder diffraction holder. While it has been shown that lengthy ball-milling affects the crystal structure of carbons (203), the "light" grinding employed during this study was considered to have negligible influence. Such grinding (for only several seconds duration) produced no significant changes in peak position or breadth. Extended grinding, however, resulted in an increase in d(0002), peak broadening, and a loss in intensity. Step scans employing 0.025° steps and 10 seconds per step were used to scan the angular ranges corresponding to the (0002), (10$\underline{1}$0), (0004), and (11$\underline{2}$0) diffraction peaks. The same information concerning interplanar spacing, crystallite size, and strain could be obtained, but, of course, (0002) orientation could not be measured.

The intensity-diffraction angle spectrum contained the diffraction pattern of the fiber sample in addition to a diffuse background. A number of factors contributed to the background, including scattering by the composite matrix, Compton-modified scattering, non-monochromatic radiation (both bremsstrahlung and $K_{\alpha 2}$), and absorption. Fortunately, the background could be subtracted by a routine in the Scintag DMS software. The same routine also removed all peak doublets due to the $K_{\alpha 2}$ component of the incident radiation, and applied the Lorentz-polarization factor to the measured intensities.

Analysis of an individual peak meant first fitting a split-Pearson VII profile to the intensity data and determining the angular location and full-width-at-half-maximum, β. The Pearson VII profile, which has the form

$$I_{n,k} = \frac{2\sqrt{m}\,\Gamma(2^{1/m}-1)}{\pi\Gamma(m-0.5)\beta_k}\left[1+\frac{4(2^{1/m}-1)}{\beta_k^2}(2\theta_n-2\theta_k)^2\right]^{-m}, \qquad (3.14)$$

was chosen for two reasons: (1) it allows the exponent to be modified, giving the model one degree of freedom more than either the Gaussian or Cauchy models, which have the form

$$I_{n,k} = \frac{2\sqrt{\ln 2}}{\beta_k} \exp\left[\frac{-4\ln 2}{\beta_k^2}(2\theta_n - 2\theta_k)^2\right] \text{ and} \tag{3.15}$$

$$I_{n,k} = \frac{\sqrt{4}}{\pi\beta_k}\left[1 + \frac{4(\sqrt{2}-1)}{\beta_k^2}(2\theta_n - 2\theta_k)^2\right]^{-1}, \tag{3.16}$$

respectively, and (2) when used in the split form, a diffraction peak is modelled as a composite of two Pearson VII peaks (204). The latter feature is especially pertinent to carbons, because their low absorption gives rise to asymmetric peaks, skewed toward higher angles. From this type of analysis, four parameters could be used to describe each diffraction peak. They were the Pearson VII exponents for each side of the peak (indicating Gaussian or Cauchy profile character (205)), the angular position of the intensity maximum, and the full-width-at-half-maximum, β.

To perform the calculation of lattice constant, crystallite size, and lattice strain from these parameters, one additional correction was necessary that is not part of the Scintag DMS software. That correction is the angular shift and peak broadening due to imperfections in the machine. As discussed earlier, finite source and detector slit widths, non-monochromatic radiation, and imperfect diffraction geometry leads to errors in angular measurement and finite peak breadth, even for large, nearly-perfect crystals. Therefore, a strain-free reference material having precisely-known lattice constants and large crystal size was scanned at the same conditions as the fiber samples during each group of diffraction experiments. The material chosen for this work was silicon reference material NBS-640b, a strain-free powder of greater than 5 μm (50,000 Å) crystal size. Because of limits in resolution of peak breadths for materials with an average crystal size of greater than 1000 Å, the peak width for this material should have been negligible. Any measured broadening was due to the instrument. Table 3.3 shows the six crystal planes and their angular position determined using Cu $K_{\alpha 2}$ radiation, as reported by NIST (206).

Table 3.3. Diffraction data for silicon reference material NBS 640b (205).

Diffraction plane (hkil)	d_{hkl} (Å)	Diffraction angle (° 2θ) (for λ = 1.5406 Å)
111	3.136	28.442
220	1.920	47.303
311	1.638	56.122
400	1.358	69.130
331	1.246	76.376
422	1.109	88.030

The deviation of measured peak position for the silicon reference then was added to the measured peak positions of a fiber sample. Apparently because of poor alignment of the instrument optics, this deviation was not a constant, but rather a function of diffraction angle for all reference trials. The form of this dependence was found to be

$$\Delta(2\theta) = a + b \sin^2 \theta, \qquad (3.17)$$

where $\Delta(2\theta)$ is the angular deviation and a and b are constants. Constants a and b were found by linear regression using the six reference peaks.

After adding this error term to the measured diffraction angles found for the fiber samples, the lattice constants were found by determining the lattice constant for several orders of the same reflection and extrapolating to $2\theta = 180°$. Typically, the lattice constant is plotted versus $\cos^2 \theta$, the intercept being the true lattice constant (207). However, no high angle ($2\theta > 90°C$) reflections were present for the fiber samples and a different extrapolation function was required. The Nelson-Riley function (NRF), having the form

$$NRF = \frac{\cos^2 \theta}{\sin \theta} + \frac{\cos^2 \theta}{\theta}, \qquad (3.18)$$

was developed for materials having few high angle peaks and low absorption (208). The true lattice constant is the intercept of this extrapolation to NRF = 0, and the slope gives a measure of the uniform lattice strain. If the slope is negative, the low-orders of a given reflection underestimate the unit cell dimension and the crystal is said to be in

"compression". On the other hand, a positive slope indicates "tensile" strain, with the low-orders overestimating the lattice constant. Thus, the sign of this slope gave the predominant sense of strain in the crystallites that comprise the fiber.

Next, the instrumental breadth was subtracted from the breadths of the carbon fiber peaks. Its contribution was assumed to be Gaussian because the exponent of the Pearson VII profile found for the silicon reference peaks was around 10 (205). The instrumental breadth ($\beta_{instrumental}$) then was subtracted from the measured breadth ($\beta_{measured}$) by the formula

$$\beta_{sample} = \sqrt{\beta_{measured}^2 - \beta_{instrumental}^2}, \tag{3.19}$$

giving β_{sample}, the peak breadth due to the sample's crystal structure. But this breadth is the summation of two terms: the breadth due to finite crystallite size, and the breadth due to non-uniform strain (or distribution of interplanar spacings). The sample breadth then can be written

$$\beta_{sample} = \beta_{strain} + \beta_{crystallite\ size}, \tag{3.20}$$

where both the strain and crystallite size components are assumed to be Cauchy in character. This was reasonable as the Pearson VII exponents for these carbon fibers samples were found to be in the range of 1 to 4. Substituting the relationships of breadth to non-uniform strain and crystallite size (209) into the above equation gives

$$\beta_{sample} = S \tan \theta + \frac{K\lambda}{L_{(hkil)} \cos \theta}, \tag{3.21}$$

where S is proportional to the lattice strain, K is the Scherrer constant, λ is the wavelength of the incident X-radiation, and $L_{(hkil)}$ is the crystallite dimension perpendicular to the crystal plane being studied (210). Multiplying this equation by $\cos \theta$ gives

$$\beta_{sample}\cos \theta = S \sin \theta + \frac{K\lambda}{L_{(hkil)}}. \tag{3.22}$$

S and $L_{(hkil)}$ were determined by plotting $\beta_{sample}\cos \theta$ versus $\sin \theta$. The slope is S and the intercept is $K\lambda/L_{(hkil)}$, so that the crystallite size could be calculated by substituting the appropriate value of Scherrer's constant, K, and the incident wavelength. Because S is

calculated from the full peak width, including both tails of the planar spacing distribution, it is equal to twice the lattice strain. The sense of $\varepsilon = S/2$ would be unknown, if not for the previous lattice constant calculation. Typically, it is assumed that the ε is predominantly either tensile or compressive, as determined by the slope of the lattice constant extrapolation (210). If the non-uniform strain were due to bending in a direction parallel to the (hkil) plane being considered, there would always exist a region under [hkil] tensile strain and a region under [hkil] compression strain, separated by an axis of zero strain. Then, there would be no diffraction peak shift, and S could not be assumed to be predominantly tensile or compressive. However, if a crystallite exists so that localized stresses (e.g., thermal stresses at grain walls) cause a distribution of (hkil) spacings bounded by the true d(hkil), both peak shift and peak broadening will be observed. Then, the sign of the Nelson-Riley extrapolation gives the tensile or compressive sense of the strain, and its magnitude can be estimated from peak broadening. In truth, S is a measure of strain broadening, given that the average crystallite has been strained preferentially in a given sense.

The value of K used in the general case is 0.89 (212). However, for turbostratic carbons with random stacking of two-dimensionally perfect layers, Warren's random layer diffraction theory dictates a value of 1.84 for K in the case of (hki0) diffraction lines (16, 17). In this study, K(hki0) was allowed to decrease from 1.84 to 0.89 as layer stacking becomes more perfect. Using Franklin's definition of the degree of graphitization (95),

$$p = 1 - g^2, \tag{3.23}$$

where g, defined by Maire and Mering (18), is

$$g = \frac{3.44 - d(0002)}{3.44 - 3.354}. \tag{3.24}$$

The appropriate value of K for (hki0) diffraction lines was determined from

$$K = 0.89 + (1.84 - 0.89)\, p. \tag{3.25}$$

One additional correction is dictated by Warren for randomly stacked layers. It involves the anomalous shift of (hki0) diffraction peaks toward higher angles. This is caused by the convolution of (hki0) and (hkil) lines into a "sawtooth" peak, skewed toward

high angles. Warren suggests that both the (10$\underline{1}$0) and (11$\underline{2}$0) peaks must be shifted by

$$\Delta\theta = \sin^{-1}\left(\frac{0.16\,\lambda}{L_a}\right), \qquad (3.26)$$

where L_a is the layer diameter. If this correction is not made, the existence of an in-plane compressive strain may be wrongly concluded (17).

The orientation of the graphite basal plane with respect to the fiber axis was quantified by an azimuthal scan of the (0002) diffraction intensity. The same fiber sample holder described earlier was placed in the transmission attachment, with the fiber in the horizontal ($\chi = 0°$) position, as shown in Figure 3.9. Then, a two-theta scan was conducted over a small angular range containing the (0002) diffraction peak. The background subtraction and profile fitting portions of the DMS software were used to locate the angle giving maximum intensity. With the goniometer fixed at this angle, the fiber was rotated azimuthally in one degree steps over 360°. At each degree rotation, the number of counts was recorded for 20 seconds. No correction was made for the geometrical fraction of the sample that was sampled by the X-ray beam.

In addition to Bragg's law, diffraction from a given plane requires that the X-ray source, the plane normal, and the detector lie in the same plane. Therefore, the axially-oriented (0002) planes gave maximum intensity when the fiber sample was oriented horizontally. If perfect orientation were achieved, the (0002) intensity would drop to zero when the fiber bundle was rotated even slightly from horizontal. This is not the case because there is a distribution of basal plane orientations about the fiber axis. The width of the azimuthal intensity profile, then, is an indicator of the degree of preferential orientation of the basal plane. In this study, the full-width-at-half-maximum (Z, in degrees) was calculated for each azimuthal intensity profile. Rotation through 360° gave two replications of this measurement for each sample. Additional measures of basal plane orientation, such as the Bacon anisotropy function, given by equation 2.5, and the Pearson VII exponent, were also calculated for selected samples using a simplex minimization algorithm.
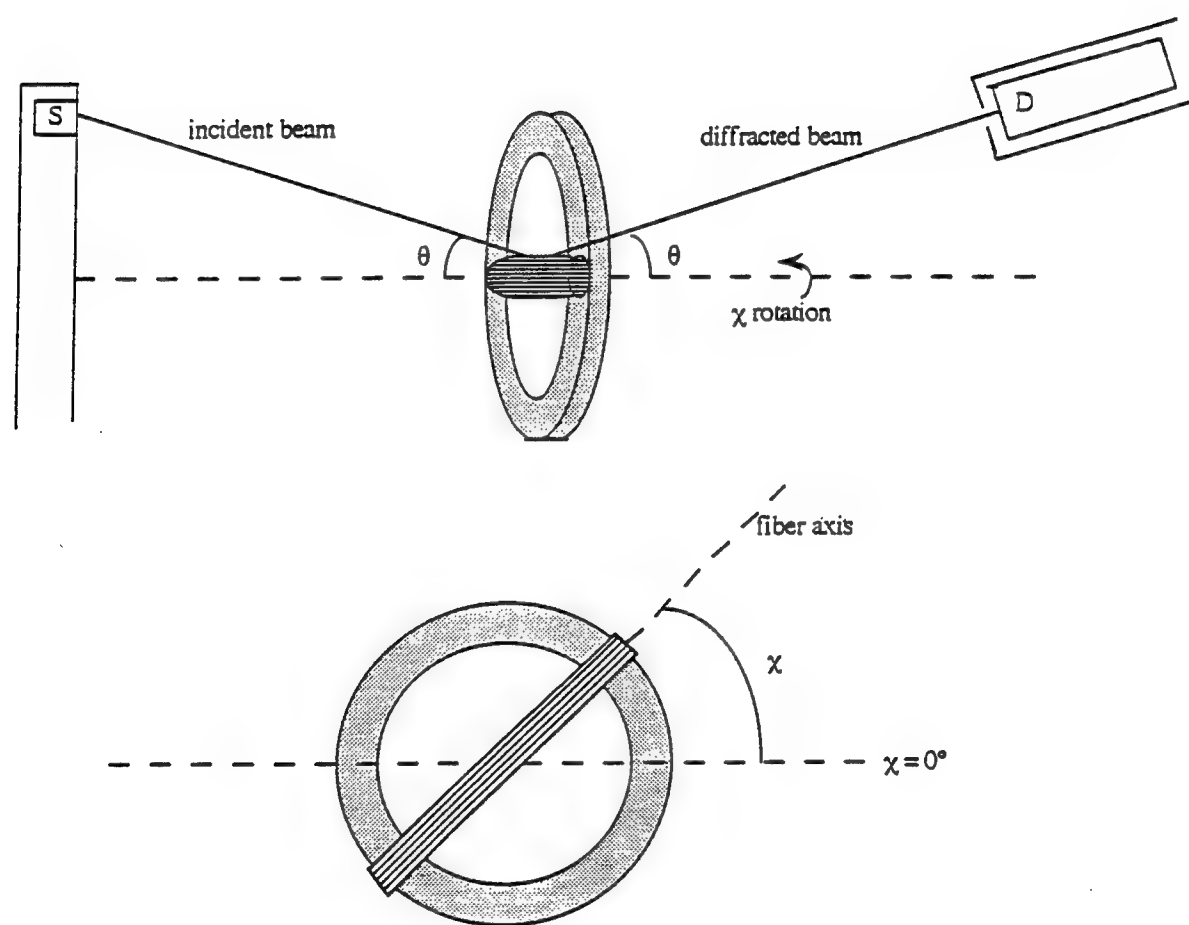
Figure 3.9. χ-scan geometry.

3.2.6 Small Angle X-ray Diffraction

The long range fluctuations in electron density that are caused by voids within a fiber were examined using small angle X-ray diffraction equipment at the Solid State Division of Oak Ridge National Laboratory. Fiber samples representing different carbonization heating rates and maximum temperatures were dipped in melted paraffin wax and formed into a unidirectional strand. Then, the strand was wrapped around both faces of a slotted aluminum washer, as shown in Figure 3.10. The ends of the strand were fastened to the washer by household cement and excess fiber was cut away. As small angle scattering is sensitive to density fluctuations, the contribution of the paraffin wax to the small angle diffracted intensity could not be neglected. Therefore, the wax was removed by placing the fiber samples in a forced convection oven and heating to 150°C for one hour. This left two unidirectional strands fastened to the washer at their ends, with no matrix to contribute small angle scattering.

Ten samples were attached to a twelve-position sample holder. The two remaining positions were taken by an empty specimen and a lead wafer. Then, the holder was affixed to a rotating sample changer and placed in the sample chamber. Together with the incident and scattered X-ray chambers, the sample chamber was evacuated to minimize absorption. In turn, each sample holder position was rotated into the X-ray path. The X-ray source-to-sample distance was 1.176 m, while the sample-to-detector distance was adjusted, by means of tubular inserts, to 5.176 m for this experiment. With the tube power set at 40 kV and 50 mA, each sample was rotated into the X-ray path and held there for five minutes. The scattered X-rays passed through a beryllium window, and were measured by a two-dimensional ionization counter, consisting of a 20 cm by 20 cm wire grid. Arrival of X-ray quanta caused the ionization of gas atoms surrounding the wires. The electrons created in this process migrated to the wires and resulted in a current, which travelled to the detector circuitry. By monitoring the RC response of the circuit, the position at which the X-ray quanta were incident upon the detector could be determined. The result was a two-

top view:

0.375 "

0.375 "

[IIIII] = fiber sample

[▒▒▒] = aluminum

0.875 "

side view:

0.0625 "

0.125 "

[▒▒▒] = fiber sample

[▒▒▒] = aluminum

0.875 "
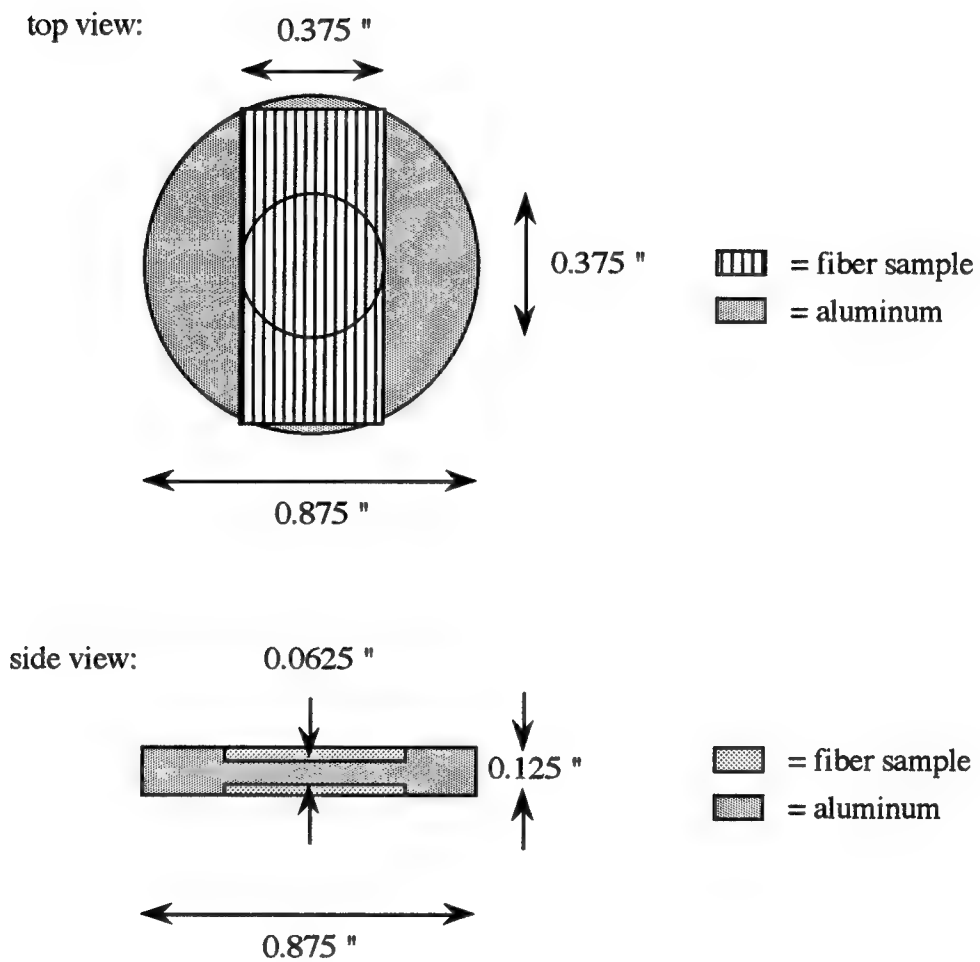
Figure 3.10. Slotted aluminum washer used as a small angle diffraction fiber holder.

dimensional map of scattered intensity, allowing pore dimension and orientation to be examined during a single trial.

Two regions of scattering have been defined, based on the magnitude of the scattering wavevector, **h**, defined as

$$h = |\mathbf{h}| = \frac{4\pi \sin \theta}{\lambda}, \tag{3.27}$$

where θ is the scattering angle and λ is the Cu Kα wavelength ($\lambda = 1.542$ Å) (5, 213). As h approaches zero, called the Guinier region, the scattered intensity, I(h), can be described by

$$I(h) = V\langle\rho^2\rangle\exp\left(-\frac{1}{3}h^2R_g^2\right), \tag{3.28}$$

in which $\langle\rho^2\rangle$ is the mean squared electron density, V is the irradiated volume, and R_g is the electron radius of gyration. Fitting the observed scattered intensity with equation 3.28 yielded a measure of the electron radius of gyration, known as the Guinier pore radius.

At larger values of h, Porod's Law holds. Porod's Law states that the scattering intensity of a two-phase material should asymptotically approach

$$I(h) = \frac{a}{h^4}, \tag{3.29}$$

where a is a constant. Then, the integrated intensity can be written

$$I(h) = \frac{2\pi\langle\rho^2\rangle S}{h^4}, \tag{3.30}$$

where S is the surface area of the interface between two phases present in the material. In a porous solid, S is the pore surface area. The smoothness of the pores can be evaluated from a plot of $h^3I(h)$ against h. Smooth phase boundaries will give rise to a maximum, while no maximum will be observed if the boundaries have sharp edges or corners. The pore volume fraction, c, can be determined by rearranging the following formula:

$$\int_0^\infty I(h)h\, dh = 4\pi^2\langle\rho^2\rangle Vc(1 - c). \tag{3.31}$$

However, I(h) can only be measured over small ranges of h, and the integral must be split:

$$\int_0^\infty I(h)h \ dh = \int_0^{h_0} I(h)h \ dh + \int_{h_0}^\infty \frac{hk}{h^3} dh = \int_0^{h_0} I(h)h \ dh + \frac{k}{h_0}. \qquad (3.32)$$

The constant k is the limiting value of $h^3I(h)$ obtained from a plot of $h^3I(h)$ against h. The value of h_0 must be in the range of scattering wavevectors where Porod's Law is applicable. Finally, pore shape can be judged by calculating the specific surface area, S/V, equal to

$$\frac{S}{V} = \frac{4c(1-c)k}{\displaystyle\int_0^{h_0} I(h)h \ dh + \frac{k}{h_0}} \qquad (3.33)$$

If the pores are determined to have sharp interfaces, then a fractal dimension can be assigned to their shape. This is parameter is determined from a linear regression of $\ln(I(h))$ on $\ln(h)$. The slope is related to the fractal dimension, D, by the equation

$$slope = D - 6. \qquad (3.34)$$

Porod's law, having a slope of -4, is a special case in which $D = 2$ for pores having smooth interfaces. In general, D increases with the increasing pore sharpness that accompanies graphitic ordering (5, 104).

3.2.7. Specific Heat Capacity Measurement

The specific heat capacities of ground fiber samples from each treatment were determined by differential scanning calorimetry. First, the system calibration constant was determined by measuring the specific heat capacity of a 60.5 mg sapphire disk provided by Du Pont Thermal Analysis Instruments. The sapphire was placed in an aluminum sample pan, and the pan placed on the sample thermocouple junction of a Du Pont 910 Differential Scanning Calorimeter, shown schematically in Figure 3.4. An empty pan of equal mass was placed on the reference junction and the cell was closed and evacuated. The DSC was heated at a rate of 5°C per minute from room temperature to 450°C, and both the temperature and the heat flow were recorded in a similar manner to that presented in section 3.2.1. for DSC analysis of stabilization and carbonization.

A calibration coefficient, E, for the DSC cell was determined by comparing the heat flow data to the specific heat capacity data provided by Du Pont for the sapphire reference material (195). At each measurement temperature, E was determined from

$$E = \frac{C_p \, hr \, m}{Q},$$ (3.35)

where C_p is the constant-pressure specific heat capacity of sapphire in J/g/K, hr is the heating rate in °C per minute, m is the mass of the sapphire disk in grams, and Q is the cell heat flow in μW. E was nearly constant and on the order of one for the entire temperature range of the trials.

Then, a sample was prepared by grinding fibers into a fine powder with a glass mortar and pestal. Approximately 20 mg, weighed to ±0.0001 g by a Mettler analog balance, was placed in an aluminum sample pan and sealed. The same DSC heating schedule used for the sapphire reference material was employed, and both the temperature and the heat flow were continuously recorded. At each temperature, the specific heat capacity of the sample was calculated from

$$C_p = \frac{Q E}{hr \, m_s},$$ (3.36)

in which m_s is the sample mass and Q is the measured heat flow for the sample trial.

Finally, the relationship of specific heat capacity to temperature was determined. One approach would be to simply fit the data for each sample with a polynomial that described the temperature dependence over the temperature range of the trial. However, this would provide very little information on the structure and quality of the graphite crystals. For that reason, a two-dimensional adaptation of the Debye theory of specific heats was used to calculate a Debye temperature, which described the shape of the heat capacity curve with temperature. Its magnitude is related to the maximum frequency of phonons within the lattice, and therefore, it is strongly related to all lattice properties, such as elastic modulus and thermal conductivity. The derivation of the two-dimensional model is presented in Appendix A.1, but the resulting equation, used here to fit the specific heat capacity data, is

$$C_p \cong C_v = \left(\frac{\partial E}{\partial T}\right)_{N,V} = \frac{4R}{\Omega^2} \int_0^\Omega \frac{x^3 e^x}{(e^x - 1)^2} dx + \zeta, \qquad (3.37)$$

where C_v is the constant-volume specific heat capacity, R is the gas constant, and Ω is a function of phonon frequency and temperature, given by

$$\Omega = \frac{h\nu}{kT}. \qquad (3.38)$$

In this equation, h is Planck's constant, ν is the maximum phonon frequency, k is Boltzmann's constant, and T is the absolute temperature at which the specific heat capacity is measured. The two-dimensional Debye temperature, θ_D, then is given by

$$\theta_D = \frac{h\nu}{k} = \Omega T. \qquad (3.39)$$

The term ζ is the contribution of the transverse phonon mode to the specific heat capacity. It is constant for temperatures above 180K (129, 130), well below the temperatures of measurement, and is responsible for the two remaining degrees of freedom.

Thus, an estimate of the material's in-plane Debye temperature could be made for each specific heat capacity measurement. Using a minimization algorithm coupled with a Simpson's Rule integration subroutine, a best-fit value for θ_D was found to describe the specific heat capacity of each fiber set.

3.2.8. Single Filament Electrical Resistivity Testing

The electrical resistivities of single filaments from each carbonized fiber set were measured using an apparatus presented by Coleman (214), consisting of a Teflon® block with an opening machined through the center. Copper terminal posts were threaded into the block at the corners, and four copper wires, each 127 μm in diameter, were stretched across the block, parallel to one another. The distance between the two inner wires was 2.54 cm, and the wires were fastened into place using household cement. When the cement had hardened, one end of each wire was wrapped around a copper terminal, as shown in Figure 3.11. The copper terminals, in turn, were connected to the leads of a Keithley 580 micro-ohmmeter. Then, a single carbon fiber was stretched across the copper

single carbon filament

silver paste at contact

I = current source (μA)
V = voltage meter

☐ = Teflon®

▨ = copper terminals

▧ = Duco® cement

☰ = masking tape

copper terminal post
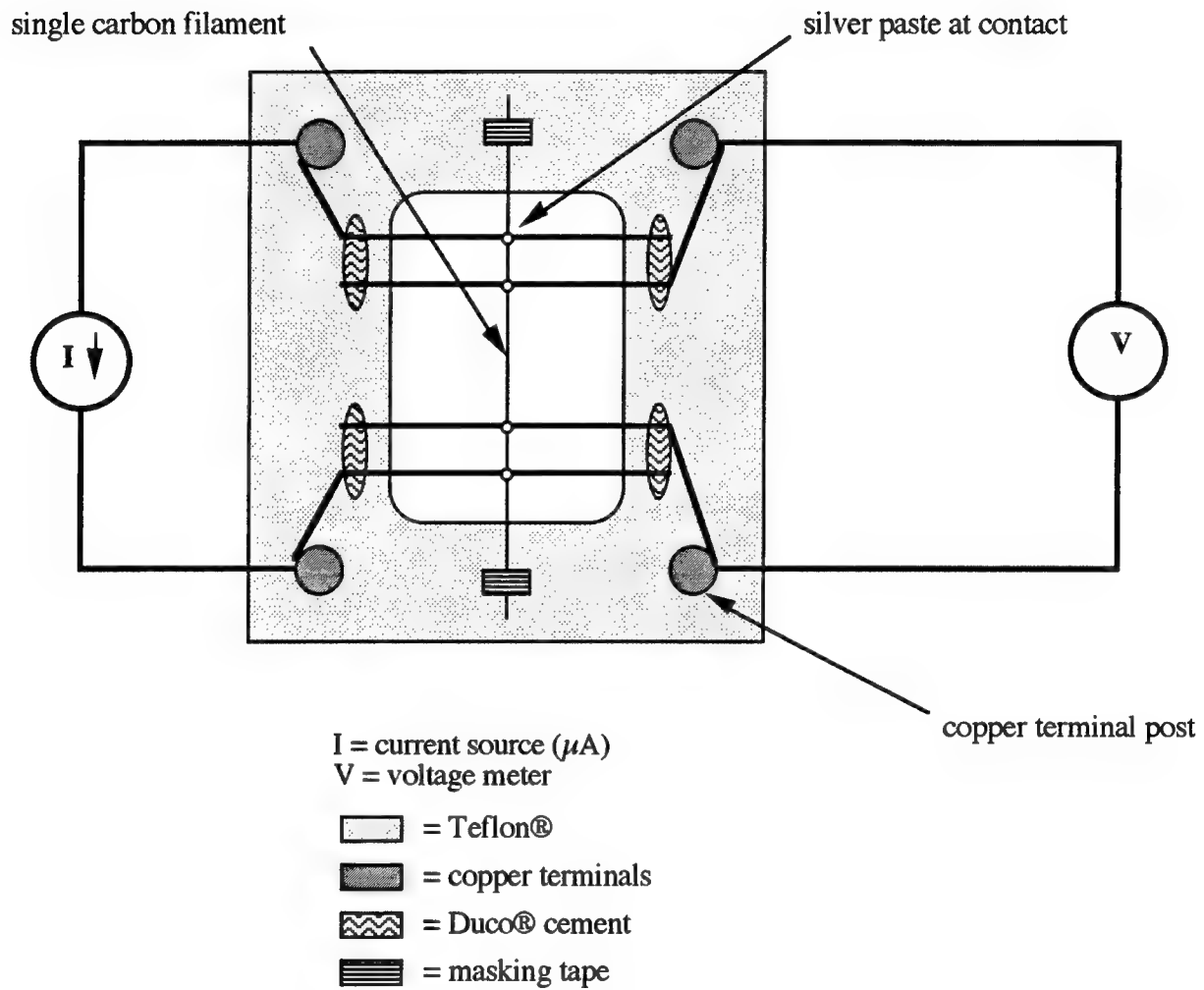
Figure 3.11. Single filament electrical resistivity measurement apparatus (214).

wires, taped in place both ends of the Teflon® block, and attached to the copper wires by silver paste. The two outer leads supplied a precise current of 10 μA and the two inner leads measured the voltage drop across the fiber. Next, the micro-ohmmeter was switched to measurement mode and the resistance was allowed to equilibrate before being recorded. In this manner, the electrical resistance of 25 to 50 fibers from each fiber set were measured. When each fiber's cross-sectional area, or the average cross-sectional area of that fiber set, had been determined by the method presented in section 3.2.10., the fiber resistivity was calculated from the formula

$$\rho = \frac{R\,A}{L},$$
(3.40)

in which R is the measured resistance, A is the cross-sectional area of the fiber, and L is the gauge length, constant at 2.54 cm.

3.2.9. Single Filament Tensile Testing

An acceptable method for single filament tensile testing is described by the American Society for Testing and Materials (ASTM) (215). Using a method based on this standard, the tensile properties of 25 to 50 filaments from selected fiber sets were measured. A filament was glued to a slotted cardboard testing tab as shown in Figure 3.12, using Epoxy 220, manufactured by Hughes Associates. The 10 mm distance between glue spots, over which the fiber would be tested, was defined as the gauge length. After curing the epoxy at room temperature for eight hours, followed by heating to 80°C for five hours, the ends of the tab were placed in the grips of an Instron universal testing machine, configured so that the upper crossbar was fixed and the lower crossbar was moveable. The side portions of the tab then were cut away, using a heated metal wire, so that the filament was supported only by the pneumatically-operated grips of the testing machine. The upper grip was free-swinging, allowing fiber alignment with the direction of loading to be maximized. The lower crossbar, or crosshead, then was driven downward at a preset speed of 0.0508 cm/s. A load cell connected to the upper grip measured the load on the filament.
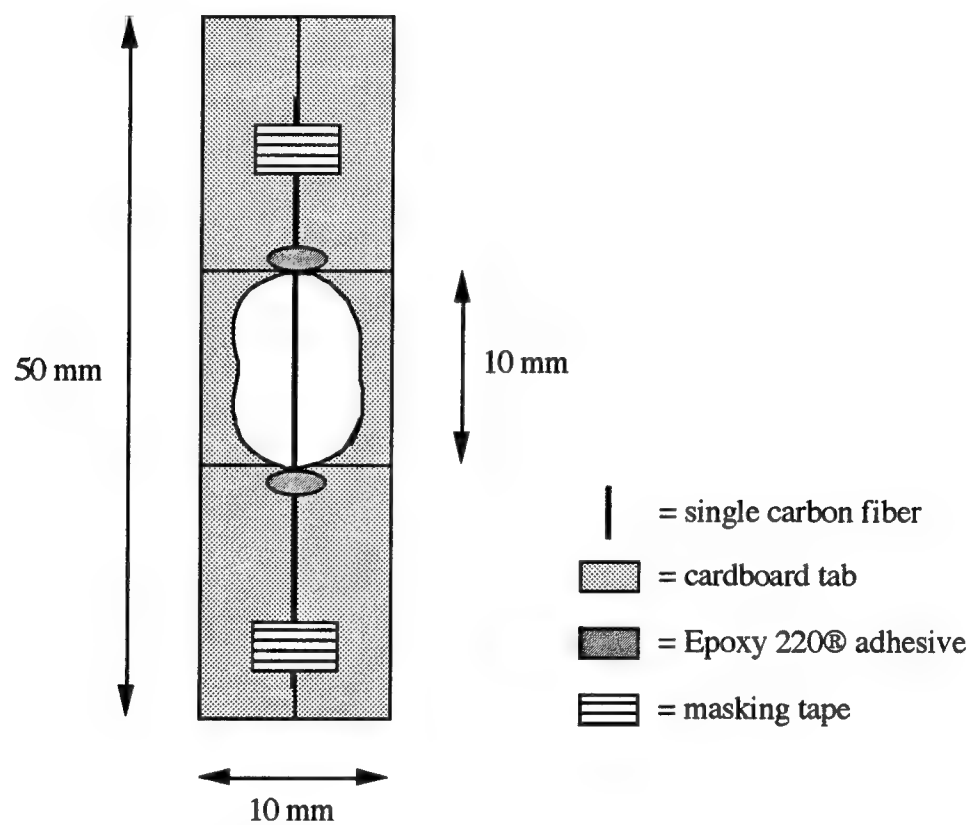
Figure 3.12. Single filament tensile test tab.

Both the load and the displacement were recorded continuously by either a chart recorder or a data acquisition system. From these values, the strain, tensile strength, and Young's modulus of a filament were calculated. Strain, ε, is defined as the ratio of elongation to the original specimen length. The strain-at-failure, then, is the ratio of the vertical distance that the crosshead moved during the test to the gauge length of the testing tab. As the filament is elongated, the tensile stress in the filament increases. This is measured as a load, F, on the load cell. The filament stress can be calculated from

$$\sigma = \frac{F}{A}, \tag{3.41}$$

where A is the cross-sectional area of the filament. Because no means of measuring the filament area during loading was available, A represents the initial fiber area and σ the nominal, or engineering, stress. Stress and strain are related by Hooke's Law,

$$\sigma = E\varepsilon. \tag{3.42}$$

The constant of proportionality, E, is the Young's modulus of the fiber. It is simply the slope of the stress-strain curve for the fiber.

Figure 3.13 shows a typical load versus displacement diagram that might be generated by a single filament test. Problems in determining the Young's modulus and strain-at-failure arise from the contributions of initial loading and system elongation. First, displacement is observed prior to load increase because the filament is usually not taut and perfectly aligned at the initiation of the test. This can be corrected by extrapolating the curve to zero load. The elongation at filament failure then is the difference between the displacements corresponding to fiber failure and the zero-load extrapolation.

A second difficulty lies in the system contribution to the measured elongation. For materials that exhibit low strain-at-failure, like carbon fibers, the contribution of the loading and grip devices is appreciable (216). The apparent elongation, ΔL_a, is the summation of that due to the system, ΔL_s, and that due to the fiber.

$$\Delta L_a = \Delta L_s + \Delta L_{fiber}. \tag{3.43}$$
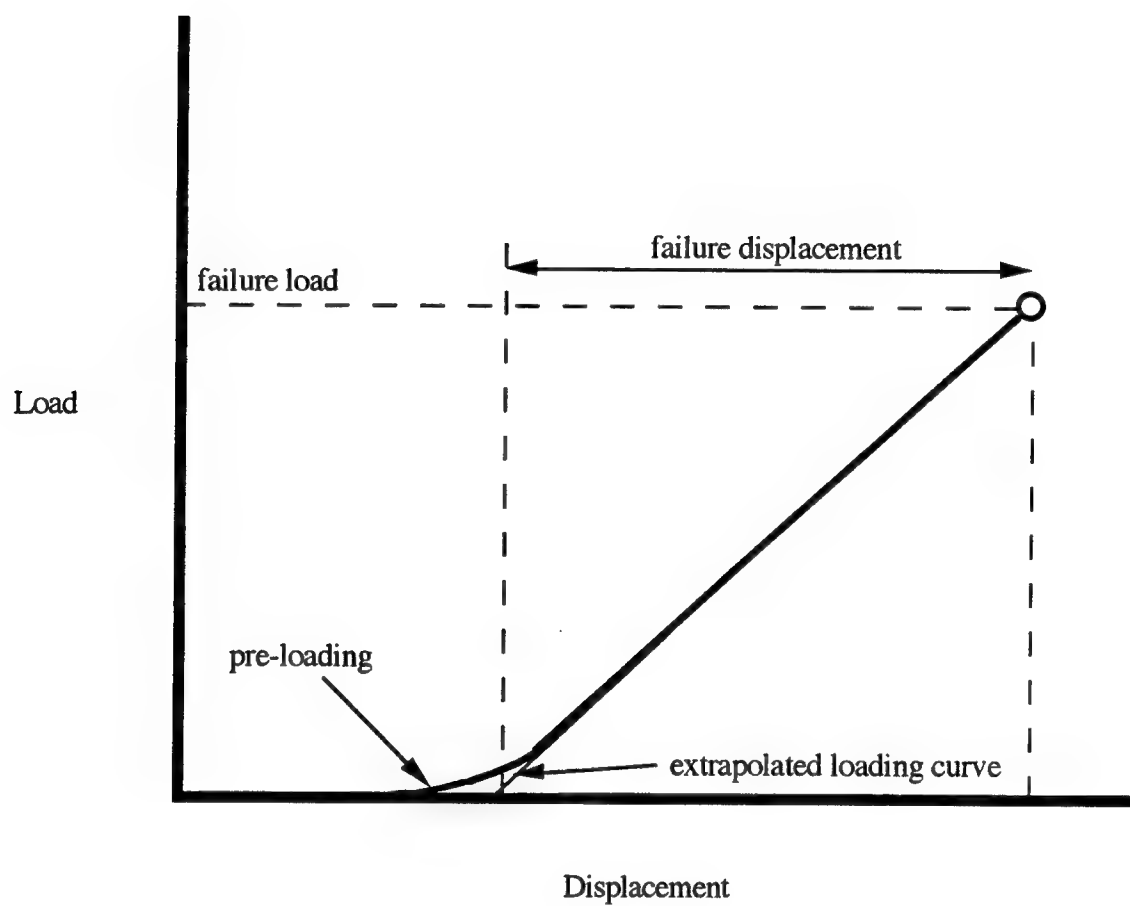
Figure 3.13 Single filament load versus displacement curve.

Filament elongation varies from test to test with load. However, the area, Young's modulus, and length of the system does not change. Thus, the contribution of the system elongation to the apparent elongation will vary. If F_f is the load at failure, the system compliance can be written as

$$C_s = \Delta L_s / F_f. \tag{3.44}$$

Similarly,

$$C_a = \Delta L_a / F_f \text{ and} \tag{3.45}$$

$$C_{fiber} = \Delta L_{fiber} / F_f. \tag{3.46}$$

Substituting these expressions into equation 3.42 allows the apparent compliance to be written as the sum of the system and fiber compliances. Only the left-hand term can be evaluated from the raw data. However, C_a is known to vary with gauge length, because shorter fibers elongate less than longer fibers before failure. The ASTM standard (215) recommends testing at least three fiber sets at several gauge lengths. The intercept of a linear regression of C_a on the gauge length, L, will give the system compliance. Stoner (216), and later A. M. Harper (192), determined the system compliance to be 0.0755 mm/N and 0.1165 mm/N using circular and ribbon-shape fibers, respectively, for the modified testing machine used in this study. Using these values, the strain-at-failure and the Young's modulus of any fiber tested in the same manner can be determined. Although a portion of the difference in system compliance may be attributed to fiber shape, this brings the significance of small differences in observed modulus into question.

Calculation of both the tensile strength and Young's modulus required knowledge of the fiber cross-sectional area. Measurement of the filament area during tensile testing was not possible, especially in the case of non-circular fibers. This necessitated estimation of the fiber area from pre- or post-testing measurements. The standard recommends that a filament's cross-sectional area be estimated from the average area of at least 10 filaments taken from the same fiber population (215). An alternative is to measure the cross-sectional area of an extension of each tested filament. Both procedures will be described in section

3.2.10. The former, using an average area, was used in later experiments, where the tensile properties were measured only for comparison between fiber sets. The latter method was used in all experiments where absolute values were important.

3.2.10. Cross-sectional Area Measurement

Bundle measurements for fiber set average areas were made from a 1.5 cm length of fiber, containing several hundred filaments, cut from the fiber set using a razor blade. The bundle was pressed together to form an oriented strand and taped to one end of a cardboard tab having dimensions of approximately 2.5 cm in height and 4.5 cm in length. When folded in-half vertically, the tab formed a "V" that carried two fiber bundles and fit into a circular casting mold, as shown in Figure 3.14. Next, Leco polyester resin (Castolite®) was poured into a polypropylene beaker, and 15 drops of the compatible hardener were added for each 30 ml of resin used. The mixture was stirred slowly to prevent air entrapment. When mixing was complete, at which time its color changed from clear to a pale yellow-green, the mixture was poured into the mold. After 30 to 60 minutes, the resin formed a gel that filled the mold. Then, the mold was placed in an oven at 55°C and held there for one hour. The cast samples then were removed from the mold and polished.

A similar process was used to mount single filaments for area measurement. The end of a fiber used for single filament tensile or electrical resistivity measurement was cut from the measurement block or the testing tab and taped to a cardboard tab, as shown in Figure 3.15. Each fiber was labelled to indicate its fiber set and test number. The cast sample was prepared as described earlier and polished.

Samples were ground and polished to provide a suitable surface for viewing under the optical microscope. A series of rotating silicon carbide laps, decreasing in grit from 240 to 600, were used for coarse polishing, with water as the lubricant. Then, their surfaces were polished further using 0.3 μm particle size α-aluminum oxide, spread on a rotating felt lap. Polishing continued until the surfaces achieved a glassy appearance, free from scratches.

cardboard tab
with 2 fiber sets

casting mold
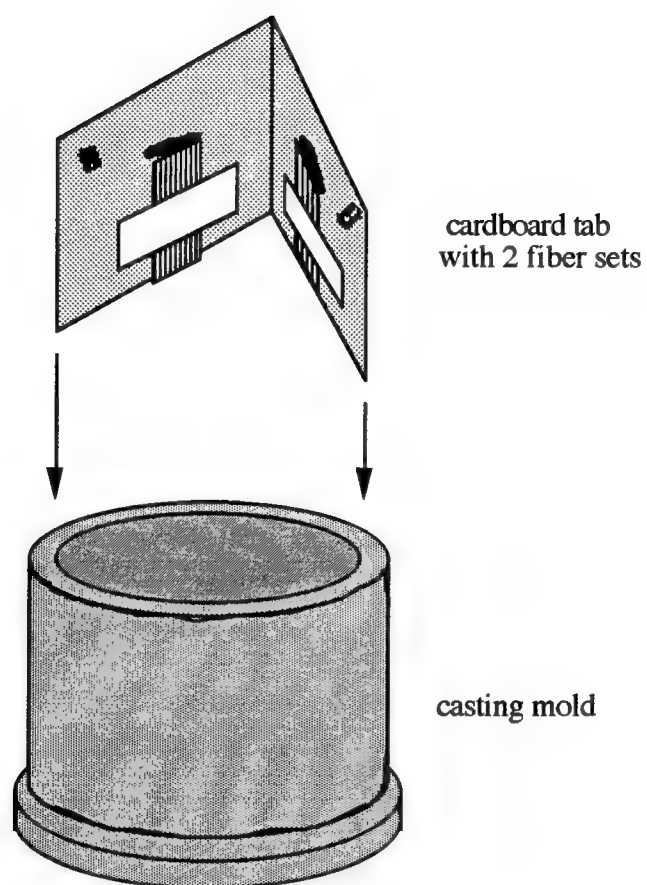
Figure 3.14. Sample for average area measurements.
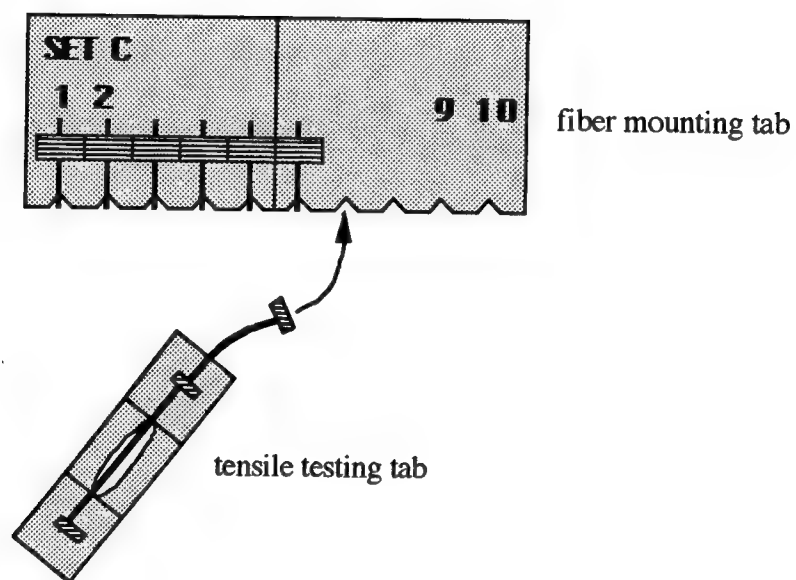
Figure 3.15. Single fibers for area measurements.

The samples were then viewed at 80x magnification (40x objective plus a 2x Barlow lens) under a Zeiss ICM405 microscope. Using a Microcomp camera system manufactured by Southern Micro Instruments and image analysis software developed by Analytical Imaging Concepts, the sample image was transferred to a Sony Trinitron® color monitor.

There, the image analysis software was used to define the fiber cross-section and calculate fiber shape and area statistics. First, the software was calibrated for the objective lense used and automatic calculations of fiber length (longest dimension), breadth (shortest dimension), shape factor (the ratio of breadth to length), and area were selected using the data filter option. Then, a threshold gray level was chosen between 1 and 256, so that the image of the resin matrix and the fiber were discernable. The parameters listed above were calculated and displayed for a single fiber when the single object option was used. Using the 80x configuration, each pixel of the monitor corresponded to a 0.309 μm by 0.247 μm area. Therefore, an approximately 12 μm diameter fiber, about the size of the fibers used in this study, would have a pixel count of between 40 and 50 across its diameter.

3.2.11. Infrared Spectroscopy

Diffuse Reflectance Fourier Transform Infrared Spectroscopy (DR FT-IR) was used to identify the functional groups present at different points in the thermal treatment process. Fibers from a given treatment were ground into a fine powder using a glass mortar and pestal. Two to five mass percent powder was mixed with IR-grade potassium bromide and stored in a convection oven at 150°C until use to prevent adsorption of moisture. Then, the mixture was pressed into a 1 cm diameter pellet and placed in the reflection holder of a Perkin-Elmer FT-IR 1600 Spectrophotometer. With the FT-IR chamber filled with nitrogen, infrared radiation ranging in wavenumber from 4000 to 400 cm^{-1} was incident on the pellet, and the reflected intensity was measured by the spectrophotometer cell. Either 16 or 64 scans, depending upon the quality of a preliminary scan, were made for each sample at 4 cm^{-1} wavenumber increments. The replications were used to form an average

FT-IR pattern for each sample. The term diffuse reflectance means that the incident radiation had travelled through a finite thickness of the material before being scattered or reflected by internal surfaces. Macroscopically, the reflected radiation does not follow the laws of reflection because the angles of diffuse reflection do not necessarily equal the angle of incident radiation (217).

3.2.12. Raman Spectroscopy

In contrast to polar groups, such as -COOH, -COO-, -H, and -CH_3, that are characteristic of raw and stabilized pitch products, functional groups such as heterocyclic ring systems, as might be expected with sulfur inclusion, strongly scatter, rather than absorb, infrared radiation. In addition, absorption maxima often occur in the same wavenumber range as the broad aromatic bands (218).

Therefore, a different technique must be used to examine the nature of these functional groups. Laser Raman spectroscopy was conducted on ground carbon fiber samples heated to 1000, 1800, and 2400°C. The work was performed by Dr. Bahne Cornilsen of the Department of Chemistry and Chemical Engineering at Michigan Technological University (219).

3.2.13. Transmission Electron Microscopy

The crystal structures of fibers carbonized at a variety of conditions were also studied using transmission electron microscopy (TEM). As early TEM work in this study was conducted without the benefit of a diamond microtome for fiber sectioning and an image analysis system for micrograph interpretation, only qualitative analysis could be performed. Samples were prepared by grinding fibers into small slivers using a glass mortar and pestal. Then, a suspension of fibers in ethyl alcohol was made. Copper grids, designed to fit in the samples holders of a JEOL JEM 100C transmission electron microscope, were coated with a 2% collodian in amyl acetate solution and dipped into the suspension. When removed, the grids were covered with fiber slivers adhering to the collodian coating, as

shown in Figure 3.16. An additional copper grid was sputtered with an approximately 600 nm thick gold coating to use as a standard for selected area electron diffraction (SAD).

In the TEM, electrons were produced by heating a tungsten filament, and accelerated by a voltage of 100 kV. Despite their high energy ($\lambda_{electron}$ = 0.037 Å at a 100 kV accelerating voltage), they are scattered by gas molecules because of their low mass and negative charge. Also, the tungsten filament will degrade rapidly when heated in the presence of air. Therefore, the column must be evacuated before electrons can be used to study the crystal structure of a sample. In this experiment, a diffusion pump, backed by a mechanical roughing pump, was used to achieve a vacuum of 10^{-7} torr.

A series of lenses and apertures serve both to focus the electron beam and to remove highly scattered rays that might cause destruction of the coherent SAD pattern. The lenses are variable-current electromagnets that are used to deflect the beam. Two condenser lenses limit its area, while the objective lens focuses the scattered beam on the diffraction aperture.

To produce a selected area diffraction (SAD) pattern, the microscope was switched from imaging to diffraction mode and the condenser aperture removed. The diffraction aperture then was used to limit area of the specimen from which the diffraction pattern was created. The SAD pattern appeared on the fluorescent screen at the bottom of the microscope column. To photograph this pattern, the viewplate was covered and the fluorescent screen opened by a trap mechanism, exposing the negative below. This produced a negative image, as the diffracted electron beam darkened the film. Bright field images of the fiber structure were collected by operating the microscope in imaging mode, removing the diffraction aperture, and inserting the condenser aperture. This gave a physical image of the crystal planes within the fiber.

Additional SAD patterns and bright field images were obtained at a later time from longitudinal and transverse thin sections of the same carbon fibers. The work was performed by K. E. Robinson (193), using a Sorvall Porter Blum MT2-B ultramicrotome and a diamond knife to section fibers mounted in a resin. The sections were collected on collodian coated copper grids, that were sputtered with a thin layer of gold. This provided
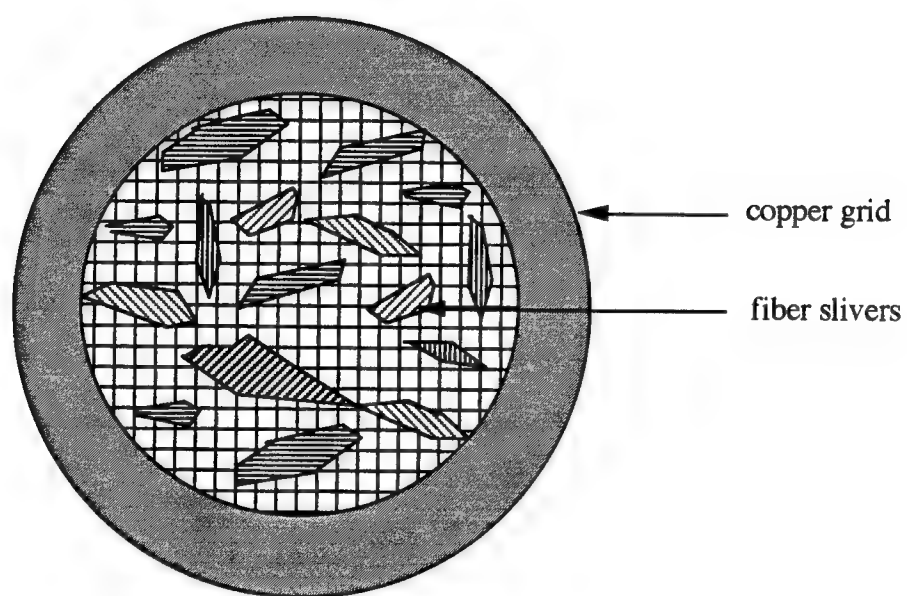
Figure 3.16. Fiber-covered copper grid used for TEM analysis.

a diffraction standard that could be photographed at the the same time as the fiber SAD pattern.

3.2.14. Scanning Electron Microscopy

Evidence of fiber morphology was obtained by scanning electron microscopy (SEM). Samples for this study were made by cutting a small length of fiber from each fiber set. Then the fibers were attached to aluminum stubs, measuring 1.5 cm in diameter by 0.5 cm thick, by copper tape, as shown in Figure 3.17. To prevent charging under the electron beam, an approximately 35 nm thick gold coating was applied by sputtering. The sample was placed in the chamber of an ETEC Autoscan scanning electron microscope and the chamber evacuated to 10^{-4} torr using both a mechanical and a diffusion pump. Photos were taken of the cross-sectional fiber surface at 30 kV tube voltage and magnifications between 1000 and 100,000 times.
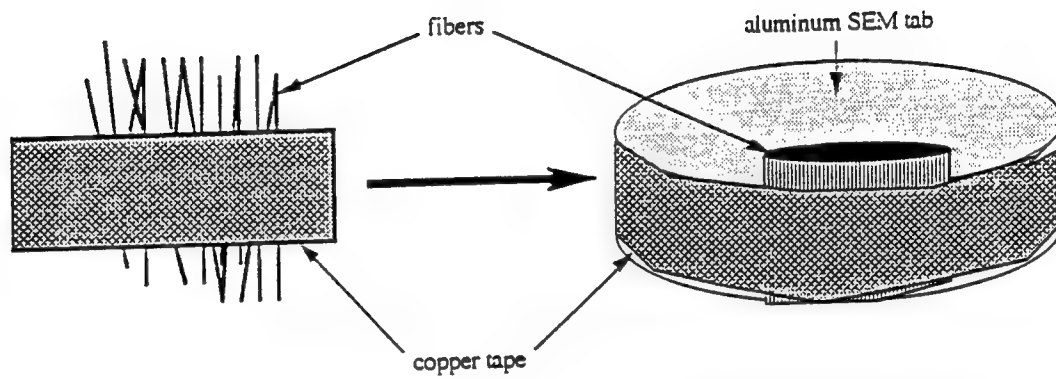
Figure 3.17. Fiber sample for SEM analysis.

CHAPTER 4

RESULTS AND DISCUSSION

The chemical and structural changes that occur during the thermal treatment of mesophase pitch-based carbon fibers are best discussed in three segments: stabilization, thermolysis, and graphitization. Three additional topics that resulted from this study must also be covered. The first is a technique for characterizing the structure of a fiber. Its relation to the lattice-dependent physical properties of the fiber make the technique useful in process monitoring and in property estimation. The final two deal with unique considerations in graphitizing some petroleum-based carbons. One is sulfur removal at high temperatures, which may cause irreversible volumetric expansion and degradation of fiber physical properties. The other is a method for promoting graphitization in fibers, or carbon bodies in general, which contain poorly ordered regions.

4.1. Specific Heat Capacity and Lattice-Dependent Physical Properties

Using the method presented in Chapter 3.2.7, the specific heat capacity was determined for several commercially available carbon fibers, and the heat-soaked pitch precursor fibers produced at Clemson University. Evidence of graphite quality could be gained from the position of the specific heat capacity curve with temperature, as shown in Figure 4.1. Curve "a" represents the theoretical low temperature specific heat capacity curve for a perfect sheet of graphite of infinite dimension. Its in-plane Debye temperature, θ_D, defined as the point at which the specific heat capacity would reach its asymptotic value of 3R, is 2350K (129,130). Impurities, lattice defects, or simply the presence of crystal boundaries serve to scatter phonons and retard the excitation of long wavelength modes. Thus, a reduction in the low temperature specific heat capacity, and an increase in the calculated in-plane Debye temperature, was observed for carbon fibers. Curves "b" and
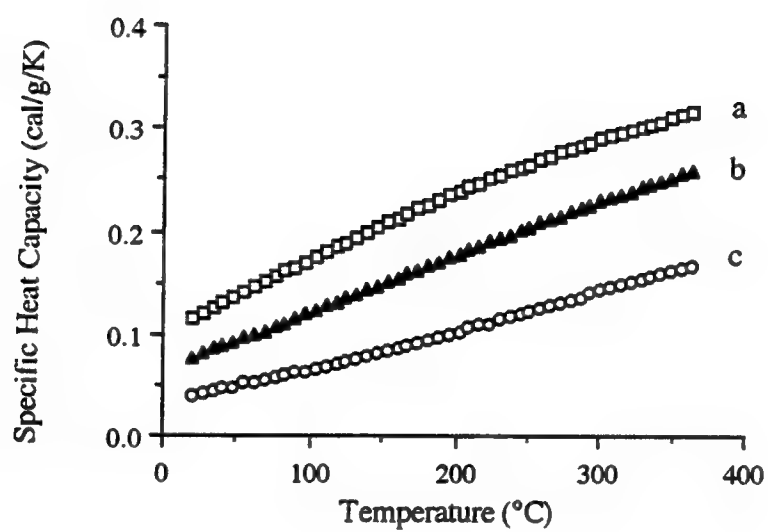
Figure 4.1. Specific heat capacity curves for (a) an infinitely large graphite plane (theoretical), (b) Thornel® P-100 fiber, and (c) Thornel® P-55 fiber.

"c" represent measured low temperature specific heat capacity data for Thornel P-100 (100 Msi Young's modulus) and Thornel P-55 (55 Msi Young's modulus) fibers, respectively.

Extrapolation of these data to temperatures near the fiber's Debye temperature was based upon the assumption that the entire specific heat capacity curve over all temperatures could be approximated by a single expression, given by equation 3.37. Thus, the calculated Debye temperature for a fiber sample was just a superposition parameter that described the displacement in temperature of that curve from the curve for perfect graphite.

The in-plane Debye temperatures calculated for several grades of mesophase pitch-based fibers produced by Amoco Performance Products correlated well with their reported coherence lengths (L_a), tensile moduli, and thermal conductivities. Table 4.1 presents the calculated Debye temperatures for these fibers, and their reported physical properties. A value of θ_D above the fusion temperature of graphite (around 4000K) may indicate that, for such a disordered carbon, fusion occurs prior to the natural thermal activation of high-energy phonon modes.

Table 4.1. Structural and physical properties of Amoco's Thornel® pitch-based fibers.

Fiber Grade	θ_D (K)	L_a[1] (Å)	K[1] (W/mK)	T.Strength[1] (GPa)	Y. Modulus[1] (GPa)
P-25	5526	40	22	1.4	160
P-55	3911	110	120	1.9	415
P-75	2950	170	185	2.1	520
P-100	2675	310	520	2.4	758

[1]   Thornel Product Information, Amoco Performance Products, Inc. (144)

Specific heat capacity is the summation of constructive vibrational energy within a solid. A high value of specific heat capacity at these low measurement temperatures would indicate that the sample has a low in-plane Debye temperature. Therefore, the in-plane Debye temperature might be expected to have an inverse relationship to the mean coherence length, L_a. As shown in Figure 4.2, such a relationship was observed, having the form

$$\theta_D = \alpha + \frac{\beta}{L_a}. \qquad (4.1)$$

The constant α was found to be near 2350K, so that infinite crystal size would result in a Debye temperature of 2350K, the ideal value for graphite. The constant β was found to be near 1.3×10^5 Å·K, but its physical meaning is unclear.

Next, the relationship of specific heat capacity to lattice-dependent physical properties was investigated. Fiber thermal conductivity could be estimated by adding its phonon and electronic contributions as described in Appendix A.2. At low temperatures, the thermal conductivity is proportional to the specific heat capacity, and the phonon mean-free-path is roughly equal to the coherence length. The phonon concentration increases monotonically with temperature, causing the mean-free-path to decrease. At some temperature, this effect becomes dominant and the thermal conductivity begins to decrease with temperature. The inclusion of Umklapp and boundary phonon scattering mechanisms gave a very good estimate of the room temperature thermal conductivities for the commercial fibers. Figure 4.3 shows the comparison between estimated and reported (142) values at room temperature. Estimates of their Young's moduli, based on the derivation presented in Appendix A.3, were also quite accurate, as Figure 4.4 shows.

In addition, two commercially available fibers produced by Du Pont from a solvent-extracted mesophase pitch were also considered. They were the E-35 (35 Msi tensile modulus) and the E-35C (same modulus, higher thermal conductivity) grades. The former exhibits the radial-folded texture, while the latter exhibits a more radial texture (33). A large difference was observed in their calculated Debye temperatures, which were 4868 and
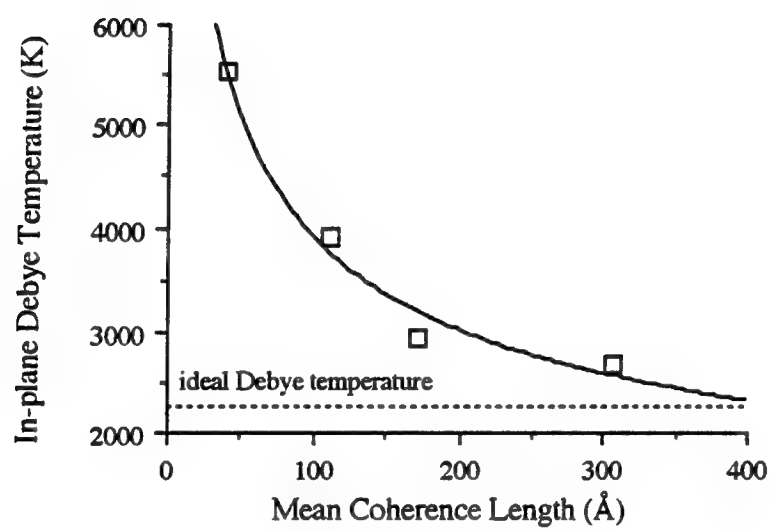
Figure 4.2. Relationship of in-plane Debye temperature and mean coherence length.
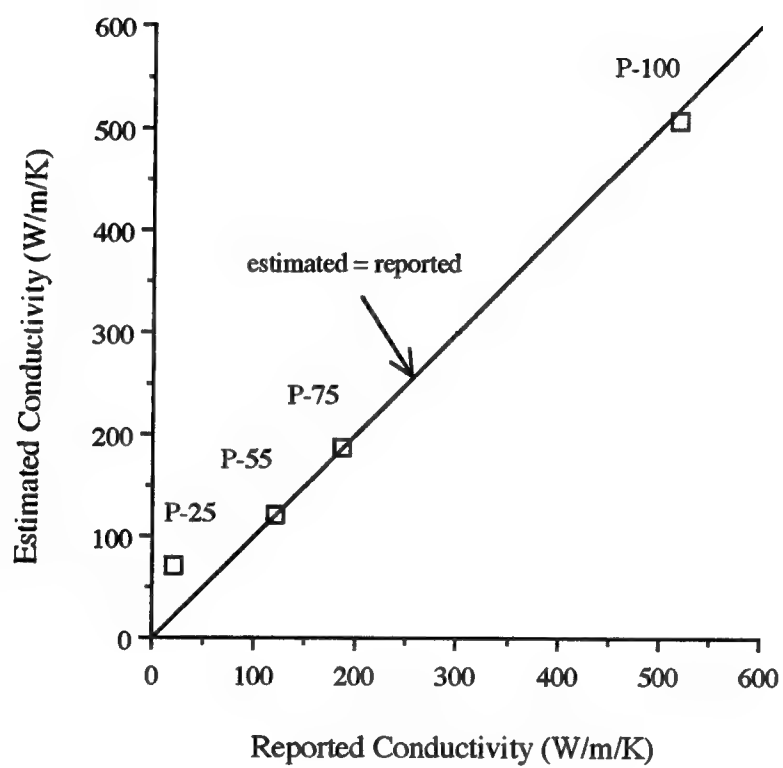
Figure 4.3. Comparison between estimated and reported thermal conductivity values.
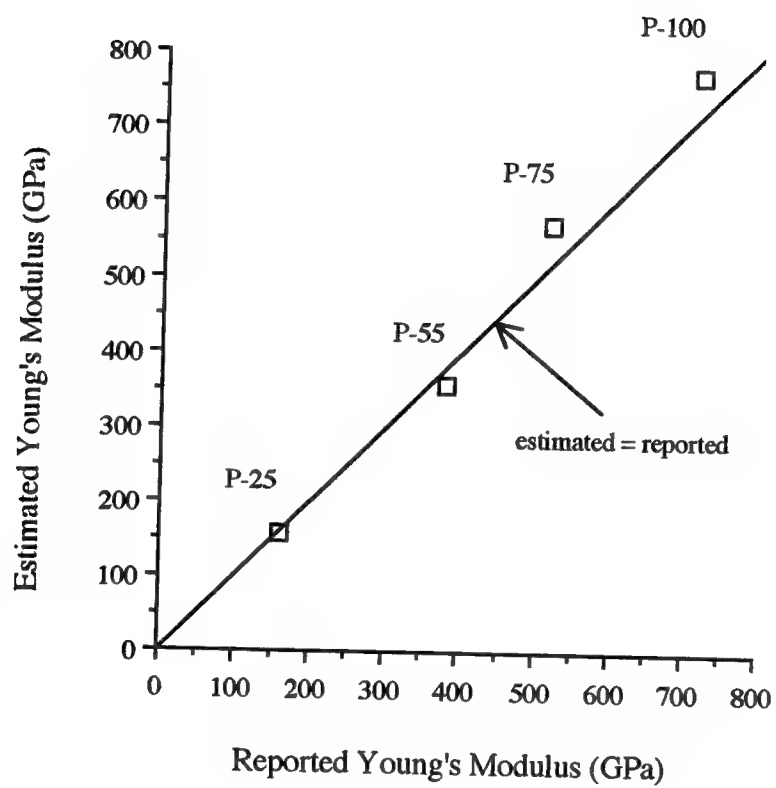
Figure 4.4. Comparison between estimated and reported Young's modulus values.

3948K, respectively. When the differences in reported coherence length and mass density between the two fibers (144) was included, the model estimated both their thermal conductivity and Young's modulus. Table 4.2 shows the estimated and reported values.

Table 4.2. Estimated and reported thermal conductivity and Young's modulus for Du Pont fibers.

Property	E-35	E-35C
Thermal conductivity (W/m/K)		
Estimated value	53	288
Reported value[1]	30	250-300
Young's modulus (GPa)		
Estimated value	233	353
Reported value[1]	245	247

[1] Du Pont Fiber-G product data sheets (146)

The ability of such a simple measurement and calculation technique to estimate accurately the lattice-dependent physical properties of a fiber make it useful as a process control tool. Its application to the study and design of the graphitization treatment will be illustrated throughout this chapter.

The first application of this technique to fibers produced for this study was the choice of a circular and a ribbon-shape fiber set of equivalent structural quality for use in the graphitization experiments. Two circular-shaped and two ribbon-shape thermolyzed fiber sets produced from the heat-soaked mesophase pitch were selected. Labelled C1 and C2, and R1 and R2, respectively, their raw DSC heat flow data between 20 and 450°C are shown in Figure 4.5. The two circular-shaped fiber sets were made using nearly equivalent melt-spinning and stabilization conditions. As a result, their heat flow curves were almost superimposed. The ribbon-shape fibers, however, had been subjected to
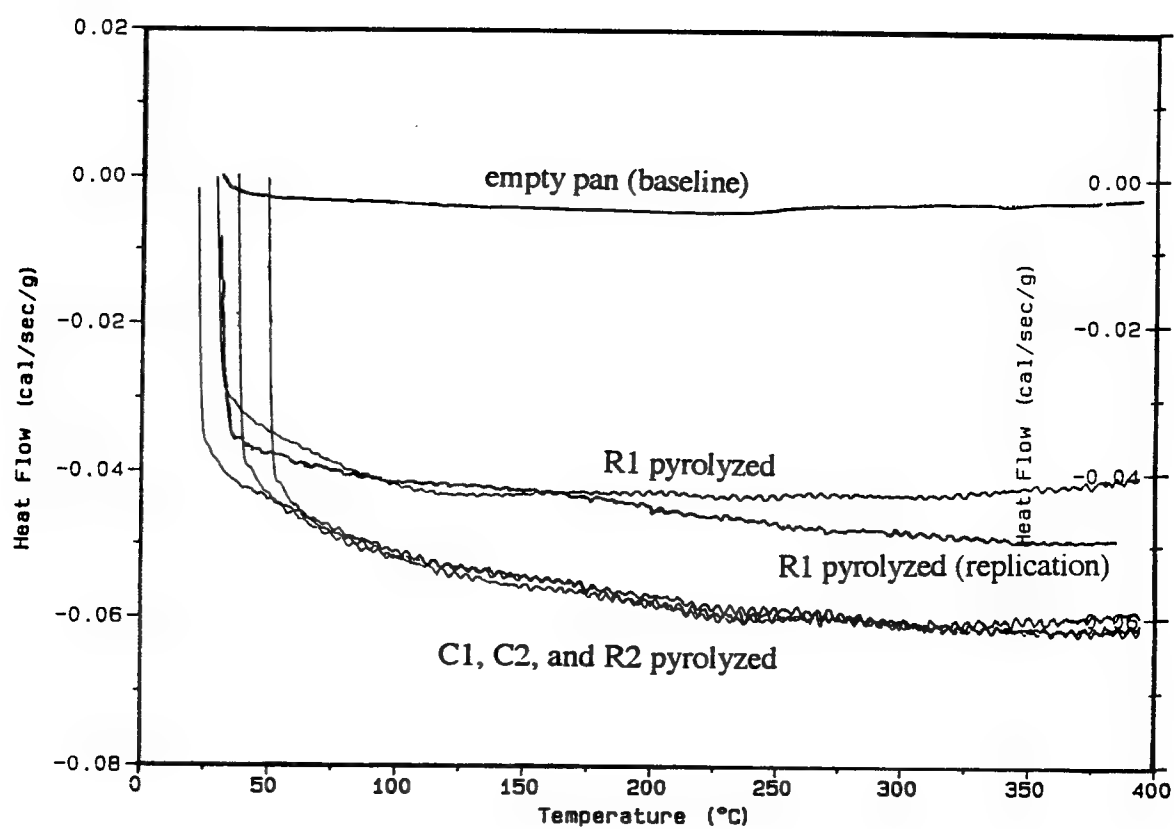
Figure 4.5. DSC heat flow curves for thermolyzed heat-soaked pitch fiber sets.

different drawdown ratios during melt-spinning and had achieved different oxygen contents during stabilization. Fiber R1 had been melt spun using a reduced winder speed and, as a result, was larger in width. It also had reached a higher oxygen content during stabilization. These two factors combined to produce a thermolyzed fiber having a reduced DSC heat flow, or specific heat capacity. Table 4.3 presents the melt-spinning and stabilization conditions, post-thermolysis composition, and the calculated in-plane Debye temperatures of fiber sets R1 and R2.

Table 4.3. Melt-spinning, stabilization, and thermolysis data for fiber sets R1 and R2.

Process variable	Fiber R1	Fiber R2
Melt-spinning temperature (°C)	339	339
Pressure (GPa)	0.91	0.99
Mass flow rate (kg/sec)	3.74×10^{-5}	5.83×10^{-5}
Winder speed (m/s)	4.318	5.67
Stabilization temperature (°C)	280	280
Time-at-temperature (minutes)	300	300
Oxygen pickup (mass %)	9.5-10.0	9.0-9.5

As the in-plane Debye temperatures were calculated after converting the data to a per-mole-of-carbon basis, and significant compositional differences did exist between thermolyzed batches R1 and R2, both chemical and structural factors may have been responsible for the differences between in-plane Debye temperatures. After treatment to higher temperatures, the assumption that the fiber is essentially 100% carbon is more accurate, and a difference in in-plane Debye temperatures can be attributed more readily to differences in crystal structure. Under those conditions, the lattice-dependent physical properties of fibers produced for this study can be estimated just as those of the commercial carbon fibers. For example, when circular fiber C2 was carbonized to 2400°C and held at that temperature for 15 minutes, it gave a calculated in-plane Debye temperature of 3964K

and an X-ray density of around 2.20 g/cm^3. Using these values, the model estimates the fiber's Young's modulus to be 465 GPa. The mean value from single filament testing was 444 GPa.

Based on their similar in-plane Debye temperatures, fiber sets C2 (circular) and R2 (ribbon) were chosen for the graphitization experiments. Their structural equivalence was supported by wide angle X-ray diffraction, as shown in Table 4.4. Use of calculated Debye temperatures in the study of the graphitization treatment will be described in sections four and five of this chapter.

Table 4.4. Debye temperatures and wide angle X-ray diffraction data illustrating equivalent initial conditions for the graphitization experiments.

Fiber set	θ_D (K)	d(0002) (Å)	L_c (Å)	L_a (Å)	Z (°)
R2	7961	3.462±0.004	15±3	37±3	39.1±6.0
C2	8031	3.450±0.004	15±3	37±3	40.0±6.0

(* confidence intervals based upon replications, using similarly treated samples)

4.2. Stabilization

Stabilization is the process by which a fiber is rendered infusible so that it may undergo the high temperature treatments necessary to produce high strength, modulus and thermal conductivity. It involves the removal of peripheral groups from the aromatic molecules, and the insertion of bridging groups containing oxygen. Therefore, a substantial change in mass, as well as a change in the proportion of elements present and in crystal structure, occur during stabilization. In order to describe these changes, this section will be divided into several sub-sections.

4.2.1. Differential Scanning Calorimetry

When mesophase pitch is heated in air, several processes occur. Those that consume or liberate heat can be observed using differential scanning calorimetry (DSC). A single fiber set that had been melt spun from the heat-soaked pitch was ground into a fine powder and subjected to a variety of stabilization conditions. This was done to insure uniformity of oxygen concentration throughout the sample. The oxygen content of powder from each treatment was determined, and the remaining material was studied using the DSC. In addition, AR pitch and samples of the same pitch that had been melt-spun under nitrogen, argon, and helium purges were studied to evaluate the effect of melt-spinning atmosphere. Figure 4.6 shows a typical DSC heat flow curve after background subtraction and specific heat capacity correction. At least three highly-convoluted exothermic events seem to occur. The first begins around 175°C, where the heat flow deviates from zero. The second begins around 200-240°C, and the third around 280-320°C. These reaction onset temperatures correspond, at least qualitatively, to changes in the rate of mass gain observed using dynamic TGA.

By the method presented in Chapter 3.2.1, the location of the reaction onset and the heat of reaction were determined for several as-spun and partially stabilized samples. These data are presented in Table 4.5, with the oxygen contents of the samples. There seemed to be an irreversible process that occurred around 175 to 180°C. As-spun pitch, or material that had not been heated to temperatures greater than 175°C underwent three exothermic processes. On the other hand, material that had been treated at higher temperatures underwent only the third, or high temperature, process. All three processes appeared to be first-order, displaying low activation energies (below 35 kcal/mole). This simple analysis indicated that three processes occur during stabilization and that the first irreversible process begins around 175°C.
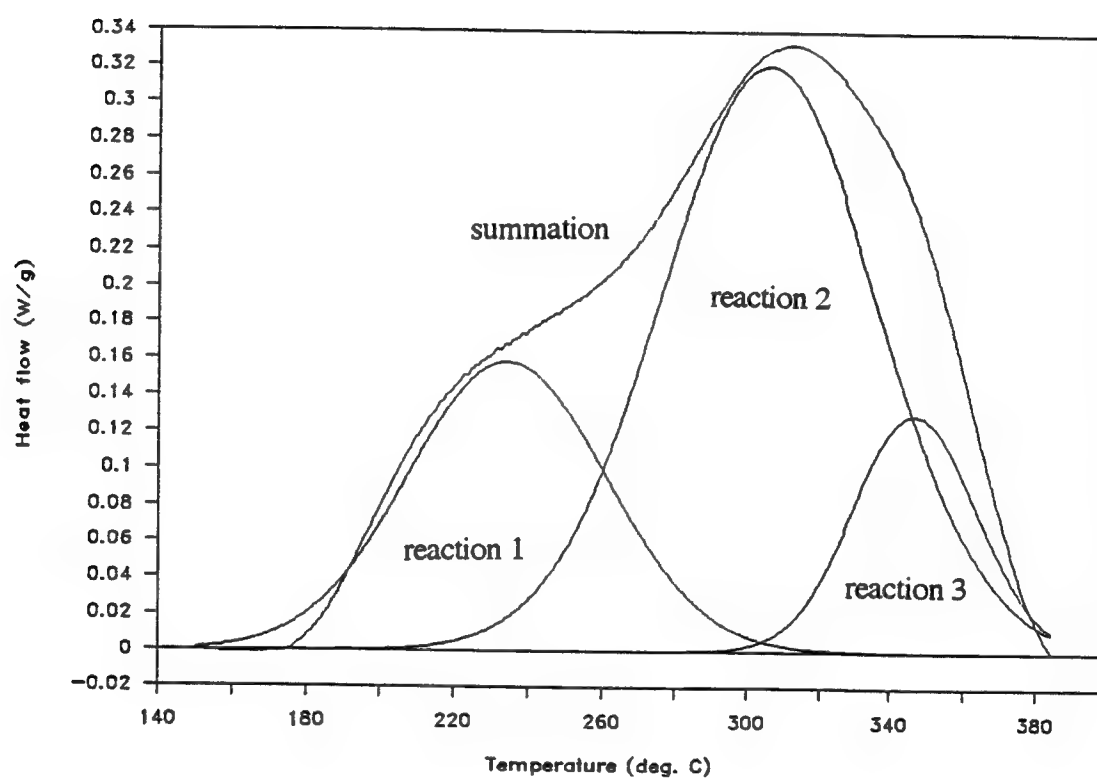
Figure 4.6. Typical DSC heat flow curve for a heat-soaked pitch sample heated in air.

Table 4.5. DSC reaction data for as-spun and partially stabilized fiber sets.

Sample	Oxygen content (mass %)	Reaction number	Reaction onset temperature (°C)	Heat of reaction (kJ/g)
as-received pitch	0.00	1	188	25.0
		2	218	61.0
		3	279	12.7
nitrogen-spun	0.00	1	181	36.6
		2	215	70.9
		3	278	16.1
argon-spun	0.00	1	181	74.8
		2	222	168.0
		3	275	38.9
helium-spun	0.00	1	178	52.0
		2	231	198.0
		3	291	93.5
175°C stabilized	1.10	1	160+	14.0
		2	226	243.0
		3	?	low (?)
179°C stabilized	2.56	3	274	960.0
230°C stabilized	5.11	3	307	1240.0
240°C stabilized	4.47	3	300+	1219.0
350°C stabilized	12.13	3	372	772.0
AR pitch	0.00	1	171	-54.8
		2	216	478.0
		3	366	212.0

4.2.2. Thermogravimetric Analysis

A parallel thermogravimetric study was conducted to evaluate mass gain occurring prior to the first reaction as well as the impact of these reactions upon mass gain. Figure 4.7 shows the mass gain of a heat-soaked pitch powder with time at two temperatures below 175°C (220). Heating this material to the same temperature under a vacuum or an inert gas would result in a mass loss if this mass gain were reversible. Snipes has shown that this does occur with time below 175°C, though not to completion (221). Thus, it is believed that low temperature mass gain is a reversible process, possibly occurring by physical absorption of oxygen or moisture (122), and the fact that no thermal event is observed with the DSC indicated that no chemical bond creation or rupture was involved.
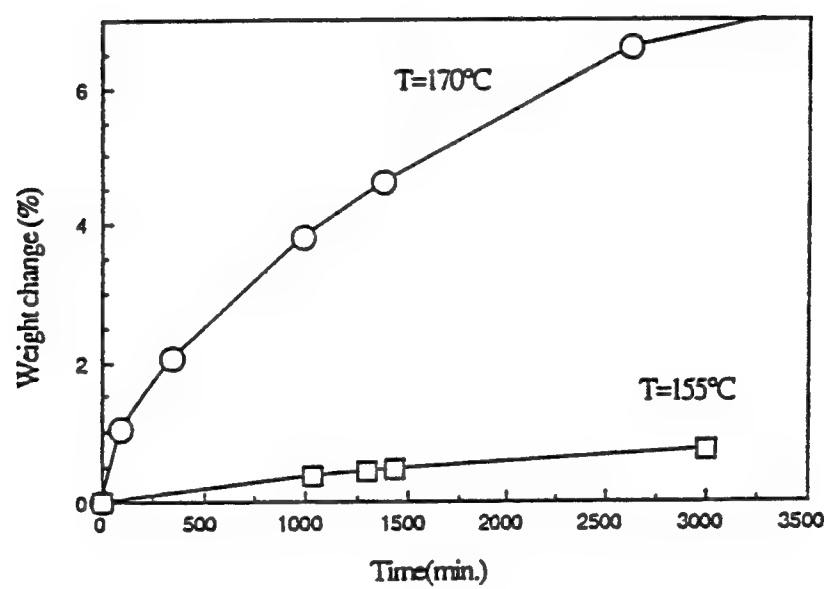
Figure 4.7. Mass gain of heat-soaked pitch at temperatures below 175°C (220).

Such a process was diffusion-limited and mass gain roughly follows a $t^{1/2}$ dependence on time at a given temperature.

When the pitch was heated to higher temperatures, however, irreversible reactions incorporated oxygen into the carbonaceous structure. Their relationship to the events observed by thermal analysis can be seen from Figure 4.8. Below 175°C, there was an almost monotonic mass gain with temperature, but at 175°C, the slope increased with the apparent onset of the first stabilization process. Again around 220°C, the slope of the mass gain versus temperature curve increased with the onset of the second stabilization process, giving a maximum rate of mass gain with temperature and time that occurs just below 250°C. With the initiation of the third process at around 280°C, the mass gain curve reached a plateau, indicating that the rate of mass gain equalled the rate of mass loss. Increasing the temperature significantly beyond 280°C resulted in a decrease in sample mass. Thus, the third process appeared to consist of destructive oxidation of the pitch to produce CO and/or CO_2 gas by the reactions

$$C(s) + \frac{1}{2}O_2(g) \rightarrow CO(g) \text{ and} \tag{4.1}$$

$$C(s) + O_2(g) \rightarrow CO_2(g). \tag{4.2}$$

The thermogravimetric study indicated that mass gain does occur below 175°C, but not by the creation or rupture of chemical bonds. It also showed that the distinct thermal events observed by differential scanning calorimetry translated into regions of different mass gain rate in the TGA curve. Finally, thermogravimetric analysis showed that the third stabilization process was actually the undesirable degradation of the pitch.

4.2.3. Elemental Analysis

The accompanying changes in chemical composition during stabilization were monitored using elemental analysis. One petroleum-based and one AR pitch sample were heated at 1°C per minute in a convection oven. At four temperatures, a sample was removed from the furnace and analyzed. The temperatures were chosen to correspond with
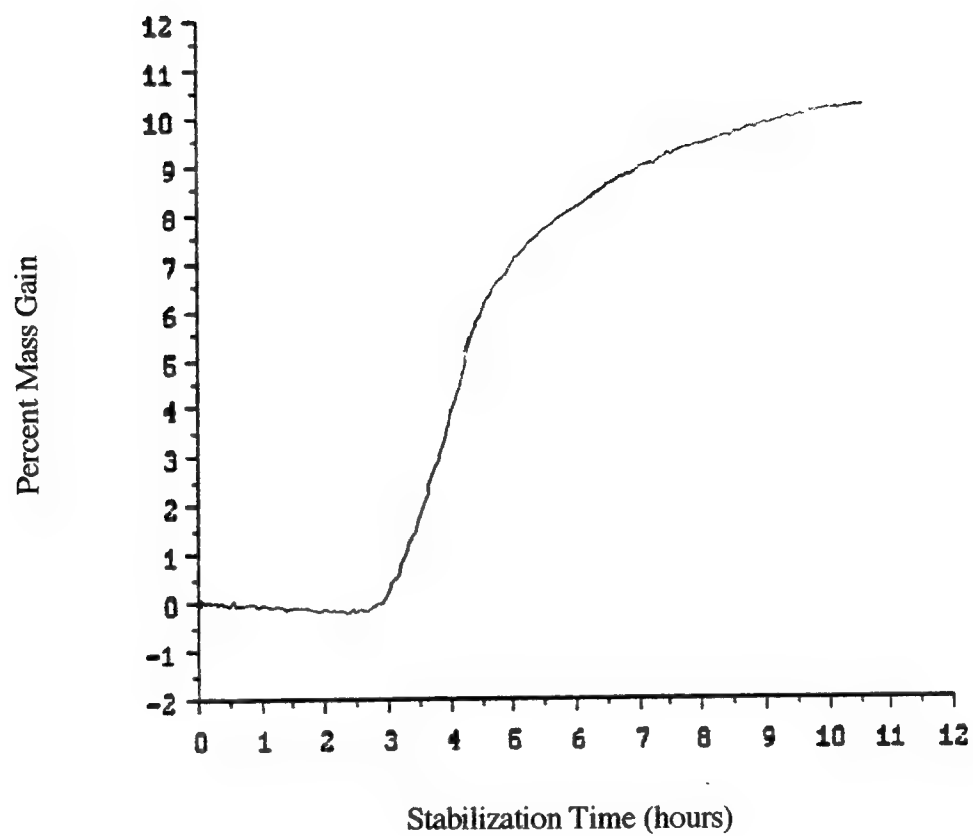
Figure 4.8. Typical TGA curve during stabilization of heat-soaked pitch fibers.

the locations of stabilization processes found in the DSC experiments. The first sample was taken at 160°C, just below the onset of the first irreversible process. A second sample was taken at 190°C to include the effects of only the first process. A third was taken at 250°C, well within the second process but before the onset of the third process. The final sample was taken during the degradation process at 310°C.

Raw data, in the form of the mass percentages reported by Galbraith Laboratories, were converted to atom percentages, and, ignoring sulfur, are given in Table 4.6 for both the heat-soaked and AR pitches. HS-OX and AR-OX denote oxygen stabilization of the heat-soaked and AR pitches, respectively. The following number indicates the maximum stabilization temperature.

Table 4.6. Atom percentages of C, H, and O present in partially-stabilized fibers.

Sample	Stabilization temperature (°C)	C (%)	H (%)	O (%)
heat-soaked pitch:				
as-spun	-	65.2	34.8	0.0
HS-OX160	160	66.3	33.1	0.5
HS-OX190	190	65.4	34.1	0.5
HS-OX250	250	65.2	33.4	1.4
HS-OX310	310	68.6	25.8	5.6
AR pitch:				
as-spun	-	63.3	36.7	0.0
AR-OX160	160	62.8	35.8	1.5
AR-OX190	190	62.6	36.0	1.5
AR-OX250	250	63.6	32.6	3.8
AR-OX310	310	68.1	21.8	10.0

(* the mass percentages from which these data are calculated have relative errors of 0.26 % for C, 1.93 % for H, and 0.75 % for O (202))

As the sulfur content is almost constant at 1.8 mass percent over this range of temperatures for the petroleum-based fibers, the only chemical changes involved carbon, hydrogen, and oxygen. An excellent way of depicting these changes is through a

van Krevelen diagram, in which the atomic H/C ratio is plotted against the atomic O/C ratio as described in Appendix A.6 (222). Figure 4.9 shows such a diagram for the stabilization of heat-soaked and AR pitch. While the curves are offset from one another (the AR pitch has a higher H/C ratio initially), stabilization did produce a similar change in chemical makeup. When compared with the master van Krevelen diagram shown in Appendix A.6, the stabilization processes can be viewed as the successive incorporation of oxygen with little change in hydrogen content, followed by dehydrogenation together with oxidation, and finally degradation, or the removal of both carbon and oxygen.

Because hydrogen was lost during stabilization, especially at temperatures above 240°C, the observed mass gain was not equal to the oxygen uptake (122). This fact can be seen in Figure 4.10, where the measured mass gain of a fiber sample is presented with the reported oxygen content. The two data sets deviated near 240°C, and the difference between the two was nearly 100% for stabilization temperatures above 280°C.

Even for fiber sets stabilized for different times at the same temperature, differences in mass gain did not always relate simply to oxygen content. This was especially true near the onset of the degradation process around 280°C. For example, production of gases such as CO kept the O/C ratio nearly constant while the mass of the fiber decreased. Table 4.7 presents the observed mass gains and oxygen mass contents for three heat-soaked pitch fiber sets stabilized at 280°C.

Table 4.7. Comparison of mass gain and oxygen mass content for heat-soaked pitch fibers stabilized at 280°C.

Sample	Mass gain (mass %)	Oxygen content (mass %)
HS280a	6.5	10.4
HS280b	9.0	13.8
HS280c	10.0	15.5
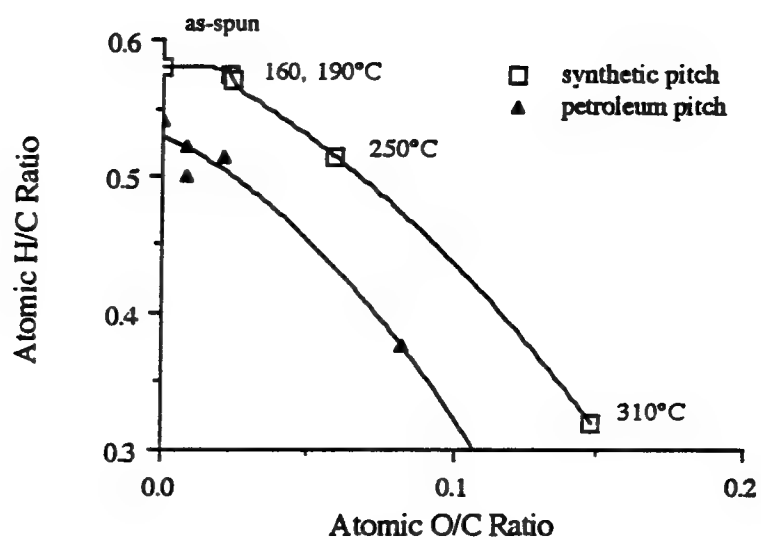
Figure 4.9. Plot of atomic H/C and O/C ratios for partially stabilized fibers.
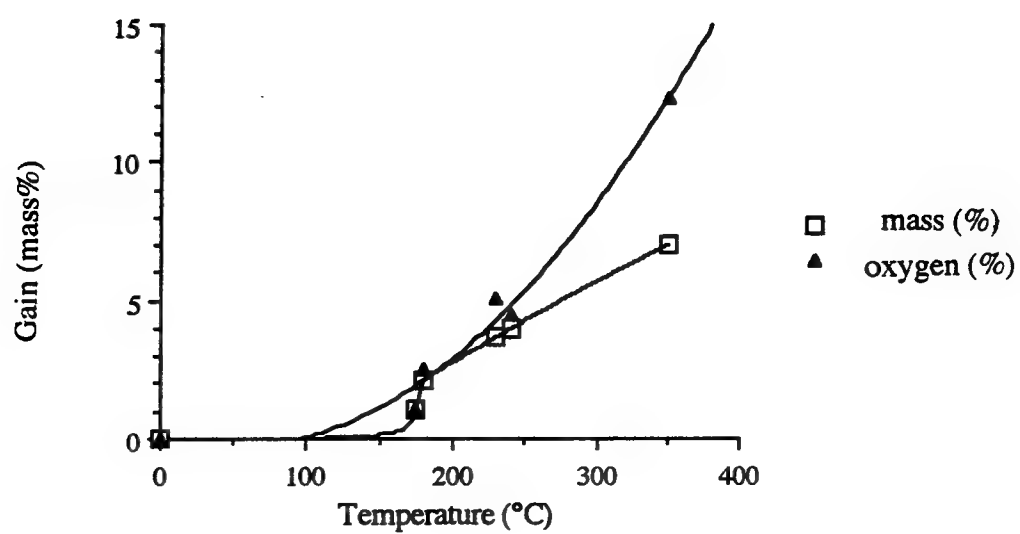
Figure 4.10. Mass gain and oxygen content of heat-soaked pitch through the stabilization process (122).

A final aspect that must be considered is how to define proper stabilization for a given fiber. Because the subsequent thermal treatments homogenize the fiber by removing non-carbon members, there was significant mass loss. Therefore, the stabilization treatment was designed to give minimum mass loss during thermolysis, based on the assumption that reduced thermolysis mass loss will cause fewer defects. The stabilized HS-OX and AR-OX fibers discussed above were heated at 5°C per minute to 1000°C under flowing argon. Their masses were recorded continuously and the results of these experiments will be discussed in the section on thermolysis, but here only the total mass loss during carbonization will be considered. Several additional heat-soaked pitch fiber sets were studied. These sets had been subjected to lengthy soaks at maximum temperature or below 175°C to give a variety of stabilization extents. Their stabilization conditions and initial chemical composition are presented in Table 4.8.

Table 4.8. Stabilization and composition (excluding sulfur) of additional heat-soaked pitch fibers.

Sample	Stabilization temperature (°C)	C (atom %)	H (atom %)	O (atom %)
HS175	175	65.1	34.3	0.6
HS179	179	64.8	33.9	1.3
HS230	230	65.1	32.1	2.7
HS240	240	65.9	31.7	2.4
HS350	350	65.6	27.2	7.2

(* the mass percentages from which these data are calculated have relative errors of 0.26 % for C, 1.93 % for H, and 0.75 % for O (202))

The TGA curves for each sample are presented in Appendix C.1, while their carbonization losses are shown in Table 4.9. Also given in the table is a parameter defined by Morita et al. (223) as the degree of stabilization, D. It is determined from the chemical composition of the stabilized pitch by the following expression:

$$D = \frac{\left(\dfrac{O \text{ mass } \%}{O \text{ atomic mass}}\right)}{\left(\dfrac{C \text{ mass } \%}{C \text{ atomic mass}}\right)} \cdot 3 \cdot 100\%. \tag{4.3}$$

Table 4.9. Carbonization mass loss of fibers from different stabilization treatments.

Sample	Degree of stabilization, D	Carbonization loss (%)
heat-soaked pitch:		
as-spun	0.00	16.0
HS-OX160	2.44	16.2
HS-OX190	2.45	12.6
HS175	2.66	13.5
HS179	6.25	8.7
HS-OX250	6.42	11.3
HS240	11.13	16.9
HS230	12.54	13.0
HS-OX310	24.59	19.7
HS280a	≈26*	17.0
HS350	33.05	21.1
HS280b	≈36*	20.1
HS280c	≈40*	41.6
AR pitch:		
AR-OX160	6.98	20.6
AR-OX190	7.12	20.4
AR-OX250	17.93	17.7
AR-OX310	44.44	31.1

* less material was available for analysis, so only the oxygen content could be measured accurately.

From Table 4.9, it is clear that an optimum degree of stabilization does exist that provided a minimum mass loss during carbonization. It appeared that a degree of stabilization, D, of around 6.2 to 6.4 was optimal for the heat-soaked pitch, while a value between 7 and 17 was optimal for the AR pitch. Also, stabilization was not dependent only upon the oxygen uptake, but rather upon the relative proportion of carbon, hydrogen, and oxygen in the fiber. In the case of the heat-soak pitch, minimized carbonization loss can be achieved by diffusing oxygen into the fiber at temperatures just below 175°C (to increase the diffusivity of oxygen without initiating the first stabilization process), followed by

quickly reacting this oxygen with the carbon host structure at temperatures just above 175°C. As an example, sample HS179 was rendered infusible by such a treatment, and yet only lost 8.7 percent of its mass during carbonization to 1000°C. A possible explanation for this behavior, concerning the efficiency of oxygen as a stabilizing agent, will be discussed in the next section.

Much less work was completed on the AR pitch, but it seems the same arguments would hold true. The major difference between the two pitches were their initial H/C ratios and molecular weights. The H/C ratio of the petroleum pitch was around 0.54, compared to around 0.58 for the AR pitch. An indication of their molecular weights and conformations can be found in the melt-spinning temperatures employed. Typically, this temperature is chosen to provide an adequate melt-spinning viscosity. For fibers produced at shear rates of greater than 1000 s^{-1}, the viscosity is around 24 Pa·s. Fleurot showed that the temperatures necessary to produce this viscosity in the AR and the petroleum-based pitches were 317 and 339°C, respectively (194). This seems to indicate that the AR pitch has a lower molecular weight or is more flexible. As a result, stabilization of the AR pitch required a greater quantity of oxygen, but the rate of reaction with oxygen was much greater and stabilization occurred more quickly.

4.2.4. Infrared Spectroscopy

In addition to the chemical composition of the fiber, the functionality of oxygen in the carbon structure is important, as oxygen has the potential to assume a variety of positions. Ignoring some of the more complicated possibilities, oxygen may link neighboring aromatic molecules by predominantly ester or ether bonding, or simply "dangle" from the molecule periphery in the from of OH, =O, or COOH groups. The latter possibilities may be labelled inefficient oxygens, as they perform no real function, other than slight viscosity increase, in stabilization. However, they must be removed during carbonization and often remove carbon atoms with them. The infrared spectra of selected fiber sets from the AR-

OX and HS-OX series are presented in Figures 4.11 and 4.12. They show the spectra observed for the 160, 250, and 310°C treatments for each mesophase. A brief table of characteristic IR wavenumbers for C-H-O systems is presented in Appendix A.8 for comparison.

The key difference between the three different stabilization temperatures was the relative proportion of ether and ester linkages between aromatic molecules. This can be observed by the intensity of the 1150-1250 cm^{-1} absorption, corresponding to $C_{aromatic}$-O-$C_{aromatic}$ stretching. As proposed by Otani (47), this bond mechanism is present at low temperatures (below 240°C), but gives way to carbonyl (C=O) and -OH groups at higher temperatures. This can be observed as an increase in the intensity of the 1700-1840 cm^{-1} absorption for the higher temperature samples. During the same period, the alkyl C-H stretching and deformation modes, located at 2945 and 1450 cm^{-1}, respectively, lost their intensity. The destruction of these alkyl side groups created active sites for stabilization, and resulted in the substantial hydrogen loss.

4.2.5 Crystallographic Aspects of Stabilization

The impact of stabilization does not end at the changes to chemistry and fusibility to the pitch. There is the possibility of changes to the crystal structure and, more importantly, the potential for developing a high-quality graphite structure. In this section, the effect of soak time and thermal history on the stabilized fiber is evaluated for petroleum-based fibers stabilized at 280°C. Then, the same fiber sets were graphitized to 2400°C and re-evaluated.

Table 4.10 shows the (0002) spacing, non-uniform strain in the [0002] direction, and the stack height, L_c, for heat-soaked pitch fibers stabilized at 280°C. Once again, there appeared to be an optimum stabilization treatment with regard to crystal structure. After 60 minutes, the fibers displayed a reduced (0002) spacing and a residual compressive strain in the [0002] direction. The accompanying decrease in stack height with increased stabilization may be the result of crystallite fracture at high oxygen contents. Unfortunately, oxygen content data could not be obtained for these fiber sets.
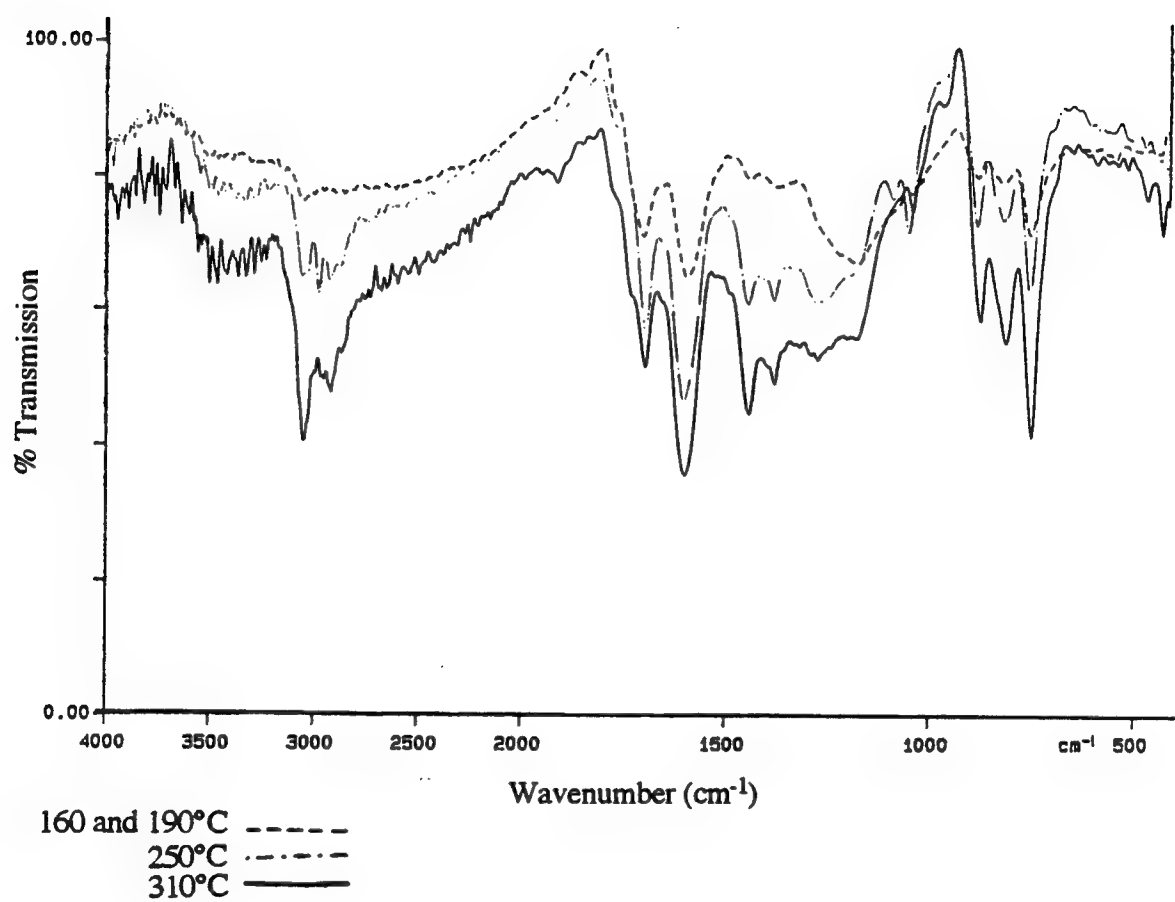
Figure 4.11. IR spectra of HS-OX series.
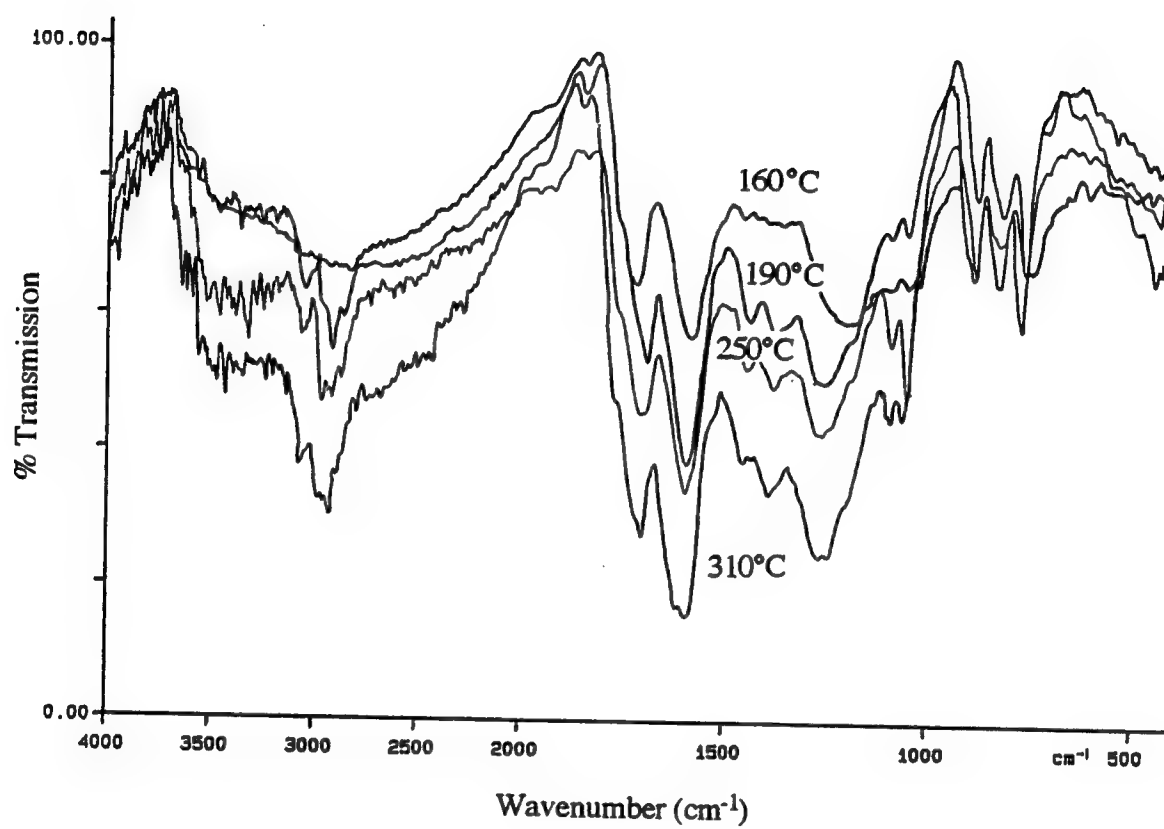
Figure 4.12. IR spectra of AR-OX series.

Table 4.10. Crystallographic data for heat-soaked pitch fibers stabilized at 280°C.

Stabilization conditions	d(0002) (Å)	[0002] strain $\Delta d/d$ (T/C*)	L_c (Å)
30 min. at 280°C	3.485	0.082(T)	55
60 min. at 280°C	3.473	0.059(C)	35
120 min. at 280°C	3.481	0.038(T)	30
240 min. at 280°C	3.485	0.023(T)	23

(* T indicates tensile; C indicates compressive)

The most important question, however, is does stabilization affect the development of a graphite-like crystal structure during high temperature treatment. As will be shown in the section on thermolysis, oxygen essentially disappears around 1000°C. Therefore, it can have no chemical effect, as do hydrogen and sulfur. But the structural changes that occur during stabilization may enhance or inhibit graphitization. Figure 4.13 shows the (0002) spacings for the graphitized fiber sets with the bars representing a ±0.004 Å error in the measurement. There is an obvious minimum at the 60 minute stabilization, and the data are similar in trend to those of the as-stabilized fiber sets.

The non-uniform [0002] strains and the fibers' cross-sectional areas, presented in Figure 4.14, and the stack heights, presented in Figure 4.15, show the same effect as observed in the stabilized fibers.

In the case of interplanar spacing, non-uniform strain, and fiber cross-sectional area, the plot exhibits a minimum, or maximum, at the 60 minute treatment. This might indicate that those properties are more dependent upon the crosslinked density profile through the fiber than upon oxygen content. This might be true if a "skin-core" structure is developed that, in turn, influences thermal stresses during high temperature treatment. The stack height, on the other hand, appears to decrease continually with stabilization extent.
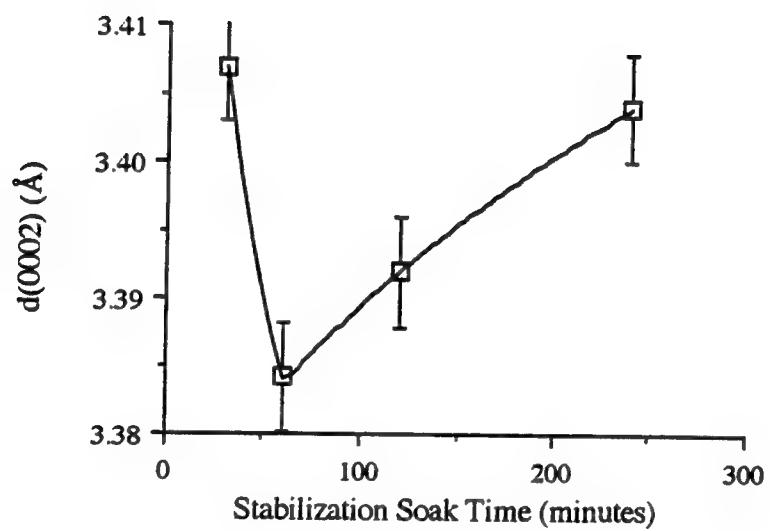
Figure 4.13. d(0002) spacings for graphitized heat-soaked pitch fibers from several stabilization treatments.
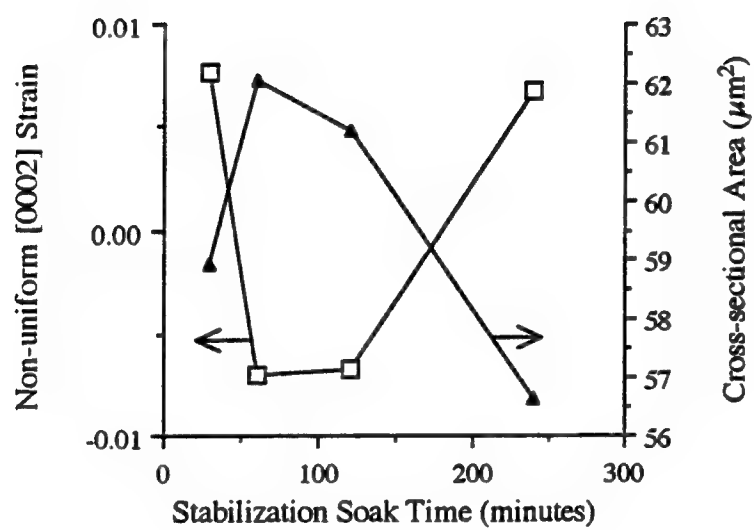
Figure 4.14. Non-uniform [0002] strain and cross-sectional area of graphitized heat-soaked pitch fibers.
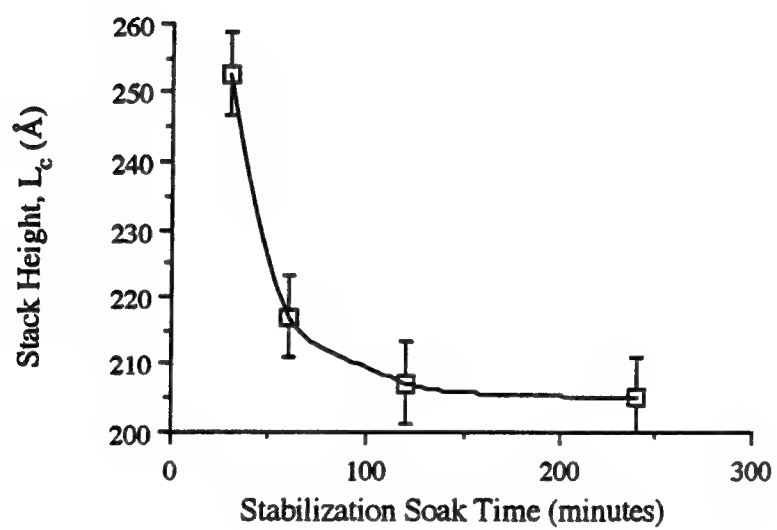
Figure 4.15. Stack heights of graphitized heat-soaked pitch fibers from several stabilization treatments.

4.2.6. Stabilization and Physical Properties

The true test of the effect of stabilization upon fiber processing, however, is the resulting fiber physical properties. Using a similar set of circular-shaped heat-soaked pitch fibers, G. Z. Liu, a co-worker, considered a series of soak times at 280°C (76). These fibers were subsequently carbonized to 2400°C at a heating rate of 20°C per minute. Based upon the measured tensile properties, presented in Table 4.11, there existed an "optimum" stabilization time at around 60 minutes. Using the same technique but with smaller time increments, Liu found the "optimum" stabilization time for the AR pitch to be 20 minutes at 270°C.

Table 4.11. Tensile properties of graphitized fibers from several stabilization soak times (76).

Soak time (minutes)	Tensile Strength (GPa)	Young's modulus (GPa)
20	1.301±0.377	185±44
60	1.950±0.579	236±47
120	1.857±0.479	225±54
300	1.166±0.419	204±63

(± indicates a 95 % confidence interval on the reported values)

When these data are compared with the calculated [0002] non-uniform strain data presented in the preceding section, it is clear that a relationship exists between stabilization, [0002] strain, and tensile properties. Fibers possessing a radial texture have the (0002) planes arranged radially so that their normal vectors point circumferentially. Therefore, a residual tensile strain in the [0002] direction might aid in the separation of neighboring (0002) planes upon the application of a load and result in reduced tensile strength. Conversely, however, decreased coupling of adjacent planes may reduce flaw sensitivity, so the actual effect may be more complicated.

4.3. Thermolysis

Thermolysis, or carbonization, is simply the removal of non-carbon members of the fiber structure. Therefore, there is a strong relationship between thermolysis and the preceding stabilization process. Also, thermolysis contributes to the potential for high temperature structural development in the fiber. The chemical and structural changes that occur were examined by dynamic thermogravimetric analysis, elemental analysis, and both wide and small angle X-ray diffraction.

4.3.1. Thermogravimetric Analysis

TGA data for the heat-soaked pitch samples were analyzed with the combined reaction/transport model presented in Appendix A.4. From the appearance of typical thermolysis TGA curves under flowing argon, presented in Appendix C.1, there seemed to be at least two gross processes occurring. The first takes place just above 100°C and results in a mass loss of <5 %. The second, resulting in the majority of mass loss, begins around 400°C and continues to near 1000°C. Only the magnitude of the first mass loss, which appears to be desorption, depends upon the oxygen content, while the magnitude, slope, and onset temperature of the second process is influenced by stabilization extent. Table 4.12 shows the desorption mass loss for heat-soaked pitch samples that exhibited a measurable desorption.

Table 4.12. Oxygen content and desorption mass loss for selected fiber sets.

Sample	Oxygen content (mass %)*	Desorption loss (mass %)
HS, as-spun	0.00	0.00
HS175	1.10	0.72
HS179	2.56	1.02
HS280a	10.40	1.68
HS280b	13.80	2.64
HS280c	15.50	>3.00

(* these data have relative errors of 0.26 % for C, 1.93 % for H, and 0.75 % for O (202))

The two process model described fiber thermolysis quite well, as shown in Figure 4.16. From this fit, the kinetics of desorption and decomposition could be modelled. Table 4.13 shows the pre-exponential terms and activation energies determined from a combined analysis of the TGA profiles presented in Appendix C.1, where each reaction has the form

$$k_d \text{ or } k_p \text{ (sec}^{-1}) = k_o \cdot \exp(-\Delta E/RT), \tag{4.1}$$

where k_d is the desorption rate constant and k_p is the thermolysis rate constant. The mass transfer coefficient, k_{mass}, describing the rate of mass transfer out of the fiber bundle, was assumed to vary with temperature as $T^{1.8}$ (199).

Table 4.13. Rate parameters for desorption, thermolysis, and mass transfer determined for several fiber sets.

Constant	Description	Value
k_{do}	temperature-independent desorption rate	8.2×10^{28} sec^{-1}
E_d	activation energy for desorption	80.71 kcal/mole
k_{po}	temperature-independent thermolysis rate	7.548×10^{-4} sec^{-1}
E_p	activation energy for thermolysis	1.913 kcal/mole
$k_{mass, o}$	slope of k_{mass} relationship to $T^{1.8}$	1.444×10^{-14} m/s/K$^{1.8}$

It was assumed that diffusion within the fiber was very rapid, and that the rate at which volatile species reached the fiber surface was limited by their rate of production. The effective mass loss rate, however, was limited by the transport of volatiles though the fiber bundle. However, the calculated activation energy gave some information about the nature of the so-called desorption reaction. The large value (around 81 kcal/mole) observed for the first reaction indicates that this is not a simple physical desorption process, but rather involves the breaking of bonds, perhaps C-O, which has a bond energy of around 83 kcal/mole.
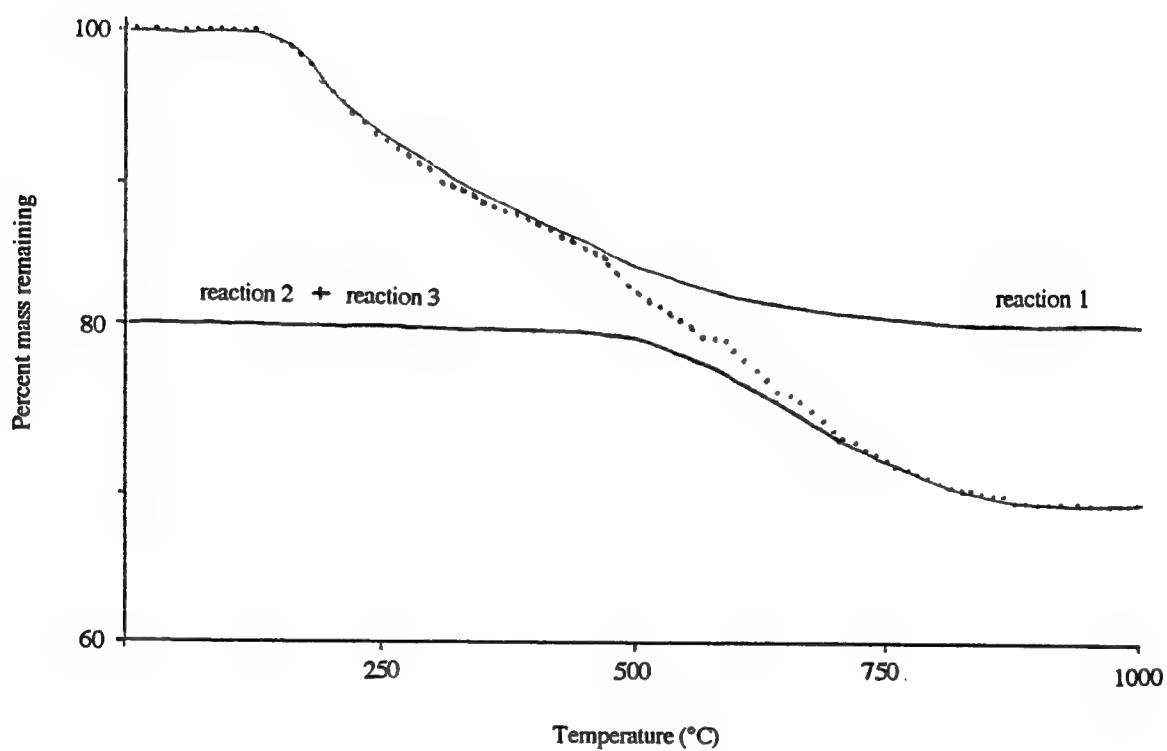
Figure 4.16. Thermolysis model applied to sample HS280a.

4.3.2. Elemental Analysis

The chemical changes occurring during thermolysis at and below 1000°C were monitored by removing samples from the furnace at several temperatures and subjecting them to elemental analysis for C, H, S, and O. Both the heat-soaked and AR pitches were examined in this manner. The data again were converted to atom, or mole, fractions and plotted on a van Krevelen diagram, as shown in Figure 4.17.

Obviously, the van Krevelen diagram for the thermolysis of the AR pitch is much clearer than that for the petroleum pitch. In both cases, however, there is similar curvature and position. When compared to the master van Krevelen diagram presented in Appendix A.6, two processes can be identified. The first is dehydration, probably the combination of severed -H and -OH groups, occurring at low temperatures. The observed curvature is the transition from this process to one of dehydrogenation, which becomes more dominant at temperatures above 800°C.

Therefore, thermolysis can be viewed, at least chemically, as the successive progression of at least three processes: desorption; CO, CO_2, and H_2O removal; and dehydrogenation. The first occurs readily just above 100°C and results in less than 5 mass percent loss. The second and third processes cannot be separated. Rather, there is a continuous transition between the two, and any other secondary processes that might occur. Thus, the effective kinetic parameters that were calculated from the model describe a process consisting of both the second and third processes.

4.3.3. Wide Angle X-ray Diffraction

Fiber samples taken from the carbonization furnace in a similar experiment were examined using wide angle X-ray diffraction. The aim was to determine the effect of these mass losses upon the crystal structure of the fiber. Samples were taken at 200, 400, 700, and 800°C during a 5°C per minute ramp. Figure 4.18 shows the change in (0002) spacing and stack height, L_c, during thermolysis of heat-soaked pitch fibers. In the case of this
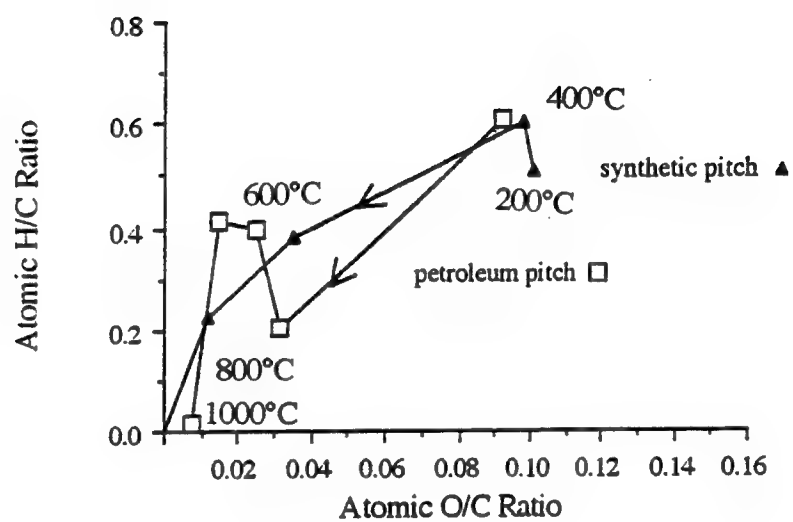
Figure 4.17. Van Krevelen diagram for fiber thermolysis.
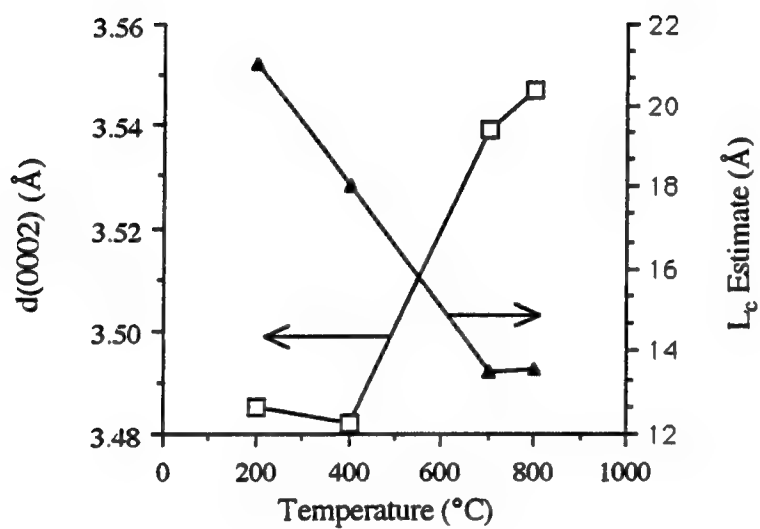
Figure 4.18. Change in d(0002) and L_c during thermolysis of heat-soaked pitch fibers.

experiment, the stack height is estimated from the (0002) diffraction peak only, and no measure of (0002) non-uniform strain is possible. This is because the (0004), or second-order (0002) peak, was not present in the 700 and 800°C fibers. Its absence indicates that severe damage had been done to the fiber crystal structure during thermolysis, and this phenomenon occurs between 400 and 700°C, where mass loss occurs at the greatest rate.

As there were no second-order diffraction peaks, the non-uniform (0002) strain could not be estimated for samples heated to 700 and 800°C. It is clear that significant structural changes occur during thermolysis, both as a result of thermal activation and volatile pressures. Therefore, the heating rate employed during this period will be a critical design parameter. A study of the influence of heating rate was not included in this study, but will be undertaken by Steve Jones for both the heat-soaked and AR pitches.

4.3.4. Small Angle X-ray Diffraction

Mass losses such as those occurring during thermolysis result in large stresses within the carbon structure. The result is an increase in strain energy that can either be relieved by plastic deformation or by cracking. To evaluate these possibilities, small angle X-ray diffraction was used to qualitatively examine voids within the fibers. Stabilized fibers were examined after heating to 400, 700, and 800°C using the small angle scattering equipment at Oak Ridge National Laboratory. Figures 4.19 through 4.21 show the two-dimensional small angle scattering patterns of stabilized fibers as well as fibers treated to 400 and 700°C, arranged so that the fiber axis is vertical. Their low intensities and isotropic appearance are evidence that little microcracking occurs during thermolysis (these patterns can, for comparison, be compared to those presented in section 4.5, obtained for some fibers treated at higher temperatures). This would indicate that creep deformation might be responsible for the relief of thermolysis stresses. This is reasonable because, if it is assumed that a "stabilized" fiber consists of regions of low crosslink density as well as under-stabilized regions, then the latter would have a much lower T_g and tend to deform.
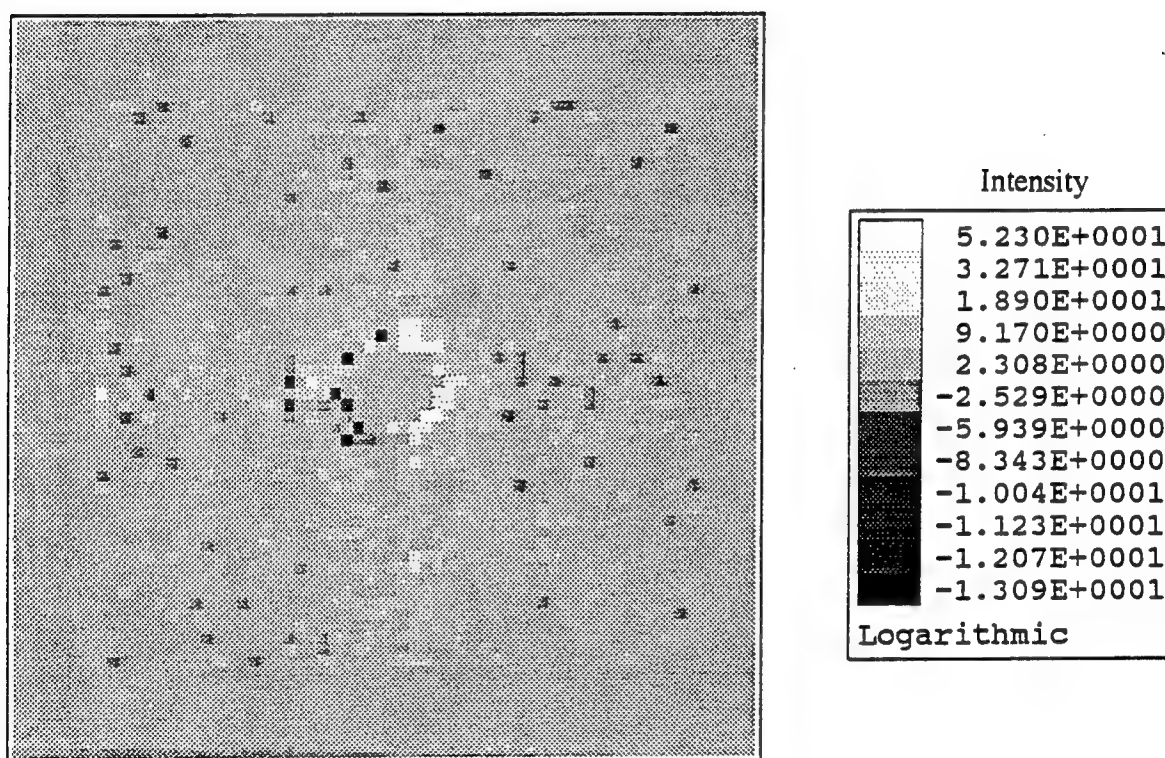
Figure 4.19. Small angle X-ray scattering pattern for stabilized heat-soaked pitch fibers.
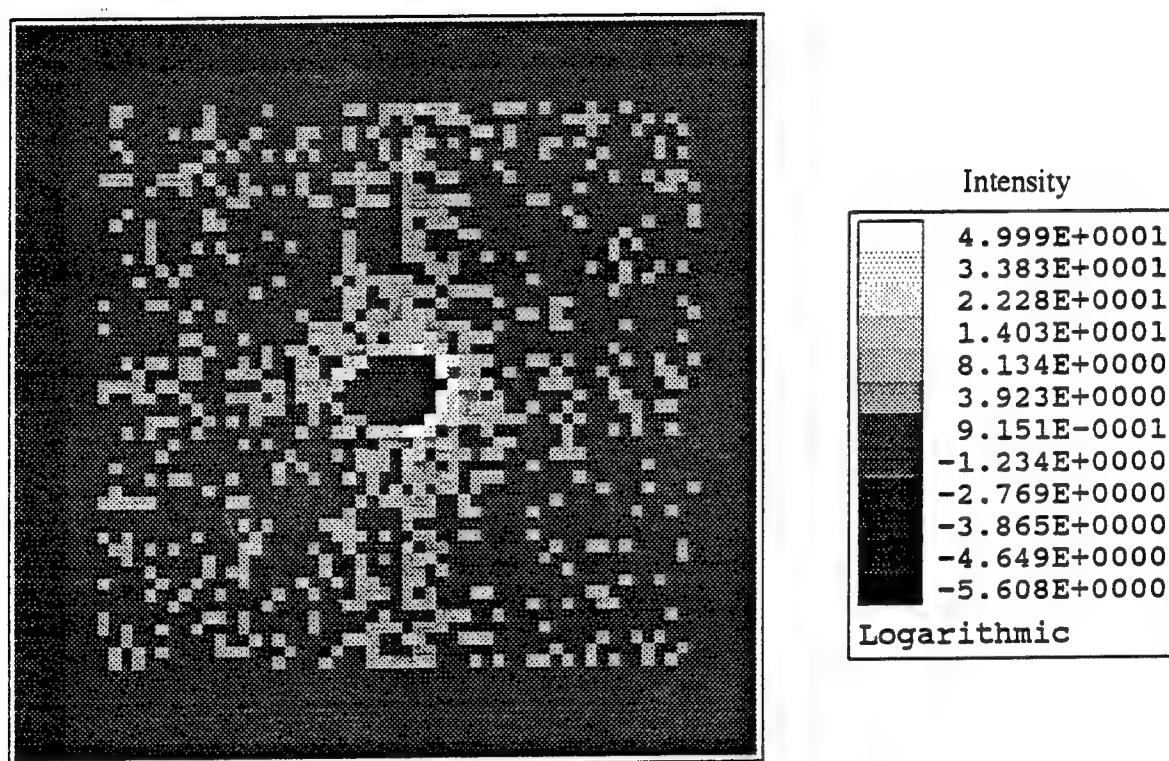
Figure 4.20. Small angle X-ray scattering pattern for HS fibers heated to 400°C.
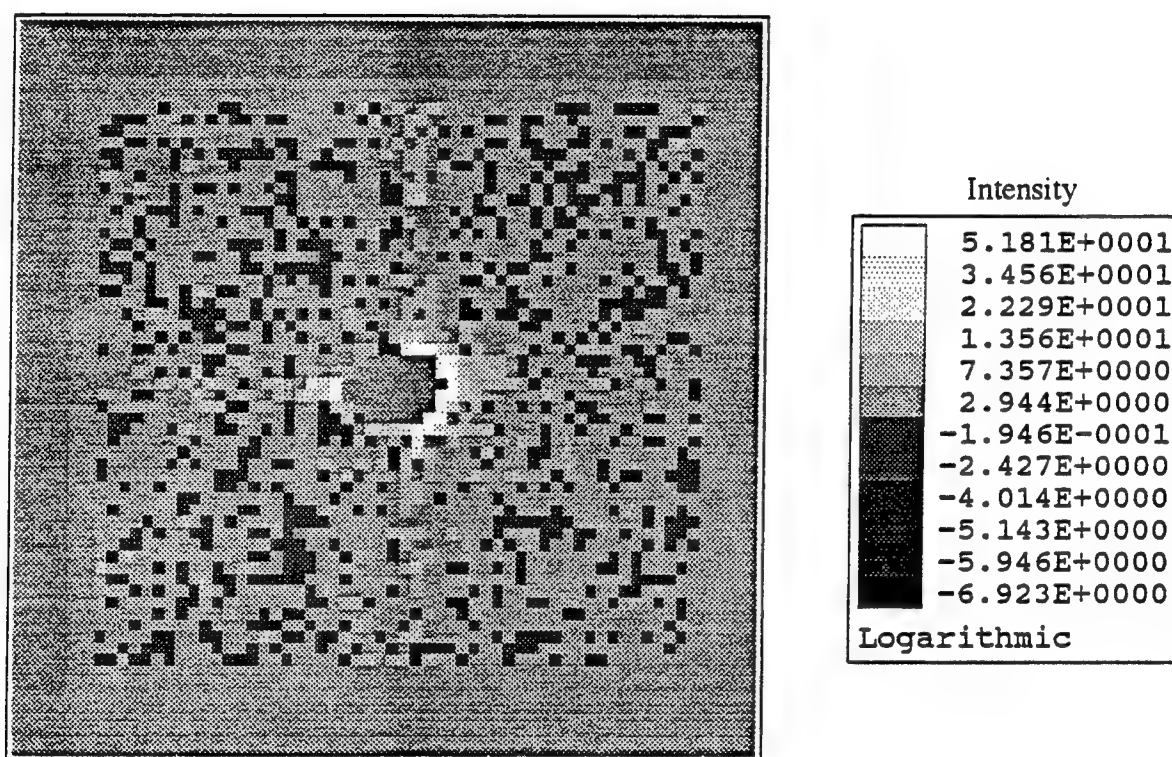
Figure 4.21. Small angle X-ray scattering pattern for HS fibers heated to 700°C.

As the fibers are carbonized to higher temperatures, carbon-carbon bonding prevents this relaxation, resulting in cracking.

4.4. Carbonization and Graphitization

Heat-soaked pitch fibers from Batch R2 were used in the temperature-time and heating rate studies. A description of their "initial" state, corresponding to the chemical and structural condition after treatment at 1000°C for 15 minutes, is given in Table 4.14.

Table 4.14. Structural state of heat-soaked pitch fiber set R2 heated to 1000°C.

$d(0002)$	3.462 ± 0.004 Å
L_c	15 ± 3 Å
L_a	37 ± 3 Å
θ_D	7961 K
Z	$39.1 \pm 6.0°$

When these fibers were heated at 20°C per minute to temperatures between 1800 and 2400°C, their (0002) spacings and Debye temperatures were observed to decrease toward the ideal value of graphite as shown in Figure 4.22. However, the apparent reversal in graphitization between 1600 and 2000°C was attributed to a secondary process, possibly a chemical reaction. Elemental analysis, presented in Appendix C.8, showed that no nitrogen was present in the heat-soaked pitch precursor, and that the oxygen content was essentially zero upon reaching 1200°C, so that only carbon, a small amount of hydrogen, and approximately 1.5 mass % sulfur remained by 1800°C. Figure 4.23 shows the change in sulfur content for fiber set R2 during graphitization.

An analysis of the desulfurization process was conducted to examine this possibility. If the "reaction", stated as

$$\text{carbonaceous solid} \Leftrightarrow \text{carbon} + \text{sulfur-bearing gas} , \tag{4.2}$$
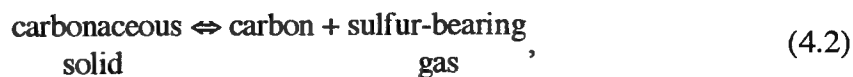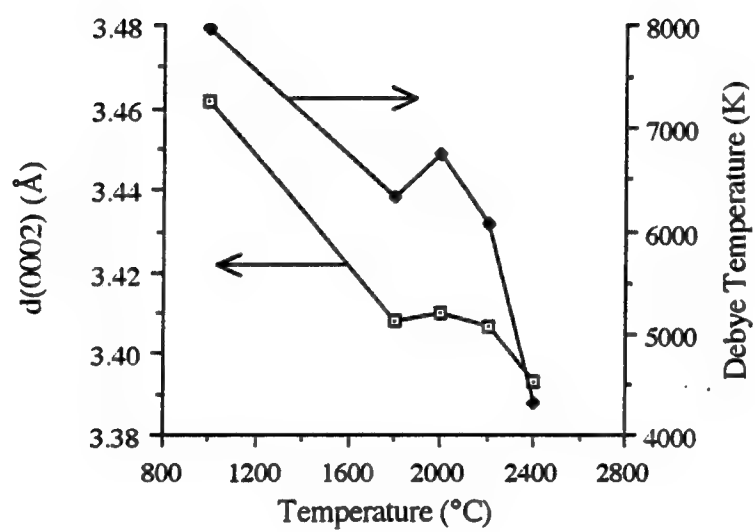
Figure 4.22. d(0002) spacings and Debye temperatures of graphitized fibers from set R2.
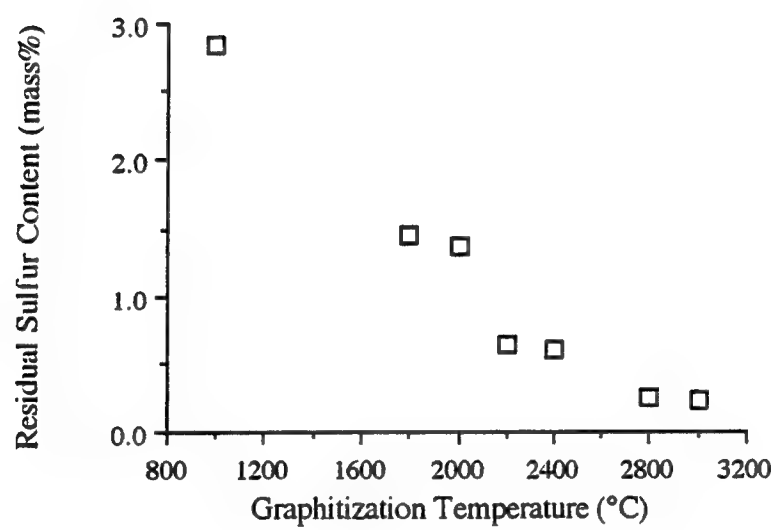
Figure 4.23. Sulfur content with graphitization temperature for fiber set R2.

is assumed to be reversible with an "equilibrium" constant, K, defined at each temperature, T, by the ratio of forward and reverse reaction rate constants,

$$K = \frac{k_{forward}}{k_{reverse}} = \frac{\theta_{D,graphite}/\theta_{D,(T)}}{\theta_{D,graphite}/\theta_{D,initial}}, \qquad (4.3)$$

then K should be related to temperature by the expression

$$\left(\frac{d \ln K}{dT}\right)_P = \frac{H_{products} - H_{reactants}}{RT^2} = \frac{\Delta H}{RT^2}. \qquad (4.4)$$

In truth, this reaction is not reversible, but here it is assumed that equilibrium lies far to the right (that is, K is very large). The process enthalpy, ΔH, then can be determined graphically by plotting $\ln(\theta_{D,initial}/\theta_{D(T)})$ versus $1/T$ for a series of treatment temperatures. The slope of this line is $-\Delta H/R$, where R is the gas constant. Figure 4.24 shows such a plot for Batch R2 fibers heated to temperatures between 1800 and 2400°C. The enthalpy of the process was estimated to be approximately 6.4 kcal/mole.

A four-step process for producing graphite from a sulfur-containing carbon, involving sulfur removal and the attachment of neighboring aromatic carbon atoms, was proposed:

(1) breaking of "sulfur linkages" (C-S bonds),

(2) attachment of neighboring aromatic bonds,

(3) formation of sulfur-bearing gas molecules, and

(4) diffusion of gas to the fiber surface.

The estimated enthalpy for the process should correspond to the summation of heats liberated and absorbed during the first three steps. The final step, involving mass transport, may have a bearing on the kinetics or internal pressure, but not upon process enthalpy. The list of possible sulfur-bearing gases that could be involved was reduced considerably by considering the energies that are absorbed when bonds are broken and energies released when bonds are formed for the evolution of a gas molecule. When possibilities such as S_2, S_8, H_2S, and CS_2 were considered, only the evolution of carbon disulfide, CS_2, seemed plausible, yielding a calculated enthalpy near 6 kcal/mole over this temperature range.
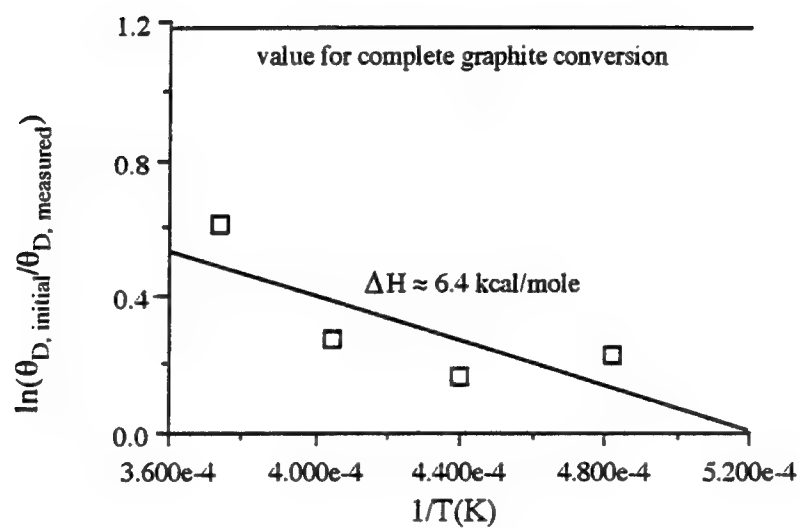
Figure 4.24. Graphical determination of reaction enthalpy for heat-soaked pitch fibers.

This finding was confirmed by mass spectroscopy. Gas samples taken from the graphitization furnace at 2000 and 2200°C duplicated the ion mass and retention time of a pure CS_2 standard run prior to the sample. The superimposed gas chromatograph/mass spectra of both the sample and the CS_2 standard are shown in Figure 4.25. Small amounts of H_2S were observed in gas samples taken at temperatures below 2000°C, as shown in Figure 4.26, but not in samples taken at higher temperatures as almost all of the hydrogen had been removed.

The rate-limiting step then was identified by considering several dwell times at temperatures between 1800 and 2400°C. A simple first-order rate expression was applied to the degree of graphitization at each temperature, and the activation energy, calculated from the temperature dependence of the graphitization rate, was used to identify the rate-limiting step for the graphitization of heat-soaked pitch.

The degree of graphitization, g, was defined as a function of Debye temperature,

$$g = \frac{\theta_{D, \text{ graphite}}}{\theta_{D, (T)}}, \tag{4.5}$$

where g approaches 1 at high temperatures and is much less than 1 at low temperatures. The numerical values of g obtained by this technique are very close to those obtained by the more conventional method employing the the (0002) interplanar spacing. Use of the specific heat capacity, however, is an indicator of bulk lattice quality and not the planar stacking in one direction.

Assuming that graphitization is a first-order process, the rate of graphitization can be written

$$\frac{dg}{dt} = -k_1 g, \tag{4.6}$$

where k_1 is the first-order rate constant. Its temperature dependence is given by the Arrhenius equation

$$k_1 = k_o \exp\left(-\frac{\Delta E}{RT}\right). \tag{4.7}$$

ΔE is the process activation energy.
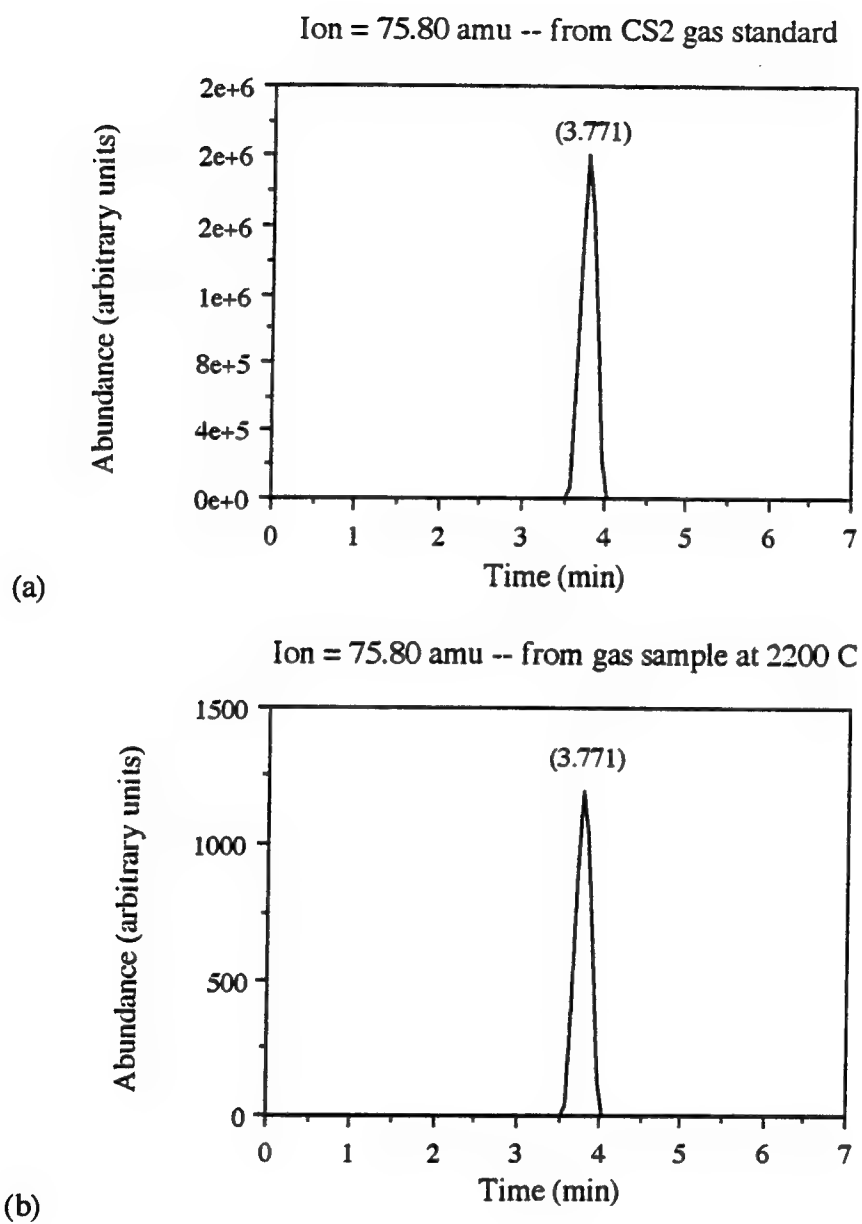
Figure 4.25. GC/MS spectra for (a) a CS_2 standard, and (b) gas sample taken between 2000 and 2200°C.

Ion = 33.80 amu. from gas sample at 1000 C
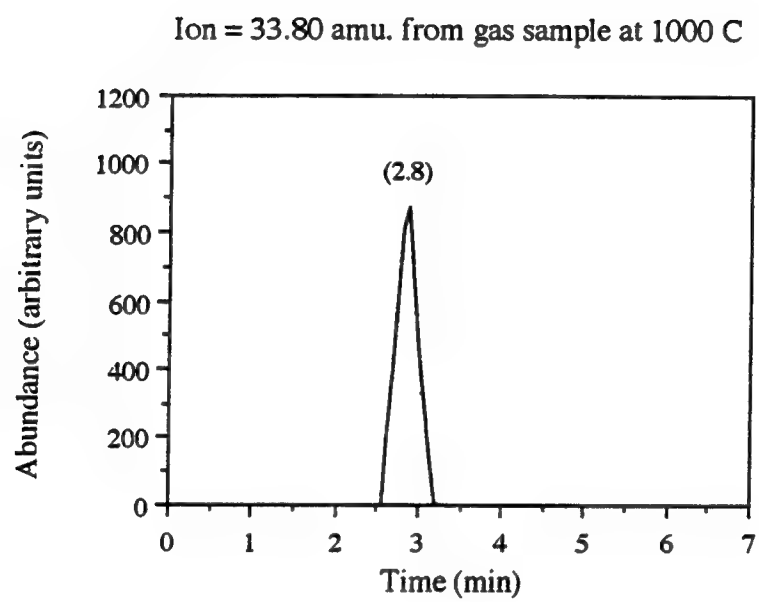
Figure 4.26. GC/MS spectrum for gas sample taken at 1000°C.

Figure 4.27 shows a plot of the degree of graphitization with treatment time and temperature. The first-order analysis gave a value for the activation energy of between 65 and 85 kcal/mole, equivalent to the values found by Fitzer and Weisenburger for the graphitization of certain pitch-cokes. The curve also corresponds with their finding that "graphitization stops temporarily between 1700 and 2100°C" (115). This value indicated that breaking the C-S bonds at the layer-plane peripheries was the rate-limiting step in the desulfurization and crystal growth process. Thus, the removal of sulfur provides a lower energy barrier to graphitization than vacancy migration. However, sulfur is responsible for the delay in graphitization in the heat-soaked pitch prior to its removal.

High pressures are created within the fiber as sulfur, in the form of hydrogen sulfide or carbon disulfide gas, is removed. These pressures lead to severe strain in the (0002) direction and can even "puff," or bloat, the fiber. Evidence of this puffing, the change in fiber cross-sectional area with graphitization temperature, is shown in Figure 4.28 along with the residual sulfur content. As the figure indicates, there was a gradual decrease in area between 1000 and 1800°C, followed by a rapid increase over the desulfurization temperature range. Only at very high temperatures, when essentially all of the sulfur was removed and the stress had been relieved, did the area decrease toward its pre-desulfurization value. This phenomenon is very similar to the irreversible expansion observed in petroleum- and coal tar-based cokes. The major differences are the temperature range over which the sulfur is removed and the sulfur-bearing gas species that are formed. While cokes often liberate sulfur below 1600°C in the form of H_2S, the heat-soaked pitch fibers used in this study required temperatures in excess of 1600°C, where the most thermodynamically favorable product is CS_2 gas (105, 111). In contrast, the AR pitch contained no sulfur and, thus, showed no increase in fiber area through this temperature range.

As expected, "puffing" and accompanied stress-cracking adversely affected fiber physical properties. Tensile strength is usually found to have an inverse dependence upon
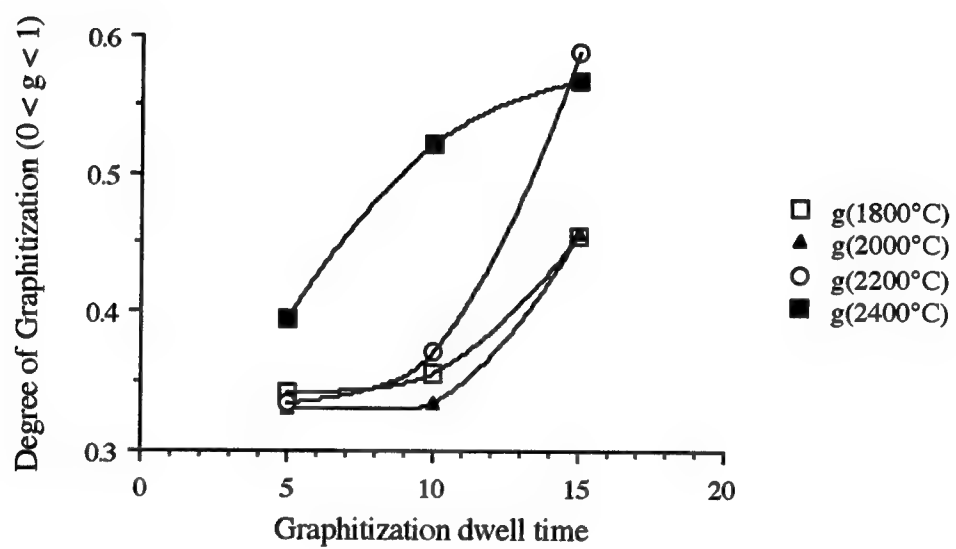
Figure 4.27. Degree of graphitization, g, with time at temperatures between 1800 and 2400°C for heat-soaked pitch fibers.
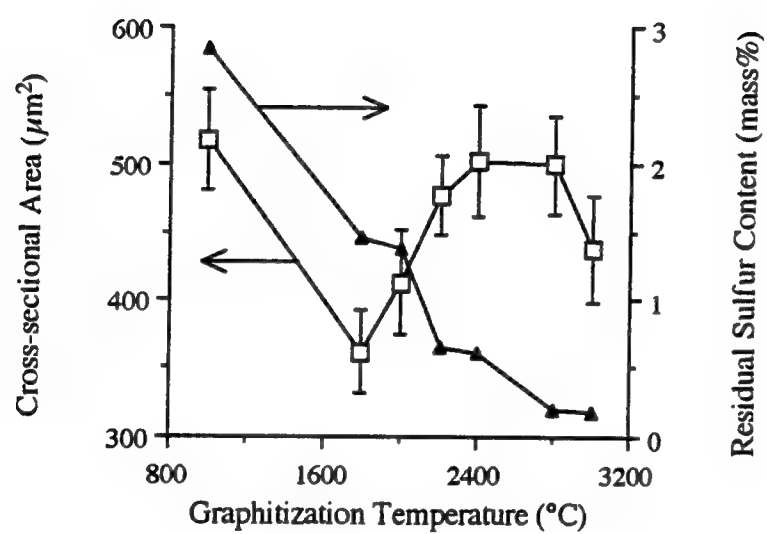
Figure 4.28. Heat-soaked pitch fiber cross-sectional area and residual sulfur content with temperature.

fiber area, and lattice properties such as modulus and conductivity are strongly influenced by crystal orientation. Figure 4.29 shows the change in single filament electrical resistivity with graphitization temperature. The poorest resistivity was observed at the same temperature that the maximum rate of change of area was observed. Apparently, crystal growth and stress-relaxation processes occurring at high temperatures improved the electrical resistivity.

To this point, all graphitization treatments had employed a 20°C per minute heating rate. When the heating rate was increased to 60, 100, and even near-infinite (sudden introduction of fibers into the heating zone) °C per minute rates, the severity of desulfurization was lessened. This contradicts past work on cokes that showed "puffing" was reduced with decreased heating rate (115). Table 4.15 shows the residual sulfur content, cross-sectional area, and electrical resistivity of batch R2 fibers, after being held at 2400°C for 15 minutes.

Table 4.15. The effect of heating rate upon sulfur content, area, and electrical resistivity of heat-soaked pitch fibers.

Heating rate (°C/minute)	Residual sulfur content (mass %)	Cross-sectional area (μm^2)	Electrical resistivity ($\mu \Omega m$)
20	0.61	502.4±83.7	9.03±0.77
60	0.26	393.0±34.2	6.10±0.42
100	0.24	401.8±28.1	6.74±0.60
≈∞	<0.20	350.8±39.9	5.21±0.47

(± denotes a 95% confidence interval)

Increased heating rate allowed greater sulfur removal and minimized the deleterious effect of sulfur removal on lattice-dependent physical properties. A simple model is proposed in Figure 4.30 to explain the heating rate influence. In Figure 4.30a, a "small-scale" graphitic structure is shown, resulting from high heating rates through the initial
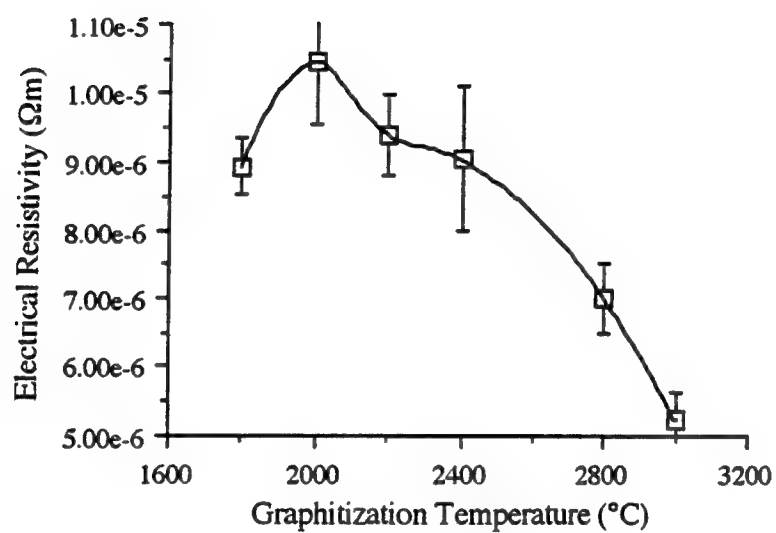
Figure 4.29. Electrical resistivity of heat-soaked pitch fibers with graphitization temperature.
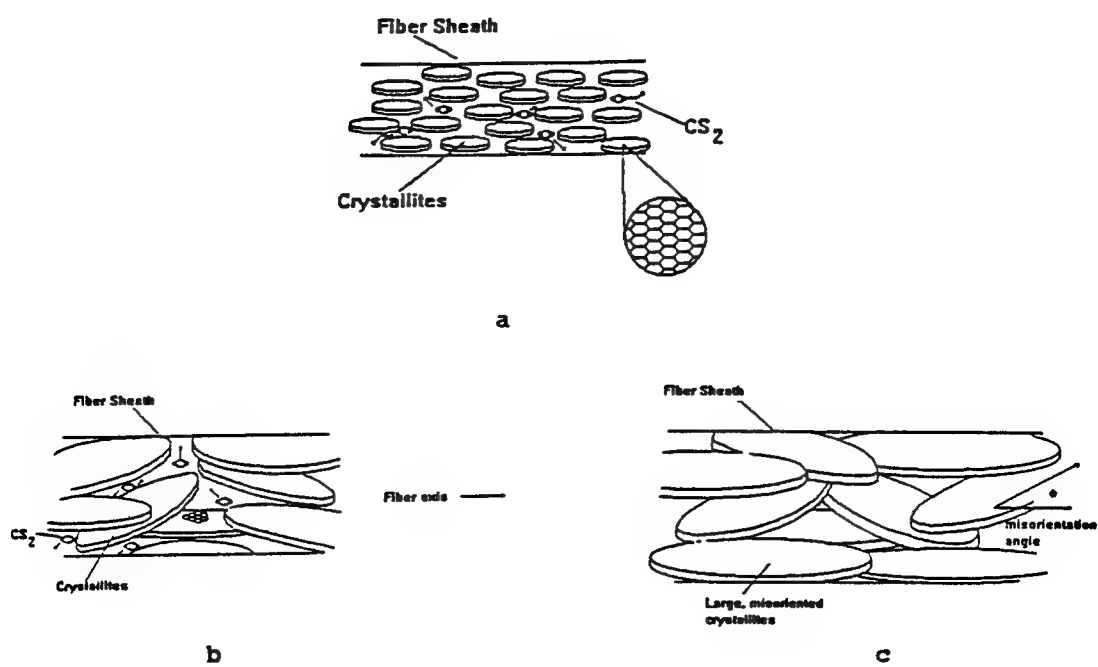
Figure 4.30. Model of the influence of heating rate upon structural damage in heat-soaked pitch fibers during desulfurization.

crystal growth period near 1700°C. When CS_2 molecules are evolved, they can migrate to the surface with only a small increase in misorientation angle, ϕ. Upon heating to higher temperatures, these layers reorient themselves and grow into large, well-oriented domains. On the other hand, "large-scale" structures like Figure 4.30b, which are created by low heating rates, present problems. It is likely that sulfur removal generates large pressures that result in [0002] strain and an increase in misorientation angle. Because these large domains have low mobility, subsequent heating to high temperatures creates an extended, misoriented structure, shown in Figure 4.30c, resulting in poor physical properties.

Graphitization, however, is a kinetic process that requires time at temperature to produce a well-ordered graphitic structure. Long dwell times or slow heating rates in the high temperature region (above 2500°C) are necessary to relieve the stresses caused during desulfurization and to grow large graphite domains. The temperature at which the heating rate is changed must be chosen so that a high heating rate is employed through the desulfurization process. Therefore, the next experiment involved treatments of "mixed" heating rates. Fibers were heated at 100°C per minute (the top furnace capability) to a selected "change-over" temperature between 1600 and 2000°C. Then the heating rate was changed to 1°C per minute and the furnace continued to 2400°C, where it remained for 15 minutes. X-ray diffraction analysis showed that, in general, the crystal quality increased with increasing change-over temperature. Figure 4.31 through 4.34 shows the change in d(0002) spacing, stack height (L_c), non-uniform (0002) strain, and misorientation angle (Z) with change-over temperature.

Electrical resistivity measurements also showed an improvement with increasing change-over temperature, as shown in Figure 4.35. At change-over temperatures just above 1600°C, there was an increase in electrical resistivity, resulting from the structural disturbance of desulfurization. Even the slow heating rate that followed did not reverse the damage. Changing the heating rate at higher temperatures provided the necessary high heating rate during desulfurization.
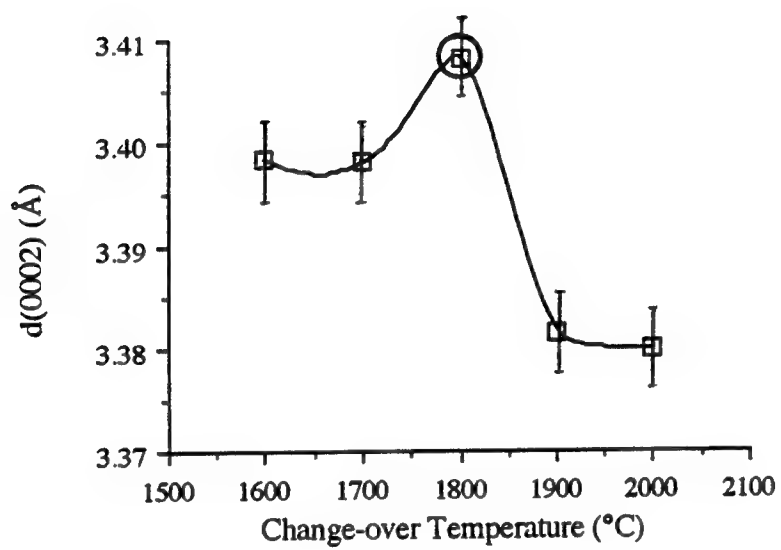
Figure 4.31. Change in d(0002) with change-over temperature for heat-soaked pitch fibers.
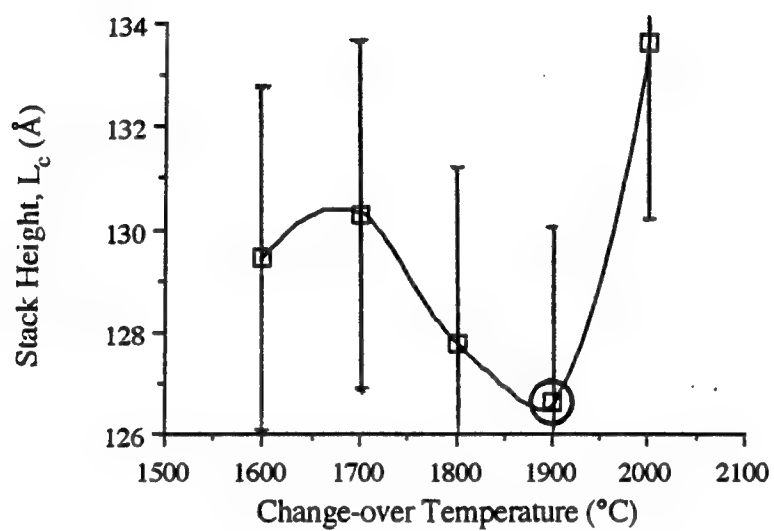
Figure 4.32. Change in stack height, L_c, with change-over temperature for heat-soaked pitch fibers.
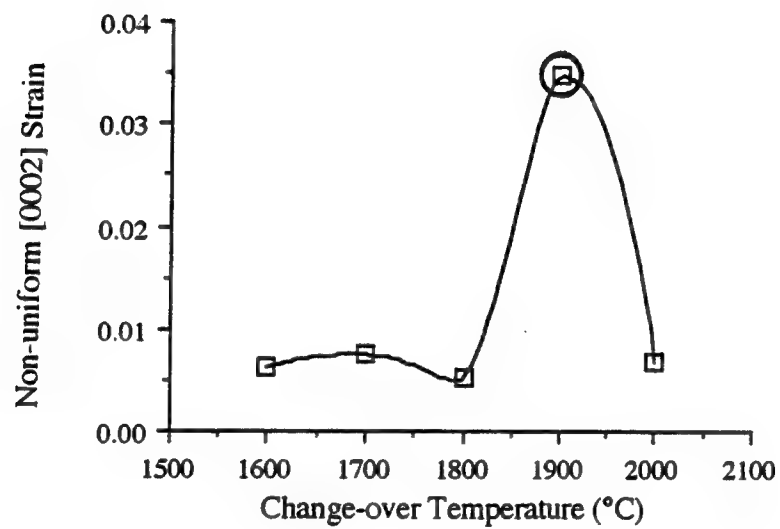
Figure 4.33. Change in non-uniform [0002] strain with change-over temperature for heat-soaked pitch fibers.
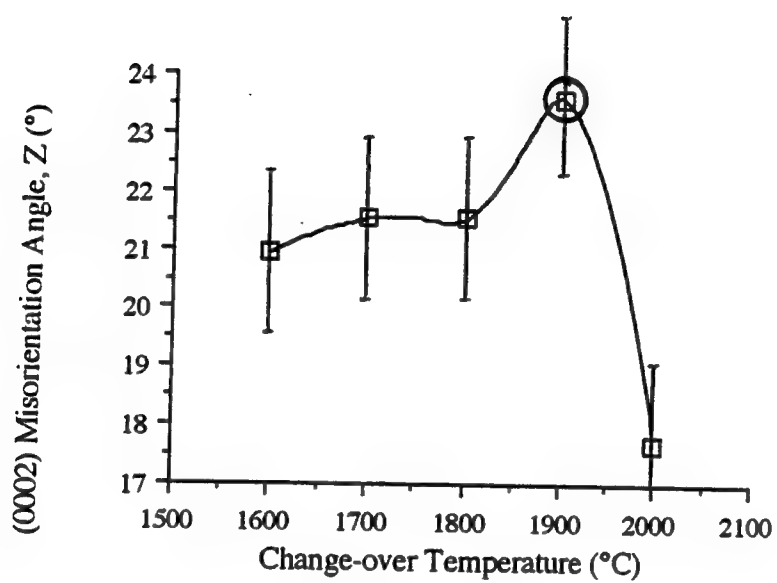
Figure 4.34. Change in misorientation angle, Z, with change-over temperature for heat-soaked pitch fibers.
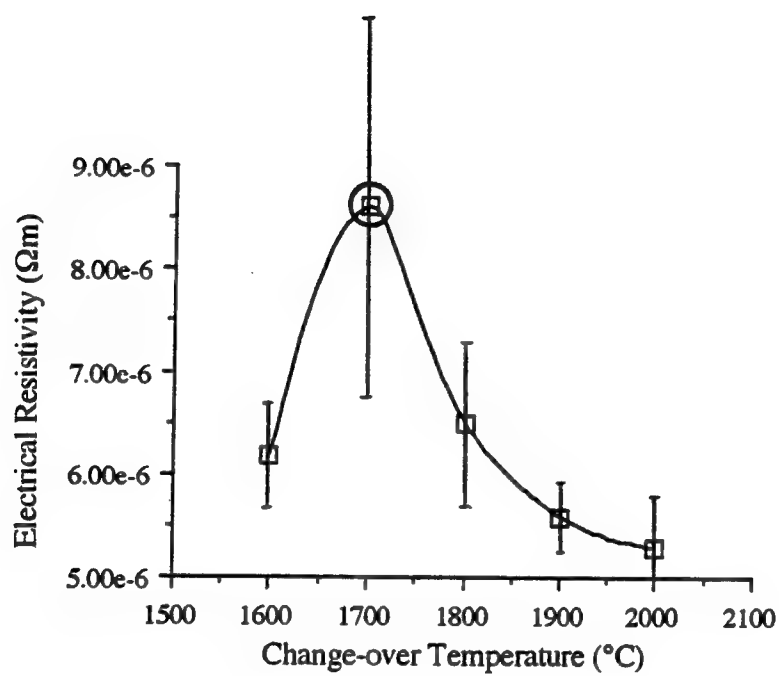
Figure 4.35. The effect of change-over temperature on the electrical resistivity of heat-soaked pitch fibers.

A discontinuity, indicated by circled data points, in L_c, strain, and Z was observed between 1700 and 1900°C. Therefore, in this range, there seems to be a secondary process occurring that may be deleterious to fiber structure and properties. To study this process, isothermal treatments of 1, 2, 4, 8, 16, and 32 minutes were conducted at 1800, 1900, and 2000°C, using heat-soaked fiber batch R2. Figure 4.36 shows the time dependence of stack height (L_c) at the three temperatures. The 1900°C stack heights were approximately parabolic with time while the two other temperatures had very different dependences, the 2000°C values being nearly constant with time. The same sort of trends were observed for the coherence length (L_a), shown in Figure 4.37.

The slight decrease in L_a with time at both 1800 and 2000°C may indicate that layer planes are fractured at the high strains created by desulfurization. Residual lattice strain, as measured by X-ray diffraction, is observed to decrease with time in a similar manner. It is possible, then, that the reduction in lattice strain energy is accomplished by fracture of the crystallites between graphite layers, similar to the "polygonization" process observed in heavily-strained metals. The (0002) interplanar spacing changed little with time but did show a slight decrease toward the value for graphite.

Interpretation of this data is difficult, but it seems to indicate that a nucleation process occurs around 1900°C. Coupled with the large amount of sulfur removed at the that temperature, it would explain the increase in strain and misorientation angle that is observed. Unfortunately, there is a great deal of scatter in the data, probably as a result of the thermal treatment conditions, and it is impossible to perform a kinetic analysis on such data. A better approach would be to perform this experiment *in situ*, using a high-temperature diffractometer, so that the changes in d(0002) and crystallite size can be measured at more controlled thermal treatment conditions.

A final test was conducted to illustrate the nature of this nucleation process. One sample of fibers from batch R2 was heated directly to 2400°C at a rate of 100°C per minute and held there for 1 hour. Another sample was heated to 1900°C at 100°C per minute and
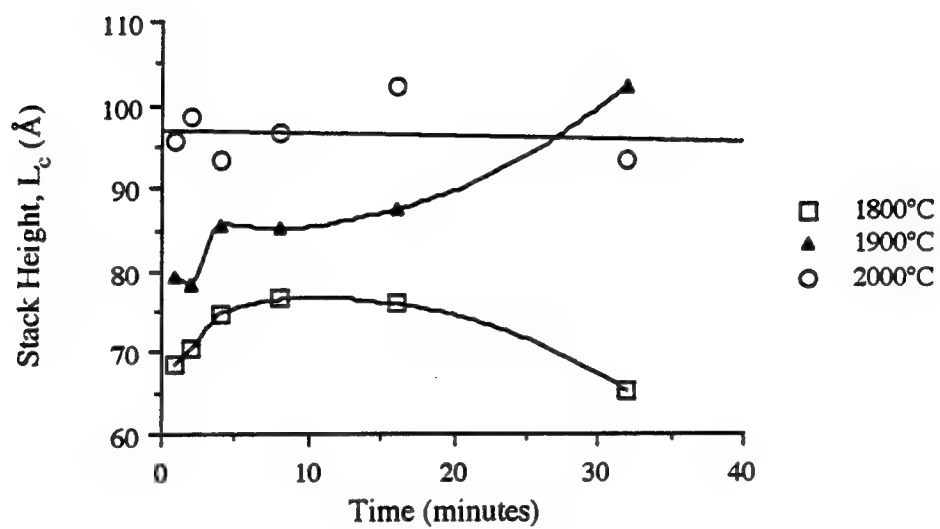
Figure 4.36. Dependence of stack height, L_c, of heat-soaked pitch fibers on time between 1800 and 2000°C.
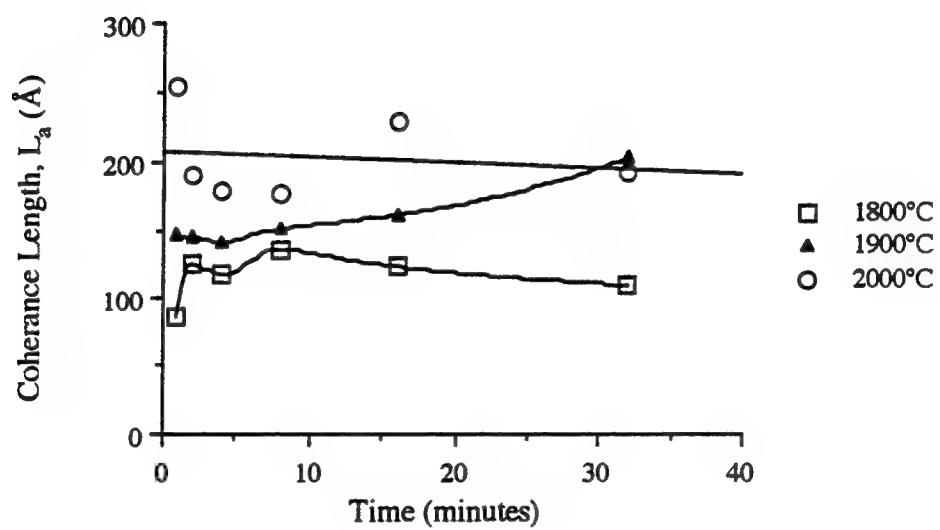
Figure 4.37. Dependence of coherence length, L_a, of heat-soaked pitch fibers on time between 1800 and 2000°C.

held there for 32 minutes, to duplicate the longest time of the 1900°C isothermal treatment. After the soak, the furnace was heated to 2400°C at the same heating rate and held there for 1 hour. The purpose was two-fold: (1) to determine if lattice strain and misorientation could be decreased by long-time annealing at 1900°C, and (2) to show that a 1900°C soak does promote secondary nucleation, resulting in lower crystallite size, despite its increased time at high temperature.

Table 4.16 presents the crystallographic data for both samples. The 1900°C soak did not reduce the misorientation angle (Z) to a value near that for direct heating to 2400°C. In addition, the coherence length (L_a) was lower, possibly because the 1900°C soak caused the nucleation of new active sites. The resulting smaller distances between active nuclei may cause earlier impingement and smaller crystallites. A greater stack height (L_c) was observed, however, so that the 1900°C soak treatment produced crystals of much lower L_a/L_c ratio. The combination of greater misalignment and smaller coherence length should give rise to reduced axial physical properties.

Table 4.16. X-ray diffraction data from 1900°C soak and direct heating to 2400°C.

Fiber set	d(0002) (Å)	L_c (Å)	L_a (Å)	Z (°)
1900°C soak	3.414±0.004	109±6	116±6	18.8±1.5
2400°C direct	3.414±0.004	102±6	122±6	14.4±1.5

Finally, an experiment was devised to determine if sulfur could be removed from the fibers at a lower temperature by thermal treatment under hydrogen, as Mochida (119) had proposed. Fibers from the same melt-spinning and stabilization trial as heat-soak pitch fiber set R2 were employed for this experiment. They were heated under helium to either 750 or 1500°C, where the graphite resistance furnace was evacuated and filled with

hydrogen. The fibers remained at that temperature for 30 minutes, and then were heated to 2400°C under helium. A control sample was heated directly to 2400°C under helium. The sulfur content remained nearly constant at 0.25 mass percent for the graphitized fibers, indicating that the sulfur present in the heat-soaked pitch fibers did not respond to the hydrogen treatment. It is believed, then, that the sulfur is tightly bound in the aromatic planes and cannot be removed until high temperatures are reached.

4.5. Cracking and Small Angle Scattering.

Selected fiber samples, representing different thermal treatment conditions for both the heat-soaked and the AR pitches, were studied by small angle X-ray diffraction. Figures 4.38 through 4.40 show the small angle diffraction patterns for heat-soaked pitch fibers heated to 1800 and 2400°C, as well as AR pitch fibers heated to 2400°C. There is significant small angle scattering, evidence of microcracking, in each sample. These are quite a contrast to Figures 4.19 through 4.21, which illustrate the lack of small angle scattering in heat-soaked pitch fibers heated to only low temperatures. Figure 4.40 is included to show the smaller azimuthal breadth observed in the AR pitch fibers, a result of greater void alignment with the fiber axis. A quantitative description of the void structure was not possible because their small angle scattering patterns did not fit accepted models. However, several general statements could be made. First, the true h-exponent was determined by regression of $\ln(I(h))$ on $\ln(h)$. Non-integer powers between 2 and 3 were found, contrary to Porod's law for scattering from smooth interfaces (5, 213). This indicates that the voids may consist of non-circular surfaces. The value of this exponent gave a measure of the degree of graphitic ordering: values nearer 3 indicated a higher degree of graphitization (105). As a result of this non-integer power law, the Guinier plots of $\ln(I(h))$ versus h^2 were highly curved, as shown in Figure 4.41. Therefore, only a lower limit could be determined for void dimension (R_g) in the equatorial direction. Comparison of these lower limits, however, showed that AR pitch fibers had a finer void

Intensity

	2.505E+0003
	1.302E+0003
	6.758E+0002
	3.496E+0002
	1.797E+0002
	9.124E+0001
	4.515E+0001
	2.115E+0001
	8.646E+0000
	2.134E+0000
	-1.258E+0000
	-3.944E+0000

Logarithmic
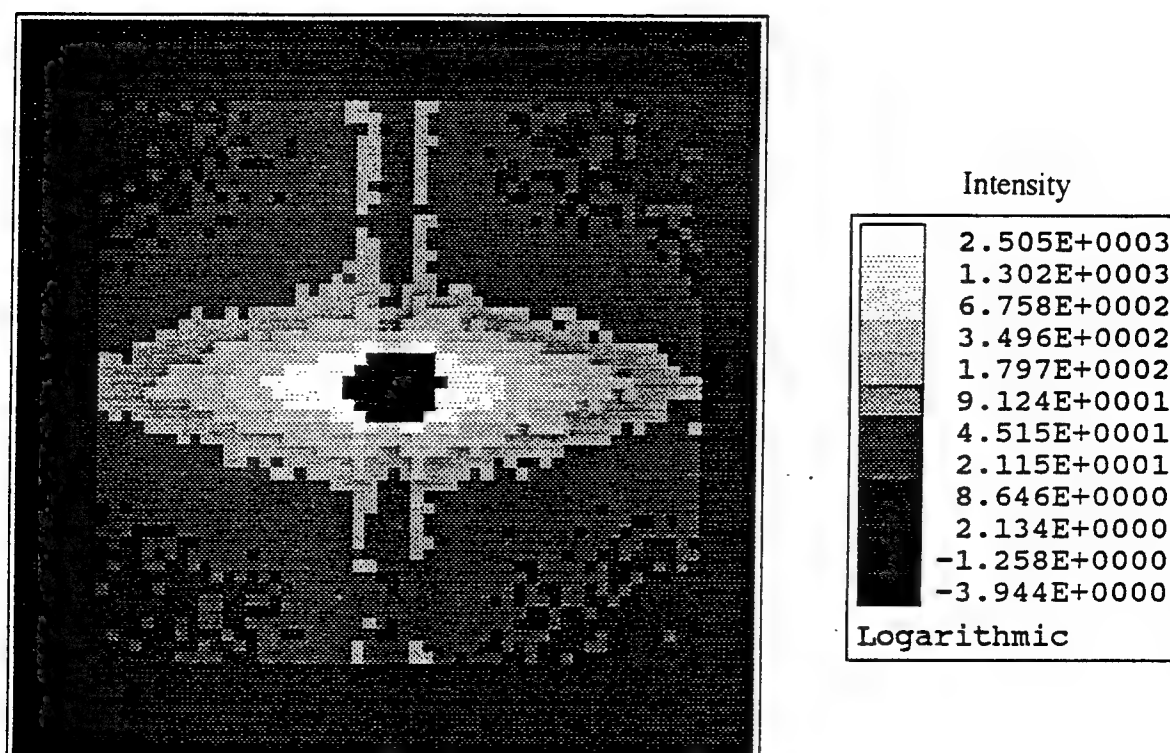
Figure 4.38. Small angle X-ray diffraction pattern for a heat-soaked pitch fiber heated to 1800°C.
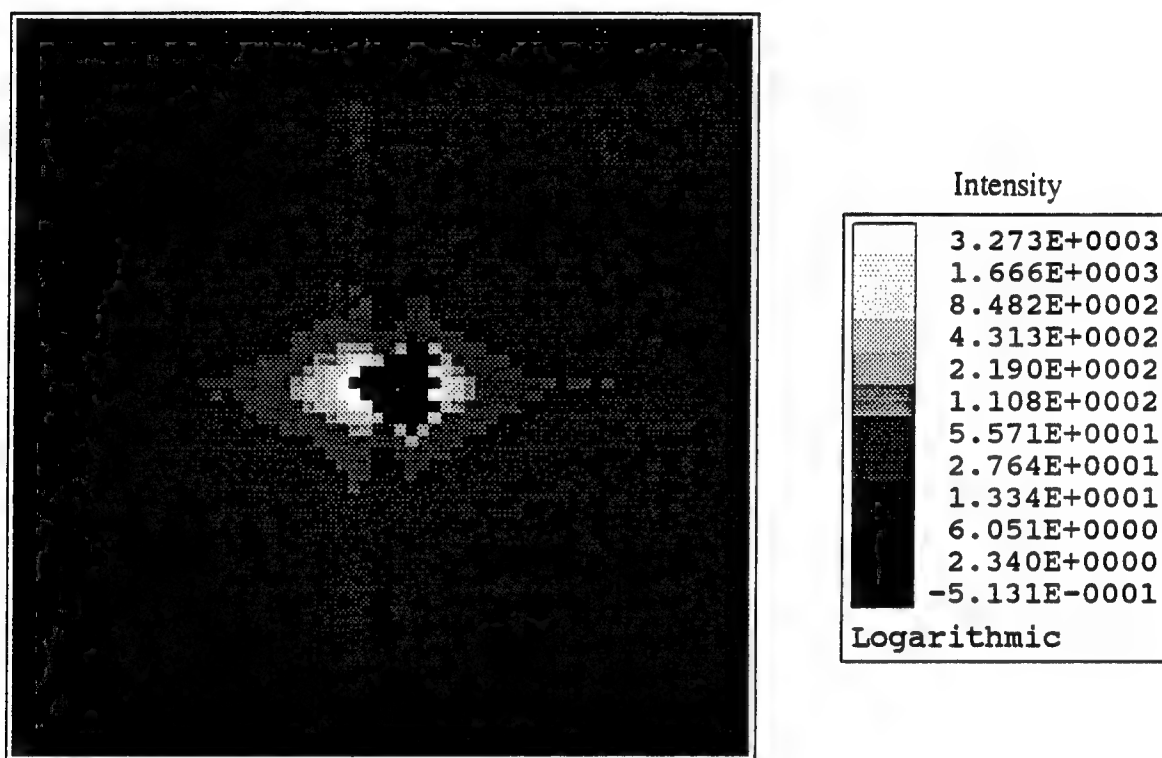
Figure 4.39. Small angle X-ray diffraction pattern for a heat-soaked pitch fiber heated to 2400°C.

	Intensity
	2.969E+0003
	1.525E+0003
	7.832E+0002
	4.022E+0002
	2.066E+0002
	1.061E+0002
	5.450E+0001
	2.799E+0001
	1.438E+0001
	7.391E+0000
	3.800E+0000
	1.009E+0000
Logarithmic	
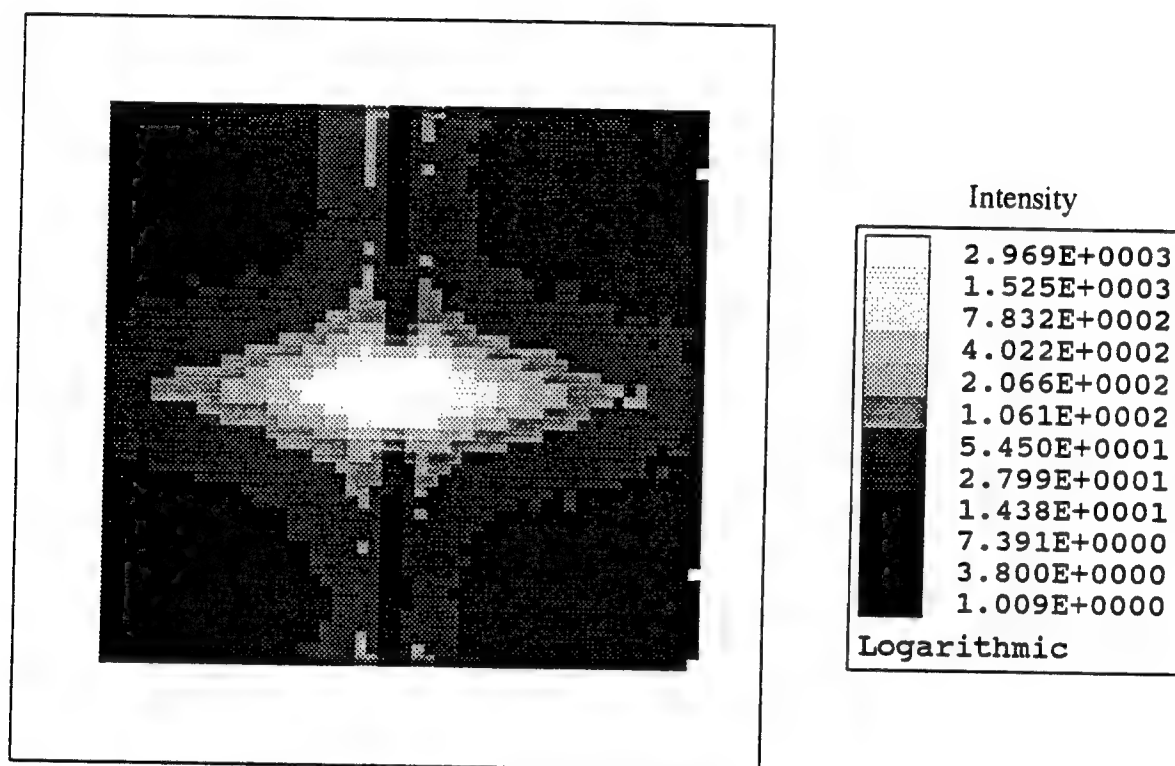
Figure 4.40. Small angle X-ray diffraction pattern for a AR pitch fiber heated to 2400°C.
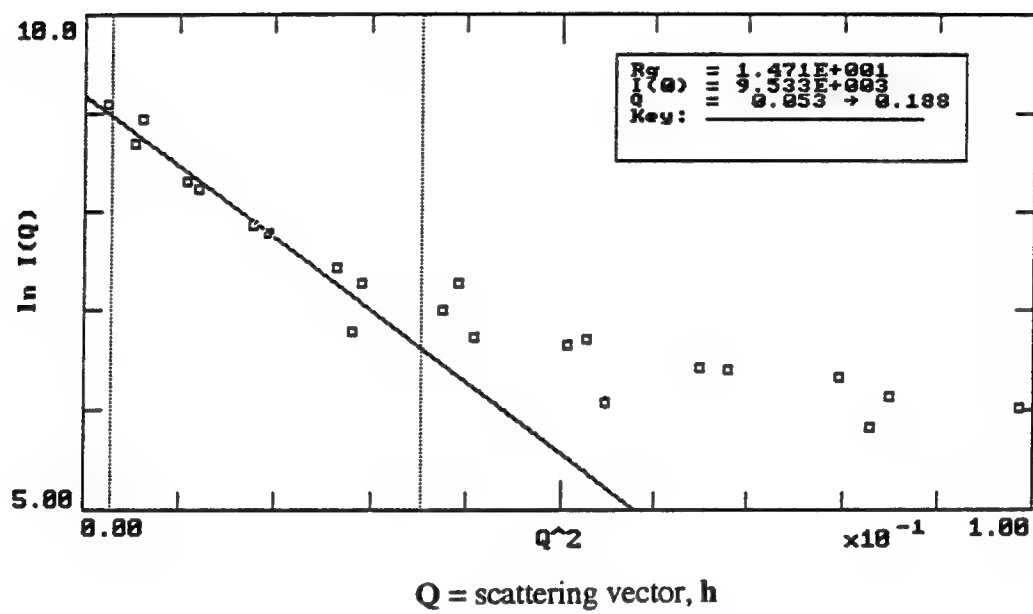
Figure 4.41. Typical Guinier plot for a graphitized fiber.

structure than did heat-soaked pitch fibers. Finally, the orientation of voids could be determined from azimuthal scattering profiles, such as shown in Figure 4.42. The parameter Z again is used to describe the breadth of the orientation distribution at half-maximum intensity. Values of both R_g and Z for several fiber sets from both precursors are presented in Table 4.17.

Table 4.17. Void misorientation and the lower limit of void width for several fibers.

Fiber set	Z (°)	$R_g > x$ (Å)
heat-soaked pitch:		
HSR1000	26.6	75
HSR1800	17.0	72
HSR2000	17.3	71
HSR2200	18.2	69
HSR2400	17.0	72
HSR2800	15.2	72
AR pitch:		
ARR1800	16.7	66
ARR2000	16.7	64
ARR2200	15.7	60
ARR2400	15.6	55

(* error on Z is estimated at ±1°, and the R_g are simply lower limits with error around ±3)

The first two letters of the sample nomenclature indicates the type of pitch, heat-soaked (HS) or AR. The third letter indicates that the fibers were ribbon-shape (R), as opposed to circular (C), and the following number gives the maximum treatment temperature.

The void dimension and misorientation decrease with graphitization temperature for AR pitch fibers. On the other hand, a local maximum in pore misorientation was observed at a graphitization temperature around 2200°C for the heat-soaked pitch fiber, as Figure 4.43 shows.
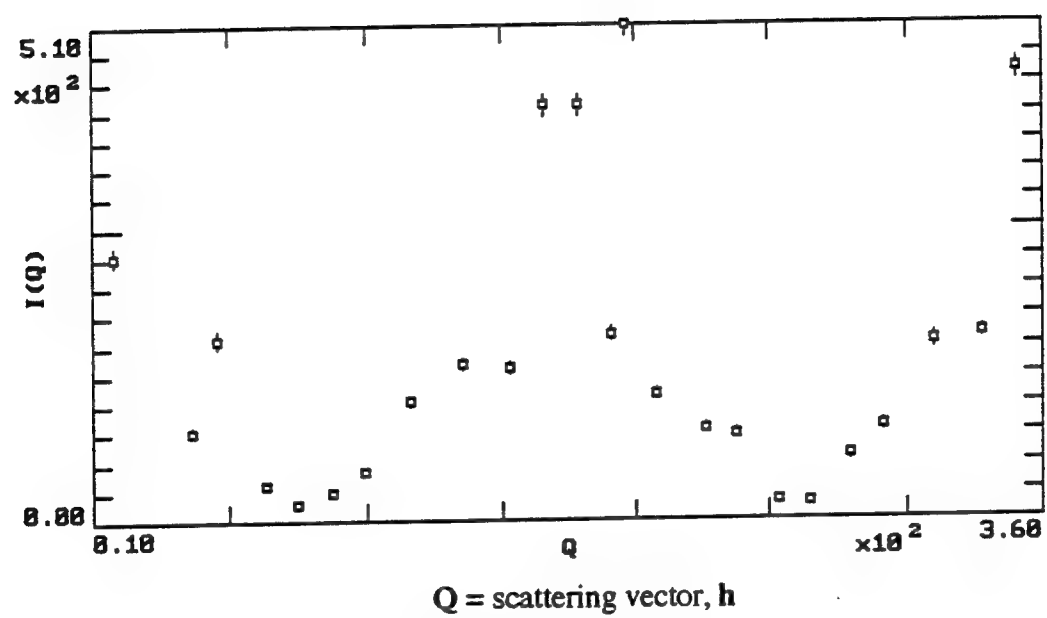
Figure 4.42. Typical azimuthal slice of scattered intensity at constant h.
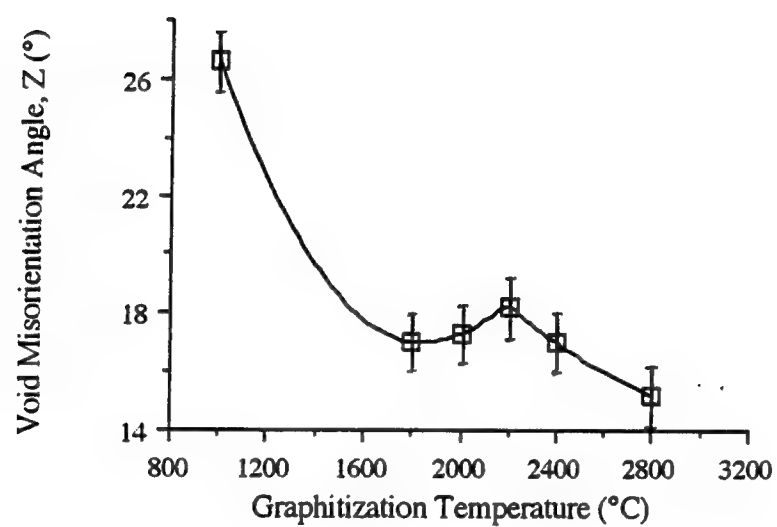
Figure 4.43. Change in void misorientation angle, Z, with treatment temperature for heat-soaked pitch fibers.

4.6. Raman Spectroscopy Analysis

It was hoped that Raman spectroscopy would allow identification of the sulfur bonding mechanism operative within the heat-soaked pitch. Samples R1000-15, R1800-15, and R2400-15 were analyzed at Michigan Technological University by Dr. Bahne Cornilsen, and their Raman spectra are presented in Figure 4.44. Unfortunately, the spectra contained little information other than the relative degree of disorder, determined from the ratio of peak intensities at 1360 cm^{-1} to that at 1580 cm^{-1}. The first is associated with phonon modes that are not centered in the first Brillouin zone, but represent a local maximum density of states at a frequency of 1360 cm^{-1}. The second represents the only allowed peak in perfect graphite, corresponding to zone-center phonons. The ratio of the integrated intensities of these two peaks is often used to characterize the degree of disorder and, as both peaks are derived from the E_{2g2} vibration in the crystallographic a-direction, this ratio is often related to the coherence length, L_a (5, 166). Data for these three fiber samples are presented in Appendix C.14, but Figure 4.45 illustrates the relationship of L_a and I_{1360}/I_{1580}).

4.7. Enhanced Graphitization through Solvent Etching

Impurities and misaligned regions may cause large lattice strains in neighboring well-ordered regions during graphitization (80). If these regions can be removed at some point in the process without extensive damage to the fiber, it may be possible to produce a well-ordered graphitic structure during a subsequent thermal treatment. An oxidizing solvent similar to that described by Maire and Mering (18) for the grading of graphitic carbons was used to preferentially dissolve disordered regions prior to high temperature thermal treatment.

One AR and one heat-soaked fiber set were employed for this experiment. After equivalent stabilization at 280°C, both sets could be oxidized by a 0.15 M solution of potassium dichromate in sulfuric acid within one minute. However, when thermolyzed to
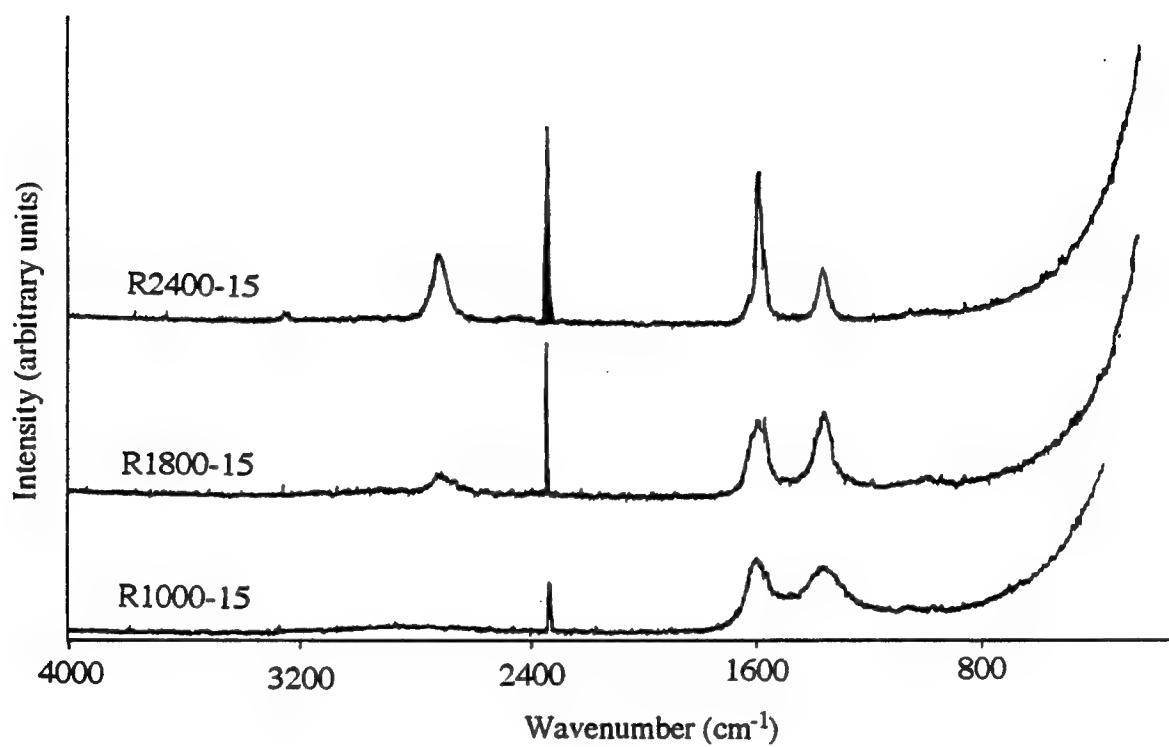
Figure 4.44. Raman spectra of heat-soaked pitch fibers (a) R1000-15, (b) R1800-15, and (c) R2400-15.
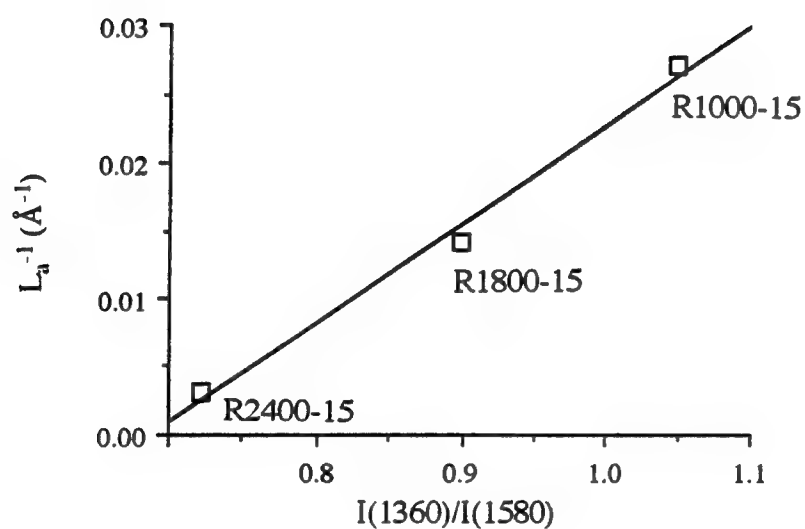
Figure 4.45. Relationship of coherence length, L_a, and the ratio I_{1360}/I_{1580} of the 1360 and 1580 cm^{-1} Raman peaks for heat-soaked pitch fibers.

1000°C, the fibers remained intact, even through significant amounts of material could be removed from the heat-soaked pitch fibers (evident from darkening of the solution). By comparison, the solution affected carbonized AR pitch fibers to a lesser degree.

Infrared spectra of the solvent treated petroleum-derived fibers, presented in Figure 4.46, showed an increase in the proportion of aromatic C-H bonding, and a decrease in the proportion of aliphatic C-H bonding with increasing treatment time. Signalled by an decrease in absorption in the 1450 to 1300 cm^{-1} wavenumber range, corresponding to bending of aliphatic hydrocarbons, this is evidence that aliphatic regions are preferentially attacked by the oxidizer. There is a limit to this improvement, however, as there is significant damage to the aromatic layers themselves at times greater than 10 minutes. This can be seen in the decreased absorption of the aromatic C=C stretching modes from 1610 to 1470 cm^{-1}. AR pitch fibers are essentially 100% anisotropic, and their infrared spectra showed little change prior to degradation of the aromatic layers.

Therefore, the 10 minute treatment was chosen as optimum for both fiber sets. Fibers from that treatment, in addition to the untreated fibers used as a control, were graphitized to 2400°C in a carbon resistance furnace. X-ray diffraction, single filament tensile testing, and electrical resistivity measurements were used to evaluate the structural improvement resulting from solvent etching. Table 4.18 shows the (0002) spacing, stack height (L_c), coherence length (L_a), and misorientation parameter (Z) of graphitized fibers. Oxidation caused an apparent reduction in d(0002) and in misorientation angle, Z, for the heat-soaked pitch fibers, while the coherence length, L_a, was reduced slightly. AR pitch fibers, however, showed no statistically significant change in d(0002), but the coherence length was drastically reduced and the misorientation angle appeared to increase with oxidative treatment.
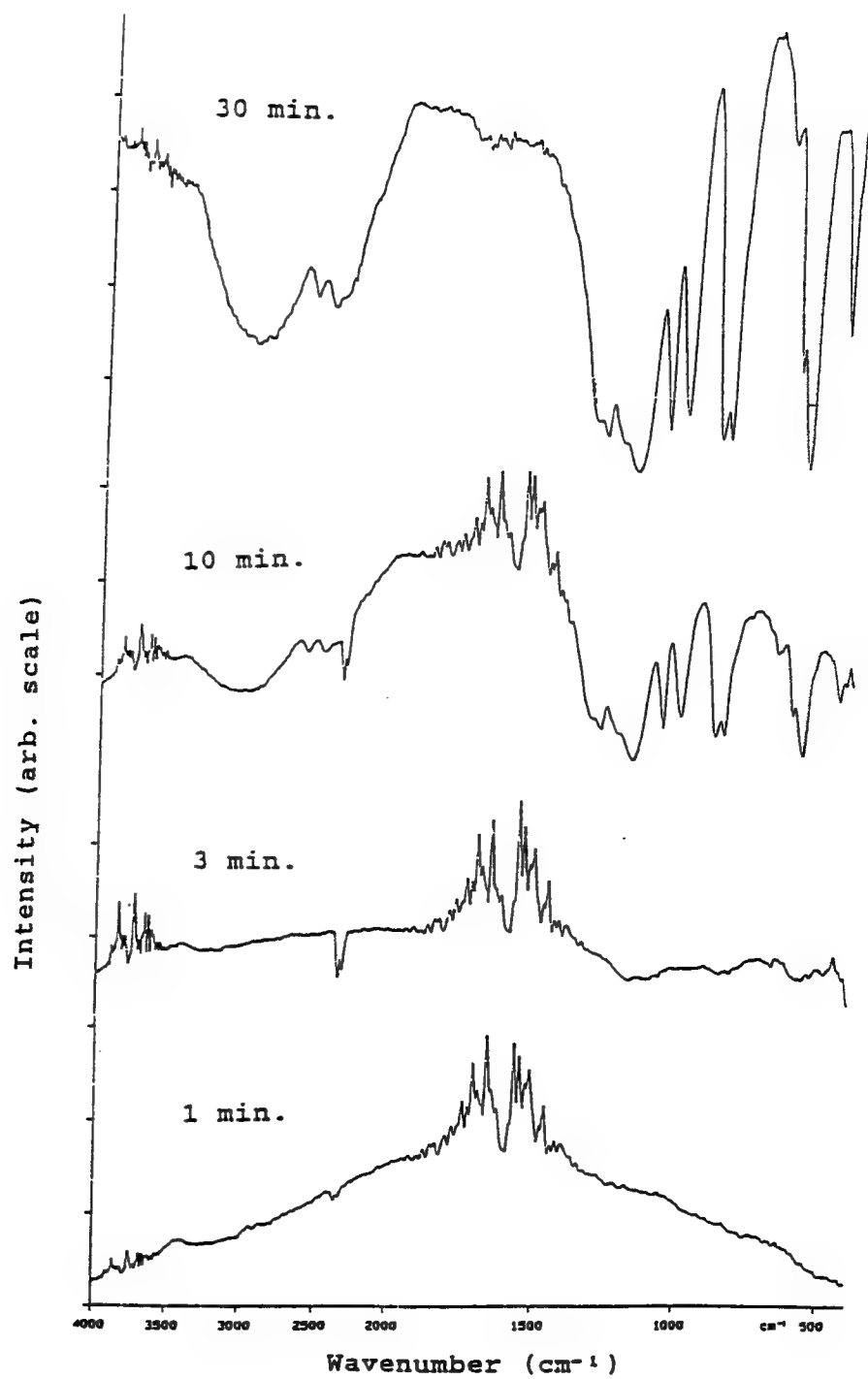
Figure 4.46. Infrared spectra of thermolyzed heat-soaked fibers after solvent treatment.

Table 4.18. X-ray diffraction data for solvent treated and untreated heat-soaked pitch fibers after thermal treatment at 2400°C.

Fiber set	d(0002) (Å)	L_c (Å)	L_a (Å)	Z (°)
petroleum-derived:				
untreated	3.414±0.004	136±6	151±6	16.3±1
treated	3.395±0.004	144±6	133±6	14.8±1
naphthalene-derived:				
untreated	3.405±0.004	136±6	325±6	12.7±1
treated	3.409±0.004	146±6	115±6	14.4±1

The ultimate criteria by which this technique must be judged, however, are the resulting physical properties. It can only be viewed as practical if it leads to improved physical properties for equivalent thermal treatment, or equal properties at a reduced cost. Table 4.19 shows the mean tensile strength, tensile modulus, and electrical resistivity from single filament tests of the treated and untreated petroleum-derived fibers. Included for comparison are the properties of the same untreated fiber set graphitized to 3000°C.

Table 4.19. Physical properties of treated and untreated heat-soaked pitch fibers after graphitization.

Fiber set	Tensile strength (GPa)	Young's modulus (GPa)	Electrical resistivity (10^{-6} Ωm)
untreated, 2400°C	1.76±0.20	226	9.03±3.05
untreated, 3000°C	1.60±0.21	697	5.23±0.41
treated, 2400°C	1.71±0.18	624±151	4.81±0.47

The physical properties of the solvent treated fibers are superior to those of the untreated fibers, even when the latter are graphitized to a much higher temperature. Again, the physical properties of the AR pitch fibers showed little change with solvent etching.

The fact that AR pitch fibers, originally melt spun from a nearly 100% mesophase, show no improvement with solvent etching further confirms the belief that the solvent more readily attacks regions of disorder. Long treatment times, however, result in damage of even the most well-ordered regions. Therefore, an optimum treatment time exists for a given pitch, depending upon its morphology and mesophase content. The tensile modulus and electrical resistivity depend upon lattice perfection throughout the fiber. Thus, their improvement shows that the oxidizing treatment at least indirectly affects the entire volume of the fiber and not just the surface. For example, surface oxidation may result in dimensional changes that, in turn, alter the stress profile across the fiber.

Solvent etching has been shown to enhance the graphitizability and, as a result, the physical properties of petroleum-derived mesophase carbon fibers. If this result can be generalized to any pitch of moderate mesophase content, this technique could prove useful in the production of many carbon products.

4.7. Fiber Morphology

The structure and texture of fibers produced during this study were also examined by K. E. Robinson using SEM and TEM. Figures 4.47 and 4.48 illustrate the textures typically obtained for circular and ribbon-shape fibers, respectively, as observed under the SEM. The circular fiber exhibits a pseudo-radial texture with regions of random transverse arrangement, while the ribbon-shape fiber displays the line-origin texture, but with highly-curved radial-like ends. Figures 4.49 and 4.50 show longitudinal and transverse thin sections of a ribbon-shape fiber heated to 2400°C, respectively, as observed using TEM, together with selected area diffraction patterns from the same region (taken using a 0.2 μm spot size).
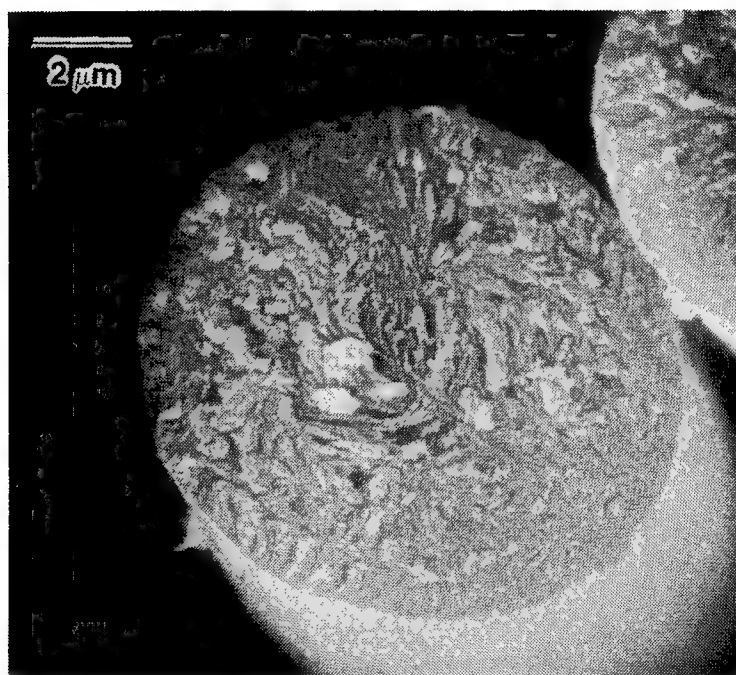
Figure 4.47. SEM micrograph of a circular heat-soaked pitch fiber showing the radial texture.
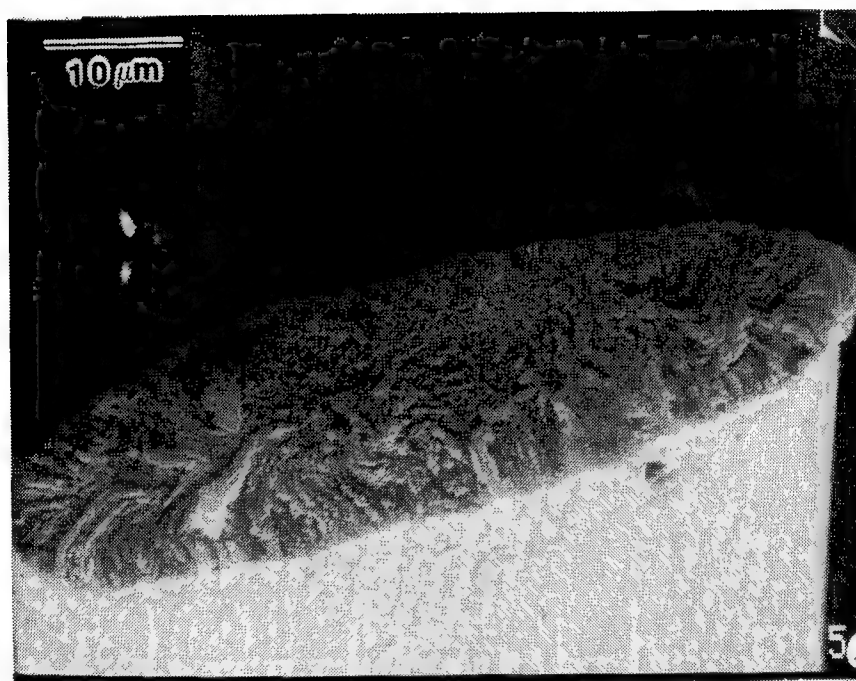
Figure 4.48. SEM micrograph of a ribbon-shape heat-soaked pitch fiber showing the line-origin texture.
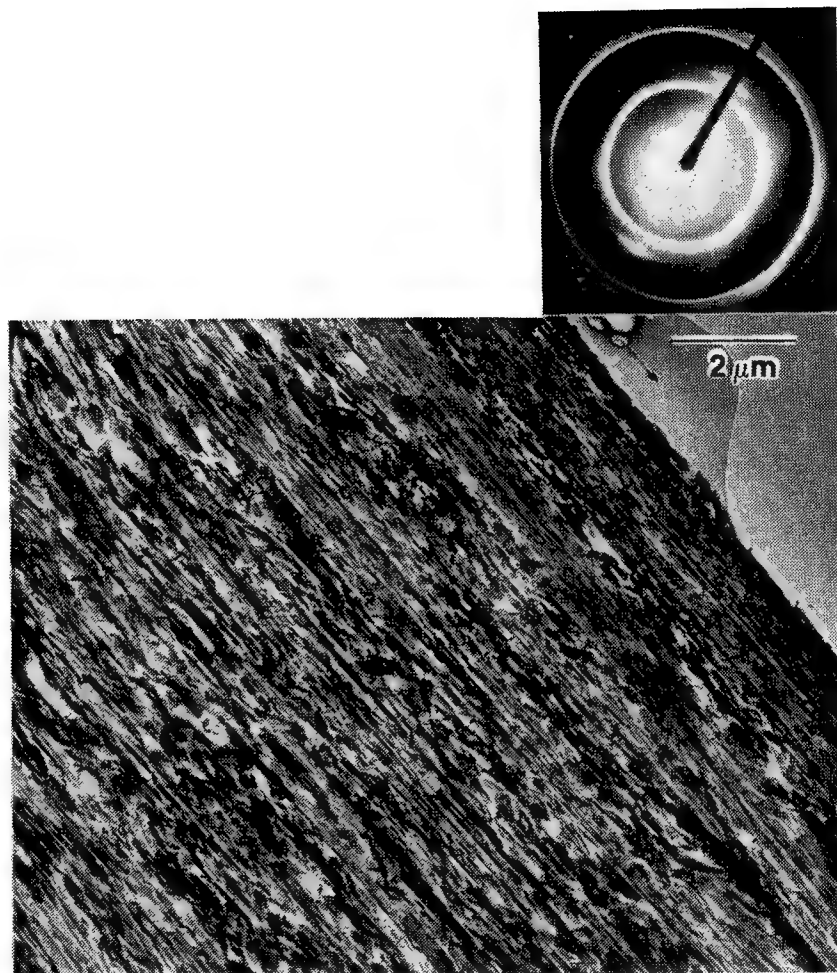
Figure 4.49. TEM micrograph (and SAD pattern) of a longitudinal slice of a ribbon-shape heat-soaked pitch fiber.
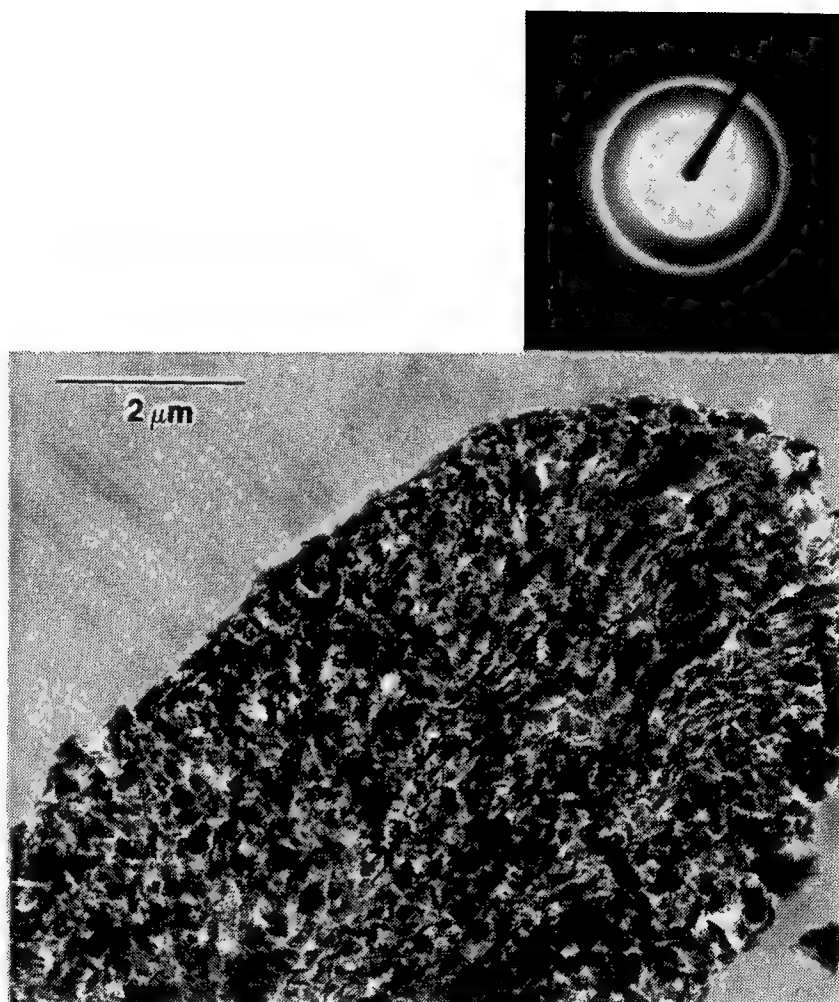
Figure 4.50. TEM micrograph (and SAD pattern) of a transverse slice of a ribbon-shape heat-soaked pitch fiber.

CHAPTER 5

CONCLUSIONS

The results of this study lead to the following conclusions:

1. The lattice-dependent physical properties of carbon fibers could be described by a model based on the motion of phonons through the graphite lattice. Only low temperature specific heat capacities and crystalline parameters, such as the coherence length and the X-ray density, were required.

2. Stabilization consists of multiple exothermic reactions, the first beginning around 170°C in air. Oxygen pick-up below this temperature may have occurred by physisorption and was reversible.

3. A high degree of stabilization (or high oxygen content) caused excessive mass loss during thermolysis. An optimum amount of oxygen existed for both the heat-soaked and the AR pitches that provided sufficient stabilization and minimum mass loss during thermolysis.

4. Graphitization was inhibited in the heat-soaked pitch by the presence of sulfur. The release of carbon disulfide at temperatures above 1600°C caused irreversible expansion, cracking, and misorientation of layer planes about the fiber axis.

5. Increased heating rate during this period reduced basal plane misorientation, resulting in improved lattice-dependent physical properties. However, more cracks were created to facilitate sulfur removal. Thus, tensile strength decreased.

6. Employing longer dwell times at the maximum graphitization temperature following a rapid heating schedule reduced the severity of cracking and resulted in improved physical properties.

7. Structural development in pitches containing less than 100 percent mesophase was enhanced by oxidative etching of isotropic parts or aliphatic side arms at an intermediate point in thermal treatment and subsequent graphitization.

8. Fibers produced from the synthetic AR pitch graphitized more readily than those produced from the heat-soaked pitch, and exhibited improved physical properties at equivalent treatment conditions.

9. Reductions can be made in the production cost of fibers made from heat-soaked pitch by employing efficient stabilization conditions and increasing the heating rate during graphitization. However, if synthetic precursors can be made inexpensively, they have greater potential for producing a high thermal conductivity carbon fiber at low cost.

CHAPTER 6

RECOMMENDATIONS

The following recommendations are suggested for further investigation in this field:

1. As sulfur appears to inhibit structural development during thermal treatment, ways of removing the sulfur from the raw pitch prior to mesophase formation should be considered.

2. The sulfur content, mesophase conversion, and impurity levels may vary between mesophase batches, or within a given batch. Therefore, the variability of the mesophase(s) used in fiber production should be studied.

3. Stabilization has a pronounced effect on thermolysis mass loss and the physical properties of the resulting fibers. The effect of stabilization conditions upon the oxygen concentration profile in the fiber and, in turn, physical properties, should be examined.

4. The lack of available techniques for in situ examination of graphitization kinetics has limited this research. Application of high temperature X-ray diffraction would give a better understanding of the graphitization process.

5. Ways of altering the graphitizability of pitches by selective oxidative attack might be applicable in the production of pitch-bonded materials (e.g. mag-chrome refractories, graphite electrodes).

APPENDICES

Appendix A

Theoretical Development

A.1 Debye Theory of Specific Heat Capacity

All materials have similar specific heat capacity-temperature profiles, with a value of zero at zero degrees Kelvin and increasing as T^n at low temperatures (n usually near 3). As temperature is increased, greater numbers of phonon modes are activated, and the constant volume specific heat capacity reaches a constant value of 3R (R is the gas constant) at the material's Debye temperature (224). This temperature fully characterizes the shape of the profile and varies widely from one material to another. More subtle differences, however, are observed for samples of differing crystal quality but from the same material. Defects, such as inclusions, point defects, dislocations, and grain boundaries, scatter phonons and retard the excitation of long wavelength phonon modes. As their concentration is increased, greater temperatures are required to activate phonon modes; thus, the Debye temperature increases (225).

The theory of heat capacity was developed by Einstein and advanced by Debye. Einstein's model predicted specific heat capacities, based on the assumption of a single frequency for all phonons. This was a simple approach, and Einstein himself realized its limited accuracy. Debye contributed the idea of a phonon frequency distribution with the probability of a given phonon frequency (ν) proportional to ν^2 below a maximum allowed value, ν_{max}. This addition increased the accuracy of the model at higher temperatures and became the basis of specific heat capacity theory. The so-called Debye temperature, θ_D, was defined as a function of this maximum phonon frequency,

$$\theta_D = \frac{h\nu_{max}}{k}, \tag{A.1}$$

where h is Planck's constant and k is Boltzmann's constant (224).

Specific heat capacity is defined as the quantity of heat required to change the temperature of a sample. The constant volume and constant pressure heat capacities are

given by

$$C_v = \left(\frac{\partial E}{\partial T}\right)_{N,V} \quad \text{and} \quad C_p = \left(\frac{\partial H}{\partial T}\right)_{N,P}, \qquad (A.2)$$

respectively, and the specific heat capacities are found by normalizing these values to a constant mass unit. Typically, the constant pressure specific heat capacity is measured in the laboratory. It differs from the constant volume value only by the increase in sample volume with temperature. This difference can be stated as

$$C_p = C_v + \frac{\alpha^2 VT}{\beta}, \qquad (A.3)$$

where α is the volume thermal expansion coefficient, V is the molar volume, and β is the compressibility, given by

$$\alpha \equiv \frac{1}{V}\left(\frac{\partial V}{\partial T}\right)_p \quad \text{and} \quad \beta \equiv -\frac{1}{V}\left(\frac{\partial V}{\partial p}\right)_T \quad (226). \qquad (A.4)$$

Figure A.1 shows that the volume thermal expansion of graphite is near zero for temperatures below 450°C, and that most of the expansion is in the crystallographic c-direction (7). If the specific heat capacity measurement is limited to these temperatures, then the volume expansion term can be neglected and C_p approaches C_v. The quantity of heat needed to raise the sample temperature becomes equal to the change in internal energy and the Debye model can be applied. The total internal energy, E, of a crystal is the sum of several terms,

$$E = \varepsilon_{rot} + \varepsilon_{vib} + \varepsilon_{elec} + \varepsilon_{nuc} + \varepsilon_{chem}, \qquad (A.5)$$

where the subscripts refer to rotational, vibrational, electronic, nuclear, and chemical energy components, respectively. But graphite has no rotational freedom and the electronic contribution is negligible except at temperatures near zero degrees Kelvin. Nuclear and chemical terms also can be ignored, leaving the total energy approximately equal to the vibrational component. The crystal then can be visualized as an array of 3N atoms oscillating about their equilibrium positions, each with energy (n+1/2)hv. Using the general form of the partition function,
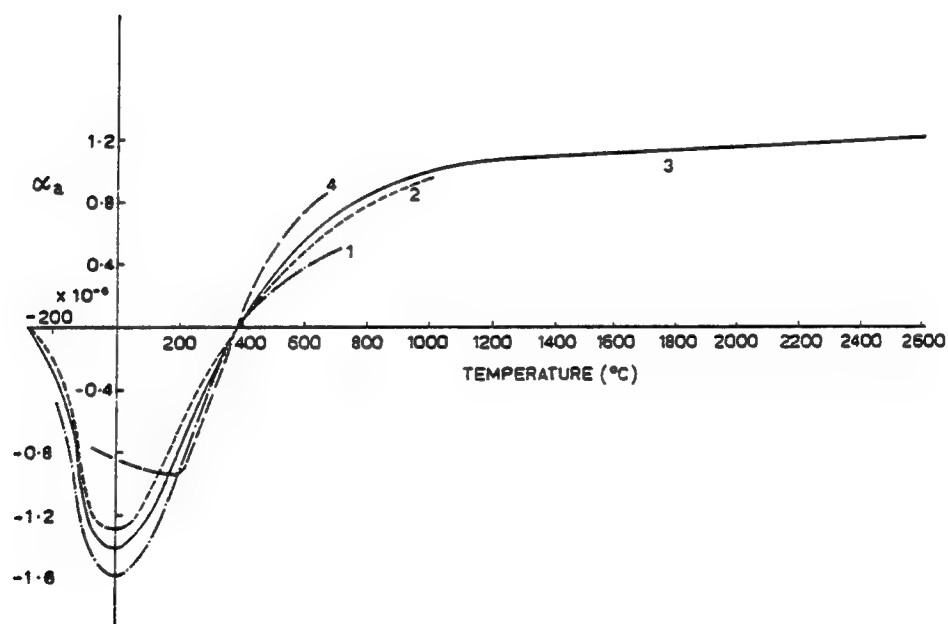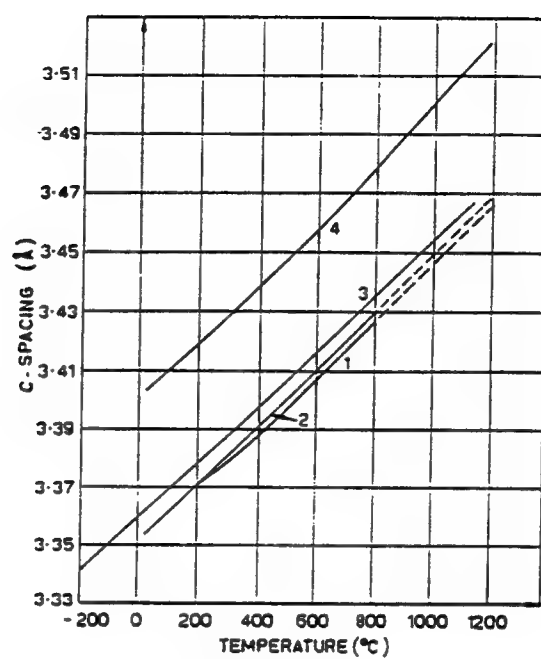
Figure A.1. Volumetric thermal expansion of graphite with temperature (7).

$$Z_{vib} = \sum_{n=0}^{n=\infty} \exp(-\beta \varepsilon_i), \tag{A.6}$$

where the n are eigenvalues, $\beta = 1/kT$, and ε_i is the energy contribution of the ith component, the partition function for vibrational energy can then be written

$$Z_{vib} = \sum_{n=0}^{n=\infty} \exp\left[\frac{-\left(n+\frac{1}{2}\right)h\nu}{kT}\right]. \tag{A.7}$$

Summing the energy of a single oscillator over the total number of oscillators, 3N, would give the total energy of the crystal.

However, three-dimensional propagation of phonons, as assumed in the general theory, is precluded by the anisotropic nature of graphite. Phonons will propagate differently in the basal planes than in the transverse, or c-, direction. This is reasonable since the graphite basal plane consists of strong sp^2-hybridized C-C bonds, while neighboring planes are bound only by secondary (van der Waal's) forces (11). Because lattice-dependent physical properties depend strongly upon the size and orientation of these planes, graphite can be viewed as a collection of rigid, two-dimensional plates that are only loosely coupled. The observation of a T^2, rather than a T^3, dependence of specific heat capacity at temperatures near zero Kelvin led to the "two-dimensional" model of specific heat capacity developed by Komatsu (129, 130), Kelly (165), and Taylor (170). Thus, the total crystal energy is simply the energy of a single oscillator summed over 2N in-plane oscillators,

$$E = 2N\left(\frac{\displaystyle\sum_{n=0}^{n=\infty} \left(n+\frac{1}{2}\right)h\nu \cdot \exp\left[-\left(n+\frac{1}{2}\right)\frac{h\nu}{kT}\right]}{\displaystyle\sum_{n=0}^{n=\infty} \exp\left[-\left(n+\frac{1}{2}\right)\frac{h\nu}{kT}\right]}\right). \tag{A.8}$$

Because this expression includes a phonon frequency term, it must be integrated over the frequency distribution to give the total crystal energy. For the two-dimensional solid, where phonon motion is polarized in the basal plane, the frequency distribution is written as

$$g(v) = 2\pi A\left(\frac{1}{\vartheta_l^2} + \frac{1}{\vartheta_t^2}\right)v, \tag{A.9}$$

where A is the area of the first Brillouin zone, ϑ_l is the longitudinal (axial) in-plane phonon velocity, and ϑ_t is the transverse in-plane phonon velocity.

The constant volume heat capacity is just the derivative of the total crystal energy with respect to temperature, and is equal to

$$C_v = \left(\frac{\partial E}{\partial T}\right)_{N,V} = \frac{4R}{\Omega^2}\int_0^\Omega \frac{x^3 e^x}{(e^x - 1)^2}dx + \zeta. \tag{A.10}$$

The ζ term is the contribution of the out-of-plane phonon mode, and accounts for the two additional degrees of freedom. It is a constant for temperatures above the out-of-plane Debye temperature of around 180K. In this expression, R is the gas constant and Ω is a fittable parameter given by

$$\Omega = \frac{hv_{max}}{kT} = \frac{\theta_D}{T}, \tag{A.11}$$

where θ_D is the Debye temperature. Therefore, the Debye temperature of a graphitizing carbon is found by fitting this model to the measured specific heat capacity profile. A perfect graphite crystal of infinite dimension will have an in-plane Debye temperature of 2350K, and the introduction of any defects, even finite crystal size, increases this value (135, 165, 225).

The population of phonon modes of various energies is characterized by the Debye temperature. Because thermal conductivity and elastic modulus depend upon the propagation and scatter of phonons, the Debye temperature can provide information concerning both thermal conductivity and elastic modulus.

A.2 Application to Thermal Conductivity

Development of the theory of thermal conduction in solids proceeds from the kinetic theory of gases, with phonons replacing gas particles as the energy carrying species. The phonon flux in a given direction x, parallel to the fiber axis, can be written

$$J_{phonon} = \frac{1}{2}n\langle\vartheta_x\rangle, \tag{A.12}$$

where n is the number of activated phonons and $\langle\vartheta_x\rangle$ is the average velocity. In moving from a region of temperature $T + \Delta T$ to a region of lower temperature, T, an amount of energy $c\Delta T$ is lost (c being the heat capacity of a single phonon mode). A quantity Λ, the phonon mean free path, is defined as the average distance that a phonon travels between collisions with other phonons. It is equal to the product of phonon velocity and time between collisions, τ, giving

$$\Delta T = \frac{dT}{dx}\Lambda = \frac{dT}{dx}\langle\vartheta_x\rangle\tau. \tag{A.13}$$

The net energy flux in this direction is just the product of the phonon flux in this direction and the amount of energy lost in moving down the temperature gradient.

$$J_x = -n\langle\vartheta_x^2\rangle c\tau\frac{dT}{dx}. \tag{A.14}$$

If the phonon velocity is assumed to be constant, the mean velocity designation can be dropped. The net energy flux can then be rewritten as

$$J_x = \frac{1}{2}C_v\vartheta\Lambda\frac{dT}{dx}, \tag{A.15}$$

after applying the conditions that $C_v = nc$ and $L = \vartheta\tau$. Recalling Fourier's law of heat conduction, the thermal conductivity, K, is found by inspection to be

$$K_x = \frac{1}{2}C_v\vartheta\Lambda\varphi, \tag{A.16}$$

where the added term, φ, is the molar density (168, 169, 172). The presence of the C_v term indicates that the thermal conductivity should increase with the same temperature dependence as the specific heat capacity, between T^2 and T^3. This would be true if the other terms were temperature independent. The phonon mean free path, however, decreases with temperature in a way predicted by the Debye temperature. At low temperatures, the phonon concentration is small and the mean free path is roughly equal to the coherence length (L_a). Phonon scattering occurs at physical obstructions, such as grain boundaries or pores, and is termed geometrical scattering. Phonon-phonon interaction, or Umklapp scattering, requires phonon energies of $(1/2)k\theta_D$, so that the collision vector extends out of the first Brillouin zone. Since the population of phonons having this energy varies as $\exp(-\theta_D/2T)$, K is proportional to $\exp(\theta_D/2T)$ at high temperatures (169). The

result is a maximum thermal conductivity at the point where decreasing mean free path from Umklapp processes overtakes the coherence length, or geometrical mean free path. For well-ordered graphite, this maximum takes place near 100K; for fibers and less ordered carbons, the maximum occurs near room temperature (5, 166).

For carbons with Debye temperatures much higher than that of ideal graphite, a correction must be made. The electronic contribution to thermal conductivity, negligible in ideal graphite above about 10K, becomes appreciable even above room temperature. This contribution is described by the Wiedemann-Franz law, which states that the thermal conductivity due to electrons is proportional to the absolute temperature of interest divided by the electrical resistivity at that temperature,

$$K_{electronic} = \frac{T}{\rho}\xi.$$
(A.17)

The constant of proportionality is ξ, the Lorentz number, found to be constant with a magnitude of 2.45×10^{-8} $A^2\Omega^2/K^2$ for most conductors (169). Adding the electronic contribution to the phonon contribution should give a thermal conductivity near the measured value.

Thus, the specific heat capacity and the Debye temperature of a carbon are indicators of the slope and position of the thermal conductivity profile with temperature. A similar relationship can be seen with axial elastic modulus.

A.3 Application to Young's Modulus

Lattice vibrations confined to the two-dimensional basal planes involve only stretching and shearing actions. Therefore, only the C_{11} and C_{12} terms of the stiffness tensor are applicable. Substituting v_{max} for v in the frequency distribution expression and combining with the definition of θ_D, gives the Debye temperature as a function of the directional phonon velocities,

$$\theta_D = \frac{h}{k}\left[2\pi A\left(\frac{1}{\vartheta_l^2} + \frac{1}{\vartheta_t^2}\right)\right]^{-1}.$$
(A.18)

The velocities are related to components of the stiffness tensor by elastic theory. There

relationships are

$$\vartheta_l = \left(\frac{C_{11}}{\rho}\right)^{\frac{1}{2}} \quad \text{and} \quad \vartheta_t = \left[\frac{(C_{11} - C_{12})}{2\rho}\right]^{\frac{1}{2}}, \tag{A.19}$$

where ρ is the density of the carbon (129,130). Again, making the assumption that the in-plane phonon velocities are equal, E_x, Young's modulus parallel to the fiber axis, can be determined from

$$E_x \cong C_{11} = \frac{\pi \rho h^2}{k^2 \theta_D^2 d(0002) A}, \tag{A.20}$$

where A is a constant. Constant C_{11} is normally the theoretical tensile modulus parallel to the layer plane. Here, however, it is the tensile modulus calculated for a "defect" crystal structure and should equal the measured tensile modulus.

A.4. Thermolysis Reaction and Transport Model

The nature of mesophase pitch prevents accurate description of its molecular make-up, but its thermolysis is treated here as a gross decomposition reaction of the form

carbonaceous solid 1 → volatile product + carbonaceous solid 2, or

$$AB(s) \rightarrow A(g) + B(s). \tag{A.21}$$

For pitch-coke similar to stabilized mesophase pitch, several authors have shown this process to obey first-order kinetics with an activation energy of 50 to 100 kcal/mole (69-71). Volatile species must then migrate radially (axial transport is neglected) to the fiber surface. And if transport through the fiber bundle is included, the process can be described by

$$\frac{\partial c_A}{\partial t} = D\nabla^2 c_A + k_1''' c_A, \tag{A.22}$$

where

c_A = molar concentration of volatile species {moles/m^3},

t = time {seconds},

D_{AB} = mass diffusivity of A in B {m^2/sec}, and

k_1''' = first-order reaction rate constant {moles/m^3/sec}.

This expression is a special case of the general equation of change for mass transfer,

$$\frac{\partial c_A}{\partial t} + \left(\overline{\nabla \cdot N_A}\right) = R_A, \tag{A.23}$$

where N_A is the molar flux and R_A is the molar rate of reaction; constant values of density and diffusivity of A in B are assumed and the velocity term is neglected for solid B. The initial concentration of species A is a non-zero function of bundle "radius", f(r), determined by the initial pitch composition and stabilization extent. At the bundle surface, transport is hindered by a stagnant gas film of thickness δ. Outside this film, $c_A = 0$ in a flowing inert gas, but the fiber surface concentration is an unknown constant. Therefore, the boundary conditions are (1) constant flux at the bundle surface, and (2) zero flux at the fiber axis. A summary of these conditions and a sketch of the problem geometry are given in Figure A.2. Transport of volatile species A from the fiber bundle is described by a mass transfer coefficient, k_c, having units of moles/cm^2/sec. The concentration of A at the bundle surface is given by C_{A_s}, while the concentration at an infinite distance from the bundle is given by C_{A_∞} (199).

Equation A.22 was solved by Todd Brandes (201) for each process that comprises thermolysis using a finite difference algorithm. Thus, the process rate constants and their activation energies were estimated, as well as a general diffusion coefficient and its activation energy.

A.5 Kinetic Expressions for DSC and TGA Analyses

If the mechanism (order, etc.) of a process is unknown but can be postulated, then a method derived by Sharp et al. (227) can be used. Chosen because of its general form, it is based upon the expression

$$\ln\left(\frac{1}{f(\alpha)} \cdot \frac{d\alpha}{dT}\right) = \ln\frac{A}{B} - \frac{\Delta E}{RT}, \tag{A.24}$$

in which α is a degree of reaction completion, A and B are fittable constants, ΔE is the activation energy of the rate-limiting process, and R is the gas constant. The function f(α) is a kinetic form dependent upon the mechanism involved. It is related to the general rate
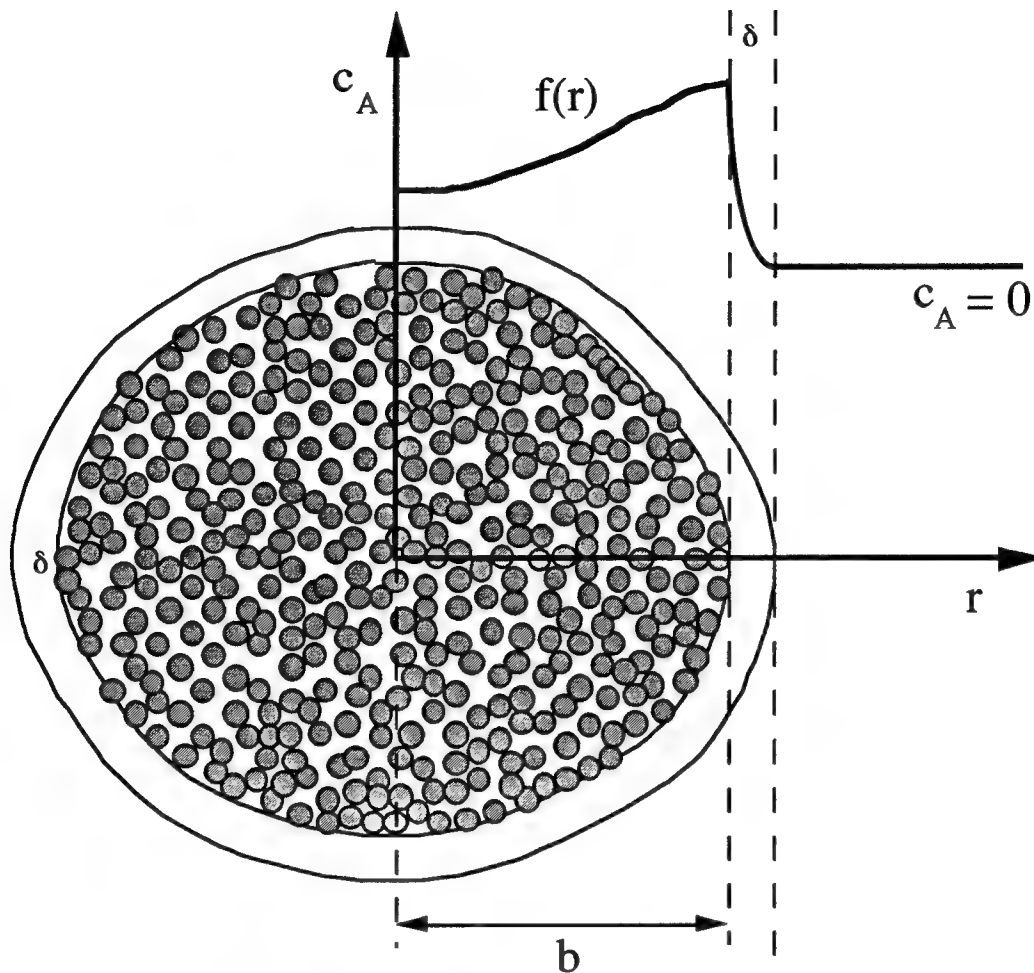
$\bullet$ = circular carbon fiber

initial condition: $c_A = f(r)$ at $t = 0$ (A.25)

boundary condition 1: flux $= -D_{AB} \nabla c_A = 0$ at $r = 0$ for all t (A.26)

boundary condition 2: flux $= -D_{AB} \nabla c_A = k_c(C_{A_s} - C_{A_\infty})$ for all t (A.27)

Figure A.2. System geometry and boundary conditions.

equation,

$$g(\alpha) = kt, \tag{A.28}$$

by the expression

$$f(\alpha) = \frac{1}{\dfrac{dg(\alpha)}{d\alpha}}. \tag{A.29}$$

Several commonly used forms of $g(\alpha)$ and $f(\alpha)$ are presented in Table A.1 (198).

Table A.1. Forms of $g(\alpha)$ and $f(\alpha)$ for different mechanisms (198).

mechanism	$g(\alpha)$	$f(\alpha)$
one-dimensional diffusion	α^2	$\dfrac{1}{2\alpha}$
two-dimensional diffusion	$(1-\alpha)\cdot \ln(1-\alpha) + \alpha$	$-\dfrac{1}{\ln(1-\alpha)}$
three-dimensional diffusion (Jander)	$\left[1-(1-\alpha)^{1/3}\right]^2$	$\dfrac{1}{-1+\frac{2}{3}(1-\alpha)^{-2/3}-\frac{2}{3}(1-\alpha)^{-1/3}}$
three-dimensional diffusion	$\left(1-\frac{2}{3}\alpha\right)-(1-\alpha)^{2/3}$	$\dfrac{1}{\frac{1}{3}+\frac{2}{3}(1-\alpha)^{-1/3}}$
random nucleation; one nucleus per particle	$-\ln(1-\alpha)$	$(1-\alpha)$
random nucleation; Avrami eqn. I	$[-\ln(1-\alpha)]^{1/2}$	$2(1-\alpha)[-\ln(1-\alpha)]^{1/2}$
random nucleation; Avrami eqn. II	$[-\ln(1-\alpha)]^{1/3}$	$3(1-\alpha)[-\ln(1-\alpha)]^{2/3}$
phase boundary reaction (cylindrical sym.)	$1-(1-\alpha)^{1/2}$	$\dfrac{1}{-1+\frac{1}{2}(1-\alpha)^{-1/2}}$
phase boundary reaction (spherical sym.)	$1-(1-\alpha)^{1/3}$	$\dfrac{1}{-1+\frac{1}{3}(1-\alpha)^{-2/3}}$
first-order reaction	$(1-\alpha)$	$-\ln(1-\alpha)$
second-order reaction	$(1-\alpha)^2$	$\dfrac{1}{(1-\alpha)}$
third-order reaction	$(1-\alpha)^3$	$\left[\dfrac{1}{(1-\alpha)}\right]^2$

A.6. Van Krevelen Approach to Elemental Analysis of Hydrocarbons

A great deal of information about the size and condensation of the aromatic macromolecules that make up the fiber at any point in the thermal treatment process can be gained from elemental analysis. The methods presented here are found in older literature on coal science and technology, by such authors as van Krevelen (222).

First, the elemental mass percentages determined by elemental analysis techniques must be converted to atom, or mole, fractions. This is done by dividing each element's mass percentage by its atomic mass to give the relative number of moles of that element present. That number, divided by the sum of moles of all elements present gives the atom, or mole, fraction of that element present. Table A.2 illustrates this calculation, assuming the presence of C, H, S, and O.

Table A.2. Conversion of mass percentages to atom, or mole, fractions.

Element	Mass %	Relative no. of moles	Atom fraction
carbon	c	$C = c/12.011$	$\overline{C} = C/A$
hydrogen	h	$H = h/1.008$	$\overline{H} = H/A$
sulfur	s	$S = s/32.060$	$\overline{S} = S/A$
oxygen	ø	$\emptyset = \emptyset/15.999$	$\overline{O} = \emptyset/A$
		$A = C + H + S + \emptyset$	

In a pure hydrocarbon, the proportions of hydrogen and carbon that are present will indicate the proportion of aliphatic and aromatic C-H bonding. In a linear hydrocarbon molecule, such as shown schematically in Figure A.3, the hydrogen fraction is given by

$$\overline{H} = 2\overline{C} + 2.$$ (A.30)

As aromatic rings are added, the hydrogen fraction will decrease. With the closing of each aromatic ring, the number of hydrogen atoms decreases by two, while substitution of
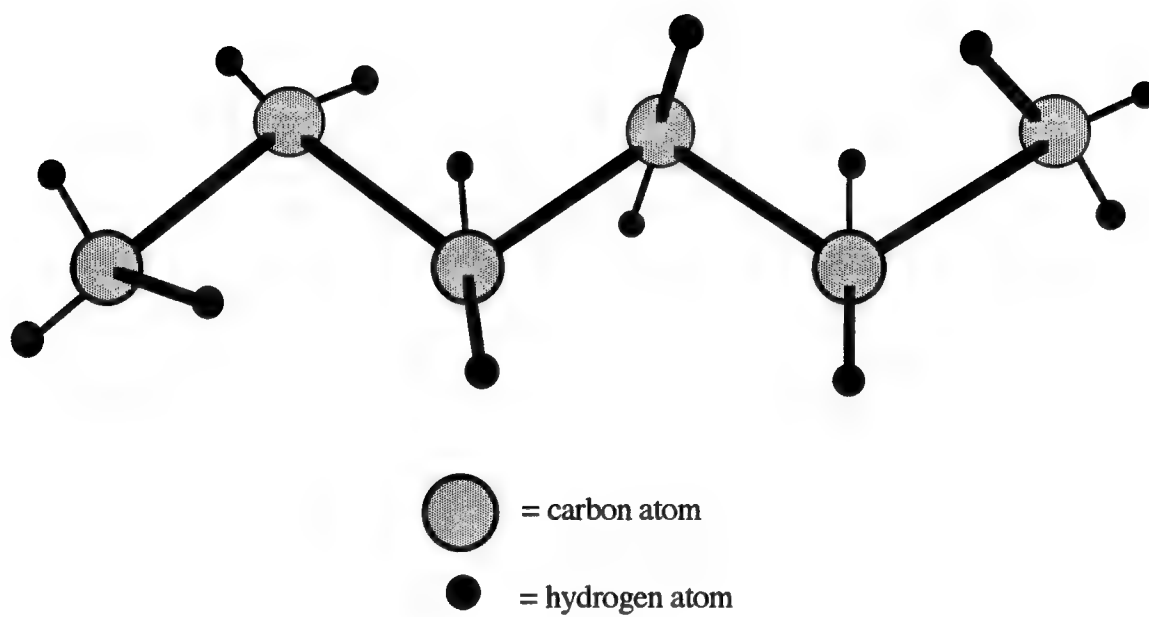
Figure A.3. Linear hydrocarbon molecule.

a saturated carbon atom by an aromatic carbon atom causes the elimination of one hydrogen atom. Therefore, the hydrogen atom fraction can be expressed as

$$\overline{H} = 2\overline{C} + 2 - 2\overline{R} - \overline{C}_a, \tag{A.31}$$

where $\overline{R}$ is the number of aromatic rings and $\overline{C}_a$ is the fraction of carbon atoms that belong to aromatic rings.

The approach presented above is applicable only to carbon-hydrogen systems. Real systems, such as coal and petroleum pitch, may contain large quantities of nitrogen, oxygen, and sulfur. Also, because their molecular weight is often unknown, this method is restricted to the determination of the constitution of a mean structural unit, similar to the monomer in a polymer compound. Therefore, a "reduced molecular weight per carbon atom," designated by M_c, is defined to describe the fiber composition. Assuming that only carbon, hydrogen, sulfur, and oxygen are present, this quantity is given by

$$M_c = 12.011 + 1.008\frac{\overline{H}}{\overline{C}} + 32.060\frac{\overline{S}}{\overline{C}} + 15.999\frac{\overline{O}}{\overline{C}}. \tag{A.32}$$

The aromaticity and condensation state of the average molecule is determined by considering the contributions of aromatic and aliphatic carbon, hydrogen, sulfur, and oxygen atoms to the total molecular volume. In general, a molar physical property can be written

$$\overline{MF} = \sum_i \overline{X}_i \varphi_i = \overline{C}\varphi_C + \overline{H}\varphi_H + \overline{S}\varphi_S + \overline{O}\varphi_O, \tag{A.33}$$

where $\overline{MF}$ is the additive molar function, $\overline{M}$ is the average molecular weight, $\overline{X}_i$ is the concentration of the ith species, and φ_i is the contribution of the ith species to the additive molar function. Because $\overline{M}$ is usually unknown, the reduced molecular weight is used. Equation A.32 is divided by $\overline{C}$ and becomes

$$M_c F = \frac{\overline{MF}}{\overline{C}} = \varphi_C + \frac{\overline{H}}{\overline{C}}\varphi_H + \frac{\overline{S}}{\overline{C}}\varphi_S + \frac{\overline{O}}{\overline{C}}\varphi_O. \tag{A.34}$$

If F is defined as the molar specific volume, $1/\rho$, then, from tabulated atomic volume data,

$$\frac{M_c}{\rho} = 9.9 + 3.1\frac{\overline{H}}{\overline{C}} + 14\frac{\overline{S}}{\overline{C}} + 3.75\frac{\overline{O}}{\overline{C}} - \left(9.1 - 3.65\frac{\overline{H}}{\overline{C}}\right)\frac{\overline{R}}{\overline{C}}. \tag{A.35}$$

Thus, the total number of rings per carbon atom, $\overline{R}/\overline{C}$, can be calculated from density and

elemental composition measurements. A more useful parameter, however, is the ring condensation index, RCI, which ranges from zero for non-condensed aromatic rings to one for graphite. This quantity is defined as

$$RCI = 2\frac{\overline{R} - 1}{\overline{C}}.$$
(A.36)

But, if $\overline{R}$ is assumed to be much greater than one, then $RCI \cong \overline{R}/\overline{C}$.

As the volume contribution of a given atom does depend on the nature of its bonding, corrections must be made to this general calculation to describe the specific molecular arrangement. Tabulations of atomic volume corrections for sulfur and oxygen based on their bonding are available, and these terms are simply added to the calculated molar volume, M_c/ρ. For example, if sulfur occurs primarily in the form of aromatic -S- groups, and oxygen in the form of -OH and -O- groups, then the molar volume becomes

$$\left(\frac{M_c}{\rho}\right)_{corrected} = \frac{M_c}{\rho} - \left(12.5\frac{\overline{S}}{\overline{C}} + 8.1\frac{\overline{O}}{\overline{C}}\right).$$
(A.37)

Elemental analysis can also be used to monitor the chemical changes that occur during thermal treatment, and to identify chemical reaction that occur. For example, during the early stages of carbonization, most of the chemical changes that occur involve carbon, hydrogen, and oxygen. The atomic $\overline{H}/\overline{C}$ and $\overline{O}/\overline{C}$ ratios of samples taken at various points in the process can be plotted on a van Krevelen diagram, such as shown in Figure A.4. The diagram is constructed so that matching the slope of a line through neighboring compositional data points to the slope of a line on the diagram allows the chemical process to be identified. Additional constructions could be devised to include sulfur, nitrogen, and any other constituent.

A.7. Characteristic Infrared and Raman Wavenumbers

The following tables give a brief listing of some important characteristic infrared and Raman frequencies that pertain to carbons having substituted hydrogen, oxygen, and sulfur.
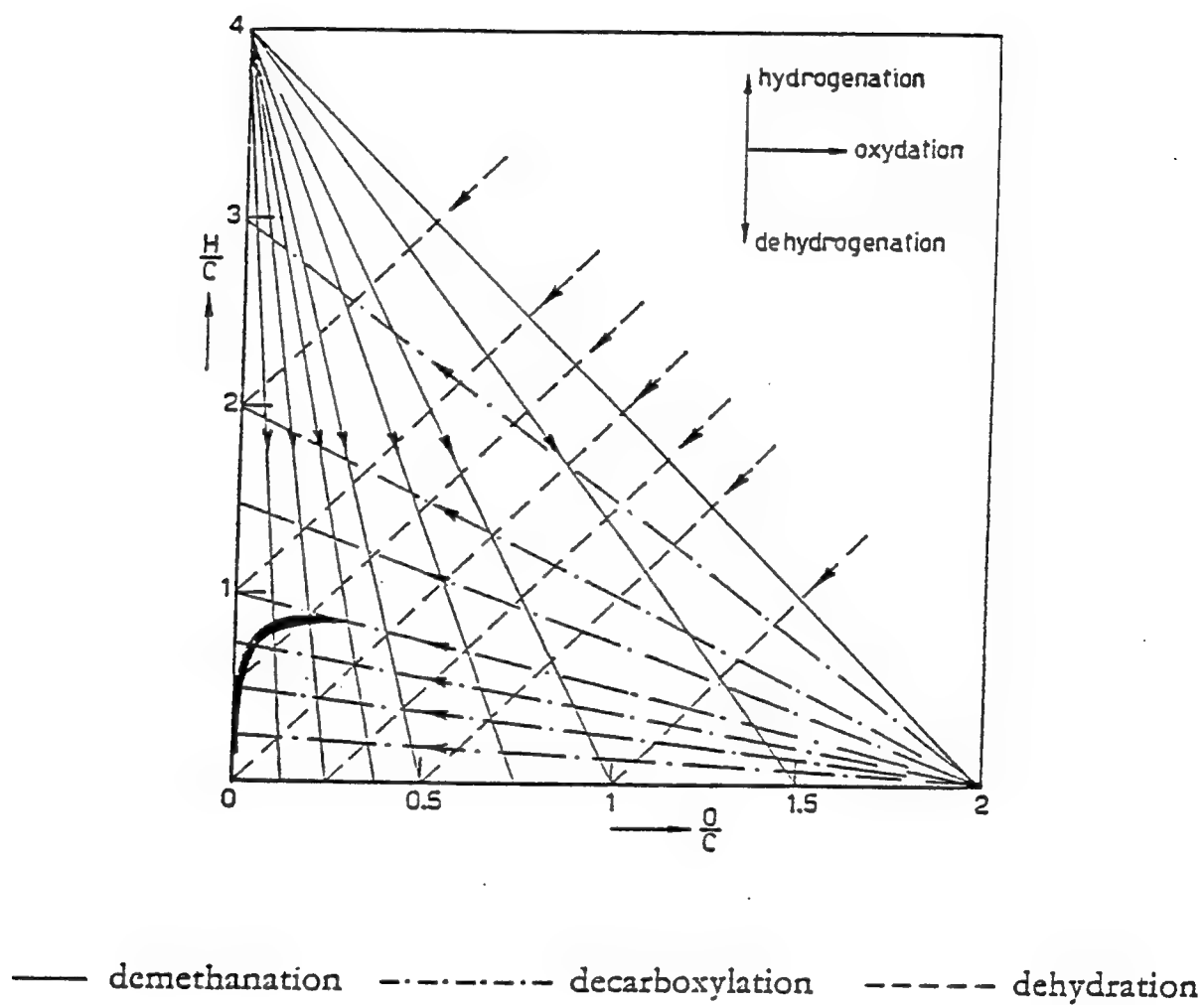
Figure A.4. Van Krevelen diagram of atomic $\overline{H/C}$ and $\overline{O/C}$ ratios (222).

Table A.3. Characteristic infrared frequencies (228, 229).
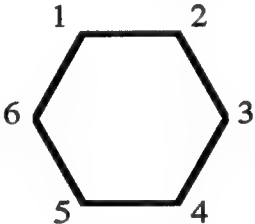
Contributing group	Mode	Wavenumber (cm^{-1})
O-H	stretching	3450
C=O	stretching	1840, 1770, 1720, and 1700
C-O	stretching	1250-1150
alkyl C-H	stretching	2945
alkyl C-H	deformation	1450
-COCH$_3$	asymmetric scissors	1450-1400
	symmetric scissors	1360-1355
CH$_3$-O-	symmetric scissors of CH$_3$	1470-1430
aromatic-COOH	stretching	1250
aromatic-OH	stretching	1235
aromatic-CH$_2$OH	stretching	1227
aromatic-H	stretching	3030
aromatic C=C	stretching	1611-1470
aromatic-H	in-plane bending	1300-100
aromatic-H	out-of-plane bending	900-700
aromatic skeleton	out-of-plane bending	438
aromatic substitution:		

mono-substituted	5 free H	770-730 and 710-690
1:2 di-substituted	4 free H	770-735
1:3 di-substituted	1 free H	900-860
	3 free H	810-750
1:4 and 1:2:3:4 substituted	2 free H	860-800
1:2:3 tri-substituted	3 free H	880-770
1:2:4 tri-substituted	2 free H	860-800
1:3:5 tri-substituted	1 free H	900-860, 865-810, and 730-675
1:2:3:5, 1:2:4:5, and 1:2:3:4:5 sub.	1 free H	900-860

Table A.4. Characteristic Raman frequencies (230, 231).

Contributing group	Mode	Wavenumber (cm^{-1})
E_{2g2}	in-plane "breathing"	1580
sp^3-hybridized C	occurs in graphites because of finite layer size	1355
benzene and its derivatives:		
CH_3	symmetric deformation	1460-1440
CH_3	asymmetric deformation	1390-1370
C-H	tertiary deformation	1360-1330
CH_2	twisting and wagging	1310-1300
C-H	out-of-plane bending	750, 800, 870, and 2920
O-H	stretching	3400
inorganics	?	580 and 1030
S-S	chain stretching (cystine)	496
S-H	stretching	2590-2560
C-SH	deformation	806
C-S	stretching	704

Appendix B

Equipment and Materials List

1. Melt-spinning equipment
    a. Akron extruder. One inch diameter screw. Manufactured by Akron Extruders, Inc., Canal Fulton, Ohio. Used to spin circular- and ribbon-shape fibers from mesophase pitch.
    b. Screen filters. 0.99 inch diameter, 1400 mesh screen. Manufactured by Jelliff Corporation, Southport, Connecticut. Used to filter impurities from pitch during spinning.
    c. Spinnerettes. Manufactured by National Jet Company, Inc., Cumberland, Maryland. Used to spin mesophase into fiber from.
    d. Winder. Motor controller model 2301. Manufactured by Fincor Incom International, Inc. York, Pennsylvania, and distributed by Industrial Power Drives and Controls, Inc., Greenville, South Carolina. Used to draw and collect spinning filaments.

2. Stabilization equipment.
    a. Oven. Oven from a dismantled gas chromatograph, model 2625-4X. Manufactured by Bendix Corporation, Columbia, Maryland.
    b. Temperature sensor. Type K inconel overbraid thermocouple, part number XCIB-K-5-2-3. Manufactured by Omega Engineering, Inc., Stamford, Connecticut.
    c. Contoller. Electromax® V single-loop controller, model 6011-3-15-1--7-50-02-000. Manufactured by Leeds and Northrup Company, North Wales, Pennsylvania. Used to control temperature of stabilization furnace.

Because of the wide range of temperatures and heating rates employed in this study, three furnaces, each having different attributes, were used in this study. Furnace I was used for carbonization at temperatures between 1800 and 2400°C. Designed similarly but with higher temperature capability, Furnace II was used to carbonize fibers to temperatures as high as 3000°C. Finally, Furnace III was used at temperatures at and below 1000°C.

3. Carbonization Furnace I.
    a. Astro Furnace. Carbon resistance element furnace, model 1000-3560-FP20. Manufactured by Thermal Technology, Inc., Santa Barbara, California. Used to carbonize fibers to temperatures between 1000 and 2400°C.
    b. Temperature sensor. Thermalert 4 Pyrometer. Manufactured by Raytec, Inc., Santa Cruz, California.
    c. Controller. Electromax® V single-loop controller, model 6011-3-15-1--7-50-02-000. Manufactured by Leeds and Northrup Company, North Wales, Pennsylvania. Used to control temperature of carbonization furnace.

4. Carbonization Furnace II.
    a. Carbon resistance furnace manufactured by American Furnace Company, Inc., Knoxville, Tennessee. Used to carbonize fibers to temperatures up to 3000°C.
    b. Temperature sensor. Pyrometer. Manufactured by Ircon, Niles, Illinois.

    c.   Controller. Model MAQ. Manufactured by Barber-Coleman Company, Loves Park, Illinois.

5.   Carbonization Furnace III.
    a.   Furnace. Lindberg Hevi-Duty Single Zone Tube Furnace. Manufactured by Lindberg / Blue M, a unit of General signal, Watertown, Wisconsin.
    b.   Temperature sensor. Type K general purpose thermocouple. Manufactured by Omega Engineering, Inc., Stamford, Connecticut.
    c.   Controller. Model MAQ. Manufactured by Barber-Coleman Company, Loves Park, Illinois.

6.   Thermal Treatment Accessories.
    a.   Steel Gauze. 18 mesh. Used to support fibers during stabilization.
    b.   Fiber tow. Thornel T-300 ex-PAN carbon fiber. Manufactured by Amoco Performance Products, Parma, Ohio. Used to tie fiber samples to wire or push rods.
    c.   Carbon rods. 6.5 mm diameter spectroscopic grade carbon rods, part number L4303. Manufactured by National Spectroscopic Carbon. Used to load/remove fiber samples from Furnace II during carbonization treatments.
    d.   Nickel-chrome alloy wire. Tophet® A. Manufactured by Wilbur B. Driver Co., Newark, New Jersey. Used to load/remove fiber samples from Furnace III during carbonization treatments.
    e.   Graphite Adhesive. Part 931. Manufactured by Cotronics Corporation, Brooklyn, New York. Used to repair graphite furnace parts as well as to join lengths of carbon rod.
    f.   High temperature anti-seize lubricant. Hi-Temp C5-A. Manufactured by Fel-Pro, Inc., Skokie, Illinois. Used to prevent seizing of metal parts in Furnace I during operation.
    g.   High temperature sealant tape. Manufactured by General Sealants, City of Industry, California. Used to improve vacuum seal in Furnace I.

7.   Differential Scanning Calorimetry Equipment
    a.   DSC. Model 910 Differential scanning calorimeter. Manufactured by Du Pont Thermal Analysis Instruments, Wilmington, Delaware.
    b.   Sample pans and lids. Part numbers 900786.901 and 900779.901, respectively. Manufactured by Thermal analysis Instruments, Wilmington, Delaware.
    c.   Controller. Model 990 Thermal analyzer. Manufactured by Du Pont Thermal Analysis Instruments, Wilmington, Delaware. Used to control the 910 DSC cell and to collect data.
    d.   Data Logger. Model OM-160. Manufactured by Omega Engineering, Inc. Stamford, Connecticut. Connected to 990 Thermal analyzer and used to record data.
    e.   Input modules. Models MOD13/14 and MOD12. Manufactured by Omega Engineering, Inc., Stamford, Connecticut. Accept 0-2 V and 0-100 mV analog signals, respectively, and interface with the OM-160 data logger.
    f.   Data acquisition software. "Pronto," manufactured by Omega Engineering, Inc., Stamford, Connecticut. Used to read data from the OM-160 data logger and create usable data files.

Two thermogravimetric analysis systems were employed in this study. The first,

consisting of a Cahn electrobalance and wire-wound tube furnace, was used for the bulk of

the measurements. The second dealt with a smaller sample size and was used only to confirm results from the former.

8. Thermogravimetric Analysis Equipment I.
    a. Balance. Model RH Electrobalance. Manufactured by Cahn Instruments, Cerritos, California.
    b. Furnace. High-alumina refractory castable and silicon carbide heating elements.Manufactured at Clemson University.
    c. Temperature sensor. Type S (platinum vs. platinum-13% rhodium) thermocouple manufactured at Clemson University.
    d. Cam controller.
    e. Temperature chart recorder. Manufactured by Barber-Coleman Company, Rockford, Illinois.
    f. Mass chart recorder. Manufactured by Omega Engineering, Inc., Stamford, Connecticut.

9. Thermogravimetric Analysis Equipment II.
    a. TGA. Model 951 Thermogravimetric Analyzer. Manufactured by Du Pont Thermal Analysis Instruments, Wilmington, Delaware.
    b. Controller. Thermal Analyst 2100. Manufactured by Du Pont Thermal Analysis Instruments, Wilmington, Delaware.

10. Elemental Analysis Equipment (located at Galbraith Laboratories, Knoxville, Tennessee).
    a. CHN measurement. CHN 800 Determinator. Manufactured by Leco Corp., St. Joseph, Michigan. Used to determine carbon, hydrogen, and nitrogen contents in fiber samples.
    b. Oxygen measurement. Model RO-478 Oxygen Determinator. Manufactured by Leco Corp., St. Joseph, Michigan. Used to determine oxygen content in fiber samples.
    c. Sulfur analyzer. SC 432DR Sulfur Analyzer. Manufactured by Leco Corp., St. Joseph, Michigan.Used to determine sulfur content in fiber samples.

11. Evolved Gas Analysis Equipment.
    a. Septum. Neoprene, Teflon®-faced HTLB septa 0.394 75805. Manufactured by Hamilton Company, Reno, Nevada.
    b. Syringe. Gas-tight syringe 1725LTCH81103. Manufactured by Hamilton Company, Reno, Nevada.
    c. Gas sampling vials. 12 mm x 32 mm sampler vials. Part number 2-2123. Manufactured by Supelco, Inc., Bellefonte, Pennsylvania.
    d. Seals and Septa. 11mm seals and double-faced Teflon®-silicone septa. Part number 3-3119. Manufactured by Supelco, Inc., Bellefonte, Pennsylvania.
    e. Gas chromatograph/mass spectrometer. HP5890A Gas chromatograph. Manufactured by Hewlett-Packard Company, Avondale, Pennsylvania.

12. Wide Angle X-ray Diffraction Equipment.
    a. X-ray diffractometer. Model XDS 2000. Manufactured by Scintag X-ray Diffraction Systems, Inc., Santa Clara, California.
    b. Aluminum washers. 2 cm ID by 2.54 cm OD by 0.8 cm thick aluminum washers. Manufactured by Bokkers, Inc., Minneapolis, Minnesota. Used as fiber sample holders.
    c. Paraffin wax. Manufactured by Walnut Hill Company, Bristol, Pennsylvania. Used to create a rigid fiber-paraffin composite diffraction sample.

    d.   Adhesive. Krazy Glue® Gel. Manufactured by Borden, Inc., Columbus, Ohio. Used to affix composite to aluminum washer.

13. Small Angle X-ray Diffraction Equipment (located at Oak Ridge National Laboratory, Knoxville Tennessee).
    a.   Aluminum sample holders. Provided by Dr. S. Spooner of ORNL, Knoxville, Tennessee.
    b.   Small angle X-ray diffractometer. Rigaku X-ray tube with a Cu target.

14. Electrical Resistivity Measurement.
    a.   Copper wire. 0.005 in. diameter. Manufactured by Omega Engineering, Inc., Stamford, Connecticut.
    b.   Duco® cement. Manufactured by Devcon Corp., Wood Dale, Illinois.
    c.   Silver conducting paint. Type SC-12. Manufactured by Micro-Circuits Co., New Buffalo, Michigan.
    d.   Micro-ohmmeter. Model 580. Manufactured by Keithley Instruments, Inc., Cleveland, Ohio.

15. Tensile Property Measurement.
    a.   Cardboard tensile testing tabs.
    b.   Adhesive. Epoxy 220 resin molecular connector. Manufactured by Hughes Associates, Victoria, Minnesota. Used to attach fibers to testing tabs.
    c.   Phoenix single filament testing machine. Manufactured from previously existing Instron model TM universal testing machine, equipped with Instron model 3A pneumatic jaws and a 500g load cell. Manufactured by Measurements Technology, Inc., Roswell, Georgia.

16. Grinding and Polishing.
    a.   Thermosetting polyester resin. Castolite and hardener. Manufactured by Leco Corporation, St. Joseph, Michigan.
    b.   Silicon carbide grinding laps. Carbimet® Paper Discs (240, 320, 400, and 600 grit). Manufactured by Buehler, Ltd., Lake Bluff, Illinois.
    c.   Aluminum oxide paste. 0.3 μm particle size. Manufactured by Buehler, Ltd., Lake Bluff, Illinois.
    d.   Felt polishing laps. Manufactured by Buehler, Ltd., Lake Bluff, Illinois.
    e.   Grinder/polisher. Manufactured by Buehler, Ltd., Lake Bluff, Illinois. Used to polish the surfaces of cast samples.

17. Image Analysis System.
    a.   Optical light microscope. Model ICM 405. Manufactured by Ernst Zeiss, Wetzlar, Germany. Used to obtain images of fiber cross-sections.
    b.   Video camera. Part number NC-65DX. Manufactured by Dage-MTI, Inc., Michigan City, Indiana. Subsequently modified by Georgia Instruments, Inc., Roswell, Georgia. Used to transfer image from microscope to monitor.
    c.   Monitor. Sony Trinitron monitor, model PVM-13420. Manufactured by Sony Corporation of America, and distributed by Georgia Instruments, Inc., Roswell, Georgia. Used to display image from the microscope.
    d.   Computer system. Model 9671 and monitor model M-200. Manufactured by Eltech Research, Inc., and modified by Georgia Instruments, Inc., Roswell, Georgia. Used to run the image analysis software.
    e.   Image analysis software. Developed by Analytic Imaging Concepts, Irvine, California, and distributed by Georgia Instruments, Inc., Roswell, Georgia.

18. Infrared Spectroscopy Equipment.
    a. IR-grade KBr. Distributed by Fisher Scientific, Norcross, Georgia. Used as a carrier material fro infrared spectroscopy samples.
    b. Spectrometer. FT-IR 1600 Spectrophotometer. Manufactured by Perkin-Elmer, Norwalk, Connecticut.

19. Raman Spectroscopy Equipment (located at Michigan Technological University, Department of Chemistry and Chemical Engineering, Houghton, Michigan).

20. Electron Microscopy Equipment.
    a. SEM. ETEC Autoscan scanning electron microscope. Manufactured by ETEC, Inc., Hayward, California. Used to obtain high resolution images of fiber cross-sections.
    b. Ultramicrotome. Sorvall Porter Blum model NT2-B. Manufactured by Sorvall Inc., Norwalk, Connecticut. Used to section carbon fibers.
    c. TEM. JEOL 100C transmission electron microscope. Manufactured by JEOL USA, Inc., Peabody, Massachusetts. Used to examine sections of carbon fibers.

21. Miscellaneous.
    a. Fortran '77 compiler. Version 3.30. Developed by the Microsoft Corporation, Redmond, Washington.
    b. Lotus 123. Release 2.01. Developed by the Lotus Development Corporation, Cambridge, Massachusetts.
    d. MathCAD. Version 2.01. Developed by MathSoft Inc., Cambridge, Massachusetts.

Appendix C

Experimental Data

C.1 Thermogravimetric Analysis Trials
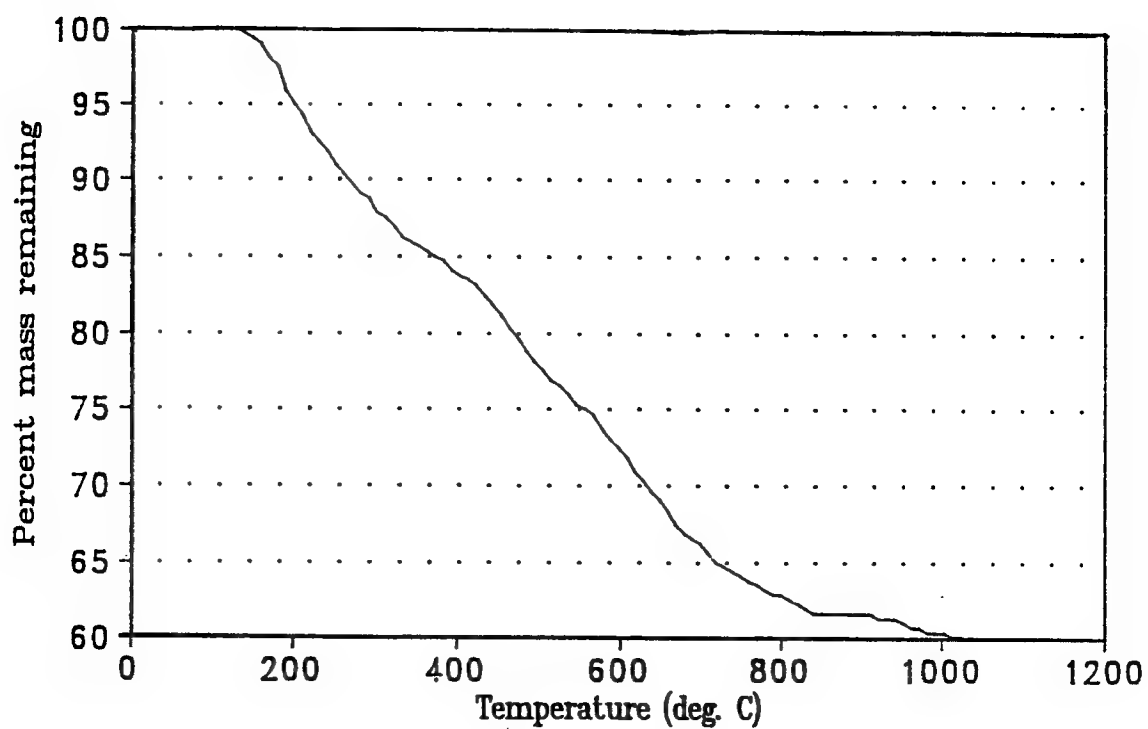
Figure C.1. TGA profile of sample HS280c (280°C, 15.5% O) in argon.
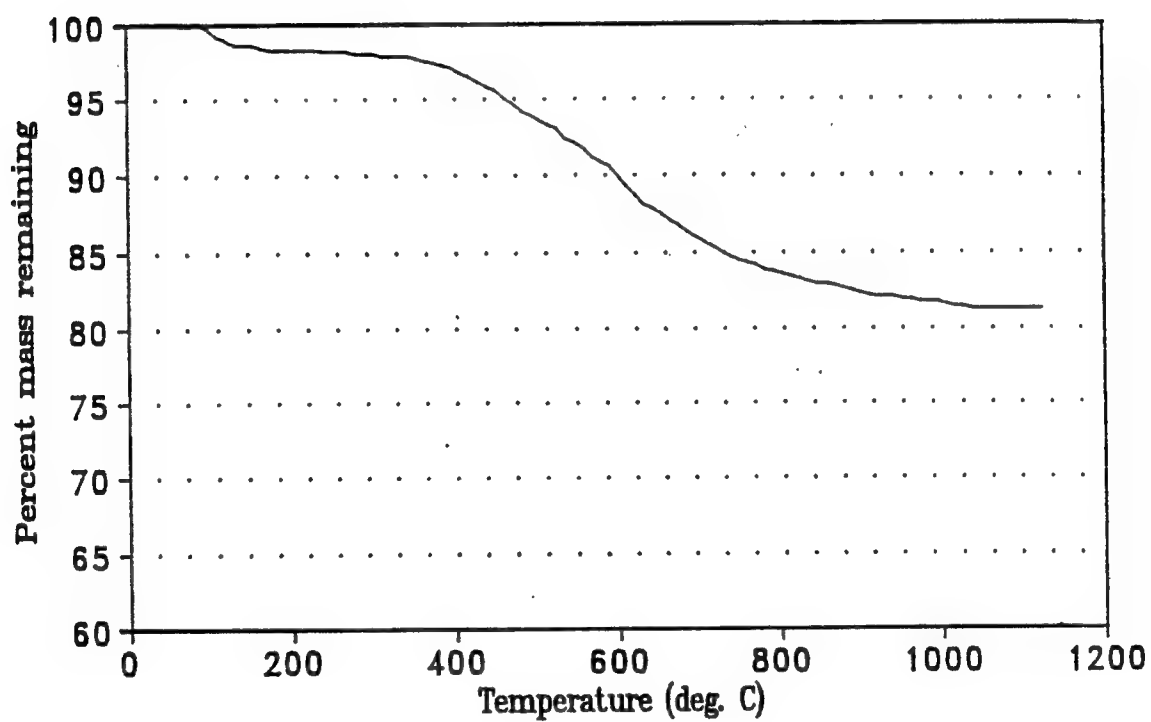
Figure C.2. TGA profile of sample HS280a (280°C, 10.4% O) in argon.
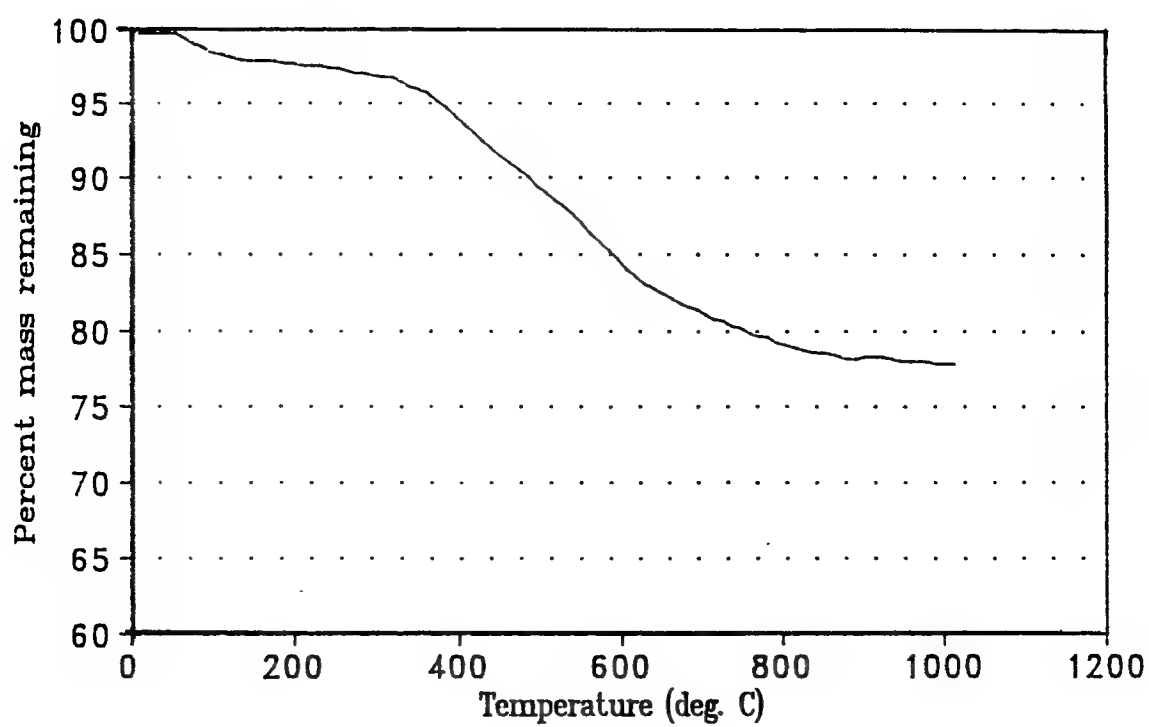
Figure C.3. TGA profile of sample HS280b (280°C, 13.8% O) in argon.
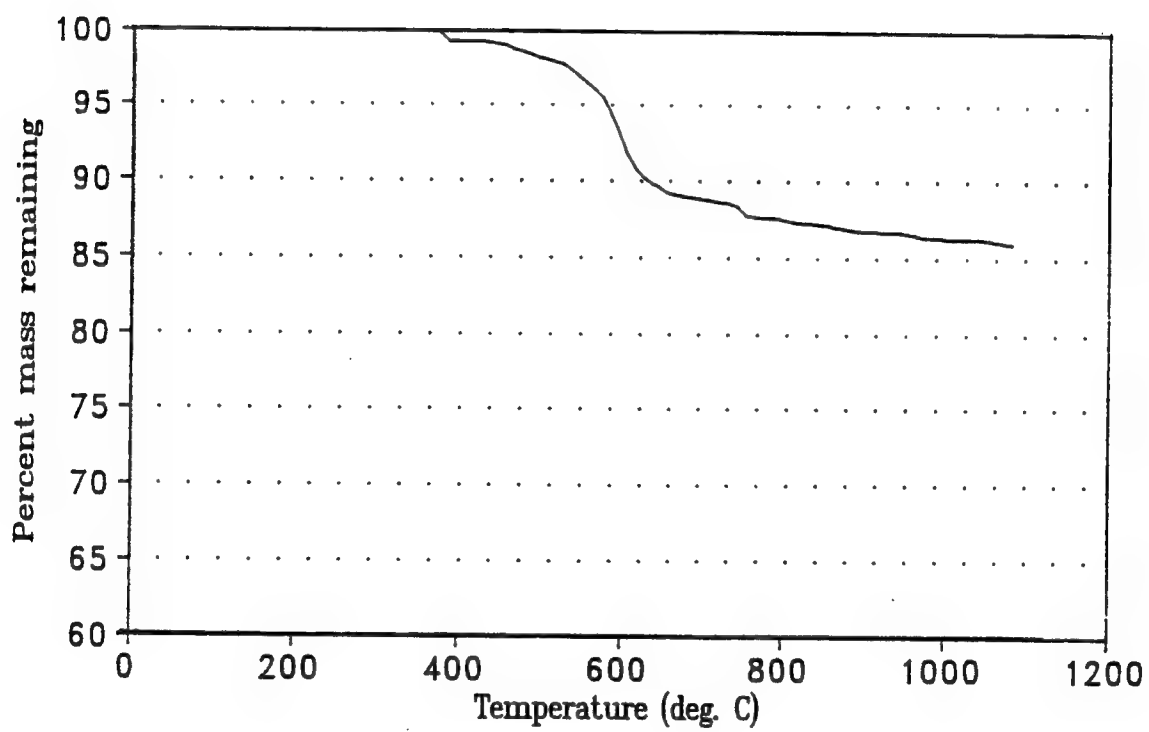
Figure C.4. TGA profile of sample HS175 (175°C, 1.2% O) in argon.
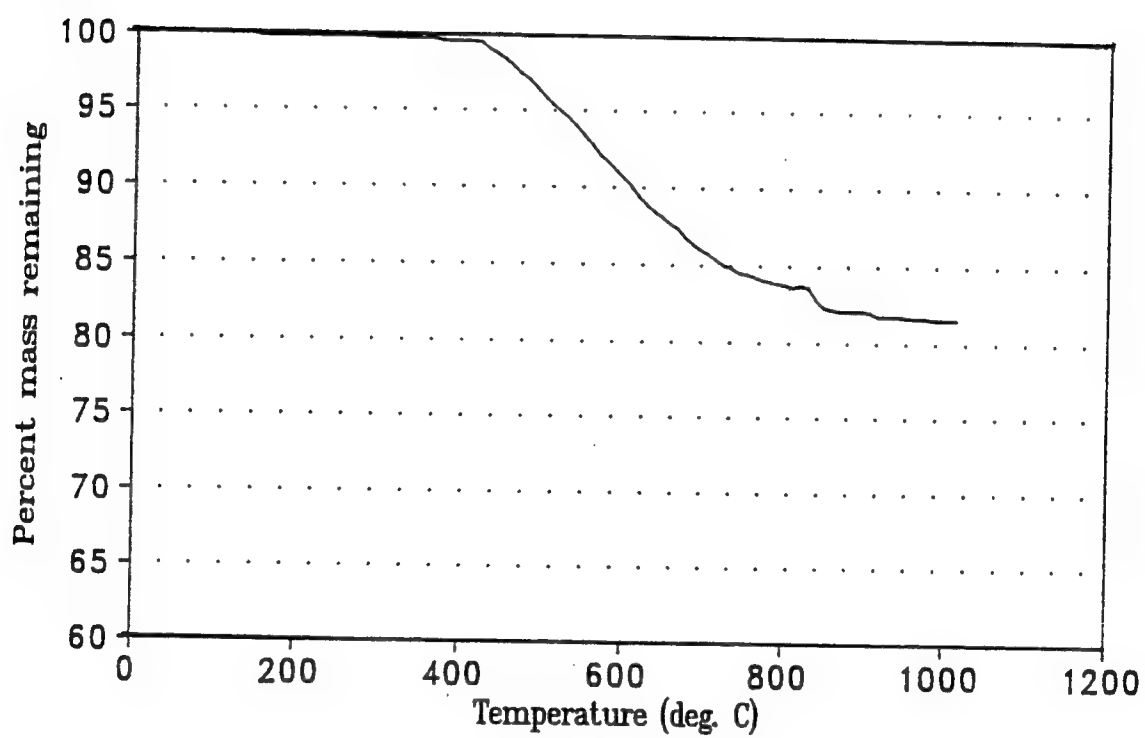
Figure C.5. TGA profile of sample HS350 (350°C, 6.3% O) in argon.
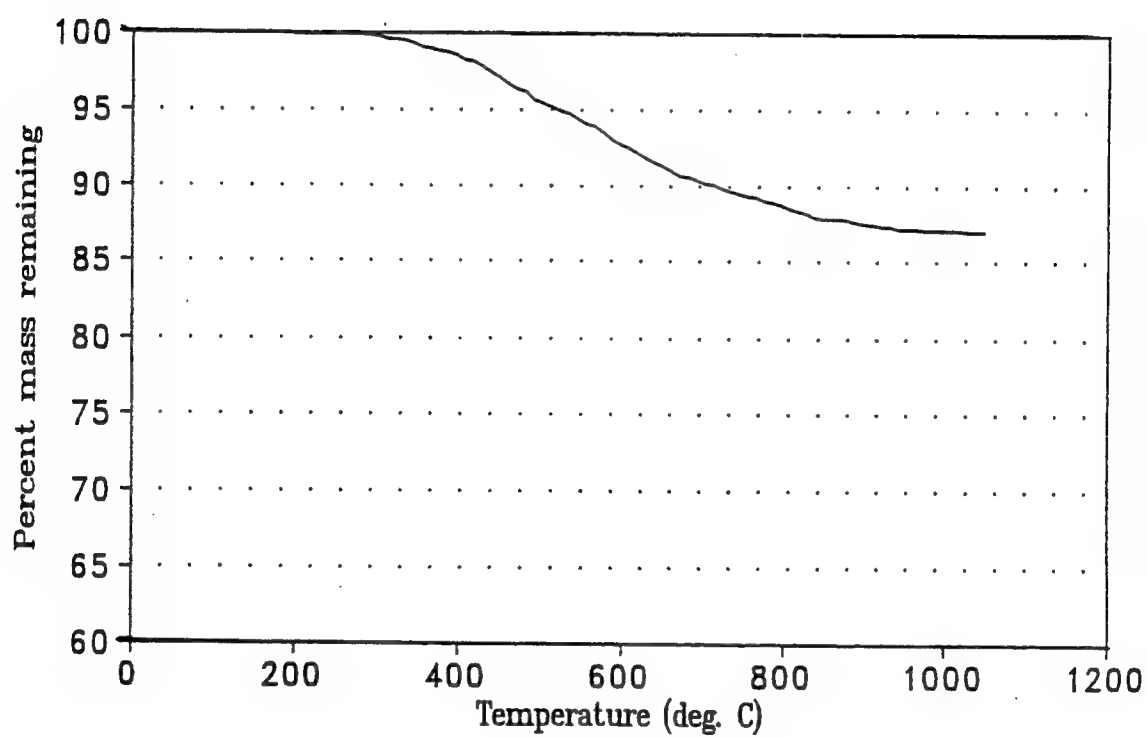
Figure C.6. TGA profile of sample HS230 (230°C, 4.0% O) in argon.
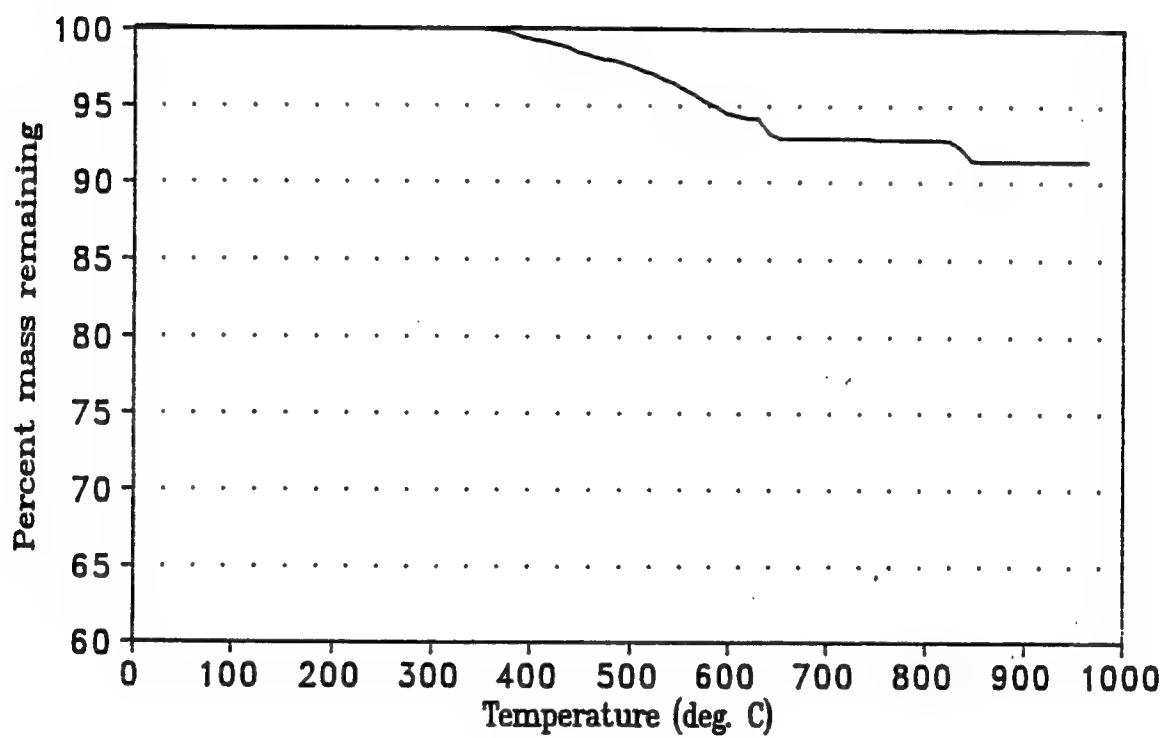
Figure C.7. TGA profile of sample HS179 (179°C, 1.9% O) in argon.
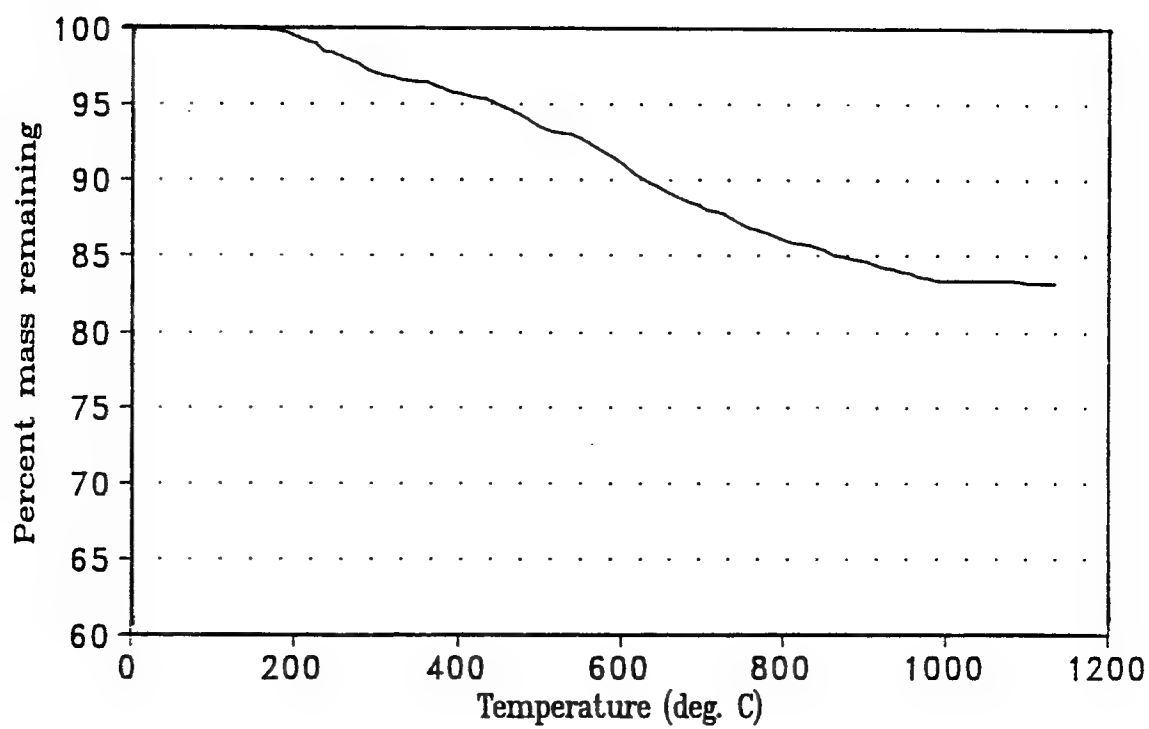
Figure C.8. TGA profile of sample HS240 (240°C, 2.7% O) in argon.
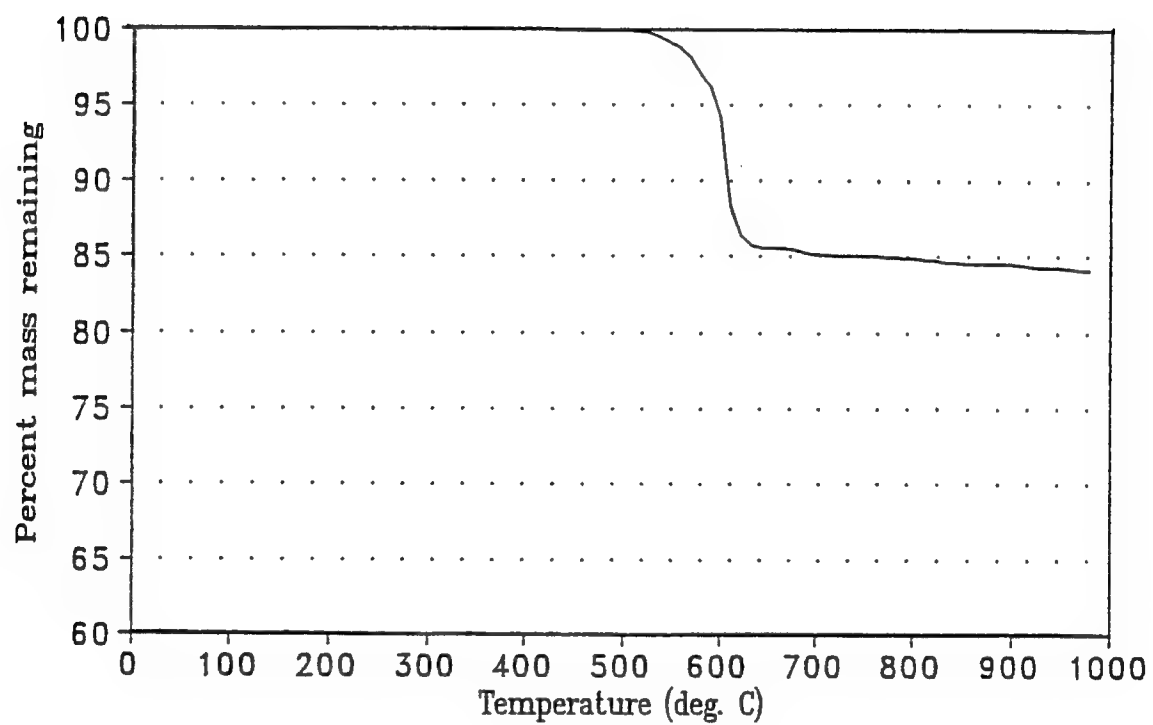
Figure C.9. TGA profile of sample HS, as-spun (0.0% O) in argon.

C.2 Wide Angle X-ray Diffraction Data

Table C.1. Summary of wide angle X-ray diffraction data (Bragg scans).

Fiber set	d(0002) (Å)	L_c (Å)	(0002) strain	a (Å)	L_a (Å)	(hki0) strain	L_a/L_c
R1000	3.464	15	0.327(T)	N/A	37	N/A	2.47
C1000	3.456	15	0.021(T)	N/A	37	N/A	2.47
AR1000	3.433	20	0.151(T)	N/A	N/A	N/A	N/A
R1800-15	3.453	65	0.058(T)	2.460	71	0.025	1.09
C1800-15	3.430	88	0.005(T)	N/A	N/A	N/A	N/A
AR1800-15	3.437	131	0.023(T)	2.446	695	0.001(C)	5.32
R2000-15	3.450	130	0.012(T)	N/A	N/A	N/A	N/A
C2000-15	3.507	224	0.017(T)	N/A	N/A	N/A	N/A
AR2000-15	3.411	162	0.002(C)	2.449	612	0.002(C)	3.78
R2200-15	3.441	147	0.009(T)	N/A	N/A	N/A	N/A
C2200-15	3.409	145	0.008(C)	N/A	N/A	N/A	N/A
AR2200-15	3.405	199	0.003(C)	2.442	942	0.000	4.73
R2400-15	3.414	162	0.007(T)	2.463	312	0.007(C)	1.93
C2400-15	3.360	182	0.016(T)	N/A	N/A	N/A	N/A
AR2400-15	3.355	175	0.000	2.446	1057	0.000	6.04
R(60)2400	3.430	155	0.006(T)	N/A	N/A	N/A	N/A
R(100)2400	3.393	179	0.010(C)	N/A	N/A	N/A	N/A
R(fast)2400	4.403	194	0.002(T)	N/A	N/A	N/A	N/A
R(E)2400	3.395	185	0.006(C)	2.463	276	0.008(C)	1.49
AR(E)2400	3.409	175	0.000	2.448	482	0.005(C)	2.75
R2800-15	3.412	190	0.008(T)	N/A	N/A	N/A	N/A
R3000-15	3.392	189	0.006(C)	N/A	N/A	N/A	N/A
C3000-15	3.369	189	0.005(C)	N/A	N/A	N/A	N/A
HS-CFS16	3.398	129	0.006(C)	2.463	346	0.007(C)	2.68
HS-CFS17	3.398	130	0.007(C)	N/A	N/A	N/A	N/A
HS-CFS18	3.408	128	0.005(C)	N/A	N/A	N/A	N/A
HS-CFS19	3.382	127	0.003(C)	N/A	N/A	N/A	N/A
HS-CFS20	3.380	134	0.007(C)	2.464	314	0.000	2.34
ISO1800-1	3.460	68	0.026(T)	2.440	86	0.026(C)	1.26
ISO1800-2	3.442	70	0.020(T)	2.448	125	0.009(T)	1.79
ISO1800 -4	3.454	75	0.018(T)	2.447	118	0.015(C)	1.57
ISO1800-8	3.449	77	0.019(T)	2.456	136	0.009(C)	1.77
ISO1800-16	3.452	76	0.015(T)	2.454	123	0.015(C)	1.62
ISO1800-32	3.455	65	0.025(T)	2.445	110	0.006(C)	1.69
ISO1900-1	3.449	79	0.014(T)	2.449	146	0.000	1.85
ISO1900-2	3.460	78	0.018(T)	2.451	145	0.000	1.86
ISO1900-4	3.450	86	0.014(T)	2.453	141	0.005(C)	1.64
ISO1900-8	3.448	85	0.012(T)	2.456	151	0.008(C)	1.78
ISO1900-16	3.446	87	0.011(T)	2.457	161	0.004(C)	1.85
ISO1900-32	3.439	102	0.011(T)	2.462	203	0.000	1.99
ISO2000-1	3.443	96	0.011(T)	2.460	255	0.000	2.66
ISO2000-2	3.442	98	0.009(T)	2.457	191	0.005(C)	1.95
ISO2000-4	3.440	93	0.008(T)	2.464	178	0.004(C)	1.91

Table C.1 (Continued).

Fiber set	d(0002) (Å)	L_c (Å)	(0002) strain	a (Å)	L_a (Å)	(hki0) strain	L_a/L_c
ISO2000-8	3.446	96	0.010(T)	2.463	177	0.005(C)	1.84
ISO2000-16	3.433	102	0.010(T)	2.466	229	0.004(C)	2.25
ISO2000-32	3.434	93	0.011(T)	2.458	191	0.006(C)	2.05
nucleate1900	3.414	109	0.011(T)	2.465	240	0.000	2.20
no-nucl.1900	3.414	102	0.012(T)	2.462	253	0.000	2.48
HS280-30	3.485	29	0.030(T)	N/A	N/A	N/A	N/A
HS280-60	3.473	35	0.060(C)	N/A	N/A	N/A	N/A
HS280-180	3.481	30	0.038(T)	N/A	N/A	N/A	N/A
HS280-240	3.485	23	0.023(T)	N/A	N/A	N/A	N/A
G(280-30)	3.407	151	0.008(T)	N/A	N/A	N/A	N/A
G(280-60)	3.384	142	0.007(C)	N/A	N/A	N/A	N/A
G(280-120)	3.392	140	0.007(C)	N/A	N/A	N/A	N/A
G(280-240)	3.404	139	0.007(T)	N/A	N/A	N/A	N/A
ISO3000-4	3.420	166	0.006(T)	2.460	376	0.000	2.27
ISO3000-8	3.436	166	0.006(T)	2.463	178	0.000	1.07
ISO3000-16	3.402	155	0.004(T)	2.463	142	0.000	0.91

A word on nomenclature: the first letter or letters indicates either the type of pitch (HS = heat-soaked and AR = synthetic AR) or the shape of the fiber (R = heat-soaked ribbon-shape fiber and C = heat-soaked circular fiber) for fibers produced from the heat-soaked pitch. The following number gives the maximum treatment temperature employed. If this number is preceded by an item in parentheses, that item indicates any special treatment conditions. For example, (E) means that the fiber was subjected to solvent etching prior to graphitization. Another example is (60), which means that the fiber was heated at 60°C per minute to the maximum temperature. No such term means that the fiber was heated at 20°C per minute without prior solvent treatment. A number following a hyphen indicates the dwell time at maximum temperature. Finally, CFS refers to the change-over study, ISO refers to the isothermal study conducted at 1800, 1900, 2000, and 3000°C, and G(*) means the graphitized version of the fiber set name inside the parentheses.

The (0002) spacing and the lattice constant a are reported to ± 0.004 Å, according to

an estimate of error made from several replications of the same sample. The crystallite size in the c-direction is reported to $\pm$ 6 Å, while the error in a-direction measurement is greater. This is true because of the inherent difficulty in measuring the breadth of the $(10\underline{1}0)$ and $(11\underline{2}0)$ reflections. These peaks are often asymmetric and convoluted with other reflections, such as the $(11\underline{2}2)$. Some measurements were not available (denoted N/A) because of insufficient sample quantity and/or poor diffracted intensities.

Table C.2. Preferred basal plane orientation data (χ-scans).

Fiber Set	$Z(°)$	Herman's f (204) $(0 \leq f \leq 1)$
R1000-15	39.1	0.819
C1000-15	40.0	0.811
AR1000-15	27.4	0.910
R1800-15	15.5	0.971
C1800-15	17.0	0.965
AR1800-15	17.1	0.964
R2000-15	18.8	0.957
C2000-15	16.8	0.966
AR2000-15	14.1	0.976
R2200-15	21.3	0.946
C2200-15	16.8	0.966
AR2200-15	12.7	0.981
R2400-15	16.3	0.968
C2400-15	13.0	0.980
AR2400-15	10.6	0.986
R(60)2400-15	15.0	0.973
R(100)2400-15	11.6	0.984
R(fast)2400-15	13.0	0.980
R(E)2400-15	14.8	0.974
R2800-15	13.2	0.979
R3000-15	14.1	0.976
HS-CFS16	20.9	0.948
HS-CFS17	21.5	0.944
HS-CFS18	21.5	0.944
HS-CFS19	23.6	0.933
HS-CFS20	17.7	0.962
G(280-30)	13.6	0.978
G(280-60)	16.8	0.966
G(280-120)	14.4	0.975
G(280-240)	13.6	0.978

C.3 Small Angle X-ray Diffraction Data

Table C.3. Estimates of void radius (R_g), orientation (Z), and fractal dimension (D).

Sample	R_g (Å)	Z(°)	D
R1000-15	74.9	26.6	3.19
R1800-15	72.3	17.0	2.65
R2000-15	70.8	17.3	2.61
R2200-15	69.1	18.2	2.66
R2400-15	71.9	17.0	2.42
AR1800-15	65.8	16.7	2.13
AR2000-15	63.8	15.7	1.95
AR2200-15	59.8	15.6	1.87
AR2400-15	54.8	14.7	1.73

C.4 Calculated Debye Temperatures

Table C.4. Calculated in-plane Debye temperatures for commercial and experimental fibers.

Sample	Treatment temperature (°C)	Dwell time (min)	θ_D (K)
Amoco pitch-based fibers:			
P-25	****	**	5526
P-55	****	**	3911
P-75	****	**	2950
P-100	****	**	2675
Du Pont pitch-based fibers:			
E-35	****	**	4868
E-35c	****	**	3948
experimental pitch-based fibers:			
R1000-15	1000	15	7961
R1800-5	1800	5	6583
R1800-10	1800	10	6319
R1800-15	1800	15	4937
R2000-5	2000	5	6806
R2000-10	2000	10	6733
R2000-15	2000	15	4934
R2200-5	2200	5	6717
R2200-10	2200	10	6069
R2200-15	2200	15	3827
R2400-5	2400	5	5689
R2400-10	2400	10	4324
R2400-15	2400	15	3964
C1000-15	1000	15	8031
C1800-5	1800	5	6439
C1800-10	1800	10	6204
C1800-15	1800	15	6193
C2000-5	2000	5	6187
C2000-10	2000	10	5374
C2000-15	2000	15	4727
C2200-5	2200	5	5369
C2200-10	2200	10	5180
C2200-15	2200	15	4747
C2400-5	2400	5	5470
C2400-10	2400	10	5046
C2400-15	2400	15	4625

C.5 Electrical and Mechanical Property Data

Table C.5. Single filament electrical and mechanical property data.

Fiber set	Area (μm^2)	Strength (GPa)	Modulus (GPa)	Resistivity ($\mu\Omega$m)
R1000-15	517.8±36.9	N/A	N/A	N/A
R1800-15	361.3±30.8	N/A	N/A	8.94±0.41
R2000-5	647.3	1.23	162	10.6±1.83
R2000-15	550.1	1.84	182	10.5±3.04
R2200-10	530.6	2.01	243	8.72±3.20
R2400-5	521.4	1.26±0.13	190	9.15±3.05
R2400-15	502.4	1.76	226	9.03±3.05
R(60)2400-15	393.0±34.2	1.27±0.19	*	6.10±0.42
R(100)2400-15	401.8±28.1	1.22±0.18	*	6.74±0.60
R(fast)2400-15	350.8±39.9	0.96±0.19	*	5.21±0.47
R(E)2400-15	338.7±24.1	1.71±0.18	624±151	4.81±0.47
R2800-15	499.4±36.6	N/A	N/A	7.00±0.50
R3000-15	437.8±38.8	N/A	N/A	5.23±0.41
C2000-5	147.5	2.12	224	12.1±1.44
C2000-15	82.9	2.96	367	9.31±1.70
C2200-10	97.8	2.49	362	9.56±1.38
C2400-5	173.7	1.49	240	8.64±2.55
C2400-15	80.0	2.95	444	8.86±2.51
C3000-15	166.7±5.3	N/A	N/A	5.21±0.26
HS-CFS16	209.5	N/A	N/A	5.28±0.37
HS-CFS17	240.0	N/A	N/A	5.58±0.25
HS-CFS18	226.2	N/A	N/A	6.49±0.59
HS-CFS19	228.8	N/A	N/A	8.60±1.37
HS-CFS20	175.5	N/A	N/A	6.18±0.38
AR1000-15	208.5±11.3	N/A	N/A	N/A
AR1800-15	180.7±9.6	N/A	N/A	7.81±0.33
AR2000-15	172.4±8.8	N/A	N/A	7.58±0.41
AR2200-15	181.6±10.0	N/A	N/A	6.67±0.34
AR2400-15	166.0±8.5	N/A	N/A	4.39±0.25

(± indicates a 95% confidence interval about the mean.)
(* indicates a high modulus value that is unreliable due to compliance considerations)

C.6 Infrared and Raman Spectroscopy Data Lists

The following is a listing of observed infrared and Raman data for selected fiber sets.

Table C.6. IR wavenumbers for sample HS-OX160.

Wavenumber (cm^{-1})	Wavenumber (cm^{-1})	Wavenumber (cm^{-1})
425	460	530
580	589	604
640	747	811
870	960	1034
1062	1374	1437
1595	1692	1728
1774	1818	1844
1908	1942	1985
2028	2858	2907
3039		

and numerous small peaks between 2028 and 2858 cm^{-1}, and above 3039 cm^{-1}

Table C.7. IR wavenumbers for sample HS-OX190.

Wavenumber (cm^{-1})	Wavenumber (cm^{-1})	Wavenumber (cm^{-1})

same as those observed in sample HS-OX160, with the addition of:
1768

Table C.8. IR wavenumbers for sample HS-OX250.

Wavenumber (cm^{-1})	Wavenumber (cm^{-1})	Wavenumber (cm^{-1})

same as those observed in sample HS-OX190, with the addition of:

430	460	492
950	1045	1082
1892		

and numerous peaks above 2000 cm^{-1}

Table C.9. IR wavenumbers for sample HS-OX310.

Wavenumber (cm^{-1})	Wavenumber (cm^{-1})	Wavenumber (cm^{-1})
same as those observed in sample HS-OX190, with the addition of:		
429	538	877
1698	1843	
and numerous small peaks near 400-600 cm^{-1}		

Table C.10. IR wavenumbers for sample AR-OX160.

Wavenumber (cm^{-1})	Wavenumber (cm^{-1})	Wavenumber (cm^{-1})
425	754	815
820	877	1044
1082	1254	1375
1440	1592	1706
2867	2912	2963
3060	3318	3456

Table C.11. IR wavenumbers for sample AR-OX190.

Wavenumber (cm^{-1})	Wavenumber (cm^{-1})	Wavenumber (cm^{-1})
same as those observed in sample AR-OX 160		

Table C.12. IR wavenumbers for sample AR-OX250.

Wavenumber (cm^{-1})	Wavenumber (cm^{-1})	Wavenumber (cm^{-1})
same as those observed in sample AR-OX160, with the addition of:		
413	431	471
757	813	879
1045	1082	1234
1252	1379	1442
1578	1606	1696
1762	1841	2917
2936	2971	3055

Table C.13. IR wavenumbers for sample AR-OX310.

Wavenumber (cm^{-1})	Wavenumber (cm^{-1})	Wavenumber (cm^{-1})
same as those observed in sample AR-OX250, with the addition of:		
418	446	555
592	746	1837
and numerous peaks near 1400 cm^{-1} and above 1800 cm^{-1}		

Table C.14. Raman spectrum data for fiber sets R1000-15, R1800-15, and R2400-15.

Sample	$1/L_a$ ($Å^{-1}$)	I_{1360}/I_{1580}
R1000-15	0.0270	1.0490
R1800-15	0.0141	0.8996
R2400-15	0.0032	0.7222

C.8. Elemental Analysis Data

Table C.15. Derived quantities from elemental analysis data (stabilization).

Sample	$\overline{H/C}$	$\overline{O/C}$	D, degree of stabilization
HS, as-spun	0.541	0.004	0.00
HS175	0.527	0.009	2.66
HS179	0.523	0.021	6.25
HS230	0.494	0.042	12.54
HS240	0.481	0.037	11.13
HS350	0.415	0.110	33.05
HS-OX160	0.499	0.008	2.44
HS-OX190	0.522	0.008	2.45
HS-OX250	0.513	0.021	6.42
HS-OX310	0.377	0.082	24.59
AR-OX160	0.570	0.024	7.12
AR-OX190	0.575	0.023	6.98
AR-OX250	0.514	0.060	17.93
AR-OX310	0.519	0.148	44.44

Table C.16. Derived quantities from elemental analysis data (thermolysis and graphitization).

Sample	$\overline{H/C}$	$\overline{O/C}$	M_c	$\overline{R/C}$	RCI	f_a
HSOX280b	0.541	0.067	13.9	0.528	1.06	0.404
HS200	0.607	0.092	14.4	0.553	1.11	0.287
HS400	0.416	0.014	12.9	0.479	0.96	0.627
HS600	0.205	0.031	13.0	0.512	1.02	0.772
HS800	0.400	0.025	13.1	0.492	0.98	0.616
HS1000	0.015	0.007	12.5	0.503	1.01	0.979
R1800-15	≈ 0	≈ 0	12.2	0.493	0.99	1.013
R2000-15	≈ 0	≈ 0	12.2	0.494	0.99	1.012
R2200-15	≈ 0	≈ 0	12.1	0.493	0.99	1.014
R2400-15	≈ 0	≈ 0	12.1	0.498	1.00	1.005
AR200	0.507	0.101	14.1	0.559	1.12	0.375
AR400	0.600	0.098	14.2	0.550	1.10	0.300
AR600	0.381	0.035	13.0	0.495	0.99	0.628
AR800	0.227	0.012	12.4	0.483	0.97	0.806
AR1000	≈ 0	≈ 0	12.1	0.500	1.00	1.000
graphite	0.000	0.000	12.1	0.500	1.00	1.000

Appendix D

DSC Data Analysis Program

This section presents a DSC analysis program that was developed for this study. The program analyzes several deconvoluted thermal events, such as those observed during stabilization. Its output includes three parameters that describe the height, width, and position of each event, followed by an estimate of he heat of reaction and reaction rate.

Program name: DSCURVE

Compiler: Fortran 77

User input: Sample mass, heating rate, number of observations, number of thermal events, and peak position(s)

File input: DSC.DAT (DSC heat flow raw data)

Output: Peak position and shape parameters, heats of reaction, kinetic parameters

Code:

```
$NODEBUG
$NOFLOATCALLS
$STORAGE:4
PROGRAM DSCURVE
IMPLICIT REAL*8(A-H,O-Z)
DIMENSION P(16,15), Y(16), X(1500), B(1500), BASE(1500), ADD(15), A(15),
+Z(25), RITHMK(1000), TINV(1000)
COMMON /INFO/ X, B, NDATA, NVAR
COMMON /STUFF/ ADD
EXTERNAL FUNK, FORM
OPEN (10,FILE='DSC.DAT', STATUS='OLD', ACCESS='SEQUENTIAL',
+FORM='FORMATTED')
OPEN (11,FILE='OUTPUT.DAT', STATUS='NEW', ACCESS='SEQUENTIAL',
+FORM='FORMATTED')
WRITE (*,4)
4   FORMAT (1X, 'Enter the sample mass in grams.')
READ (*,*) WEIGHT
WRITE (*,3)
3   FORMAT (1X, 'Enter the heating rate in degrees C. per minute.')
READ (*,*) HR
E = 138.4394
SCALE = 200.0
WRITE (*,5)
```

```
 5   FORMAT (1X, 'Enter the number of data pairs.')
     READ (*,*) DATA
     NDATA = DINT(DATA)
     WRITE (*,10)
10   FORMAT (1X, 'Enter the number of peaks present.')
     READ (*,*) PEAK
     NPEAK = DINT(PEAK)
     NVAR = NPEAK * 3
     IPASS = 0
     DO 15 I =1, NDIM - 2, 3
         A(I) = 10.0
         KOUNT = (I + 2) / 3
         WRITE (*,20) KOUNT
20       FORMAT (1X, 'Enter the position (deg. C) of peak number', I3,' .')
         READ (*,*) SITION
         A(I + 1) = SITION + 273.15
         A(I + 2) = 20.0
15   CONTINUE
     DO 77 I = 1, NDATA
         READ (10,*) X(I), B(I)
         IF (B(I).EQ.0) THEN
             LOOK = I
         ENDIF
77   CONTINUE
     DO 6 I = 1, NDATA
         X(I) = X(I) + 273.15
         IF (I.GT.LOOK) THEN
             SLOPE = (B(NDATA) - B(LOOK)) / (X(NDATA) - N(LOOK))
             BASE(I) = SLOPE * (X(I) - X(LOOK))
         ELSE
             BASE(I) = 0.0
         ENDIF
         B(I) = B(I) - BASE(I)
 6   CONTINUE
     DO 25 I = 1, 16
         DO 30 J = 1, 15
             P(I,J) = 0.0
30       CONTINUE
         Y(I) = 0.0
25   CONTINUE
100  IPASS = IPASS + 1
     DO 35 I = 1, NDIM + 1
         DO 40 J = 1, NDIM - 2, 3
             P(I,J) = A(J)
             P(I,J + 1) = A(J + 1)
             P(I,J + 2) = A(J + 2)
40       CONTINUE
         IF (I.NE.NDIM + 1) THEN
             P(I,I) = P(I,I) * 1.1
         ENDIF
35   CONTINUE
     DO 42 I = 1, NDIM + 1
         DO 45 J = 1, NDIM
             A(J) = P(I,J)
```

```
45      CONTINUE
        Y(I) = FUNK(A)
42  CONTINUE
    FTOL = 0.00001
    MP = NDIM + 1
    NP = NDIM
    CALL AMOEBA (P, Y, MP, NP, NDIM, FTOL, FUNK, ITER)
    DO 50 J = 1, NDIM
        ADD(J) = 0.0
        DO 55 I = 1, NDIM + 1
            ADD(J) = ADD(J) + P(I,J)
55      CONTINUE
        ADD(J) = ADD(J) / (NDIM + 1)
50  CONTINUE
    IF (IPASS.EQ.1) THEN
        DO 90 J = 1, NDIM
            A(J) = ADD(J)
90      CONTINUE
        GOTO 100
    ENDIF
    ERROR = FUNK(ADD)
    WRITE (*,*) ITER, ERROR
    WRITE (11,*) ITER, ERROR
    DO 60 J = 1, NDIM
        WRITE (*,*) ADD(J)
        WRITE (11,*) ADD(J)
60  CONTINUE
    R = 0.0
    RESLT = 0.0
    DO 605 I = 1, NDIM, 3
        START = ADD(I + 1) - 3.0 * ADD(I + 2)
        END = ADD(I + 1) + 3.0 * ADD(I + 2)
        WHAT = REAL(I)
        CALL SIMPSN (WHAT, RESLT, FORM, START, END, 1000)
        KOUNT = (I + 2) / 3
        DELH = RESLT / WEIGHT * E * 60.0E-6 * SCALE / HR
        WRITE (*,610) KOUNT, DELH
610     FORMAT (1X,'The heat of reaction (J/g)for peak',I2,' is ',F15.7)
        DO 615 J = 1, 1000
            UPPER = START + REAL(J) * (END - START) / 1000.
            CALL SIMPSN (WHAT, R, FORM, START, UPPER, 1000)
            EXTENT = R / RESLT
            RITHMK(J) = DLOG(DLOG(1 - EXTENT) * HR / (START - UPPER))
            TINV(J) = 1.0 / UPPER
615     CONTINUE
        CALL REGRES (1000, RITHMK, TINV, SLOPE, YINT, R2)
        SLOPE = -1.987E-3 * SLOPE
        WRITE (*,620) KOUNT, SLOPE
        WRITE (11,620) KOUNT, SLOPE
620     FORMAT (1X, 'The activation energy of reaction',I2,' is ',F15.7,' kcal/mole.')
        WRITE (*,625) R2
        WRITE (11,625) R2
625     FORMAT (1X, 'With a correlation coefficient of',F15.13)
605 CONTINUE
    END
```

```fortran
      SUBROUTINE AMOEBA (P, Y, MP, NP, NDIM, FTOL, FUNK, ITER)
C     (see reference 196)
      PARAMETER (NMAX=20, ALPHA=1.0, BETA=0.5, GAMMA=2.0, ITMAX=500)
      DIMENSION P(MP,NP), Y(MP), PR(NMAX), PBAR(NMAX)
      MPTS = NDIM + 1
      ITER = 0
1     ILO = 1
      IF (Y(1).GT.Y(2)) THEN
          IHI = 1
          INHI = 2
      ELSE
          IHI = 2
          INHI = 1
      ENDIF
      DO 11 I = 1, MPTS, 1
          IF (Y(I).LT.Y(ILO)) ILO = I
          IF (Y(I).GT.Y(IHI)) THEN
              INHI = IHI
              IHI = I
          ELSE IF (Y(I).GT.Y(INHI)) THEN
              IF (I.NE.IHI) INHI = I
          ENDIF
11    CONTINUE
      RTOL = 2.0 * DABS(Y(IHI) - Y(ILO))/(DABS(Y(IHI)) + DABS(Y(ILO))
      IF (RTOL.LT.FTOL) RETURN
      IF (ITER.EQ.ITMAX) PAUSE 'Amoeba exceeding maximum iterations.'
      ITER = ITER + 1
      DO 12 J = 1, NDIM, 1
          PBAR(J) = 0.0
12    CONTINUE
      DO 14 I = 1, MPTS, 1
          IF (I.NE.IHI) THEN
          DO 13 J = 1, NDIM, 1
              PBAR(J) = PBAR(J) + P(I,J)
13        CONTINUE
      ENDIF
14    CONTINUE
      DO 15 J = 1, NDIM, 1
          PBAR(J) = PBAR (J) / FLOAT(NDIM)
          PR(J) = (1.0 + ALPHA) * PBAR(J) - ALPHA * P(IHI,J)
15    CONTINUE
      YPR = FUNK(PR)
      IF (YPR.LE.Y(ILO)) THEN
          DO 16 J = 1, NDIM, 1
              PBR(J) = GAMMA * PR(J) + (1.0 - GAMMA) * PBAR(J)
16        CONTINUE
          YPRR = FUNK(PRR)
          IF (YPRR.LT.Y(ILO)) THEN
              DO 17 J = 1, NDIM, 1
                  P(IHI,J) = PRR(J)
17            CONTINUE
              Y(IHI) = YPRR
          ELSE
```

```
                DO 18 J = 1, NDIM, 1
                    P(IHI,J) = PR(J)
18              CONTINUE
                Y(IHI) = YPR
            ENDIF
        ELSE IF (YPR.GE.Y(INHI)) THEN
            IF (YPR.LT.Y(IHI)) THEN
                DO 19 J = 1, NDIM, 1
                    P(IHI,J) = PR(J)
19              CONTINUE
                Y(IHI) = YPR
            ENDIF
            DO 21 J = 1, NDIM, 1
                PRR(J) = BETA * P(IHI,J) + (1.0 - BEAT) * PBAR(J)
21          CONTINUE
            YPRR = FUNK(PRR)
            IF (YPRR.LT.Y(IHI)) THEN
                DO 22 J = 1, NDIM, 1
                    P(IHI,J) = PRR(J)
22              CONTINUE
                Y(IHI) = YPRR
            ELSE
                DO 24 I = 1, MPTS, 1
                    IF (I.NE.ILO) THEN
                        DO 23 J = 1, NDIM, 1
                            PR(J) = 0.5 * (P(I,J) + P(ILO,J))
                            P(I,J) = PR(J)
23                      CONTINUE
                        Y(I) = FUNK(PR)
                    ENDIF
24              CONTINUE
            ENDIF
        ELSE
            DO 25 J = 1, NDIM, 1
                P(IHI,J) = PR(J)
25          CONTINUE
            Y(IHI) = YPR
        ENDIF
        GO TO 1
        END


        SUBROUTINE REGRES (KOUNT, Y, X, Q, YINT, R2)
C********************************************************************
C*              LINEAR LEAST SQUARES CURVE-FITTING                 *
C********************************************************************
        IMPLICIT REAL*8 (A - H, O - Z)
        DIMENSION Y(100), X(100)
        SUMX = 0.0
        SUMX2 = 0.0
        SUMY = 0.0
        SUMY2 = 0.0
        SUMXY = 0.0
        IBEGIN = DINT(0.2 * KOUNT)
        IEND = DINT(0.8 * KOUNT)
```

```
      DO 10 N = IBEGIN, IEND
          SUMX = SUMX + X(N)
          SUMX2 = SUMX2 + X(N)**2
          SUMY = SUMY + Y(N)
          SUMY2 = SUMY2 + Y(N)**2
          SUMXY = SUMXY + X(N) * Y(N)
 10   CONTINUE
      XAVG = SUMX / FLOAT(IEND - IBEGIN + 1)
      YAVG = SUMY / FLOAT(IEND - IBEGIN + 1)
      SSX = SUMX2 - (SUMX**2) / 4.0
      SSY = SUMY2 - (SUMY**2) / 4.0
      SSXY = SUMXY - (SUMX * SUMY) / 4.0
      SLOPE = SSXY / SSX
      Q = -1 * SLOPE * 1.987E-3
      CEPT = YAVG - SLOPE * XAVG
      YINT = DEXP(CEPT)
      R2 = (SSXY**2) / (SSX * SSY)
      RETURN
      END

      SUBROUTINE SIMPSN (WHAT, AREA, FORM, XMIN, XMAX, N)
C*******************************************************************
C*           NUMERICAL INTEGRATION BY SIMPSON'S RULE            *
C*******************************************************************
      IMPLICIT REAL*8 (A - H, O - Z)
      SUM = 0.0
      RULER = 0.0
      SCALE = 0.0
      H = (XMAX - XMIN) / FLOAT(N)
      FCN1 = FORM (WHAT, XMIN)
      FCN2 = FORM (WHAT, XMAX)
      M = N - 1
      MM = N - 2
      X = XMIN - H
      DO 10 I = 2, M, 2
          X = XMIN + REAL(I) * H
          RULER = SUM
          SUM = SUM + 4.0 * FORM(WHAT, X)
          IF (I.EQ.2) THEN
              GOTO 10
          ELSE
              SCALE = DABS((SUM - RULER) / RULER)
          ENDIF
          IF (SCALE.LT.0.005) THEN
              GOTO 30
          ENDIF
 10   CONTINUE
 30   X = XMIN - H
      DO 20 J = 3, MM, 2
          X = XMIN +J * H
          RULER = SUM
          SUM = SUM + 2 * FORM(WHAT,X)
          SCALE = DABS((SUM - RULER) / RULER)
          IF (SCALE.LT.0.005) THEN
              GOTO 40
```

```fortran
         ENDIF
20   CONTINUE
40   AREA = (H / 3.0) * (FCN1 + SUM + FCN2)
     RETURN
     END

     FUNCTION FUNK(A)
     IMPLICIT REAL*8 (A - H, O - Z)
     DIMENSION A(15), B(1500), X(1500), ARG(15), EX(15)
     COMMON/INFO/ X, B, NDATA, NVAR
     SS = 0.0
     DO 10 I = 1, NDATA
         SUM = 0.0
         DO 20 J = 1, NVAR - 2, 3
             ARG(J) = (X(I) - A(J + 1)) / A(J + 2)
             EX(J) = DEXP(-1.0 * ((ARG(J))**2)
             SUM = SUM + A(J) * EX(J)
20       CONTINUE
         SS = SS + ((B(I) - SUM)**2)
10   CONTINUE
     FUNK = SS
     RETURN
     END

     FUNCTION FORM(WHAT, XXX)
     IMPLICIT REAL*8 (A - H, O - Z)
     DIMENSION ADD(15)
     COMMON/STUFF/ ADD
     I = DINT(WHAT)
     FORM = ADD(I) * (-1.0 * ((XXX - ADD(I + 1)) / ADD(I + 2))**2)
     RETURN
     END
```

LITERATURE CITED

1. B. Rand, "Carbon Fibers from Mesophase Pitch," in <u>Handbook of Composites, Vol. 1, Strong Fibers</u>, edited by W. Watt and B. V. Perov, Elsevier, New York, 497, (1985).

2. D. M. Riggs, R. F. Shuford, and R. W. Lewis, "Graphite Fibers and Filaments," in <u>Handbook of Composites</u>, edited by G. Lubin, VanNostrand Reinhold Co., New York, 196, (1982).

3. R. J. Diefendorf, in <u>Carbon Fibres and Their Composites</u>, edited by E. Fitzer, Springer-Verlag, New York, 46, (1985).

4. D. D. Edie, "Pitch and Mesophase Fibers," In <u>Carbon Fibers Filaments and Composites</u>, edited by J. L. Figueiredo, C. A. Bernardo, R. T. K. Baker, and K. J. Huttinger, Kluwer Academic Publishers, Dordrecht, The Netherlands, 43, (1990).

5. M. S. Dresselhaus, G. Dresselhaus, K. Sugihara, I. L. Spain, and H. A. Goldberg, <u>Graphite Fibers and Filaments</u>, Springer-Verlag, New York, (1988).

6. C. A. Coulson, <u>Valence</u>, Clarendon Press, Oxford, (1952).

7. W. N. Reynolds, <u>Physical Properties of Graphite</u>, Elsevier, Amsterdam, (1968).

8. R. E. Franklin, Transactions of the Faraday Society, **45**, 668, (1949).

9. A. R. Ubbelohde and F. A. Lewis, <u>Graphite and its Crystal Compounds</u>, Clarendon Press, Oxford, (1960).

10. S. Ergun, Journal of Physical Chemistry, **60** (4), 480, (1960).

11. E. I. Shobert, <u>Carbon and Graphite</u>, Academic Press, New York, (1964).

12. L. C. F. Blackman, editor, <u>Modern Aspects of Graphite Technology</u>, Academic Press, New York, (1970).

13. H. Lipsom and A. R. Stokes, Proceedings of the Royal Society of London, **A181**, 101, (1942).

14. U. Hoffman and A. Clauss, Proceedings of the Third Carbon Conference, Buffalo, NY, 241, (1959).

15. G. E. Bacon, Nature, **166**, 794, (1950).

16. B. E. Warren, Physical Review B, **59**, 693, (1941).

17. J. Biscoe and B. E. Warren, Journal of Applied Physics, **13**, 364, (1942).

18.   J. Maire and J. Mering, Journal of Chemical Physics, **57**, 803, (1960).

19.   G. E. Bacon, Acta Crystallographica, **3**, 137, (1950).

20.   J. C. Bokros, "Deposition, Structure, and Properties of Pyrolytic Carbon," in <u>Chemistry and Physics of Carbon, Vol. 5</u>, edited by P. L. Walker, Jr., Marcel Dekker, New York, 1, (1969).

21.   M. A. Ali and C. A. Coulson, Journal of the American Chemical Society, **81**, 1558, (1959).

22.   J. M. Thomas and C. Roscoe, "Nonbasal Dislocations in Graphite," in <u>Chemistry and Physics of Carbon, Vol. 3</u>, edited by P. L. Walker, Jr., Marcel Dekker, New York, 1, (1968).

23.   S. Mrozowski, "Kinetics of Graphitization," in <u>Kinetics of High Temperature Processes, Part IV</u>, edited by W. D. Kingery, Technology Press, Cambridge, MA, and Wiley and Sons, New York, 264, (1959).

24.   J. Lachter, B. N. Mehrotra, L. G. Henry, and R. H. Bragg, Carbon, **25** (6), 775, (1987).

25.   H. Brown, <u>Advances in Liquid Crystals, Vol. 5</u>, 157-213, Academic Press, New York, 1982.

26.   L. S. Singer, "High Modulus High Strength Fibers Produced from Mesophase Pitch," U. S. Patent 4,005,183, (1977).

27.   I. C. Lewis, "Process for Producing Fibers from Mesophase Pitch," U. S. Patent 4,032,430, (1977).

28.   S. Chwastiak and I. C. Lewis, Carbon, **16** (2), 156, (1978).

29.   R. J. Diefendorf and D. M. Riggs, "Forming Optically Anisotropic Pitches," U. S. Patent 4,208,267, (1980).

30.   I. Mochida, S. Shimizu, and Y. Korai, Carbon, **26** (2), 843, (1988).

31.   I. Mochida, S. Shimizu, and Y. Korai, Carbon, **28** (2,3), 311, (1990).

32.   R. Fujiura, T. Kojima, Y. Korai, and I. Mochida, Extended Abstracts of the International Conference on Carbon, Essen, Germany, 735, (1992).

33.   M. Endo, Journal of Materials Science, **23** (2), 598, (1988).

34.   D. D. Edie and M. G. Dunham, Carbon, **27** (2), 647, (1989).

35.   S. Whitehouse and B. Rand, Proceedings of the International Conference on Carbon, University of Newcastle upon Tyne, U. K., 175, (1988).

36.   M. B. Sumner, Proceedings of the International Conference on Carbon, Newcastle upon Tyne, U. K., 52, (1988).

37. I. Mochida, K. Shimizu, Y. Korai, Y. Sakai, S. Fujiyama, H. Toshima, and T. Hono, Carbon, **30** (1), 55, (1992).

38. T. Hamada, T. Nishida, M. Furuyama, and T. Tomioka, Carbon, **26** (6), 837, (1988).

39. T. Matsumoto, Pure and Applied Chemistry, **57**, 1553, (1985).

40. D. M. Riggs and H. E. Redick, "Process for Adjusting the Fiber Structure of Mesophase Pitch Fibers," U. S. Patent 4,576,811, (1986).

41. D. D. Edie, N. D. Fox, and B. C. Barnett, Carbon, **24** (4), 477, (1986).

42. S. Kase and T. Matsuo, Journal of Polymer Science A, **3**, 2541, (1965).

43. S. Kase, "Mathematical Simulation of Melt Spinning Dynamics," in High-Speed Fiber Spinning, edited by A. Ziabicki and H. Kawai, Wiley Interscience, New York, 67, (1985).

44. J. J. McHugh and D. D. Edie, Proceedings of the International Conference on Carbon, Essen, Germany, 683, (1992).

45. J. B. Donnet and R. C. Bansal, Carbon Fibers, Marcel Dekker, Inc., New York, (1984).

46. C. A. Stirling and B. Rand, Proceedings of the International Conference on Carbon, Newcastle upon Tyne, U. K., 22, (1988).

47. S. Otani, Carbon, **5** (3), 219, (1967).

48. J. B. Barr and I. C. Lewis, Carbon, **16** (6), 439, (1978).

49. I. Mochida, S.M. Zeng, Y. Korai, and H. Toshima, Carbon, **28** (1), 193, (1990).

50. J. L. White and P. M. Schaeffer, Proceedings of the 17th Biennial Conference on Carbon, 626, (1985).

51. W. C. Stevens and R. J. Diefendorf, Proceedings of the International Conference on Carbon, Baden-Baden, Germany, 37, (1986).

52. W. C. Stevens and R. J. Diefendorf, Proceedings of the International Conference on Carbon, Baden-Baden, Germany, 40, (1986).

53. A. J. Kazmer and R. J. Diefendorf, Proceedings of the 20th Biennial Conference on Carbon, Santa Barbara, CA, 178, (1991).

54. T. Kasuh and H. Marsh, Proceedings of the 18th Biennial Conference on Carbon, Worcester, MA, 292, (1987).

55. H. E. Rast III, M. S. Thesis, "A Thermosetting Study on Mesophase Pitch Based Carbon Fibers," Clemson University, Clemson, SC, (1991).

56. M. Hein and H. Weber, Proceedings of the International Conference on Carbon, Newcastle upon Tyne, U. K., 404, (1988).

57. J. G. Lavin, Carbon, **30** (3), 351, (1992).

58. J. E. Bailey and A. J. Clarke, Nature, **229**, 234, (1971).

59. D. J. Johnson, Journal of Physics D: Applied Physics, **20** (2), 286, (1987).

60. W. A. DuBose, M. S. Thesis, "Melt-Spinning of Non-Circular Carbon Fibers," Clemson University, Clemson, SC, (1988).

61. K. E. Fosaaen, Clemson University, unpublished data, (1990).

62. T. Kasuh and H. Marsh, Proceedings of the International Conference on Carbon, Newcastle upon Tyne, U. K., 452, (1988).

63. K. Miyazawa, T. Yokono, and Y. Sanada, Carbon, **17** (3), 223, (1979).

64. S. E. Stein, Carbon, **19** (6), 421, (1981).

65. J. S. Hayward, B. Ellis, and B. Rand, Carbon, **26** (1), 71, (1988).

66. K. Azami, T. Yokono, Y. Sanada, and S. Uemura, Carbon, **27** (2), 177, (1989).

67. T. J. Peters, R. G. Jenkins, A. W. Scaroni, and P. L. Walker, Jr., Carbon, **29** (7), 981, (1991).

68. N. A. Lapina, V. S. Ostrovskii, and K. I. Syskov, Carbon, **14** (1), 39, (1976).

69. K. Kawamura and R. H. Bragg, Carbon, **24** (3), 301, (1986).

70. B. A. Newman, Proceedings of International Conference on Carbon, Baden-Baden, Germany, 147, (1986).

71. L. S. Singer and I. C. Lewis, Carbon, **16** (6), 417, (1978).

72. I. C. Lewis, Carbon, **18** (3), 191, (1980).

73. E. Fitzer, W. Frohs, and G. Liu, Proceedings of the International Conference on Carbon, Baden-Baden, Germany, 873, (1986).

74. E. Fitzer and W. Frohs, Proceedings of the International Conference on Carbon, Newcastle upon Tyne, U. K., 298, (1988).

75. R. C. Schikner, M. S. Thesis, "The Effect of Pre-Carbonization on the Physical Properties of C-Shape Melt-Spun Carbon Fibers," Clemson University, Clemson, SC, (1989).

76. G. Z. Liu, personal communication, (1991).

77. H. N. Murty, D. L. Biederman, E. A. Heintz, Carbon, **7** (6), 667, (1969).

78. J. Maire and J. Mering, "Graphitization of Soft Carbons," in <u>Chemistry and Physics of Carbon, Vol. 6</u>, edited by P. L. Walker, Marcel Dekker, New York, 125, (1970).

79. D. B. Fischbach, "The Kinetics and Mechanism of Graphitization," in <u>Chemistry and Physics of Carbon, Vol. 7</u>, edited by P. L. Walker, Jr., 1. Marcel Dekker, New York, (1971).

80. S. Mrozowski, "Kinetics of Graphitization," in <u>Kinetics of High Temperature Processes</u>, edited by W. D. Kingery, 264, John Wiley and Sons, New York, (1958).

81. W. Ruland, "X-ray Diffraction Studies on Carbon and Graphite," in <u>Chemistry and Physics of Carbon, Vol. 4</u>, edited by P. L. Walker, Jr., 1, Marcel Dekker, New York, (1968).

82. S. Ergun, "Structure of Carbon," in <u>Chemistry and Physics of Carbon, Vol. 3</u>, edited by P. L. Walker, Jr., 211. Marcel Dekker, New York, (1967).

83. R. R. Saxena and R. H. Bragg, Carbon, **16** (5), 373, (1978).

84. R. H. Bragg, D. F. Baker, L. G. Henry, and B. N. Mehrotra, Proceedings of the 16th Biennial Conference on Carbon, San Diego, CA, 122, (1983).

85. C. Yokokawa, K. Hosokawa, Y. Takegami, Carbon, **5** (5), 475, (1967).

86. E. A. Heintz, Proceedings of the International Carbon and Graphite Conference, Buffalo, NY, 575, (1978).

87. B. P. Richards, Journal of Applied Crystallography, **1** (1), 35, (1968).

88. A. Oberlin, Carbon, **17** (1), 7, (1979).

89. D. J. Johnson, I. Tomizuka, O. Watanabe, Carbon, **13** (6), 529, (1975).

90. C. A. Coulson and M. D. Poole, Carbon, **2** (3), 275, (1964).

91. A. Pacault, "The Kinetics of Graphitization," in <u>Chemistry and Physics of Carbon, Vol. 7</u>, edited by P. L. Walker, Jr., 107. Marcel Dekker, New York, (1971).

92. J. Lachter, R. H. Bragg, Proceedings of the International Conference on Carbon, Baden-Baden, Germany, 248, (1986).

93. R. W. Henson and W. N. Reynolds, Carbon, **3** (3), 277, (1965).

94. E. Fitzer and S. Weisenburger, Carbon, **14** (4), 195, (1976).

95. R. E. Franklin, Acta Crystallographica, **4**, 253, (1951).

96. R. M. Mayer, Carbon, **7** (4), 512, (1969).

97. P. A. Thrower and R. T. Loader, Carbon, **7** (4), 467, (1969).

98. T. Noda, Carbon, **18** (1), 2, (1980).

99. E. G. Steward, H. W. Davidson, Proceedings of the First International Conference on Industrial Carbon and Graphite, Buffalo, NY, 207, (1958).

100. E. G. Steward, B. P. Cook, Zeitschrift fur Kristallographie, **114**, 245, (1969).

101. J. W. Patrick, M. J. Reynolds, and F. H. Shaw, Carbon, **13** (6) 509, (1975).

102. W. V. Kotlensky, Carbon, **9** (4), 523, (1971).

103. C. H. Chang, R. A. Beyerlein, and S. S. Chan, Carbon, **22** (4-5), 393, (1984).

104. H. P. Boehm, in <u>Advances in Catalysts, Vol. 16</u>, 179, Academic Press, New York, (1966).

105. X. Bourrat, A. Oberlin, and J. C. Escalier, Fuel, **66**, 542, (1987).

106. R. J. Diefendorf, Clemson University, Clemson, SC, personal communication, 1992.

107. I. Letizia, High Temperatures-High Pressures, **9**, 291, (1977).

108. M. P. Whittaker and L. I. Grindstaff, Carbon, **7** (5), 615, 1969.

109. I. Mochida, S. Nakamo, T. Oyama, Y. Nesumi, and Y. Todo, Carbon, **26** (4), 751, 1988.

110. Y. Sugimoto, F. J. Derbyshire, and A. W. Scaroni, Carbon, **23** (4), 411, 1985.

111. S. R. Brandtzaeg, Ph. D. Thesis, "Structural Changes During Calcination of Coke and Anthracite," Institutt for Uorganisk Kjemi, Norges Tekniske Høgskole, Universitetet I Trondheim, Norway, (1985).

112. E. Fitzer and H. P. Janoschek, High Temperatures-High Pressures, **9**, 243, (1977).

113. S. R. Brandtzœg and H. A. Øye, Carbon, **26** (2), 163, 1988.

114. K. Fujimoto, M. Sato, M. Yamada, R. Yamashita, and K. Shibata, Carbon, **24** (4), 397, (1986).

115. E. Fitzer and S. Weisenburger, Carbon, **14** (4), 195, (1976).

116. M. L. Pearce and E. A. Heintz, Journal of Physical Chemistry, **70** (6), 1935, (1966).

117. J. Gillot, B. Lux, P. Cornuault, and F. du Chaffaut, Carbon, **6** (3), 389, (1968).

118. D. K. Rogers, S. P. Jones, C. C. Fain, and D. D. Edie, Carbon, **31**, in press, (1993).

119. I. Mochida, S. Nakamo, T. Oyama, Y. Nesumi, and Y. Todo, Carbon, **26** (4), 751, (1988).

120. E. Fitzer, M. Heine, and H. P. Rensch, Proceedings of the International Conference on Carbon, Baden-Baden, Germany, 859, (1986).

121. I. Mochida, Y. D. Park, and Y. Korai, Proceedings of the International Conference on Carbon, Baden-Baden, Germany, 632, (1986).

122. L. P. Cornec, unpublished M. S. Thesis, Clemson University, Clemson, SC, (1991).

123. W. S. Hummers and R. E. Offerman, Journal of the American Chemical Society, **80**, 1339, (1958).

124. A. M. Rodriguez and P. S. Valerga Jiminez, Carbon, **24** (2), 163, (1986).

125. K. Honjo and A. Shindo, Carbon, **24** (2), 230, (1986).

126. A. Oya, Y. Ida, M. Takabatake, S. Otani, and H. Marsh, Journal of Materials Science, **16** (7), 1809, (1981).

127. D. Tsoubar and J. Mering, Journal of Applied Crystallography, **2**, 128, (1969).

128. D. J. Johnson, D. Crawford, and C. Oates, Proceedings of the Tenth Biennial Conference on Carbon, Bethlehem, PA, 29, (1971).

129. K. Komatsu and T. Nagamiya, Journal of the Physical Society of Japan, **6** (6), 438, (1951).

130. K. Komatsu, Journal of the Physical Society of Japan, **10** (5), 346, (1955).

131. L. A. Girifalco and R. A. Lad, Journal of Chemical Physics, **25**, 693, (1956).

132. B. T. Kelly and M. J. Duff, Carbon, **8** (1), 77, (1970).

133. R. Al-Jishi and G. Dresselhaus, Physical Review B, **26** (8), 4514, (1982).

134. H. J. F. Jansen and A. J. Freeman, Physical Review B, **35** (15) 8207, (1987).

135. B. T. Kelly, Physics of Graphite, Applied Science Publishers, London, (1981).

136. M. F. Collins and B. C. Haywood, Carbon, **7** (6), 663, (1960).

137. J. C. Bowman and J. A. Krumhansl, Journal of the Physics and Chemistry of Solids, **6**, 367, (1958).

138. B. J. C. van der Hoeven and P. H. Keesom, Physical Review, **130** (4) 1318, (1963).

139. G. E. Bacon, Journal of Applied Chemistry, **6** (11), 477, (1956).

140. D. A. Ratkowsky, Carbon, **24** (2), 211, (1986).

141. W. Ruland, Journal of Applied Physics, **38** (9), 3585, (1967).

142. J. B. Barr, S. Chwastiak, R. Didchenko, I. C. Lewis, R. T. Lewis, and L. S. Singer, Applied Polymer Symposia No. 29, John Wiley and Sons, New York, 161, (1976).

143. A. A. Bright and L. S. Singer, Carbon, **17** (1) 59, (1979).

144. Thornel Product Information, Amoco Performance Products, Inc., Atlanta, GA, (1991).

145. D. P. Anderson, University of Dayton Research Institute, Dayton, OH, personal communication, (1990).

146. E. I. Du Pont de Nemours & Company, Wilmington, DE, Fiber G product data sheets, (1989).

147. B. Nysten, J-P. Issi, R. Barton, Jr., D. R. Boyington, and J. G. Lavin, Proceedings of the International Conference on Carbon, Paris, France, 630, (1990).

148. Mitsubishi Gas Chemical Company, product data sheet, (1992).

149. D. A. Schulz, SAMPE Journal, **23** (2), 27, (1987).

150. M. Guigon and A. Oberlin, Composite Science and Technology, **25**, 231, (1986).

151. B. W. Rosen and B. J. Sullivan, Proceedings of the 19th Biennial Conference on CArbon, University Park, PA, 300, (1989).

152. D. J. Johnson and H. M. Dyson, Proceedings of the International Conference on Carbon, Newcastle upon Tyne, U. K., 383, (1988).

153. D. D. Edie, G. J. Hayes, H. E. Rast III, and C. C. Fain, High Temperatures-High Pressures, **22**, 289, (1990).

154. D. D. Edie and C. C. Fain, Proceedings of the International Conference on Carbon, Baden-Baden, Germany, 629, (1986).

155. B. S. Rhee and S. K. Ryu, Proceedings of the International Conference on Carbon, Paris, France, 178, (1990).

156. B. S. Rhee, S. K. Ryu, S. J. In, J. P. Kim, and Y. G. Jo, Proceedings of the 20th Biennial Conference on Carbon, Santa Barbara, CA, 306, (1991).

157. D. A. Jaworske, J. R. Gaier, C. Maciag, and M. E. Slabe, Proceedings of the 18th Biennial Conference on Carbon, Worcester, MA, 235, (1987).

158. D. K. Rogers, K. E. Robinson, C. C. Fain, and D. D. Edie, Proceedings of the Twentieth Biennial Conference on Carbon, Santa Barbara. CA, 248, (1991).

159. W. De Sorbo and W. W. Tyler, Journal of Chemical Physics, **21**, 1660, (1953).

160. P. H. Keesom and N. Pearlman, Physical Review, **99** (4), 1119, (1955).

161. W. De Sorbo and G. E. Nichols, Journal of the Physics and Chemistry of Solids, **6**, 352, (1958).

162. J. A. Krumhansl and H. Brooks, Journal of Chemical Physics, **21**, 1663, (1963).

163. U. Bergenlid, R. W. Hill, E. T. Webb, and J. Wilks, Philosophical Magazine, Seventh Series, **45** (367), 851, (1954).

164. J. E. Hove, Proceedings of the First International Conference on Industrial Carbons and Graphites, London, U. K., 201, (1957).

165. B. T. Kelly, "Thermal Conductivity of Graphite," in Physics and Chemistry of Carbon, Vol. 5, edited by P. L. Walker, Jr., 119, (1969).

166. J. Heremans, I. Rahim, and M. S. Dresselhaus, Physical Review B, **32** (10), 6742, (1985).

167. J-P. Issi, B. Nysten, and L. Piraux, Journal of Physics D: Applied Physics, **20** (3), 257, (1987).

168. J. M. Ziman, Electrons and Phonons: The Theory of Transport Phenomena in Solids, Clarendon Press, Oxford, (1960).

169. C. Kittel, Introduction to Solid State Physics, Sixth Edition, John Wiley and Sons, New York, (1986).

170. R. Taylor, Philosophy Magazine, Eighth Series, **13** (121), 157, (1966).

171. R. P. Tye, Thermal Conductivity, Vols. 1 and 2, Academic Press, Inc., New York, (1969).

172. R. Pierels, Quantum Theory of Solids, Oxford University Press, New York, (1954).

173. J. Heremans and C. P. Beetz, Physical Review B, **32** (4), 1981, (1985).

174. K. Siguhara, I. L. Spain, and H. A. Goldberg, Graphite Fibers and Filaments, John Wiley and Sons, New York, (1988).

175. C. A. Klein, Review of Modern Physics, **34** (1), 56, (1962).

176. J. C. Bowman, J. A. Krumhansl, and J. T. Meers, First Conference on Industrial Carbon and Graphite, London, 1957, Society of Chemical Industry, 52, (1958).

177. G. A. Slack, Physical Review, **127** (3), 694, (1962).

178. M. G. Holland, Physical Review, **113**, 1046, (1959).

179. M. W. Pilling, B. Yates, M. A. Black, and P. Tattersall, Journal of Materials Science, **14** (6), 1326, (1979).

180. D. J. Radcliffe and H. M. Rosenberg, Cryogenics, 245, May (1982).

181. D. P. H. Hasselman, L. F. Johnson, R. Syed, M. P. Taylor, and K. Chyung, Journal of Materials Science, **22**, 701, (1987).

182. L. F. Johnson, D. P. H. Hasselman, and E. Milford, Journal of Materials Science, **22**, 3111, (1987).

183. "High-Thermal-Conductivity Composites for Passive Thermal Management," DOD Metal Matrix Composites Information Analysis Center Current Highlights, **8** (2), (1988).

184. C. C. Hung and J. Miller, Carbon, **25** (5), 679, (1987).

185. B. J. Sullivan, Proceedings of the 19th Biennial Conference on Carbon, University Park, PA, 284, (1989).

186. D. K. Rogers and G. J. Hayes, unpublished data, (1993).

187. B. T. Kelly, Carbon, **5** (3) 247, (1967).

188. I. M. Kowalsky, Advanced Materials Technology '87 - Volume 32 of the International SAMPE Symposium and Exhibition, edited by R. Carson, M. Burg, K. J. Kjoller, and F. J. Riel, 953, (1987).

189. N. K. Fox, "Melt-Spinning of Non-Circular Carbon/Graphite Fibers from Mesophase Pitch," M. S. Thesis, Clemson University, Clemson, SC, (1984).

190. M. G. Harrison, "Microscopic Examination and Mechanical Testing of Circular Hollow and C-shaped Carbon Fibers Melt-Spun from a Mesophase Pitch," M. S. Thesis, Clemson University, Clemson, SC, (1985).

191. J. W. Cogburn, "Process Optimization for C-shape Melt-spun Carbon Fibers," M. S. Thesis, Clemson University, Clemson, SC, (1986).

192. A. M. Harper, "The Electrical Resistivity of Pitch-Based Carbon Fibers," M. S. Thesis, Clemson University, Clemson, SC, (1990).

193. K. E. Robinson, Clemson University, Clemson, SC, unpublished data, (1993).

194. O. Fleurot, "High Thermal Conductivity Carbon Fibers Melt Spun from a Naphthalene-Based Mesophase," M. S. Thesis, Clemson University, Clemson, SC, (1992).

195. Instruction Manual, 910 Differential Scanning Calorimeter System, E. I. Du Pont de Nemours and Company, Scientific and Process Instruments Division, (1978).

196. W. H. Press, B. P. Flannery, S. A. Teukolsky, and W. T. Vetterling, <u>Numerical Recipes</u>, Cambridge University Press, New York, (1989).

197. R. V. Hogg and J. Ledolter, <u>Engineering Statistics</u>, Macmillan Publishing Co., New York, (1987).

198. M. E. Brown, <u>Introduction to Thermal Analysis: Techniques and Applications</u>, Chapman and Hall, New York, (1988).

199. R. B. Bird, W. E. Stewart, and E. N. Lightfoot, <u>Transport Phenomena</u>, Wiley & Sons, New York, (1960).

200. H. S. Carslaw, <u>Introduction to the Mathematical Theory of the Conduction of Heat in Solids</u>, Dover Publication, New York, (1945)

201. T. Brandes, Clemson University, Clemson, SC, personal communication, (1992-1993).

202. Galbraith Laboratories, service information sheets, (1991).

203. M. Tidjani, J. Lachter, T. S. Kabre, and R. H. Bragg, Carbon, **24** (4), 447, (1986).

204. S. A. Howard and K. D. Preston, "Profile Fitting of Powder Diffraction Patterns," in Modern Powder Diffraction, Volume 20: Reviews in Mineralogy, edited by D. L. Bish and J. E. Post, The Mineralogical Society of America, Washington, DC, 217, (1989).

205. D. P. Anderson, "Carbon Fiber Morphology: Wide-Angle X-ray Studies of Pitch- and PAN-based Carbon Fibers," Doc. No. WRDC-TR-89-4072, Air Force Materials Laboratory, Wright Research and Development Center, Wright-Patterson AFB, Dayton, OH, (1989).

206. National Bureau of Standards Certificate, Standard Reference Material 640b, (1987).

207. M. U. Cohen, Review of Scientific Instruments, **6**, 68, (1935).

208. J. B. Nelson and D. P. Riley, Proceedings of the Physical Society of London, **57**, 160 (1945).

209. B. E. Warren and B. L. Averbach, Journal of Applied Physics, **21**, 595, (1950).

210. H. P. Klug and L. E. Alexander, X-Ray Diffraction Procedures, Wiley and Sons, New York, (1974).

211. P.V. Danckwerts, Transactions of the Faraday Society, **47**, 1014 (1951).

212. B. D. Cullity, Elements of X-ray Diffraction, Second Edition, Addison-Wesley Publishing Co., Reading, MA, (1978).

213. S. Bose and R. H. Bragg, Carbon, **19** (4), 289, (1981).

214. L. B. Coleman, Review of Scientific Instruments, **46** (8), 1125, (1975).

215. ASTM Standard D3379-75, (re-approved 1989).

216. E. G. Stoner, "The Effect of Shape on the Tensile Strength of Pitch-Based Carbon Fibers," Ph. D. Dissertation, Clemson University, Clemson, SC, (1991).

217. Y. S. Lim, "Study of Mesophase Formation and Stabilization from a Petroleum Pitch," Ph. D. Dissertation, Clemson University, Clemson, SC, (1985).

218. E. L. Fuller, Oak Ridge National Laboratory, Oak Ridge, TN, personal communication, (1992).

219. B. Cornilsen, Michigan Technological University, Houghton, MI, personal communication, (1992).

220. L. P. Cornec, D. K. Rogers, C. C. Fain, and D. D. Edie, Proceedings of the International Conference on Carbon, Essen, Germany, 710, (1992).

221. J. A. Snipes, Clemson University, Clemson, SC, unpublished data, (1993).

222. D. W. van Krevelen and J. Schuyer, <u>Coal Science: Aspects of Coal Constitution</u>, Elsevier Publishing Co., Princeton, NJ, (1957).

223. K. I. Morita, H. Miyachi, and T. Hiramatsu, Carbon, **19** (1), 11, (1981).

224. A. Munster, <u>Statistical Thermodynamics, Vol. 2</u>, Springer-Verlag, New York, (1974).

225. B. T. Kelly and R. Taylor, "The Thermal Properties of Graphite," in <u>Chemistry and Physics of Carbon, Vol. 10</u>, edited by P. L. Walker, Jr. and P. A. Thrower, Marcel Dekker, New York, 1, (1973).

226. G. W. Castellan, <u>Physical Chemistry, Third Edition</u>, Addison-Wesley Publishing, Reading, MA, (1983).

227. J. H. Sharp and I. A. Wentworth, Analytical Chemistry, **41**, 2060, (1969).

228. F. F. Bentley, L. D. Smithson, and A. L. Rozek, <u>Infrared Spectra and Characteristic Frequencies ~700-300 cm^{-1}</u>, Interscience Publishers, London, (1968).

229. L. M. Sverdlov, M. P. Kovner, and E. P. Krainov, <u>Vibrational Spectra of Polyatomic Molecules, John Wiley and Sons</u>, New York, (1974).

230. F. R. Dollish, W. G. Fateley, and F. F. Bentley, <u>Characteristic Raman Frequencies of Organic Compounds</u>, John Wiley and Sons, New York, (1974).

231. F. Tuinstra and J. L. Koenig, Journal of Chemical Physics, **53**, 1126, (1970).